A STUDY OF THE MICRO-MECHANICS OF GRANULAR MEDIA

DAVID JULIAN BARNES, B.Sc.

A Thesis submitted for the Degree of

Doctor of Philosophy

at

The University of Aston in Birmingham

March 1985

The University of Aston in Birmingham

A STUDY OF THE MICRO-MECHANICS OF GRANULAR MEDIA

A thesis submitted for the degree of Doctor of Philosophy, by David Julian Barnes, March 1985

SUMMARY

The development of more realistic constitutive models for granular media, such as sand, requires ingredients which take into account the internal micro-mechanical response to deformation. Unfortunately, at present, very little is known about these mechanisms and therefore it is instructive to find out more about the internal nature of granular samples by conducting suitable tests.

In contrast to physical testing the method of investigation used in this study employs the Distinct Element Method. This is a computer based, iterative, time-dependent technique that allows the deformation of granular assemblies to be numerically simulated. By making assumptions regarding contact stiffnesses each individual contact force can be measured and by resolution particle centroid forces can be calculated. Then by dividing particle forces by their respective mass, particle centroid velocities and displacements are obtained by numerical integration. The Distinct Element Method is incorporated into a computer program 'Ball'. This program is effectively a numerical apparatus which forms a logical housing for this method and allows data input and output, and also provides testing control. By using this numerical apparatus tests have been carried out on disc assemblies and many new interesting observations regarding the micro-mechanical behaviour are revealed.

In order to relate the observed microscopic mechanisms of deformation to the flow of the granular system two separate approaches have been used. Firstly a constitutive model has been developed which describes the yield function, flow rule and translation rule for regular assemblies of spheres and discs when subjected to coaxial deformation. Secondly statistical analyses have been carried out using data which was extracted from the simulation tests. These analyses define and quantify granular structure and then show how the force and velocity distributions use the structure to produce the corresponding stress and strain-rate tensors.

KEY WORDS: COMPUTER SIMULATED EXPERIMENTATION
IDEALISED PARTICULATE ASSEMBLIES
MICROSTRUCTURAL CHARACTERISATION
INDUCED ANISOTROPY
MICROMECHANICAL MECHANISMS

ACKNOWLEDGEMENTS

I would like to thank my research supervisor, Dr. C. Thornton, for his much appreciated and enthusiastic support throughout the research period. I am grateful to him for the invaluable and frequent, lengthy discussion periods which took place during this time.

An acknowledgement is also expressed to Gail, who did not only type the manuscript but also gave a substantial input into its production and presentation.

I must also take this opportunity to thank my wife Deborah, who has given me loving support throughout all aspects of my career.

C O N T E N T S

C O N T E N T S continued

C O N T E N T S continued

LIST OF FIGURES

LIST OF FIGURES continued

LIST OF FIGURES continued

L I S T O F F I G U R E S continued

LIST OF FIGURES continued

1 INTRODUCTION

By considering particulate media to be a continuum it is possible to analyse complex, heterogeneous problems using sophisticated computer based techniques such as the Finite Element Method. Such an approach, however, depends on the validity of the constitutive laws incorporated into the formulation. To date, no entirely satisfactory constitutive model for granular material, such as sand, exists. This is due to the complex macroscopic behaviour which is the result of its internal discrete nature. It is, therefore, instructive to investigate the deformation processes which may occur in particulate assemblies. In this way, a better understanding of the mechanics of particulate material can be obtained from which it is possible to develop more realistic constitutive laws. These laws may then be incorporated into conventional Finite Element programs.

Three basic features of granular materials which constitutive laws try to model are stiffness, strength and volume change. Based on experimental observations of these features many constitutive models have been proposed. Some proposals oversimplify the problem (perhaps by placing restrictions on the stress state) and others require the determination of many parameters, some of which have no clear physical meaning. Rowe (1962) stated that 'The way out of the difficulty lies in dropping the old fundamental principles and starting again from the elementary fact that sand consists of individual grains'. It is now widely recognised that the description of the overall macroscopic behaviour of particulate media requires a micromechanical formulation of stress and strain-rate. It has been reported by Nemat-Nasser (1982) that one concept which is becoming firmly established is to describe the overall stress in terms of micromeasures and a definition of structure. It is therefore very important to find out more about

the internal mechanisms of deformation.

Traditional laboratory tests on real granular material do not give sufficient information regarding the internal deformation processes. Elementary parameters like the components of stress must be estimated from boundary measurements. New experimental techniques have been developed to detect internal deformation patterns by using infra-red thermography (Luong (1982)) and measuring the displacements of embedded lead shot in samples by using X-ray photography (Roscoe et al (1963)). None of these techniques, however, are capable of describing microscopic particle interactions. It is this problem of experimental measurement that has led to the investigation of simpler systems of particles for which microscopic forces and displacements can be either calculated or measured. These systems consist of particles which are geometrically less complicated in shape and packing. The method of investigation may be physical, analytical or numerical.

1.1 RESEARCH ON IDEALISED GRANULAR MATERIAL

By utilising the photoelastic property of certain materials, e.g. pyrex glass or perspex, it is possible to optically measure parameters that directly relate to stresses. When large particles are used for testing, contact forces can be satisfactorily determined, which means that the internal force distribution of the assembly can be obtained. Drescher and de Josselin de Jong (1972), Oda and Konishi (1974) and others have used this technique to observe the internal behaviour of 2-dimensional random assemblies of discs. Konishi, Oda and Nemat-Nasser (1982) employed the same technique in similar tests but with elliptically shaped particles to investigate the effects of inherent anisotropy due to particle deposition.

Drescher (1976) and Allersma (1982) have also used photoelasticity to visually determine the stress distribution within specimens of crushed pyrex glass whose voids are filled with a liquid of identical refractive index. Allersma (1982) also developed a technique to optically measure the local stress tensor within the specimen. From using such material, however, it is not possible to determine the microscopic quantities associated with individual particles or particle contacts. This drawback is due to the fact the the particles themselves are invisible and hence it is not possible to make any reference to structure or the microscopic mechanisms of deformation.

Davis and Deresiewicz (1977) presented an analysis which considered the two-dimenstional random packing of identical frictionless discs. The normal compliance at interparticle contacts obeyed a Hertz type law. It was assumed, in order to simplify the analysis that the geometric randomness could be transferred to the assembly stiffness matrix. This meant that the randomness of packing was removed from the particle configuration and incorporated by random variation of contact stiffness. Then by applying boundary loading, to the essentially regular array, the resultant force distribution was found to be inhomogeneous. Useful results from this analysis were limited as contact stiffnesses had been generated randomly in a manner whereby their implication on array geometry had been lost. Since both geometry and stiffness were prescribed arbitrarily the mutual development of the force transmission and structure were unnaturally constrained.

A more realistic approach was developed by Round (1976). The basis of this model was the individual particle contact properties and incorporated a non-linear elastic interaction law at contacts, the

inability of particle contacts to transmit tensile forces, sliding, and also rolling between particles. For convenience the analysis was restricted to 2-dimensional assemblies of discs, but did allow different particle sizes. The computational algorithm incrementally solved the complete load-displacement development both microscopically and macroscopically for stress loading or strain loading. This work has two major drawbacks. Firstly, the validation tests did not support theoretical predictions and no contact force details were provided for comparison with other tests. Secondly, the method had large processing requirements because much computational effort was required to gain internal equilibrium after the application of a load increment. For this reason, the method would be unsuitable where assemblies containing many discs are concerned. Only 33 discs were used in the validation test.

Discrete quantities cannot be applied directly to continuum modelling and therefore statistical averaging is required in order to determine their overall effect on deformation processes. For example, if anisotropy of structure can be related to the inclination of particle contact then a suitable single tensor must be extracted from experimental data that is capable of quantifying the global structural state. Analyses must be carried out in order to quantify microscopic phenomena globally. Hopefully it will then be possible to relate these quantities to the stress and strain-rate tensors. Unfortunately, in physical tests, although the above measurements are possible, they are impractical when considering the accuracy and number of measurements required. Some quantities would require constant monitoring, e.g. accurate determination of contact slip requires a constant checking procedure to ensure that the respective particles have not broken contact. Representation of results by plotting also requires a large manual commitment. It is possibly for

this reason that physical testing has not revealed any more than superficial observations.

Experimentation into idealised particle assemblies can be undertaken by employing computer simulation techniques. Cundall (1971b) has developed such a technique which was termed the Distinct Element Method. Numerical simulation using the Distinct Element Method has been adopted as the method of investigation in this research program. Complete details of the method will be provided later in the thesis.

Numerical simulation is a very powerful tool. Based on very simple assumptions regarding interparticle contacts the system can predict extremely complex behaviour. The study of such systems is called Complex Systems Theory in which the computational method plays the central role. Any physical process can be described by an algorithm, and so any physical process can be described by a computational process. Experimentation using such a system allows the use of hypothetical natural laws. For example, the interparticle friction law at contacts can be set to allow any coefficient of friction (even frictionless). Tests can also be repeated from initial or earlier points in the test but with some parameters changed. Indeed, the future of numerical simulation is directly dependent upon advances in computer hardware capabilities, and hence, looks most promising and exciting.

It was stated earlier that the future development of constitutive laws should be based on the internal micromechanics. However, suppose the elements of the system under analysis became sufficiently complex such that the accurate prediction of assembly behaviour became computationally irreducible, then no such constitutive formulae could

ever be found. In this case, explicit simulation by computer experimentation would be the only available method of investigating or predicting granular media response. Of course, a great deal of work still needs to be done regarding simulation before accurate prediction is possible. With reducing computing costs computer support for this research is becoming inexpensive.

1.2 ORDER OF PRESENTATION

The main text, that describes the study which has been undertaken is given in the following chapters. This work can be classified under three general headings. The methodology and computational requirements are provided in Chapters 2 and 3. Details of computer simulated experiments and results are presented in Chapters 4 and 5. Chapters 6 and 7 give theoretical and statistical analyses. A breakdown of these chapters is given below.

The derivation of equations which describe the Distint Element Method are given in Chapter 2. This section not only gives the proposed force-displacement law to be used at interparticle contacts but also discusses numerical stability and the suppression of natural assembly oscillations by viscous damping. Chapter 3 gives details of the logic framework within the computer program which allows efficient control of the numerical apparatus. Program facilities are discussed which include methods of assembly boundary control and the extraction of printed and plotted hard copy data.

Chapter 4 describes the 1000 disc test carried out. Preliminary testing and initial considerations are explained and this includes the choice of particle size distribution, assembly generation, choice of physical and control parameters, method of compaction and consolidation, and the method of shearing. In Chapter 5 qualitative

observations are provided based on computer generated graphical output. Individual and interrelated mechanisms are identified and explained. The observations constrain the future development of microstructurally based constitutive models.

Two-dimensional and three-dimensional regular assemblies of spherical particles are analysed in Chapter 6 in an attempt to understand the deformation of simple structures. From this analysis a mathematical theory of plasticity is developed from considerations of load-deformation at interparticle contacts. Included is the full derivation of the yield function, flow rule and translation rule. This work will prove useful if the future development of a constitutive model adopts a plasticity theory approach. Chapter 7 provides statistical analyses of stress and strain-rate for the random assembly tested above. These analyses show the dependence of such tensorquantitieson the assembly structure.

2 THE DISTINCT ELEMENT METHOD

2.1 INTRODUCTION

The Distinct Element Method is a time-dependent finite difference technique which may be used to simulate the progressive movements of particles within an assembly. The method was developed by Cundall (1971a, 1971b, 1974) for the analysis of movements within block systems. Later Cundall and Strack (1979a, 1979b) incorporated the method in the computer program 'Ball', which is capable of simulating the behaviour of irregular assemblies of discs under given boundary conditions.

The application of the Distinct Element Method to assemblies of particles requires cyclic calculations. Particle force increments are calculated at the contact points from the relative velocities of neighbouring particles by using a simple force displacement law. New particle accelerations are then given by Newton's second law of motion by dividing the sum of the contact forces for each particle by its mass. Numerical integration of these accelerations is then performed over a small timestep to give new velocities. These velocities are then used to find new force increments at the contacts providing a check is made to ensure that contact still exists.

The calculation cycle is shown diagrammatically in Figure 2.1 where dashed lines indicate the effect of the assembly boundary conditions.

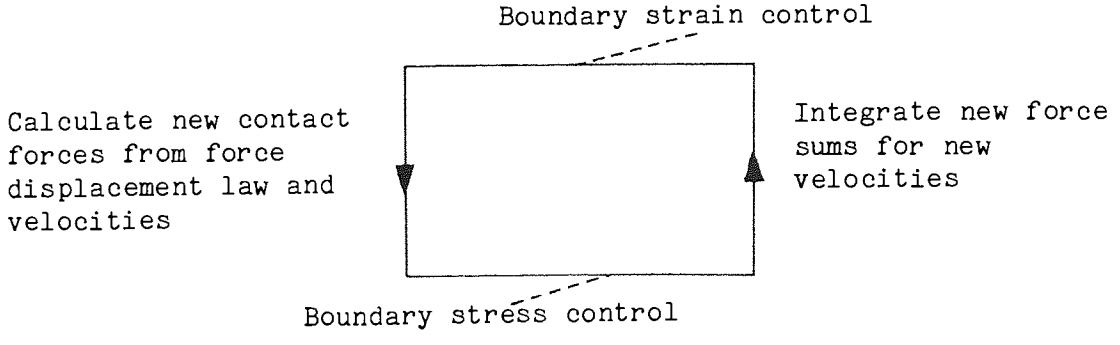

Figure 2.1 The calculation cycle

Equations used to describe the method are derived in the following sections for two dimensional disc assemblies. A guide is also given as to the choice of the control parameters required to ensure quasi-equilibrium during deformation.

2.2 THE FORCE DISPLACEMENT LAW AT CONTACTS

Equations will be presented for the interaction of two discs which are within an assembly. The discs are labelled A and B and their associated quantities are listed below.

DISC	A	B
Radius	R_A	R_B
Mass	m_A	m_B
Moment of inertia	I_A	I_B
Centre coordinates	x_{Ai}	x_{Bi}
Rotation	θ_A	θ_B
Linear velocity	$\dot{x}_{Ai}$	$\dot{x}_{Bi}$
Angular velocity	$\dot{\theta}_A$	$\dot{\theta}_B$
Linear acceleration	$\ddot{x}_{Ai}$	$\ddot{x}_{Bi}$
Angular acceleration	$\ddot{\theta}_A$	$\ddot{\theta}_B$

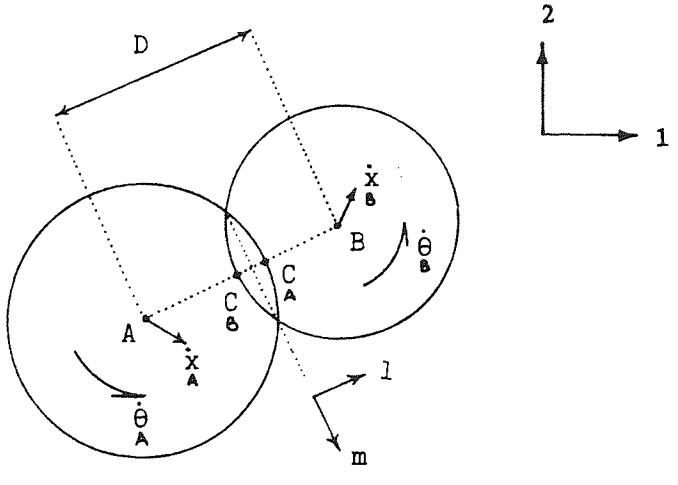

Figure 2.2 Kinematics of A and B

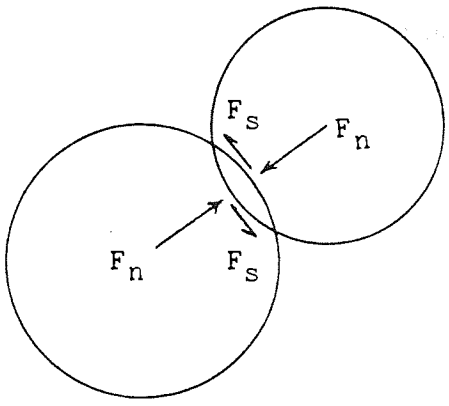

Figure 2.3 Interparticle contact forces

Figure 2.2 shows the position of disc A relative to disc B. Contact between the discs exists if the disc boundaries overlap, i.e. when

$$D < \underset{A}{R} + \underset{B}{R} \tag{2.1}$$

where $D = ((\underset{B}{x}_i - \underset{A}{x}_i)(\underset{B}{x}_i - \underset{A}{x}_i))^{1/2}$

The contact point itself is defined as being midway between point $\underset{A}{C}$ and $\underset{B}{C}$ on the disc boundaries. Unit vectors l_i and m_i are orthogonal, l_i being normal to the contact and in the direction of the line joining disc centres.

$$l_i = (\underset{B}{x}_i - \underset{A}{x}_i)/D \tag{2.2a}$$

$$l_i m_i = 0 \tag{2.2b}$$

The kinematics at the contact point may be understood as the velocity of point $\underset{A}{C}$ relative to $\underset{B}{C}$

$$\dot{\underset{c}{x}}_i = (\dot{\underset{B}{x}}_i - \dot{\underset{A}{x}}_i) - (\dot{\theta}\underset{AA}{R} + \dot{\theta}\underset{BB}{R})m_i \tag{2.3}$$

and resolving vector $\dot{\underset{c}{x}}_i$ into components $\dot{n}$ and $\dot{s}$ that are normal and tangential to the contact

$$\dot{n} = \dot{\underset{c}{x}}_i l_i \tag{2.4a}$$

$$\dot{s} = \dot{\underset{c}{x}}_i m_i \tag{2.4b}$$

and using equation (2.3) equations (2.4) may be written

$$\dot{n} = (\dot{\underset{B}{x}}_i - \dot{\underset{A}{x}}_i)l_i \tag{2.5a}$$

$$\dot{s} = (\dot{\underset{B}{x}}_i - \dot{\underset{A}{x}}_i)m_i - (\dot{\theta}\underset{AA}{R} + \dot{\theta}\underset{BB}{R}) \tag{2.5b}$$

To obtain displacement increments the integration of equations (2.5) is performed over a timestep Δt, wherein it is assumed that velocities remain constant.

$$\Delta n = [(\dot{x}_{Bi} - \dot{x}_{Ai})l_i]\Delta t \tag{2.6a}$$

$$\Delta s = [(\dot{x}_{Bi} - \dot{x}_{Ai})m_i - (\dot{\theta}_A R + \dot{\theta}_B R)]\Delta t \tag{2.6b}$$

Force increments at the contacts are now obtained by multiplying the displacement increments by their respective contact stiffnesses.

$$\Delta F_n = K_n \Delta n \tag{2.7a}$$

$$\Delta F_s = K_s \Delta s \tag{2.7b}$$

The force increments are now used to update the contact forces

$$F_n^{NEW} = F_n^{OLD} + \Delta F_n \tag{2.8a}$$

$$F_s^{NEW} = F_s^{OLD} + \Delta F_s \tag{2.8b}$$

A condition must be imposed that restricts the maximum force obliquity that may be developed at the contact

$$F_s/F_n \not> \mu \tag{2.9}$$

and therefore if $F_s^{NEW} > \mu F_n^{NEW}$ then F_s^{NEW} is reset to the value μF_n^{NEW}.

It should be appreciated that the force displacement law used above is incremental. This suggests that linearity of this law is not inherent in the Distinct Element Method. However, attention will be restricted to linear force displacement laws on the assumption that contact displacements remain small in comparison to disc radii. Contact stiffnesses may therefore be thought of as linear springs connected normally and tangentially across the contacts. The option for the normal and tangential contact stiffnesses to be different will be retained.

If all discs had the same material properties then the maximum allowable force obliquity at contacts could be assumed constant. If this is not the case then the maximum force obliquity depends on the two materials in contact.

2.3 MOTION OF THE DISC CENTRES

The procedure outlined in Section 2.2 is repeated for all contacts within the assembly. The forces F_n and F_s at contacts are resolved into directions 1 and 2 and added to the force sums of their respective discs. Similarly moments RF_s are added to the moment sum of their respective discs.

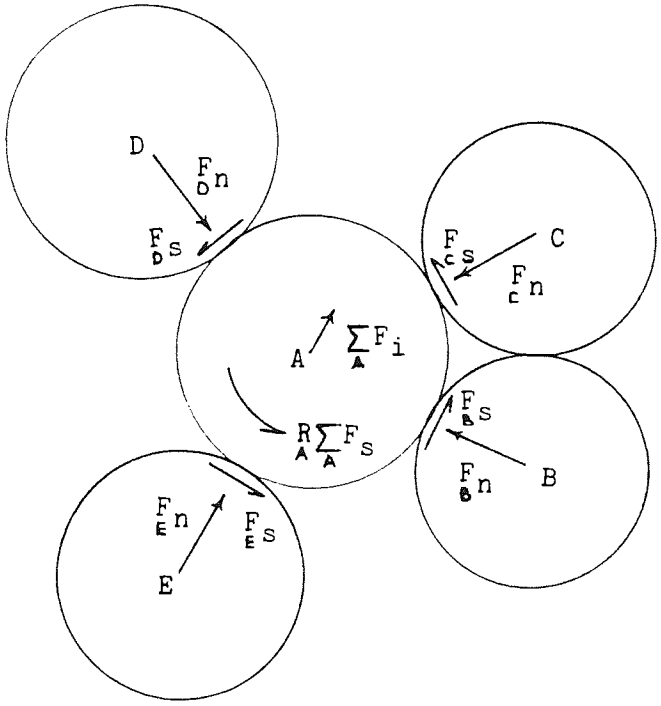

Figure 2.4 Forces acting on disc A

For the example shown in Figure 2.4 all contact forces acting on disc A are resolved to obtain $\sum_A F_i$ which is the resultant disc force. Moments acting at the centre of disc A are also summed to give $\sum_A M = R\sum_A F_s$.

External influences on these resultant quantities, e.g. body force and boundary effects, may be added to $\sum_A F_i$ and $\sum_A M$ if required.

Newton's second law of motion is now used to obtain accelerations

$$\ddot{x}_i = \sum_A F_i / m_A \qquad (2.10a)$$

$$\ddot{\theta}_A = \sum_A M/I_A \tag{2.10b}$$

and integrating equations (2.10) over timestep Δt, assuming accelerations are constant over this period, gives velocity increments

$$\Delta\dot{x}_{Ai} = (\sum_A F_i/m_A)\Delta t \tag{2.11a}$$

$$\Delta\dot{\theta}_A = (\sum_A M/I_A)\Delta t \tag{2.11b}$$

New particle velocities are given by

$$\dot{x}_{Ai}^{NEW} = \dot{x}_{Ai}^{OLD} + \Delta\dot{x}_{Ai} \tag{2.12a}$$

$$\dot{\theta}_A^{NEW} = \dot{\theta}_A^{OLD} + \Delta\dot{\theta}_A \tag{2.12b}$$

Displacement and rotation increments are given by integrating equations (2.12) over timestep Δt assuming velocities are constant over this period.

$$\Delta x_{Ai} = \dot{x}_{Ai}\Delta t \tag{2.13a}$$

$$\Delta\theta_A = \dot{\theta}_A\Delta t \tag{2.13b}$$

Finally disc coordinates and rotation are obtained as

$$x_{Ai}^{NEW} = x_{Ai}^{OLD} + \Delta x_{Ai} \tag{2.14a}$$

$$\theta_A^{NEW} = \theta_A^{OLD} + \Delta\theta_A \tag{2.14b}$$

On examination of equations (2.10), (2.12) and (2.14), it should be noted that they are not coincident in time. This is due to the method of integration as it is assumed that a quantity calculated for time t remains constant between times $t - \Delta t/2$ and $t + \Delta t/2$. As this method of integration is used, accelerations at time t are used to calculate velocities at time $t + \Delta t/2$. Velocities at time $t + \Delta t/2$ are used to calculate displacments and rotations at time $t + \Delta t$. Figure (2.5) shows diagrammatically the timing of calculations for x, $\dot{x}$ and $\ddot{x}$. Solid arrows indicate the order of calculations and dashed arrows indicate that contact, as defined by equation (2.1) exists.

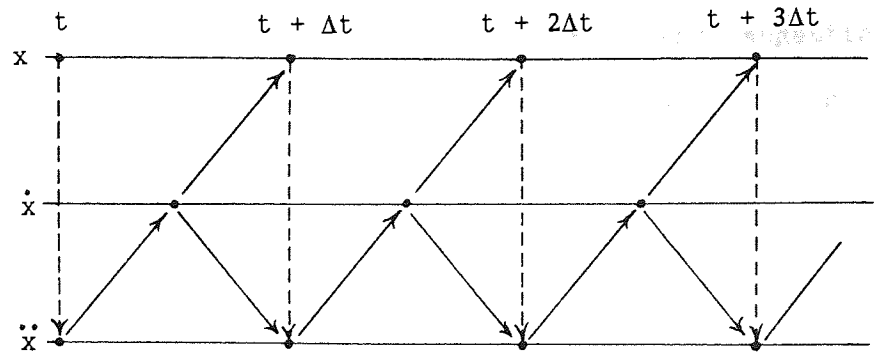

Figure 2.5 Time location of calculations for x, $\dot{x}$, $\ddot{x}$

2.4 ENERGY DISSIPATION

In order for an assembly to reach static equilibrium, after some loading period, it is essential that the free energy is dissipated by some damping process. Frictional damping is already incorporated, dissipating energy at contacts when sliding occurs, i.e. when $F_s/F_n = \mu$. However, this form of damping is not capable of dissipating all the free energy within an assembly. The remaining energy exists due to particle oscillations and rotations.

The oscillations can be split into two types. One type is the high frequency oscillation caused by the relative movement of neighbouring particles. The other type is the low frequency oscillation of the assembly as a whole, caused by the unison movement of the particles.

Three types of viscous damping need to be incorporated into the equations in order to dissipate the free energy that is used in oscillation and rotation. The first type is stiffness proportional damping which acts on the high frequency oscillation at contacts. The second is mass proportional damping which acts on the low frequency oscillation of the particles. The third is inertia proportional damping which acts on the absolute rotational velocity of particles.

Stiffness proportional damping has the effect of connecting

dashpots across the contacts in the normal and tangential directions. The resistive forces of these dashpots are proportional to the relative velocities at the contact. These resistive forces are incorporated in the force increment equations (2.7) to give

$$\Delta F_n = K_n \Delta n + D_K K_n \Delta n \tag{2.15a}$$

$$\Delta F_s = K_s \Delta s + D_K K_s \Delta s \tag{2.15b}$$

where $D_K K_n \Delta t$ and $D_K K_s \Delta t$ are the dashpot coefficients.

It should be noted that during sliding the tangential dashpot is not operational. The reason for this is that the tangential oscillation is not independent of normal oscillation. For example, if the normal force between two particles is constant then during sliding ($F_s = \mu F_n$) there will be no oscillation and therefore the resistance of the dashpot must be set to zero.

Mass proportional damping may be envisaged as dashpots connecting particles to their reference axes. These dashpots operate on the absolute velocity vector components of particles. The resistive forces associated with this type of damping need to be included in the equation of motion (2.10a) to give

$$m\ddot{x}_i + D_m m\dot{x}_i = \sum F_i \tag{2.16}$$

where $D_m m$ is the coefficient of the dashpots. Equation (2.16) may be rewritten using central finite differences (see Figure 2.5) to give

$$m\left[\frac{\dot{x}_i^{NEW} - \dot{x}_i^{OLD}}{\Delta t}\right] + D_m m\left[\frac{\dot{x}_i^{NEW} + \dot{x}_i^{OLD}}{2}\right] = \sum F_i \tag{2.17}$$

which may be rearranged for x_i

$$\dot{x}_i^{NEW} = [\dot{x}_i^{OLD}(1 - D_m \Delta t/2) + \Delta t \sum F/m]/(1 + D_m \Delta t/2) \tag{2.18}$$

Finally, inertia proportional damping is used to dissipate the energy used in rotation. If this type of damping is not used rolling may occur between particles, e.g. in regular assemblies (Figure 2.6) whose particle centres are fixed.

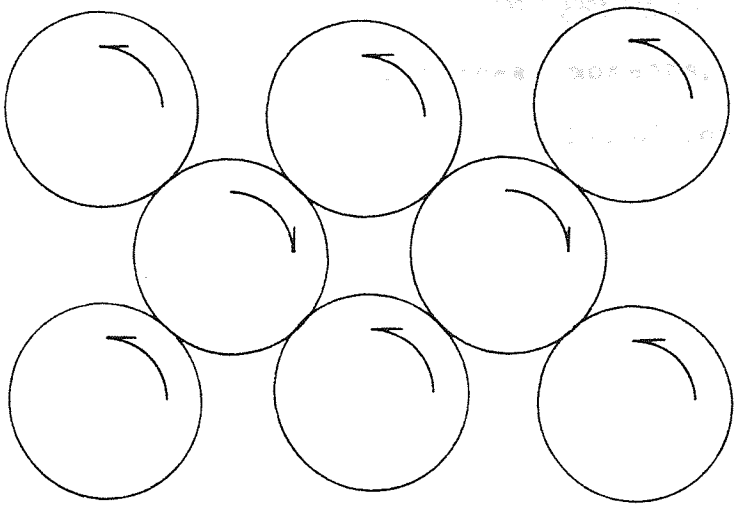

Figure 2.6 Possible rolling of particles within regular arrays

It is therefore necessary to include the resistive moments offered by this form of damping in the equation of motion (2.10(b)) to give

$$I\ddot{\theta} + D_I I\dot{\theta} = \sum M \qquad (2.19)$$

where $D_I I$ is the coefficient of resistance acting on $\dot{\theta}$. Equation (2.19) can now be operated on in a similar way to equation (2.16) to give

$$\dot{\theta}^{NEW} = [\dot{\theta}^{OLD} (1 - D_I \Delta t/2) + \Delta t \sum M/I]/(1 + D_I \Delta t/2) \qquad (2.20)$$

For irregular assemblies undergoing deformation all damping modes are combined in some way to give an overall damping. This damping is not only required to bring the assembly to equilibrium after a loading period but also to minimise the free energy during loading. This is necessary to obtain smooth deformation of the assembly and, hence, obtain meaningful results.

2.5 CONTROL PARAMETERS FOR QUASI-EQUILIBRIUM

The Distinct Element Method is to be used to simulate the slow progressive movement of particles within an assembly in such a way that the assembly can be said to be in a condition of quasi-equilibrium. For this condition to be adhered to it is required that

the particle quantities such as forces, moments, momentums and inertias be minimised. The incorrect selection of control parameters such as the timestep, loading rate and damping constants would not encourage this.

Choosing control parameters for irregular assemblies is complex and therefore tests should be carried out to obtain an understanding of their effects. However, as a guide to the choice of control parameters, simpler systems may be analysed.

2.5.1 Choice of Timestep

The effect of the timestep used in the finite difference equations is investigated using a simple mass-spring system subjected to a constant loading rate $\dot{F}$ as shown in Figure 2.7. This system has

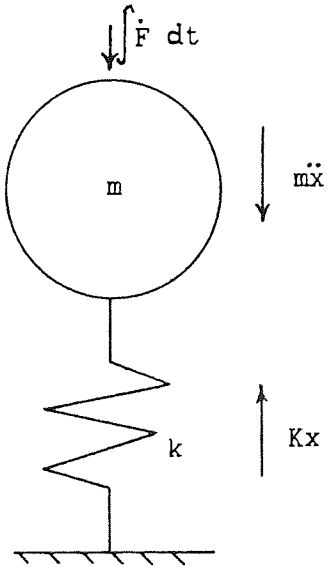

Figure 2.7 A mass-spring system

only one degree of freedom for which the equation of motion is

$$F = m\ddot{x} = -Kx - \int \dot{F} dt = -Kx - \dot{F}t \qquad (2.21)$$

where F gives the deviation from equilibrium and may be termed the out of balance force. Written in finite difference form for time t but taking account of force directions

$$F^{t+\Delta t} = \dot{F}t - Kx^{t+\Delta t} \qquad (2.22)$$

where $x^{t+\Delta t} = x^t + (\dot{x}^{t+\Delta t/2})\Delta t$

and $\dot{x}^{t+\Delta t/2} = \dot{x}^{t-\Delta t/2} + (F^t/m)\Delta t$

Figure 2.8 shows a plot of F against t for equation (2.21) given that $\dot{x} = 0$ at time $t = 0$. The curve is that of a sine wave whose periodicity is $2\pi\sqrt{m/K}$ and amplitude $\dot{F}\sqrt{m/K}$. If equation (2.22) is used to approximate equation (2.21) then accuracy depends on the size of the timestep Δt. The smaller Δt is made, the greater the accuracy. But in the interest of reducing computational effort a greater timestep must be employed.

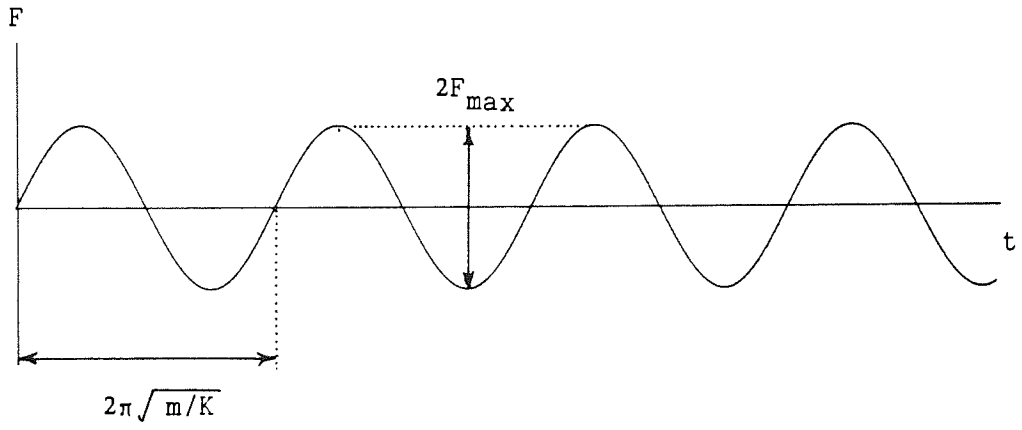

Figure 2.8 Plot of F against t from equation (2.21)

There is an overriding criterion that governs the size of the timestep. This is implemented when the timestep is such as to induce numerical instability resulting in divergent oscillation. Cundall (1971a) proves that, for the above system, the timestep must not be greater than $2\sqrt{m/K}$ to ensure steady oscillation. $2\sqrt{m/K}$ is sometimes termed the critical time step. Figure 2.9 shows approximations of the plot F against t wherein the timestep Δt has been set to various fractions of the critical timestep. From these plots it can be seen that although the time step fraction increases the oscillation is stable. In addition the amplitude of the out of balance force is

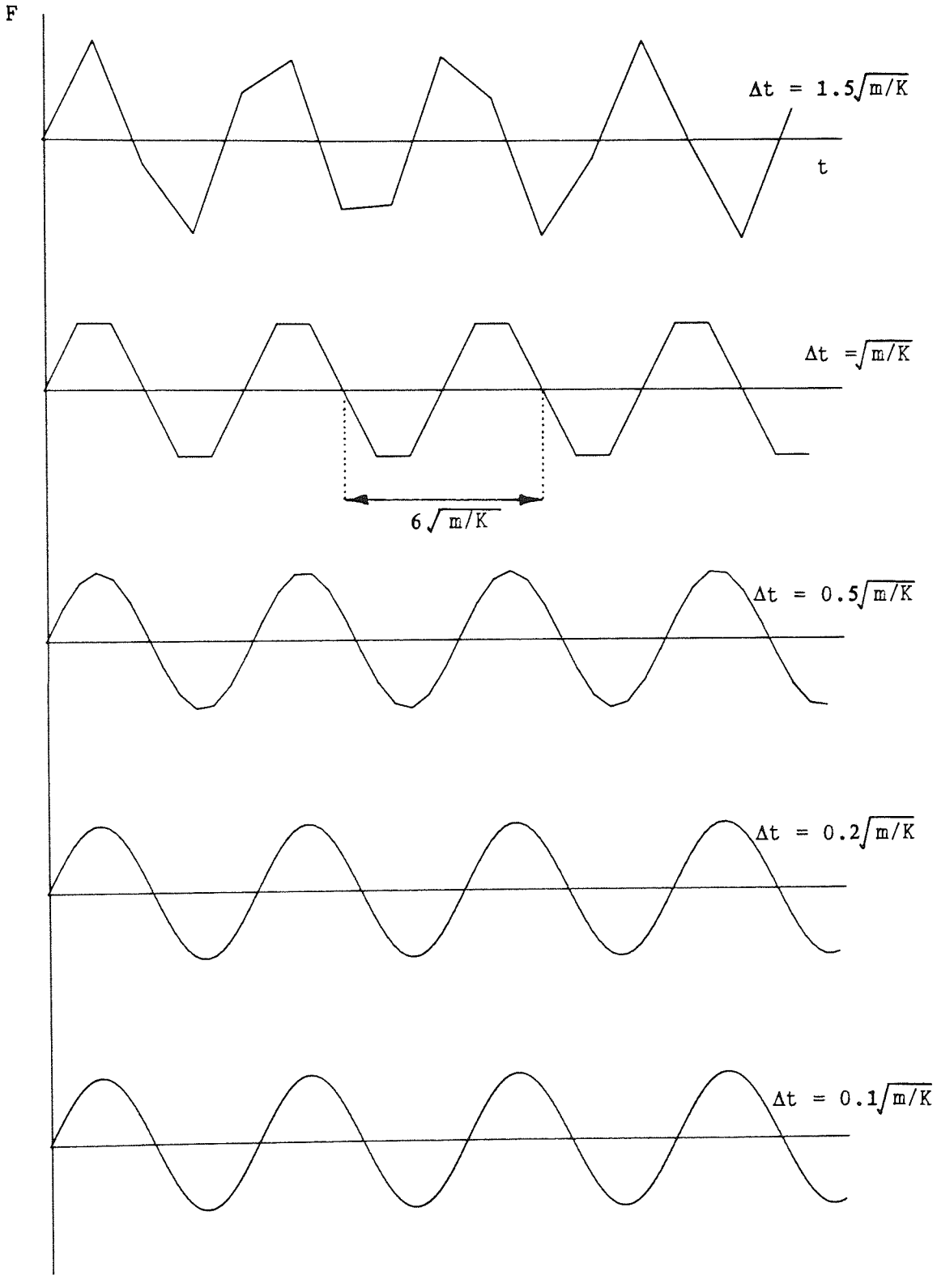

Figure 2.9 Plot of F against t from equation (2.22)

constant. But it must be noted that the periodicity of oscillation decreases as the timestep increases, e.g. the periodicity when $\Delta t = \sqrt{m/K}$ is $6\sqrt{m/K}$.

For a system of two identical discs in contact, which have only one degree of freedom in the direction of the line joining their centres, the critical timestep is $4\sqrt{m/K}$. This is due to the system having an effective mass of 2m and an effective stiffness of K/2.

2.5.2 Choice of Loading Rate and Damping Constants

For quasi-equilibrium the loading rate for an assembly should be small enough to prevent particle forces from being higher than a predetermined value. The predetermined value is usually chosen as a fraction of a typical contact force.

To gain an understanding of the effects of loading rate a simplified analysis was carried out on a system, wherein a mass is connected to ground by a spring and dashpot. Figure 2.10 shows the simplified system and the forces acting on it.

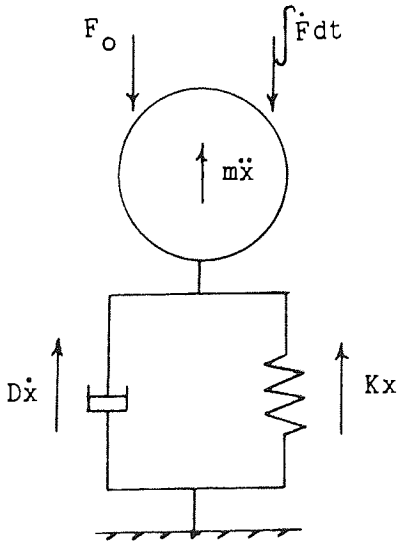

Figure 2.10 A damped mass-spring system with applied loading

Initially at time t = 0 the particle is in equilibrium and $F_o + Kx = 0$, $m\ddot{x} = 0$, $D\dot{x} = 0$ and $\int \dot{F} dt = 0$. After loading for time t the equation of motion for the system is

$$m\ddot{x} = Fo + \int_0^t \dot{F}dt + D\dot{x} + Kx \qquad (2.23)$$

and if it is assumed that the loading rate $\dot{F}$ is constant, equation (2.23) becomes

$$m\ddot{x} = Fo + \dot{F}t + D\dot{x} + Kx \qquad (2.24)$$

Equation (2.24) may now be solved for the underdamped case ($D < 2\sqrt{mK}$) to give the force in the spring (Kx) as

$$Kx = \dot{F}[e^{\alpha t}(D/K\cos(\beta t) - 1/\beta(1+ \alpha D/K)\sin(\beta t)) + (t - D/K)] + Fo \qquad (2.25)$$

where $\alpha = -D/2m \qquad \beta = K/m - \alpha^2$

The deviation of force Kx from equilbrium is

$$F_D = Kx - Fo - \dot{F}t \qquad (2.26)$$

and substituting for Kx from equation (2.25) gives

$$F_D = \dot{F}[e^{\alpha t}(D/K\cos(\beta t) - 1/\beta(1 + \alpha D/K)\sin(\beta t)) - D/K] \qquad (2.27)$$

Equation (2.27) shows that F_D has two components. One of which is independent of time and hence constant, the other being in the form of damped oscillation. The magnitudes of both are directly proportional to the loading rate $\dot{F}$.

If the effect of the damping parameter D is observed, it can be shown from equation (2.27) that the higher the damping, the quicker F_D converges to the value $-\dot{F}D/K$. But it must be noted that although damping reduces the time of oscillation the residual value of F_D is higher.

Figure 2.11 shows plots of F_D against time for various values of the damping parameter. From these it becomes apparent that even for very low values of damping the oscillation decreases in amplitude rapidly.

From the above simplified analyses it has been shown that the deviation from equilibrium, providing the system is numerically stable

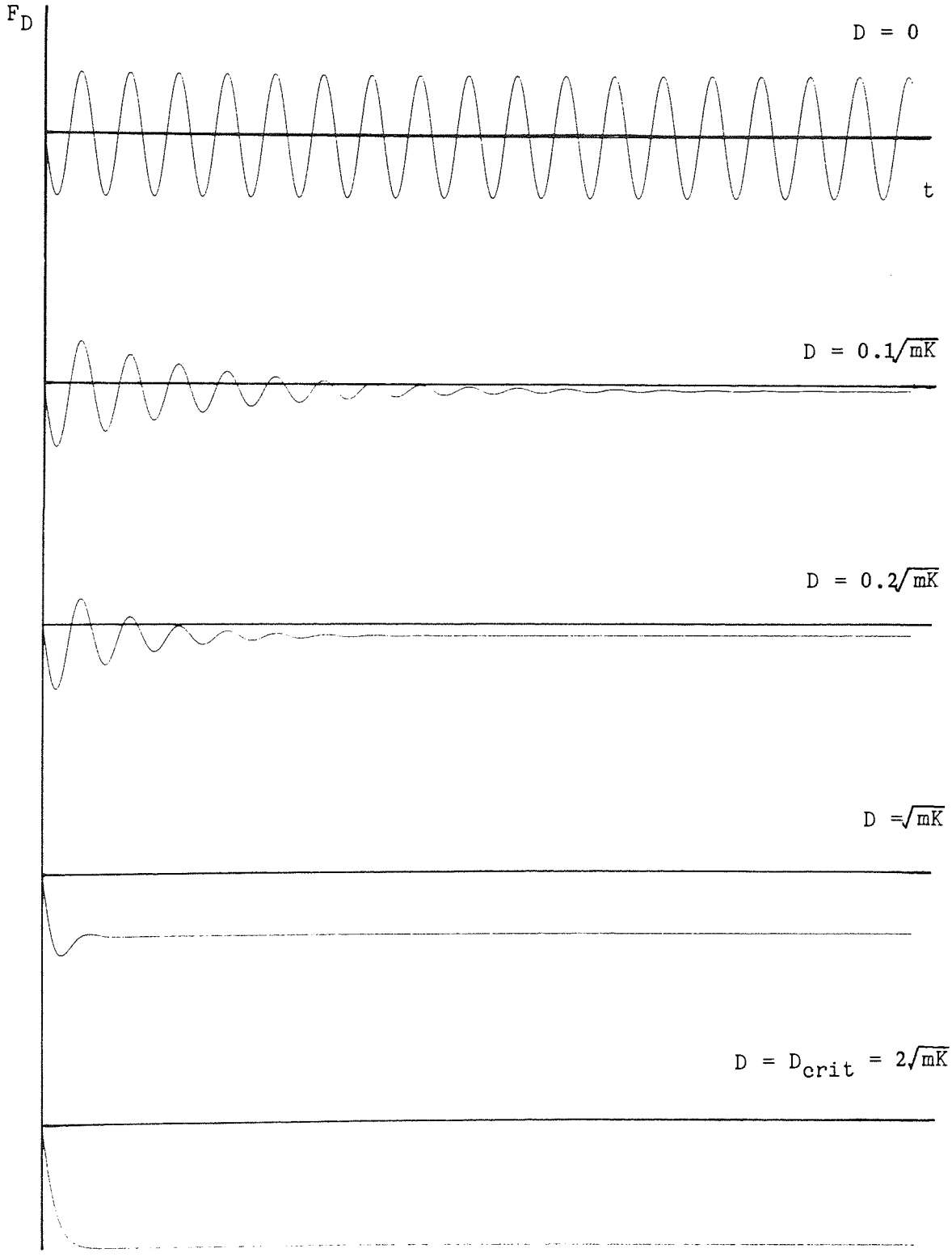

Figure 2.11 Effects of varying the damping parameter

and the timestep small, converges to a value $\dot{F}D/K$. In finite difference form the deviation from equilibrium is given by

$$\Delta F\ D/\Delta tK \tag{2.28}$$

where ΔF is a load increment applied during time Δt.

If the damping constant D and timestep Δt are represented by fraction of their critical values, i.e. $D = C_1 2\sqrt{mK}$ and $\Delta t = C_2 2\sqrt{m/K}$, then F_D converges to

$$C_1 \Delta F/C_2 \tag{2.29}$$

where C_1 and C_2 are less than unity.

3 MODELLING OF DISC ASSEMBLIES USING BALL

3.1 INTRODUCTION

The Distinct Element Method described in Chapter 2 has been incorporated into a computer program 'Ball'. This program was originally written by P.A. Cundall to simulate the slow progressive deformation of random assemblies of discs due to applied boundary conditions. A copy of 'Ball' (version 1.2M) was obtained by the author from P.A. Cundall in October 1980. This version was written in Fortran 66 and was suitable for interactive use on mini-computers. Due to the size of the program it had been necessary to split it into overlays to save on storage requirements. Each overlay, consisting of many subroutines and common blocks, was developed to give a natural partitioning of the program into specific tasks. The program could, therefore, be regarded as modular and hence additions and alterations made easily.

The best computing facilities that were available to the author was the use of a CDC computer at the University of Manchester Regional Computer Centre (UMRCC). However, as access to the CDC was to be obtained from the University of Aston Computer Centre it became necessary to re-write 'Ball' for background use. The vast storage availability at UMRCC no longer required the use of overlays. The program could, therefore, execute more quickly as overlay loading was avoided. Further modifications were required to obtain graphical output, printed output and permanent storage. Also UMRCC advised that 'Ball' be translated to Fortran 77 as Fortran 66 was to become unsupported by 1983.

During the above transition period many further problems were encountered, and in order to overcome these, new subroutines and functions have been included. The structure of the program has,

however, remained unchanged in that the subroutines and functions used to carry out a particular task are grouped together.

Many facilities available in the original version (1.2M) have been removed and many further facilities added. The new facilities include further plotting routines to aid interpretation, routines to analyse the data held in the memory map, and large, permanent storage of test data. Further facilities are constantly being added and therefore the program is not considered as a package but as a research tool which may be modified as required.

A breakdown of the main features within the program structure is given in the sections below. This breakdown applies only to the author's version of 'Ball', wherein changes have been made. Within these sections discs are often referred to as particles and some program variable names have been introduced. The symbols used to represent the quantities associated with particle contacts and centroidsare as given in Chapter 2 and subscript notation has been used wherever possible. Finally, a guide to testing procedures is given and a quantitative validation test is carried out.

The sign convention used by the program is such that tensile normal stresses and clockwise shear stresses acting on a bounded area are positive, in agreement with solid mechanics convention rather than the convention normally adopted in soil mechanics.

Neither a listing of the program nor of the data commands is given within the thesis. These are, however, available on request to the Department of Civil Engineering, The University of Aston in Birmingham, B4 7ET.

3.2 STORAGE ALLOCATION AND NUMERICAL EFFICIENCY

The Distinct Element Method outlined in Chapter 2 was shown to consist of two basic operations, namely the updating of contact forces to give new particle forces, and the subsequent integration of the particle accelerations (force/mass) for new velocities and displacements. In order to carry out the above operations storage is required for a contact data list which holds information relating to forces and displacements at contacts. During a test on an assembly this list must be restructured every time a contact is created or deleted. The updating of this list would be computationally expensive if, in the detection of potential contacts, the whole problem space was scanned. Some useful techniques have been employed in 'Ball' which reduce the time involved in detecting potential contacts. These techniques will be discussed in the following paragraphs before the complete memory map is presented.

The definition of contact in relation to storage has been extended to cover existing and potential contacts, where potential contact is assumed to exist when particles are separated by less than a predetermined distance or tolerance. From Figure 3.1 it can be seen that if $D - (R_A + R_B)$ is less than the tolerance (TOL) then potential

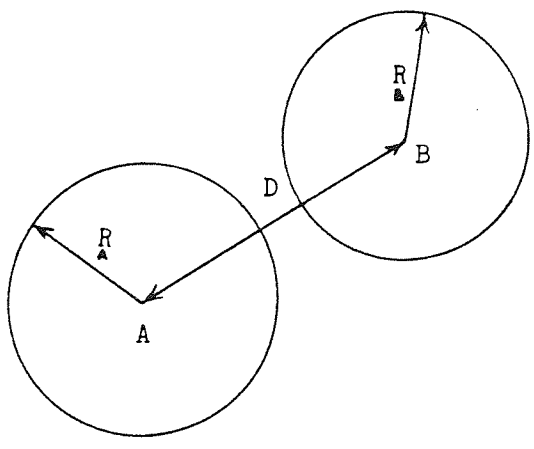

Figure 3.1 Potential contact between particles

contact is assumed to exist. A space within the contact data list is allocated even though $D - (R_A + R_B) > 0$. If, however, $D - (R_A + R_B) >$ TOL, the contact is assumed to be broken and the space previously occupied in the the contact data list becomes available for re-use by subsequent new contacts. The implication of storing potential contacts is that a search for new contacts is only necessary when the distance moved by a particle centre exceeds a value of TOL/2. In 'Ball' the cumulative coordinate increments Δx_i for particle centres are stored and a search is made for new potential contacts whenever Δx_i becomes greater than $TOL/2\sqrt{2}$, see Figure 3.2. The reason for checking the coordinates of the distance moved instead of the total

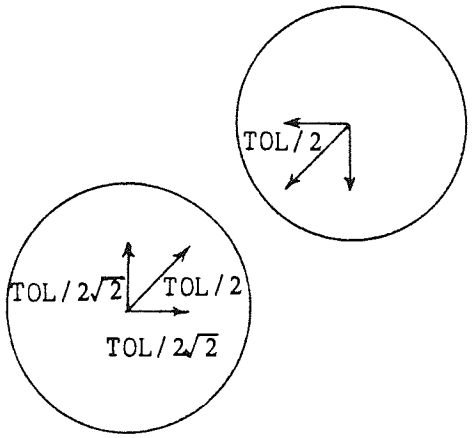

Figure 3.2 Maximum coordinate increments before a search for new contacts

distance moved is that the additional calculation for $(\Delta x_i \Delta x_i)^{1/2}$ is avoided. Once a search for new contacts has been initiated the value of the coordinate increment Δx_i is added to the respective coordinate x_i, thus resetting the value of Δx_i equal to zero. It is also required that at the time of contact deletion, coordinate increments for both particles be added to their respective value of x_i, and a search initiated for new potential contacts of both particles. This is necessary as only the absolute values of the coordinate increments are checked and hence, particles could otherwise regain contact before a search for potential contacts had been initiated.

The time involved during a search for potential contacts is further reduced by dividing up the problem space into boxes. The boxes are square having dimension DEL and form a grid of N1 boxes in the x_1-direction and N2 in the x_2-direction. If the maximum radius of a particle (RMAX) is restricted such that RMAX < (DEL/2 + TOL) the maximum number of boxes in which a particle has entries is restricted to four. These box entries are found by considering the location of the square which circumscribes the particle, with an allowance for the tolerance TOL. This is shown in Figure 3.3 where three particles A,

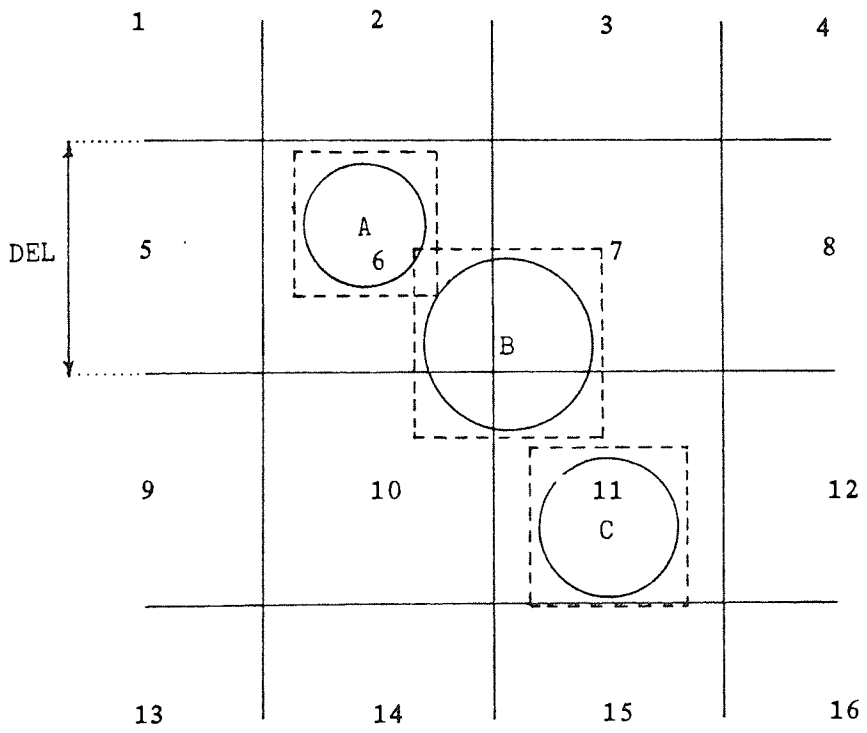

Figure 3.3 Box entries

B, and C are considered. Particle A has only one entry as all four corners of its circumscribing square map into the same box. Particle B has four entries and particle C has two. The mapping of particle C clearly shows the effect of adding a tolerance around particles. The inclusion of the boxing scheme reduces the time required in searching for new potential contacts as it is only necessary to interrogate

particles which have common entries. For example, if the centre of particle B displaces such that a search for new contacts is required, then particles having entries in boxes 6, 7, 10 and 11 need to be checked for potential contact with B. It is also necessary to check for the re-boxing of particle B and to search for potential contacts when a new box entry is found.

In the interest of numerical efficiency a scheme is required that allows a quick access to the particles and contacts that map into the boxes. To facilitate this, storage is given to linked lists which contain the order of particles and contacts that map into the boxes. Further storage is given to box data list which contains pointers to the start of the linked lists for each individual box.

The memory map holding all data on particles, boxes and contacts is stored within a single real array A(I) which contains 60 bit words. This array is equivalenced to an integer array IA(I) which allows integers to be stored within A(I). Figure 3.4 gives the overall memory map wherein pointers M1 to M3 give the starting locations within A(I) of the stored lists, pointer M4 gives the total number of words in A(I) that are in use, and M5 gives the dimensional size of array A(I). Figure 3.5 gives a further breakdown of the partitions

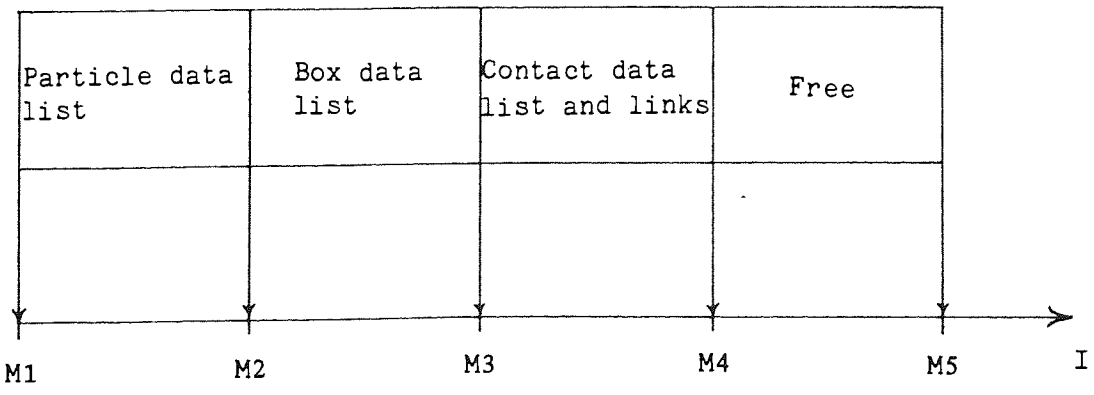

Figure 3.4 The overall memory map of array A(I)

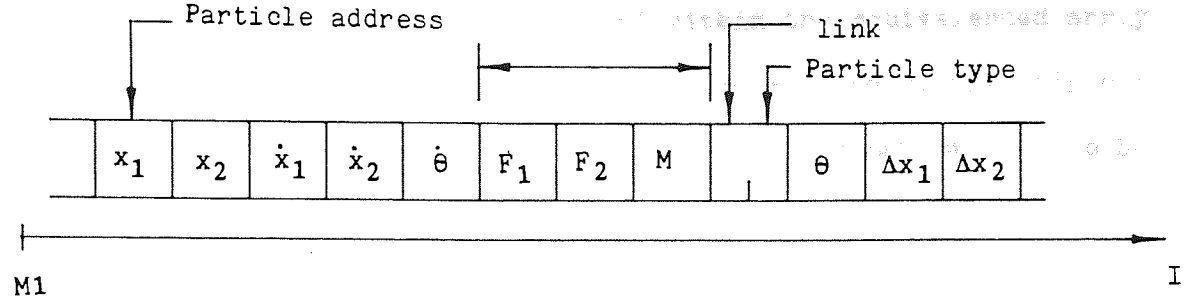

(a) Particle data

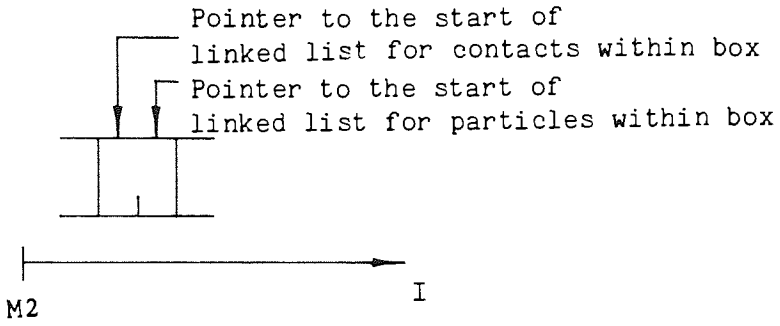

(b) Box data

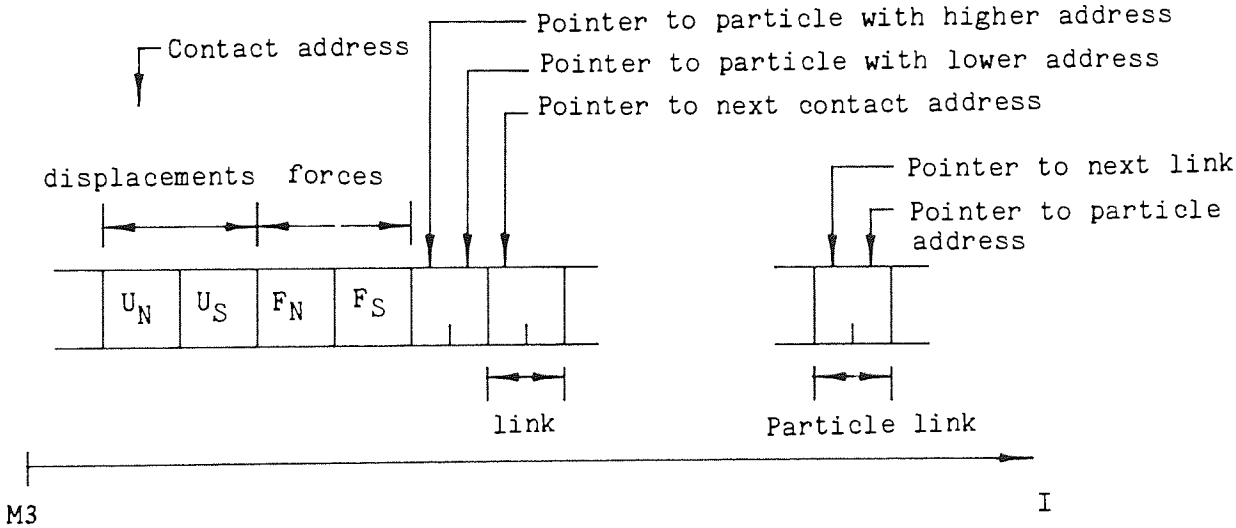

(c) Contact and link data

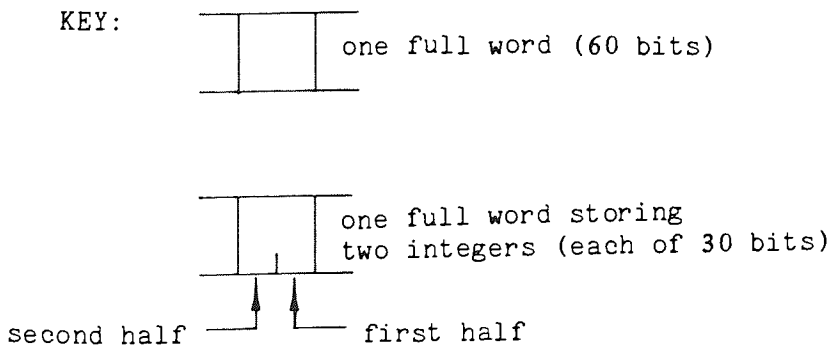

Figure 3.5 Partitions within array A(I)

within A(I). Integers have been stored within the equivalenced array IA(I) by a technique whereby two integers are able to occupy only one word. This technique was used as integers were small enough to be stored within 30 bits, hence the size of A(I) was reduced.

Figure 3.5 also shows how the data lists contained within A(I) are connected. For example, if the list of particles that have entries within a particular box are required, then this may be done by accessing the first half of the word within the respective box data array. The extracted integer is then a pointer to the links which hold information on particle addresses. A similar procedure is used for scanning the contacts which map into a particular box. The program becomes more efficient as the number of boxes within the grid is increased as fewer particles need to be scanned during the updating of contacts etc. However, increasing the number of boxes requires further storage for the box data array.

Although the main storage requirement within 'Ball' is for array A(I) other variables relating to the physical properties of the particles, boundary stress and strain tensors etc. must be stored. These are stored separately in COMMON blocks within the program.

3.3 ASSEMBLY GENERATION AND BOUNDARY LOCATION

Before an assembly can be generated the program must be given information concerning the size of the assembly area, the number of boxes, the maximum number of particles to be generated and the number of different radii to be used. This is necessary in order to set up the partitions in the memory map given in Figure 3.4. Providing this information has been given, two different methods of assembly generation may be used, namely manual and automatic. When using the manual method only the centre coordinates and radius type are

required. The program then places the particle at the given coordinates, finds its box entries and makes a search for contacts. If, however, the automatic method is used the program attempts to generate a random assembly corresponding to a given particle size distribution. Particle coordinates are randomly generated in such a way that they plot within a given boundary. This boundary may be either rectangular or circular but must not come closer than a distance equal to the maximum particle radius (including the tolerance) to the rectangular boundary of the given assembly area. This is necessary for particle boxing as shown in Figure 3.6.

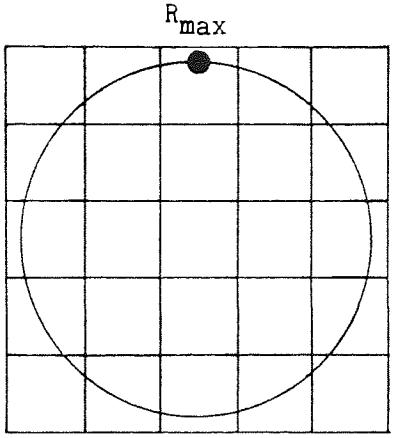

Figure 3.6 Location of circular boundary within permissable assembly area

Particles with the largest radius are generated first and the smallest last. However, unlike manual generation wherein it is the users responsibility to ensure that particles do not overlap, a check is made to detect overlap. If this is detected the newly generated particle is moved by the distance of the overlap in the direction opposite to the overlap. A further check is then made and, if required, the particle moved once again. A maximum of six attempts are made to relocate the particle before it is disregarded and new coordinates are generated. Figure 3.7 shows the method of relocation used.

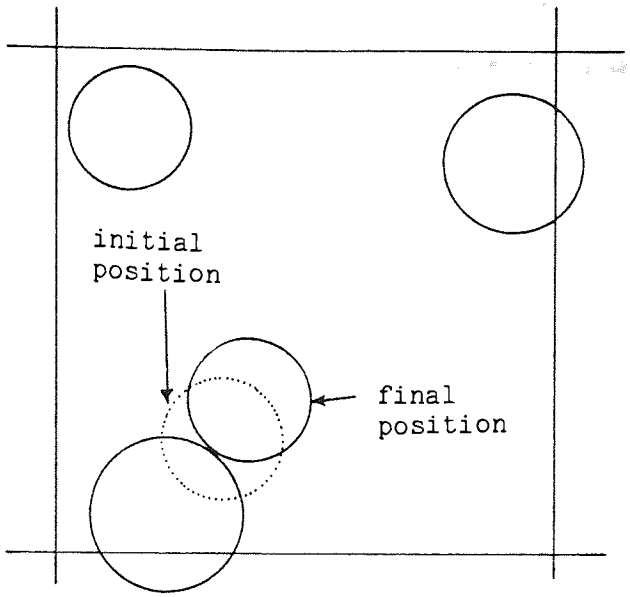

Figure 3.7 Relocating a particle during automatic assembly generation

Each time a particle has been satisfactorily placed, its box entries and potential contacts are found and its address is included within the linked lists of box entries. The number of times coordinates will need to be randomly generated to place all the required particles varies depending on the required density and on the number of particles. A limit on this number must be given by the user. If this limit is reached before full generation, the program stops and informs the user of how many particles have actually been generated. It should be noted that manual or automatic particle generation may be initiated at any time provided there is still room in the particle data list. Therefore combinations are allowed. For example, if all the small particles had not been generated automatically on the first attempt then either further tries could be made automatically or particles placed manually in the large voids.

Once an assembly has been generated a boundary must be located before any subsequent loading is applied. Again this can be done

manually or automatically. If manual boundary location is used the program expects a list of particle numbers. The boundary is then formed by linking the named particles in the same order as they appear in the list. It is, therefore, necessary that the first particle number be the same as the last to indicate that the boundary has been closed. If however automatic boundary location is used, the program attempts to find a convex boundary that encloses all particle centres. This is done by first finding the lowest particle in the assembly. The rest of the particles in the assembly are then scanned in order to find the minimum slope to the next particle centre. Once this particle has been found it is linked to the lowest particle. The procedure to find the minimum slope is now repeated from this new particle to obtain a further boundary link. This is repeated until eventually the lowest particle is found which indicates that the boundary has closed. Figure 3.8 shows the boundary as located by the automatic method.

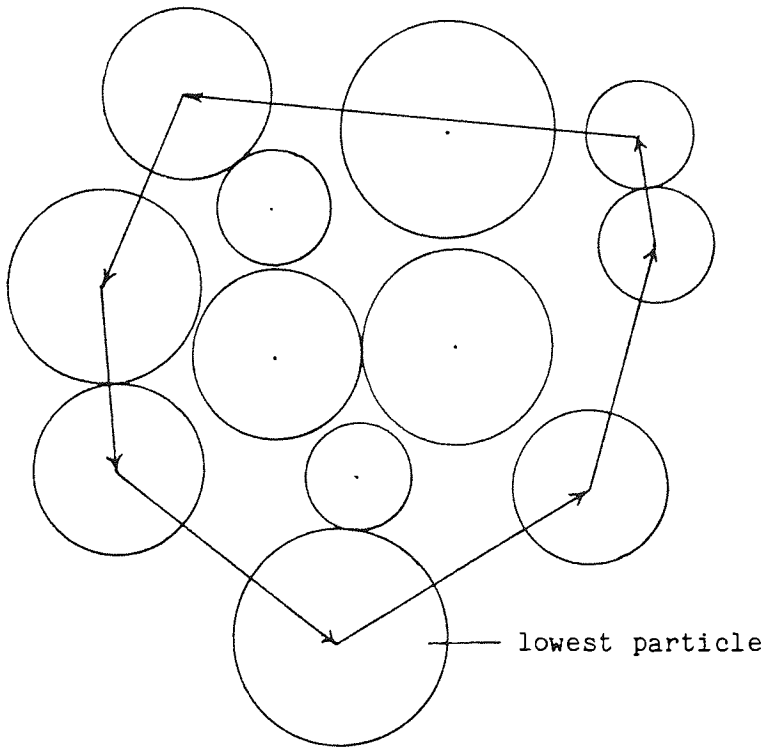

Figure 3.8 Automatic boundary location

After the list of boundary particles has been obtained the integer variable BPOINT is set to give the address of the first boundary particle. For manual generation, BPOINT gives the address of the first particle in the given list, whereas for automatic generation BPOINT gives the address of the lowest particle in the assembly. From Figure 3.5a it can be seen that the second half of word 9 contains a link. In the case of a boundary particle this link is a pointer to the next particle in the boundary list, and in the case of a non-boundary particle the link is set to zero. The list of boundary particles is therefore easily scanned by starting at address BPOINT and then proceeding through the list by extracting the pointers held in word 9. A full scan is completed when the final pointer equals BPOINT. BNUM particles have then been scanned.

During deformation of the assembly there must be a sufficient number of boundary particles to contain the assembly, as otherwise interior particles would attempt to escape through large gaps in the boundary. The logic used in the program prevents this as escaping particles are arrested and included in the boundary list. The criterion for accepting new boundary particles is that the centroid of the escaping particle touches the line joining the centroids of the two neighbouring boundary particles. A check for this must be initiated at the time particles are checked for reboxing. An example of boundary particle insertion is given in Figure 3.9. The updating of the boundary list involves rearranging the pointers which link boundary particles in the particle data list. For the example in Figure 3.9 this is achieved by first replacing the link from A to B with a link from A to C and then introducing a new link from C to B.

It should be noted that during the deformation of an assembly, whose boundary was automatically located, it is not a requirement that the boundary must remain convex. But if there is a preference for a

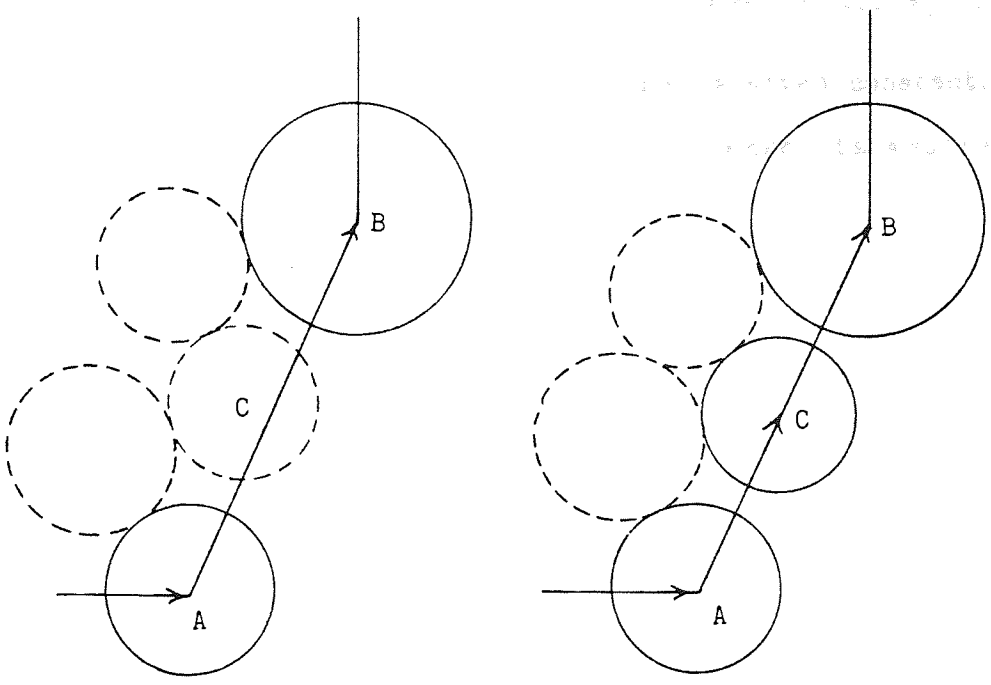

(a) (b)

Figure 3.9 Inserting a new particle in the boundary list

convex boundary the current boundary may be deleted and a new one automatically generated. However, this is not recommended for assemblies carrying high forces.

Finally, it must be added that contacts between boundary particles or between boundary and interior particles are treated in all respects the same as contacts between interior particles. However, the forces and velocities acting at boundary particle centres are unlike those of interior particles as they depend directly on the externally applied stress or strain-rate tensors.

3.4 BOUNDARY CONTROL

Three types of boundary control are at present employed within 'Ball'. The boundary may be strain-controlled, stress-controlled or servo-controlled by selecting MODE 1, 2 or 3 respectively.

When using the strain-controlled mode (MODE 1) the velocities of

the boundary particles are calculated from a given constant, uniform strain-rate tensor $\dot{e}_{ij}$. The strain-rate tensor is applied to the centre of each individual boundary particle and is independent of the implied boundary particle forces. Thus

$$\dot{x}_i = \dot{e}_{ij}x_j \qquad (3.1)$$

where it is convenient to measure x from the centroid of the assembly to minimize velocities. The rotational velocity of boundary particles $\dot{\theta}$ is set to zero, so that all points on the disc boundary approximately behave according to the given strain-rate tensor. This approximation is good if particles are small in comparison to the size of the assembly.

If the stress-controlled mode (MODE 2) is used then forces and moments are distributed to boundary particle centroids. These forces and moments are derived by considering the shape of the surface over which a uniform symmetric stress tensor σ_{ij} is applied. The shape of the surface used in the program is piecewise linear as shown in Figure 3.10. Each linear section of the surface is either within a boundary

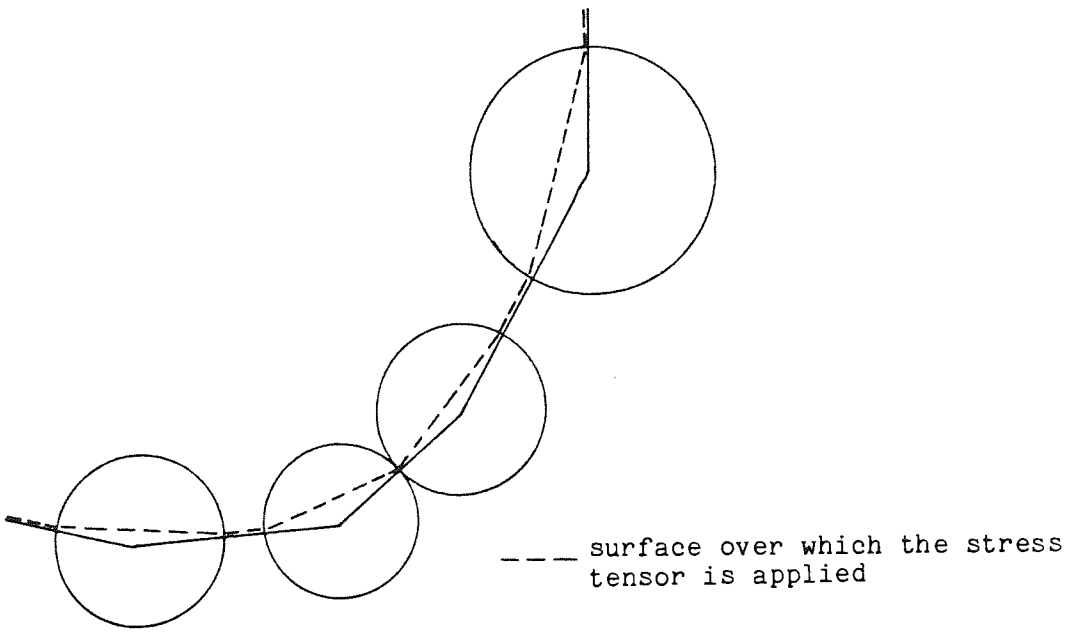

Figure 3.10 The stress controlled boundary

particle or is a bridge between two boundary particles. Sides have length L and outward unit normal vectors v_i, and since they are straight, forces F_i act at the mid-point, and are given by

$$F_i = \sigma_{ij} v_j L \tag{3.2}$$

These forces must then be distributed to the centroids of the boundary particles. The forces acting on a side within a disc are replaced by the statically equivalent system consisting of both a force and moment as shown in Figure 3.11(a). The value of the moment M is given by

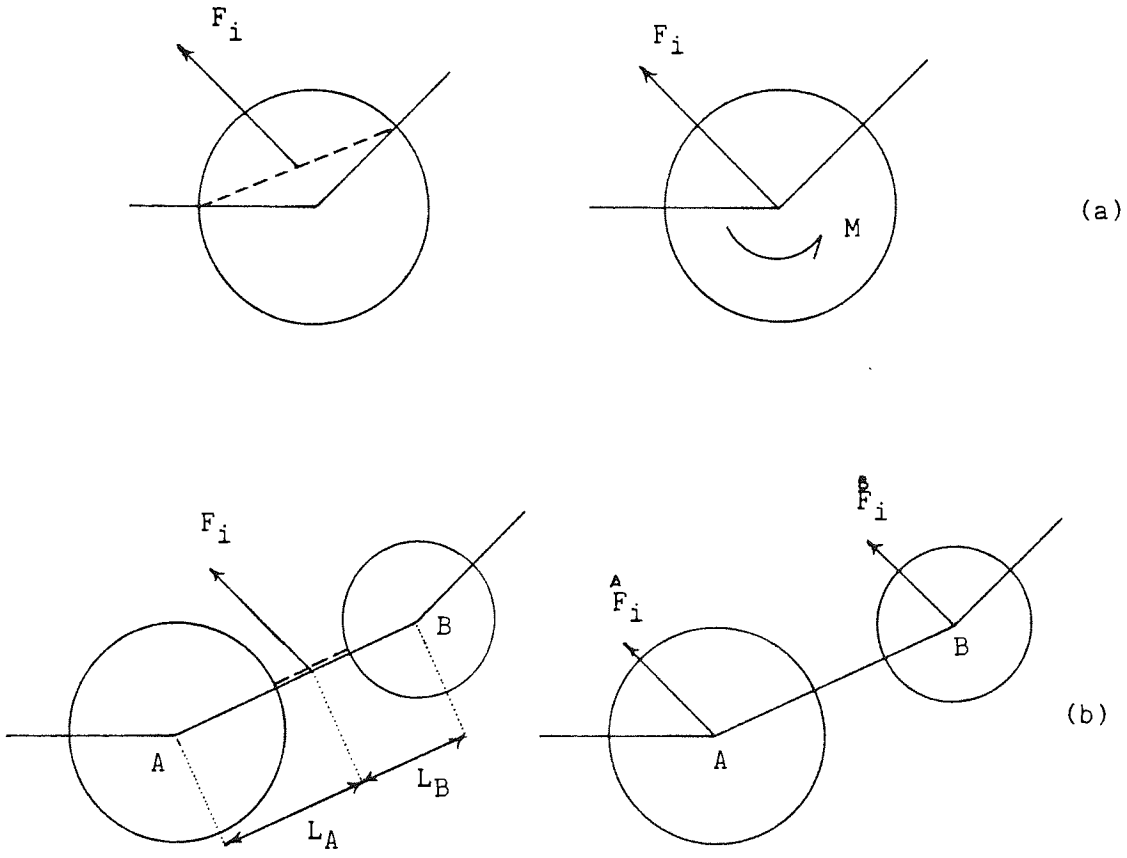

Figure 3.11 Method of distributing boundary forces to disc centroids

$$M = -\varepsilon_{ij} F_i x_j \tag{3.3}$$

where x_j is the vector from the centroid of the disc to the mid-point of the side and ε_{ij} is the second order alternating tensor. Figure 3.11(b) shows how the force acting on a side bridging two particles is replaced by a statically equivalent system consisting of two forces $\overset{A}{F}_i$ and $\overset{B}{F}_i$. These forces are then given as

$$\overset{A}{F}_i = \frac{L_B}{L_A + L_B} \cdot F_i \qquad (3.4a)$$

$$\overset{B}{F}_i = \frac{L_B}{L_A + L_B} \cdot F_i \qquad (3.4b)$$

Neither of the two forms of boundary given above are entirely satisfactory. Under stress-controlled conditions the sample tends to become unstable well before the strength of the assembly is reached. This is due to the non-uniformity of contact structure in the unconfined regions, i.e. the boundary. Although this does not occur during strain control, MODE 1 has the disadvantage that it is difficult to conduct tests wherein components of the stress tensor are controlled.

The servo-controlled boundary (MODE 3) has been introduced into the program to overcome this problem by controlling the individual components of the stress tensor during strain-controlled deformation. This is achieved by continually adjusting the individual components of the strain-rate tensor. After each calculation cycle, when contact forces have been updated, the average stress tensor $\bar{\sigma}_{ij}$ acting at the boundary, surface S and bounded area A, is given by

$$\bar{\sigma}_{ij} = 1/A \int_A \sigma_{ij} dA \qquad (3.5)$$

Because $\sigma_{ij} = \delta_{ik}\sigma_{kj} = (\partial x_i/\partial x_k)\sigma_{kj}$ and σ_{ij} satisfies the equilibrium condition $\partial \sigma_{kj}/\partial x_k = 0$ the above equation can be transformed using Gauss's Divergence Theorem into

$$\bar{\sigma}_{ij} = 1/A \int t_j x_i dS \quad \text{since } t_j = \sigma_{ij} v_i \qquad (3.6)$$

where x_i gives the coordinates at which tractions t_j act on S. Since the tractions are discrete forces equation (3.6) may be replaced by a sum over the BNUM forces acting on S. Following Thornton (1979) $\bar{\sigma}_{ij}$ is given as

$$\bar{\sigma}_{ij} = 1/A \sum_{N=1}^{BNUM} F_j^N x_i^N \qquad (3.7)$$

where $\overset{N}{F}_j$ gives the components of the forces acting on boundary particle centroids at $\overset{N}{x}_i$, and A is the area enclosed by the boundary as shown in Figure 3.12. Hence the area A is calculated during the scan of boundary particle by

$$A = 1/2 \sum_{N=1}^{BNUM} (\overset{N}{x}_1 - \overset{N+1}{x}_1)\ (\overset{N}{x}_2 + \overset{N+1}{x}_2) \tag{3.8}$$

provided boundary particles are scanned in an anticlockwise order. Note that the moments acting on boundary particles have been ignored as their effect is assumed to be insignificant.

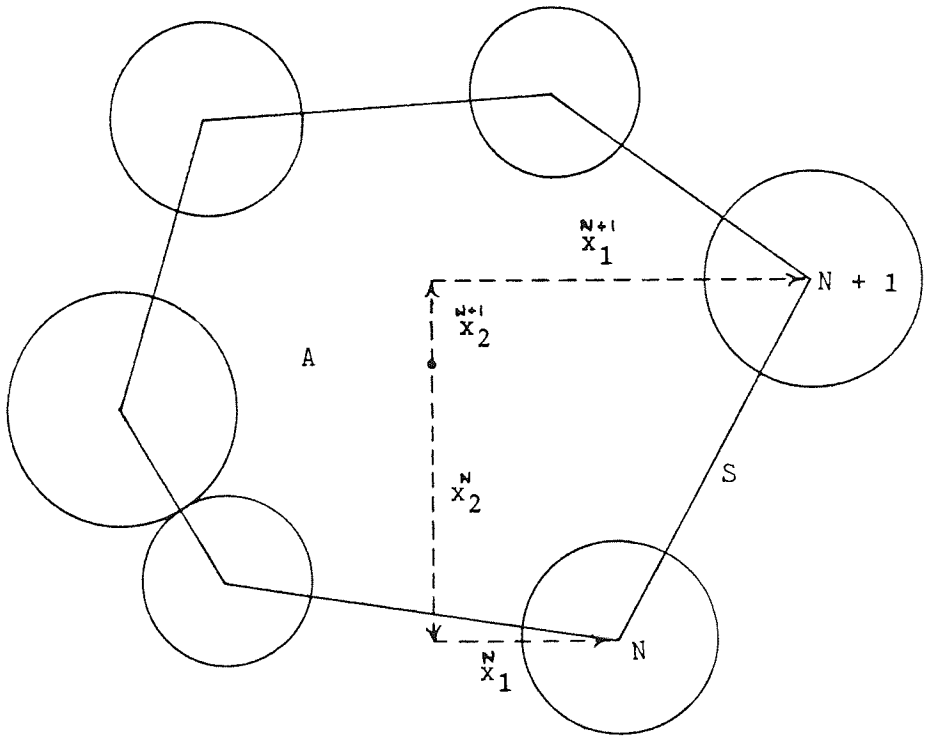

Figure 3.12 Determination of the bounded area of the assembly

The calculated average stress tensor $\bar{\sigma}_{ij}$ is then compared to the desired stress tensor $\overset{*}{\sigma}_{ij}$ and the strain-rate tensor adjusted by the following equation

$$\dot{e}_{ij}^{t+\Delta t} = \dot{e}_{ij}^{t} + G\ (\overset{*}{\sigma}_{ij}^{t} - \bar{\sigma}_{ij}^{t}) \tag{3.9}$$

where the symbol G represents the gain of the servomechanism. The choice of the parameter G is critical in that the response could be

slow or cause instability, depending on whether the value was respectively too low or too high. It is, therefore, necessary to conduct experiments to ascertain its effect. Once a satisfactory value has been obtained any stress path may be followed as long as the components of the stress tensor are not changed rapidly. It is also advisable that during a test, checks are made in order to monitor the performance of the servo.

Furthermore, it should be noted that the servomechanism described in equation (3.9) may be modified to control the invariants of the stress tensor, or even just one or two of the stress components.

During a test it is possible to change from one mode to another. However, it is not recommended that a change be made to MODE 2. The reason for this is that large forces may develop between boundary particles during strain-controlled deformation. These forces may be many times greater than a typical contact force within the assembly. Hence a change to MODE 2 could initiate explosive velocities at the boundary.

3.5 INTERPRETATION AIDS

The microscopic data held within the memory map may be either printed on paper, written to a permanent file or tape, or represented graphically. Macroscopic assembly quantities such as stress and strain tensors may be obtained by analysis routines and displayed with the printed output.

At any time during a test the data stored within the memory map may be copied onto file or magnetic tape. It is possible to store many copies of the memory map, taken at different stages of a test. The files or tapes may then be used to obtain incremental microscopic and macroscopic quantities such as particle displacement increments

and strain-increment tensors, respectively. It is advisable that if very many reference files are to be produced during a test then they should be stored in series on magnetic tape. This avoids the use of large amounts of disc storage when a test is being performed on arrays consisting of many particles. A subroutine has been written to cater for the loading and unloading of data to and from the memory map.

3.5.1 Plots

Graphical output is obtainable on 'microfiche' which is posted to the user from UMRCC. Nine basic plotting options are available and are listed below.

OPTION	PLOT
1	All discs within the assembly are plotted
2	The box grid is plotted
3	The boundary is plotted as a dashed line passing through the centroid of boundary discs
4	Provided option 1 has been used, radius vectors are plotted to represent θ, measured from the X1-axis
5	Contact forces are plotted by lines passing through the contact point. The direction of the force is represented by the inclination of the line and its magnitude by the thickness. All line thicknesses are proportional to the thickest line which represents the largest force. Forces which are less than 10% of the maximum are represented by single thickness dashed lines. Forces between boundary particles are not plotted

6 Velocity vectors of particle centres are represented as arrows originating from disc centroids. The plot is linearly scaled to the largest velocity vector

7 Cumulative sliding displacement increments are plotted. These are represented as lines of constant length across contacts. The width of the lines are linearly scaled to the maximum

8 A plot representing the direction of rotation increments is produced by comparing the data within the memory map to that which has been previously stored. Clockwise (negative) rotations greater than 5% of maximum rotation increment are represented by lines drawn through particle centres, and anticlockwise (positive) rotations greater than 5% of maximum rotation increment are represented by horizontal and vertical lines through particle centres. The length of the lines are equal to the minimum particle diameter, and the plot is not scaled to the magnitude of rotation. Rotations of less than 5% of the maximum rotation increment are not plotted

9 A connection diagram is produced which shows the change in array structure relative to a previously stored reference state. Existing contacts are shown by a single solid line joining particle centres. Deleted or created contacts are shown by a dashed line and double solid lines respectively.

Clearly there are many more plots which could be made but only the above 9 options are immediately available to the user. Further

plots have been produced to represent the results obtained from analysis routines. However, these plots will be given in later chapters when the various analyses have been explained.

3.5.2 Boundary Stress and Strain Measurements

For the methods of boundary control discussed in section 3.4 it should be noted that when a uniform strain-rate tensor is applied a non-uniform boundary stress is induced, and when a uniform stress tensor is applied non-uniform boundary strain-rates result. Nevertheless, these non-uniform quantities must be measured in order to produce plots that describe the stress-strain relationship.

When using strain-controlled modes (MODE 1 and MODE 3) the method of calculating the average stress tensor $\bar{\sigma}_{ij}$ has been given by equation (3.7). The strain-increment tensor Δe_{ij} applied between times t_1 and t_2, wherein NCYC calculation cycles have been performed, is given as

$$\Delta e_{ij} = \int_{t_1}^{t_2} \dot{e}_{ij} dt \tag{3.10}$$

or in finite difference form as

$$\Delta e_{ij} = \sum_{1}^{NCYC} \dot{e}_{ij} \Delta t \tag{3.11}$$

For the stress-controlled mode (MODE 2) a method is required to calculate the average strain-increment tensor Δe_{ij}. The chosen method makes use of an equation which gives the average displacement gradient tensor $\bar{d}_{ij} = \partial \bar{u}_j / \partial x_i$, u_j being the displacement of point x_i. Hence

$$\bar{d}_{ij} = \frac{1}{A} \int_A d_{ij} dA \tag{3.12}$$

where A is the area bounded by the lines joining boundary particle centres. Application of Gauss's Divergence Theorem yields

$$\bar{d}_{ij} = \frac{1}{A} \int_A \frac{\partial u_j}{\partial x_i} dA = \frac{1}{A} \int_S u_j v_i ds \tag{3.13}$$

where v is the outward unit normal vector to surface S. During deformation surface S remains a polygon and therefore equation (3.13) may be written

$$\bar{d}_{ij} = \frac{1}{A} \sum_{N=1}^{BNUM} \frac{1}{2} (u_j^N + u_j^{N+1}) v_i^S L^S \tag{3.14}$$

where

$$v_i^S = \varepsilon_{ij}(x_j^{N+1} - x_j^N)/[(x_k^{N+1} - x_k^N)(x_k^{N+1} - x_k^N)]^{1/2}$$

$$L^S = [(x_k^N - x_k^{N+1})(x_k^N - x_k^{N+1})]^{1/2}$$

$$A = 1/2 \sum_{N=1}^{BNUM} (x_1^N - x_1^{N+1})(x_2^N + x_2^{N+1}) \text{ (as given by equation (3.8))}$$

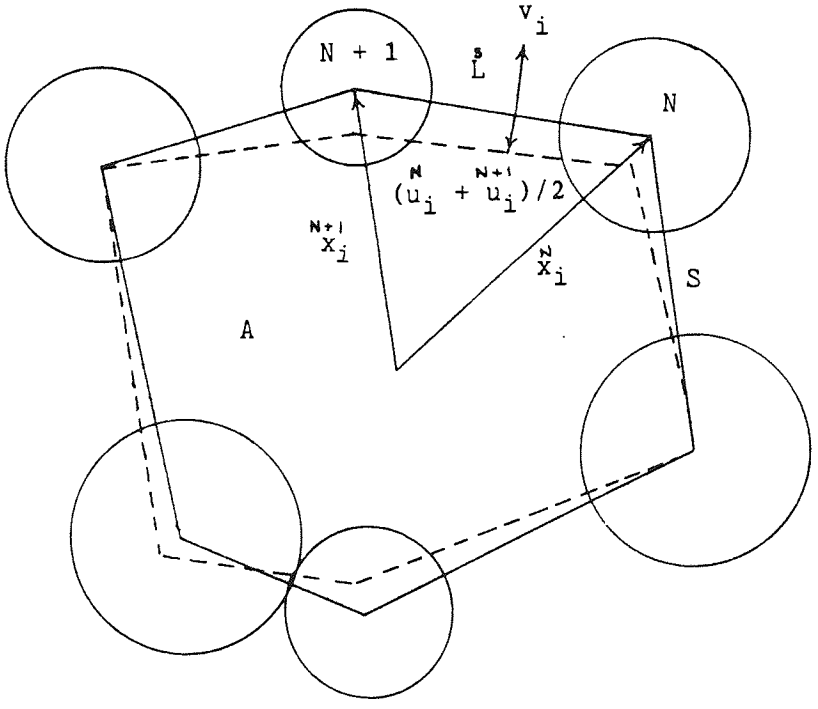

Figure 3.13 Calculation of the average strain-increment tensor

Figure 3.13 shows the boundary before and after deformation. The reference state from which the average segment displacements are calculated is given by the solid lines. However, the area, segment lengths and normals may be calculated for either the reference state or the deformed state whose boundary is shown as dashed segments. An

average is therefore taken.

$$\bar{d}_{ij} = 1/2\ (d^{R}_{ij} + d^{D}_{ij}) \tag{3.15}$$

Symbols R and D indicate that the calculations have been made for A, v_i and L by considering the reference and deformed states respectively. Finally, as the strain-increment tensor is defined as the symmetric part of $\bar{d}_{ij}$ then

$$\Delta e_{ij} = 1/2\ (\bar{d}_{ij} + \bar{d}_{ji}) \tag{3.16}$$

It has been shown in section 3.3 that during deformation the inclusion of extra boundary particles, in the boundary list, may become necessary. This leads to a problem as the number of segments in the boundary polygon increases. To overcome this the lists of boundary particles for the reference and deformed state are compared so that the unpaired entries are omitted. Inaccuracies are therefore incurred as d_{ij} is not calculated over the true boundary surface. Nevertheless, the approximation is good if strain-increments are calculated frequently. It has also been observed that even during tests on large assemblies it is not common that the inclusion of additional boundary particles is required provided the total strains e_{ij} are kept reasonably small. As stated above, stress-controlled tests become unstable well before the strength of the assembly interior is reached and hence strains are not likely to be large.

3.5.3 Internal Stress and Strain-increment Tensors

A set of subroutines has been provided in order to calculate the stress and strain-increment tensors over internal circular boundaries within the assembly. These were written by O.D.L. Strack, full details of which are given by Strack and Cundall (1978). A summary of the basic operations involved in these calculations is given below as the method will be referred to in Chapter 7, which deals with internal

analyses of the assembly.

The actual boundary used in the calculations approximates that of the given circle as shown in Figure 3.14. This boundary is constructed by considering the particles which intersect the circle. Hence if N number of particles intersect the circle then there are 2N number of intersection points. Between intersection points where the circle crosses voids, the boundary is taken to be a straight line and between intersection points where the circle crosses a particle, the boundary is curved such that it either includes or excludes the particle. A particle will be included if its centroid lies within the circle, and excluded if it does not. The reason for the construction of this approximate boundary is such that the calculations for stresses and strains may now be made over the same boundary, without making any assumption concerning the stress distribution within the particles themselves.

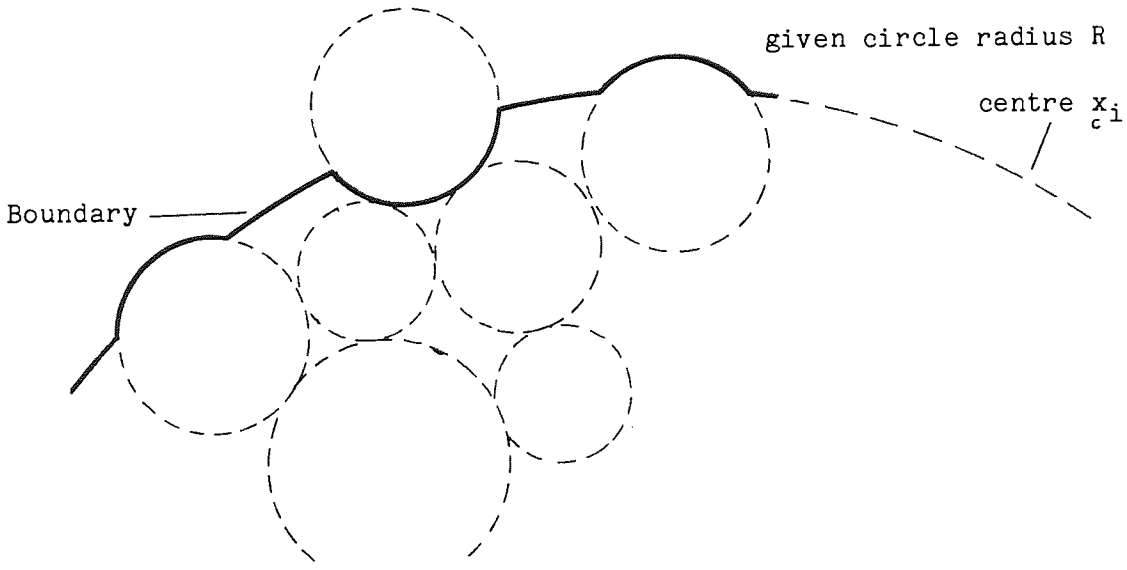

Figure 3.14 Internal boundary over which stress and strain-increment tensors are calculated

For weightless particles, (i.e. gravity set to zero) the stress tensor may be obtained from equation (3.7), where F_j are the external discrete contact forces acting at the boundary and A is calculated as the area enclosed by the boundary.

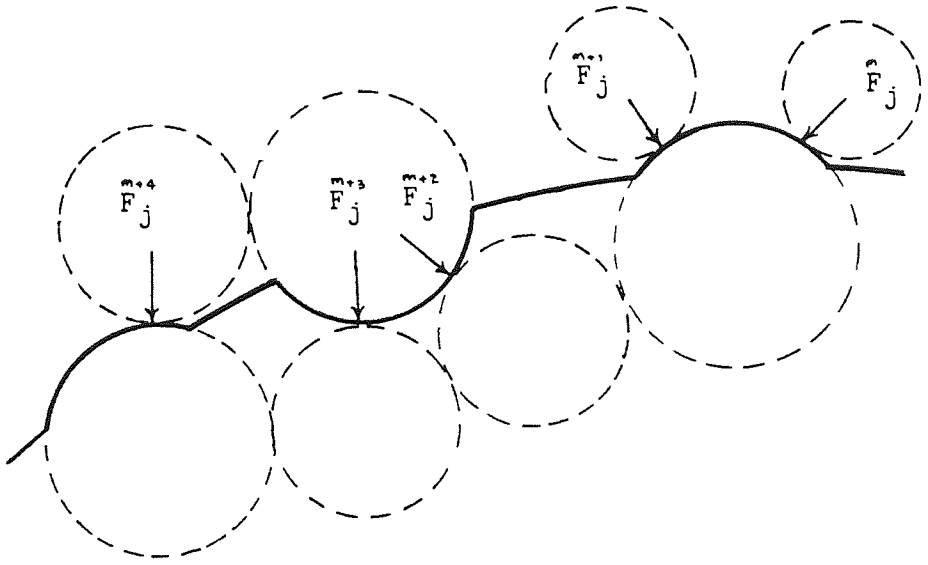

Figure 3.15 Calculation of the internal stress tensor

The strain-increment tensor, from a reference state to a deformed state, is calculated by obtaining the displacement-increments at the intersection points. These are known from the centroid displacements and rotations of discs that initially intersected the given circle. Since there are N number of straight segments and N number of curved segments making up the boundary, then using equation (3.13)

$$\bar{d}_{ij} = \frac{1}{A}\left[\sum_{m=1}^{N}\int_{S^m} u_j v_i dS + \sum_{m=1}^{N}\int_{C^m} u_j v_i dC\right] \qquad (3.17)$$

where $\bar{S}^m$ and $\bar{C}^m$ denote the straight and curved segments of the boundary respectively, and A is the area enclosed by the boundary. Strack and Cundall (1978) have shown that equation (3.17) is equivalent to

$$\bar{d}_{ij} = \frac{1}{A}\left[\sum_{m=1}^{2N} 1/2\ (\bar{u}_j^m + \bar{u}_j^{m+1})\bar{v}_i^m \bar{L}^m + \sum_{r=1}^{N} \bar{D}_{ji}^r \bar{V}^{*r}\right] \qquad (3.18)$$

where $\bar{D}_{ij}^r$ is the rotation tensor for points within a disc and $\bar{V}^{*r}$ is the

volume enclosed by the curve and straight line that join intersection points, as shown in Figure 3.16. Here, equation (3.18) may be understood as the integration over the polygon whose sides join intersection points, with an additional contribution obtained from the rotation of volumes enclosed between the boundary and this polygon.

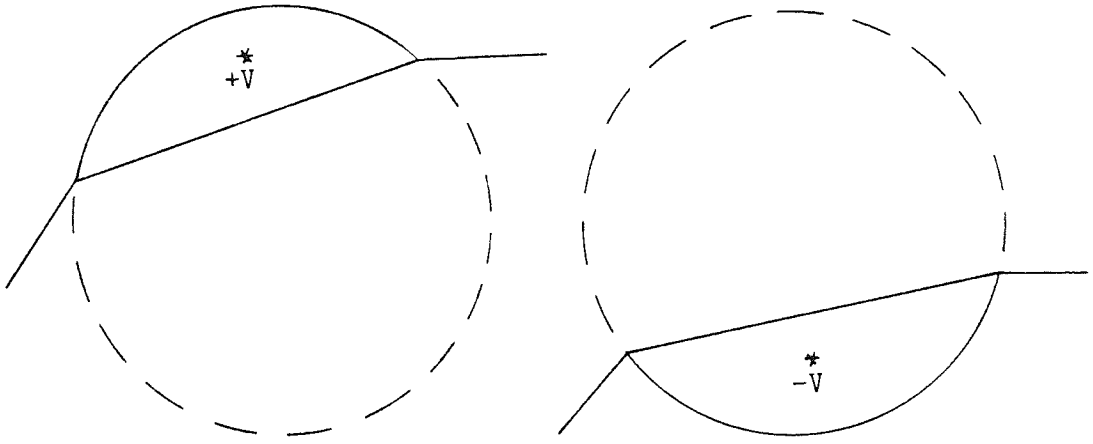

Figure 3.16 Particle volumes enclosed between the boundary and the polygon connecting intersection points

In a similar way to that described in section 3.5.2 the displacement gradient tensor may be calculated by using the geometry of the reference of deformed state. Hence, an average may be taken (equation (3.15)) before the strain-increment tensor is calculated (equation (3.16)).

3.6 INITIAL TEST CONSIDERATIONS

Before a test is carried out using 'Ball' it is important to understand the interrelationship between physical and control parameters, computational effort (program execution time), program storage requirements (extent of the memory map) and the validity of

results. Of these it is essential that valid test results are obtained. In order to ensure this, test samples must contain a sufficient number of particles so that subsequent results are representative of granular material and, in addition, control parameters such as loading rate, damping and timestep must be set with care to ensure the results are accurate. These considerations substantially increase the number of calculations made by 'Ball' which results in high computational effort. Figure 3.17 shows diagrammatically the interrelationship of testing parameters.

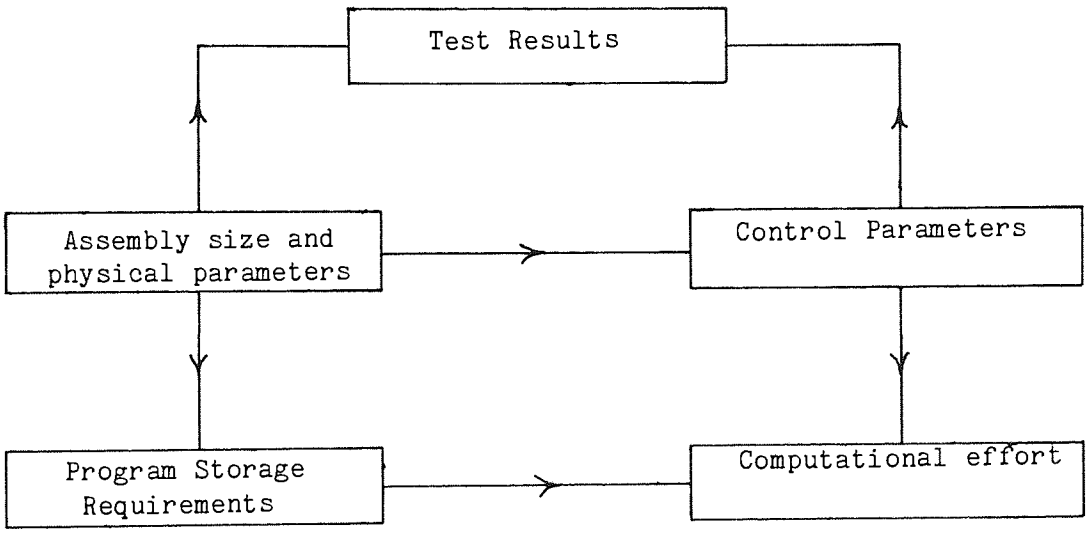

Figure 3.17 Interrelation of testing parameters

From Figure 3.17 it becomes apparent that a balance is required between the various test parameters but the program user should always bear in mind the aim of the test. In order to assist the user in setting parameters an estimate of the size of the memory map is 30 words per disc and execution speed on the CDC 7600 is 4000 disc cycles per second, e.g. An assembly of 1000 discs requires 30K (60 Bit words) for the memory map and will run at a rate of 4 complete calculation cycles per second (mill time). Hence for a 1000 disc assembly one second execution time is equivalent to $4\Delta t$ testing time. Even relatively uncomplex tests on such a sample could easily run into

hundreds of thousands of complete calculation cycles. Therefore, a test can easily take days of mill time to run. However, since the University's total allocation on the CDC 7600 amounts to 40 minutes per day, tests can take many months to complete.

3.7 TESTING PROCEDURES

After an assembly has been generated and its boundary located (section 3.3) it is common, especially if automatic particle generation has been used, that the porosity is high. There are no true contacts and very few potential contacts. It is, therefore, required that, after the physical and control parameters have been set, the assembly is compacted before it is consolidated under given stress conditions. Compaction is defined here as raising the density of an assembly, by controlling the boundary, such that it will be stable under low isotropic stresses. Consolidation is then two phase: the first phase is to raise the components of the stress tensor to their required values and the second phase is to maintain constant the stress tensor until the assembly reaches near perfect equilibrium. Once consolidation is completed any desired stress path may be followed in order to shear the assembly.

3.7.1 Parameter Setting

Before an assembly is compacted, consolidated and sheared the physical and control parameters must be set. The physical parameters require the input of data regarding particle stiffnesses, density and surface friction. Once this data is given, particle masses are computed by assuming the discs to be of unit thickness and hence

$$MASS = \pi.RAD^2.DENSITY \qquad (3.19)$$

Normal and shear contact stiffnesses, K_n and K_s respectively, for the

contact between particle type A and particle type B are calculated as

$$K_n = (\overset{A}{K}_n.\overset{B}{K}_n)/(\overset{A}{K}_n + \overset{B}{K}_n) \qquad (3.20a)$$

$$K_s = (\overset{A}{K}_s.\overset{B}{K}_s)/(\overset{A}{K}_s + \overset{B}{K}_s) \qquad (3.20b)$$

and the allowable force obliquity at the contact is set so that $F_s/F_n = \overset{*}{\mu}$, where $\overset{*}{\mu}$ is the smaller of the two surface frictions.

The control parameters are required in order to set the timestep, damping constants and the gain of the servomechanism (if MODE 3 is to be used).

The critical timestep and critical damping constants are calculated by the program for simplified systems having only one degree of freedom. These systems (described in section 2.5) are based on the oscillation of particles which have the lowest given mass/stiffness ratio. The control parameter for the timestep (variable FRAC) initialises the timestep

$$t = FRAC.\Delta t^{crit} \qquad (3.21)$$

where FRAC must be less than unity. The damping parameter (BETA) sets the fraction of critical damping that will be used in the calculations for dashpot coefficients.

It should be noted that the results obtained during the shearing of an assembly must be independant of the timestep and damping. This may be confirmed by repeating the test using higher values for the timestep and damping. If the resulting stresses and strains are unchanged then it is reasonable to assume that the results are good. As a guide, the values FRAC = 0.1-0.3, BETA = 0.05-0.10 may be used provided particle velocities and forces are low.

3.7.2 Compaction and Consolidation

Once the required physical and control parameters have been set

the assembly may be compacted to a given low isotropic stress by using boundary control MODE 1, 2 or 3. However, none are completely satisfactory. For strain-controlled boundaries (MODE 1,3) there is the disadvantage that high forces will develop between boundary particles. These high forces give rise to the boundary stress tensor being much higher than that of internal boundaries. MODE 3 may also initiate high boundary velocities when the desired stresses are higher than the actual stresses. The stress-controlled boundary (MODE 2) will also give rise to high boundary velocities which may lead to numerical instability as very high forces may develop within a single timestep. MODE 2 has a further disadvantage in that many boundary particles may be required and hence the boundary becomes irregular.

To overcome the above problems it is suggested that MODE 1 be used until the stress tensor acting on an internal boundary becomes close to a predetermined low isotropic stress. At this stage, high forces will exist between boundary particles. However, by switching to MODE 2 and regulating velocities, these forces may be relaxed and the assembly brought to equilibrium. Velocity regulation is achieved in the program by imposing a limit on the maximum allowable particle velocity. Furthermore, in order to aid this process high damping (say BETA = 0.5) may be used.

After compaction, the first phase of consolidation may be carried out using MODE 2 or 3. Care should be taken as boundary instability may occur when using MODE 2 for anisotropic consolidation. Also for assemblies which are to be consolidated to high stresses using MODE 3, forces between boundary particles may become significantly high and hence, relaxation using MODE 2 may once again be required.

The second phase of consolidation may now be carried out by maintaining constant the required stresses until the assembly reaches

equilibrium. It is advisable that the boundary control used for this phase is of the type used for the shear stage. For example, if a stress-controlled boundary is to be used in the shear stage then secondary consolidation should use MODE 2. This avoids re-adjustment problems at the start of shear.

Finally, it should be noted that the porosity at the end of the compaction stage is a function of the surface friction coefficient, i.e. the higher the interparticle friction the higher the porosity. Therefore, if a dense assembly is required, the surface friction may be set at a reduced value for the compaction stage and then raised for consolidation.

3.7.3 Control of the Shear Stage

Any boundary control may be used, provided the user understands their limitations. During this stage it is required, in order to obtain meaningful results, that the assembly deforms such that quasi-equilibrium is maintained. Frequent checks are required to confirm that:

i) Particle velocities and forces are low.

ii) Assembly oscillations are absent.

iii) The servomechanism behaves correctly (when using MODE 3).

In order to carry out the above checks printed output should be obtained at regular intervals. Also, when checking for oscillations it is useful to obtain a velocity vector plot (option 6) to detect contact oscillation and to plot boundary stresses and strains to detect assembly oscillation.

In addition to the above checks it is advisable that many reference states be saved by storing the memory map at frequent intervals in permanent files, or on magnetic tape. The stored memory

maps allow the test to be restarted from any reference state and hence, later analyses may be carried out.

3.8 PROGRAM VALIDATION

Two validation tests have already been carried out by Strack and Cundall (1978). These tests attempted to numerically simulate the results obtained from physical tests on photo-elastic disc assemblies by de Josselin de Jong and Verruijt (1969) and Oda and Konishi (1974). The comparison made from the various plots proved sufficiently good to conclude that the Distinct Element Method was a valid tool for fundamental research into the behaviour of granular assemblies. The discrepancies in the results were assumed to be due to the difficulty in obtaining the exact information from the experimental data that was available.

A further validation test has been carried out by the author. This has been done by simulating a test on a regular array of discs and comparing the results with the predictions of the regular array theory, which will be presented in Chapter 6. The numerical test was carried out on an assembly of 17 discs the boundary of which was controlled by MODE 3. Deformation of the assembly was then achieved by applying a deviator stress such that the mean-stress and the direction of the major principal stress remained constant. The results obtained are almost in exact agreement with theoretical predictions. The complete details of the validation test are given in Appendix A.

The above test not only validates the Distinct Element Method, but also serves as a check that the program is operating satisfactorily. This is particularly important as many changes have been made to it.

4 1000 DISC TEST

4.1 INTRODUCTION

All tests, carried out to date, using 'Ball' have been concerned with two main objectives. Early testing, reported by Cundall and Strack (1979a) was conducted in order to establish the validity and merits of testing with 'Ball'. Subsequent testing, on the other hand, has been directed at identifying the internal behaviour of elemental granular assemblies when subjected to slow progressive deformation. The ultimate aim of this later work is to develop a constitutive model for granular media based upon the observed internal microscopic mechanisms of deformation. Although this has not yet been achieved, observations from tests using 'Ball' can be used to set the constraints for the future rational development of such a constitutive model.

To reconfirm and reveal new observations from test results produced by 'Ball' a further element test has been carried out by the author. In planning this test it was decided that the assembly to be deformed should contain as many particles as possible. This criterion was chosen to reduce the boundary effects on the interior of the test assembly so that internal regions could be considered to behave as an element within an infinite assembly. In addition, the assembly must be large enough to ensure macroscopic homogeneity and provide sufficient data for statistical analysis. However, as explained in section 3.6, the number of discs in an assembly is directly proportional to program storage requirements and execution time. Therefore, due to time constraints, it was decided to concentrate on the deformation of a single disc assembly containing 1000 particles.

Based on published experimental work, a particle size distribution was chosen to ensure that, following compaction and

consolidation, the assembly could be considered to be random, dense, homogeneous and isotropic. The magnitude of the applied isotropic stressfield, i.e. the mean stress, was 1.0E6. Subsequent shearing of the consolidated assembly was then carried out at constant mean stress and was three phase. All three phases restricted the principal boundary strain directions to be coincident with the x_i reference axes throughout shearing. The first phase was to monotonically load the assembly by decreasing the minor principal strain (the x_i-direction) to $e_1 = -0.03$, this value of strain being relative to the consolidated state and applied linearly with respect to time. From three stored reference points the second phase was to unload the assembly by reversing the strain-rate until the strain in the x_1 direction returned to zero. The reference points required to do this were obtained from memory map dumps at $e_1 = -0.01$, -0.02 and -0.03 respectively. Finally, the third phase of shearing consisted of reloading to $e_1 = -0.03$ from a reference point stored at $e_1 = -0.01$ during the unloading of the assembly from $e_1 = -0.02$.

On the surface this amount of testing may appear to be lacking in quantity especially when compared to the number of laboratory tests that could have been performed on real disc assemblies. However, unlike physical laboratory testing, all microscopic quantities are easily accessed and, providing some kind of large data storage facility is available then many test reference states may be saved. The implication of this is that tests do not necessarily have to be repeated for future analyses to be carried out or for plots representing new microscopic quantities to be produced. This facility has been used to store the memory map at many points during deformation and hence fast access to test data is possible from magnetic tape. It is also worth emphasising that when testing with 'Ball' it is possible to 'turn the clock back', i.e. go back and

resume testing from an earlier part in the test. This facility is obviously not available in physical testing. In fact the 1000 disc test reported here could only be simulated by 4 physical tests. This very special facility means that future testing (different strain paths etc.) could utilise the same consolidated assembly.

Initial testing considerations, testing procedures and results for the 1000 disc test are given in the following sections. However, in order for the results from this test to be accurate, preliminary testing was essential. It should be understood that testing with 'Ball' is not totally dissimilar to the physical testing of disc assemblies in that testing expertise must be initially gained. It is because the Distinct Element Method incorporated within 'Ball' is used to simulate a real-time process that 'Ball' itself can be considered as a numerical apparatus. Hence, initial testing gives a 'feel' for the sensitivity and required control of the assembly under deformation. In addition, it will always be necessary to carry out preliminary tests to determine a suitable damping constant, loading rate and gain for the servomechanism (if boundary MODE 3 is used) as the correct choice of these constants will be unique for the physical properties of the assembly under consideration. However, these tests may be performed on significantly smaller assemblies as only result accuracy is sought.

No details are given in this chapter regarding the internal mechanisms of deformation. This will be dealt with in Chapter 5.

4.2 INITIAL TEST CONSIDERATIONS

Several 1000 disc tests were started but subsequently terminated when undesirable results were obtained. The majority of these early tests were abandoned due to the inexperienced choice of control

parameters which gave rise to assembly instabilities and resulted in high out of balance forces and oscillations. Fortunately these were detected very early in phase one of shearing and therefore not much time was taken up. Nevertheless this time was not wasted and early testing is now considered as a period of gaining test experience. During the period of running these preliminary tests, as they will now be termed, many additional control facilities were developed. Some of these include, for example, the introduction of velocity control for use during stress relaxation carried out in assembly compaction and consolidation, the introduction of a general boundary control, servo-mechanism algorithm (MODE 3), and tuning it for a defined deformation. Comprehensive investigations were carried out on simplified systems to show the effects of damping, timestep and loading rate (Chapter 2). Tests were then carried out on small assemblies of only 50 discs. From these tests satisfactory testing parameters were obtained for use in the 1000 disc test reported here.

In the subsections below, information is given as to the choice of particle size distribution, assembly generation, physical and control parameters, compaction and consolidation, control of deformation and checks, plots and units for the 1000 disc test.

4.2.1 Particle Types and Sizes

The disc assembly must contain more than one particle size to achieve a randomly distributed assembly after compaction. Davis and Deresiewicz (1977) conducted physical disc tests from which they showed that if only one particle size is used large regular regions develop on compaction. When compaction was aided by vibration the assembly became almost totally regular as particles formed their densest packing. Two particle sizes is probably still too few as

small regular clusters are likely to be generated. A photograph of a disc assembly generated by Murayama and Matsuoka (1973) containing only two discs types supports this. Cundall and Strack (1979a), Strack and Cundall (1978) have successfully generated random assemblies using 'Ball' for 3 and 4 particle types, the maximum radius ratios being 5/3 and 3 (approx) respectively. Physical tests have also achieved random assemblies. De Josselin de Jong and Verruijt (1969) used 8 particle types with a maximum radius ratio of 4. Drescher and De Josselin de Jong (1972) used 6 particle types with a maximum radius ratio of 5/2. Oda and Konishi (1974) and Konishi (1978) used 3 particle types with a maximum radius ratio of 5/3. Chapuis and Soulie (1981) used 4 particle types with a maximum radius ratio of 2. However, the author suggests that the limiting radius ratio is a function of the total number of particles that make up an assembly. This is based on the fact that large radius ratios will affect local regional homogenity i.e. larger regions of the assembly would be required in order for the region to be considered macroscopically homogeneous.

Figure 4.1 gives the particle size distribution used in the 1000 disc test. From information given in this figure it can be seen that there are 5 particle sizes having a maximum radius ratio of 3 but 90% of the particles (R_2, R_3, R_4) have a radius ratio of 5/3. The particle size distribution for the 50 disc test was similar to that of the 1000 disc assembly but only contained the three intermediate radii types R_2, R_3 and R_4 and the number of particles for each type was 13, 16 and 21 respectively.

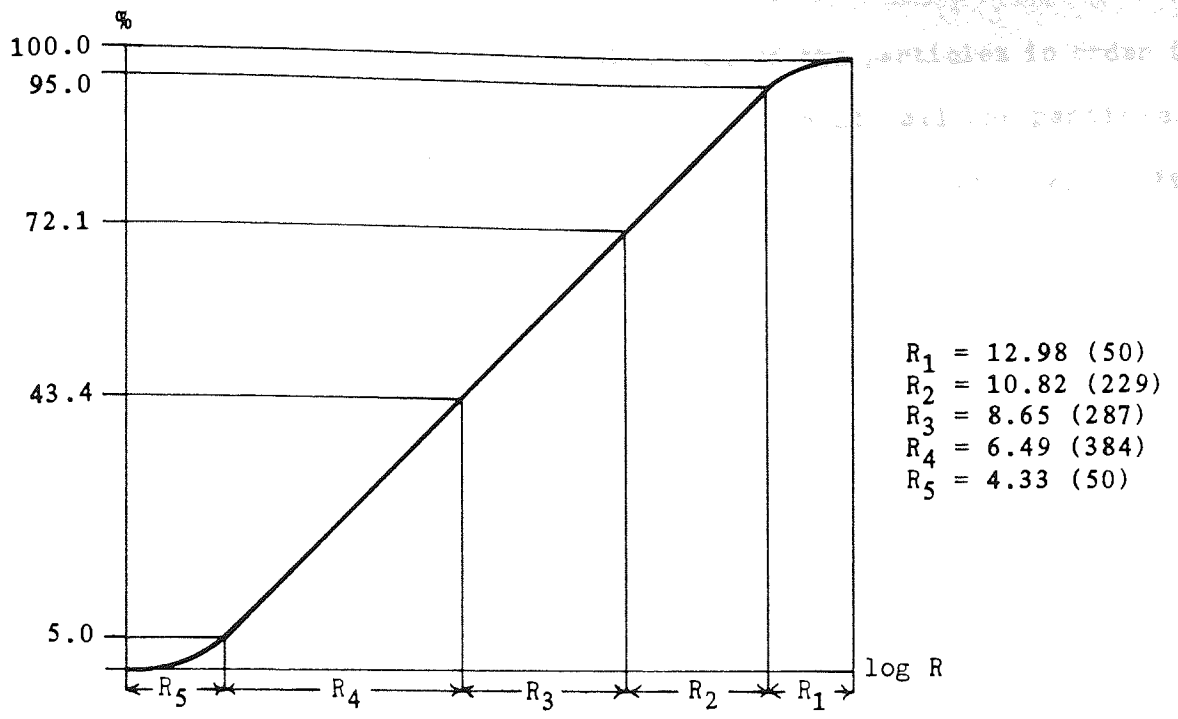

Figure 4.1 Particle size distribution for the 1000 disc test

Clearly the number of particle types and the radius ratio used in the 1000 disc test conforms to previous disc assembly tests. However there is no reason why the number of types should not be increased, provided the maximum radius ratio is reasonable. 'Ball' is at present limited to 50 disc types but this limit could easily be increased so that each particle in the 1000 disc assembly could be unique. There is, of course, a limit on types in physical tests due to the expense and time involved in manufacturing the discs.

4.2.2 Assembly Generation and Boundary Location

The automatic particle generation option described in section 3.3 was employed to achieve a truly random spacial distribution of particles within a circular region. This region was then overlayed by a square grid containing 100 boxes in order to facilitate subsequent contact searching (see section 3.2). Large particles were generated first and the area for generation defined by a circular boundary, was

set to approximately twice the solid area of the particles in order to minimise the number of attempts needed to locate all the particles. The resultant circular boundary had centre co-ordinates $x_1=x_2=390$ units and a radius of 360 units, the particle location grid having a box dimension of 72 units. After all particles had been generated, automatic boundary location was used to define a true assembly boundary so that compaction could be carried out using boundary control.

4.2.3 Physical and Control Parameters

Setting physical parameters involves choosing values for:

a) Particle stiffnesses so that contact stiffnesses may be calculated (equations (3.20)).

b) Disc density to calculate disc masses (equation (3.19)).

c) Disc surface friction in order to limit contact shear forces.

A set of suitable control parameters must also be chosen. These include:

a) The fraction of the critical timestep to be employed between calculation cycles.

b) A suitable damping constant.

c) A reasonable loading rate.

d) An appropriate gain for the servomechanism (as boundary MODE 3 was to be implemented).

It is not a simple task to set the above parameters as their influence on assembly deformation is complex and exact analysis is impossible. Even for the much simplified systems which were analysed in Chapter 2 (section 2.5) it was shown that parameters are interrelated. Nevertheless based on the analysis of these simplified systems 'Ball' is able to calculate approximate values for the

critical timestep and critical damping constants.

To maximise the real-time rate of deformation (i.e. to carry out tests as fast as possible) it is desirable to increase the calculation cycle timestep and the loading rate. This involves maximising the minimum particle mass-stiffness ratio, increasing the fraction of the critical timestep and raising the rate of force transmission from the boundary. Constraints must however be employed in order to obtain meaningful and accurate results. Stiffnesses must be great enough to ensure that contact displacements are small in comparison to disc radii. On the other hand mass and stiffnesses must be small enough to ensure results are independent of damping. The assembly must not become numerically unstable or deviate greatly from equilibrium. The latter constraints are most important and require preliminary testing to ensure that results are satisfactory.

As a starting point to set parameters for the 1000 disc test it was decided to firstly set particle stiffnesses in order to limit the elastic contact displacements. To determine normal particle stiffnesses a simple system of two contacting frictionless discs was analysed. This system is shown in Figure 4.2 in which all relevant contact and disc information is given. If it is now assumed that the individual disc displacements are inversly proportional to the curvature of the disc surface, then

$$\delta_A/R_A = \delta_B/R_B \tag{4.1}$$

where $\delta = \delta_A + \delta_B$

This assumption implies that the system could be thought of as a single linear spring connecting the disc centres. Hence, the linear strain between any two particle centres shown in Figure 4.3 is equal. It is interesting to note that Hertzian contact theory suggests that contact force and displacements are linearly related for small

displacements between discs. The proof of this is given in Appendix C.

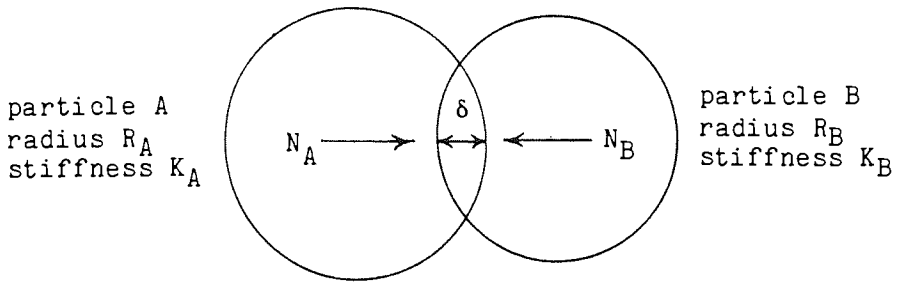

Figure 4.2 Force transmission between two unequal frictionless discs

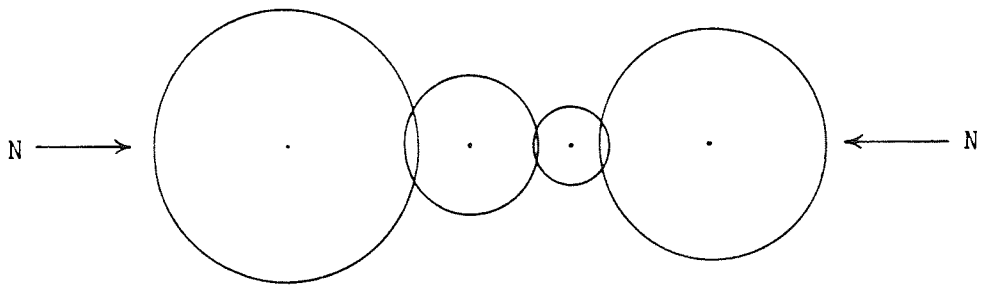

Figure 4.3 A column of discs subjected to an axial force N

If equilibrium is considered for the contact shown in Figure 4.2 then

$$N_A = N_B = K_A.\delta_A = K_B.\delta_B \tag{4.2}$$

and by using equations (4.1) and (4.2) it can be shown that

$$K_A.R_A = K_B.R_B \tag{4.3}$$

By providing the normal stiffness of one particle type the normal stiffness of all others can be calculated from eqn. (4.3). The chosen normal stiffness must nevertheless limit particle displacements. It is not possible to predict the maximum normal force that will develop in a random assembly and therefore observations obtained from simpler assemblies were used.

In the regular array theory of Chapter 6 it is shown that

$$\sigma_{kk} = -4RN/A_o \qquad (4.4)$$

where R, N and A_o are the particle radius, normal force and the area occupied by a single particle respectively. For square packing $A_o = 4R^2$ and hence

$$\sigma_{kk} = -K.\delta/R \qquad (4.5)$$

Now, by setting $\delta = 0.02R$ for the largest particle type then

$$\sigma_{kk} = -0.02K \qquad (4.6)$$

Therefore, if the mean stress is -1.0E6 then the normal stiffness of the largest particle is 1.0E8 to ensure the average linear strain between particle centres is approximately -0.02. This is nevertheless based on an average particle coordination number of 4. In the 1000 disc test the actual average coordination number varied from 4.2 to 3.6.

Shear particle stiffness was assumed to be equal to its corresponding normal stiffness. This assumption limits elastic branch rotation (i.e. the rotation of lines joining the centres of contiguous particles) to 0.02μ radians, where μ is the smaller coefficient of friction for the two particle surfaces in contact. Based on values measured from physical disc assembly tests the surface friction coefficient was to be set to 0.4, which implies that the average maximum branch (i.e. the line joining particle centres) rotation would be about 0.008 radians.

All particles were given a density of 1000 from which 'Ball' is able to calculate particle masses from eqn. (3.19).

A list of the physical properties for the particles in the 1000 disc test is given below.

TYPE	RADIUS	MASS	K_N	K_S	μ
1	12.98	529365	1.0E8	1.0E8	0.4
2	10.82	367841	1.2E8	1.2E8	0.4
3	8.65	235092	1.5E8	1.5E8	0.4
4	6.49	132341	2.0E8	2.0E8	0.4
5	4.33	58909	3.0E8	3.0E8	0.4

From these physical parameters 'Ball' is able to calculate a critical timestep and the critical damping coefficients as described in Chapter 2.

Boundary MODE 3 was chosen to control the test for the reasons to be given in section 4.2.5. The gain for the servomechanism G was set to 1.0E-7 this being based on results obtained from the preliminary 1000 disc tests. Strictly speaking this value is only applicable to the tests reported here as it relates to the physical parameters of the discs and to the magnitude of the stress field. However, finding an adequate value for G is relatively simple. G is not a very sensitive parameter for given test conditions, and hence an adequate value may be found by carrying out tests of relatively few calculation cycles (say 5000). For each test the value of G is incremented by a factor of 10 from an initially small value (say 1.0E-10). During these tests the boundary stress and strain-rate tensors should be printed out every 10 cycles or so to monitor the performance of the servomechanism. For the tests reported here any value between 1.0E-8 and 1.0E-6 was found to be satisfactory.

To obtain suitable values for the timestep, damping and loading rate, tests were carried out on the 50 disc assembly shown in Figure 4.4. Isotropic compaction and consolidation of this assembly was achieved in a single phase operation by using boundary MODE 2 together

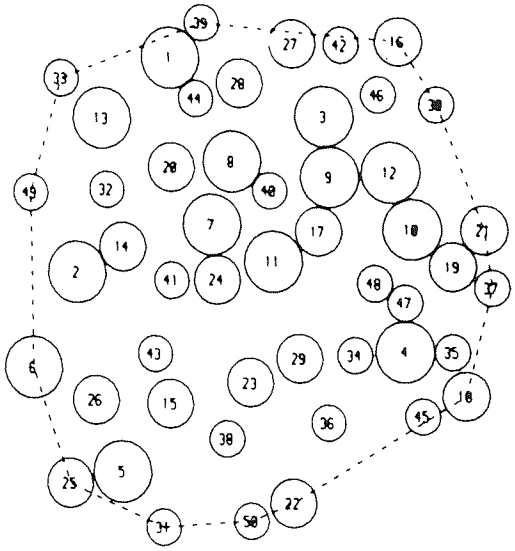

a) Assembly as generated

σ_{kk} = -2.0E6

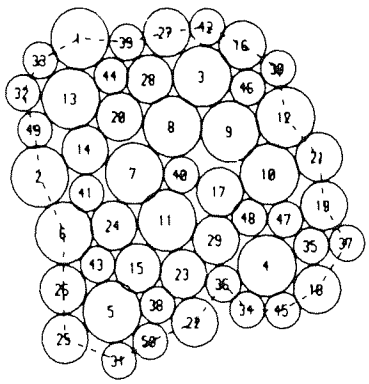

b) Assembly after isotropic compaction and consolidation

Figure 4.4 The 50 disc assembly

with particle velocity regulation. Once the assembly reached equilibrium the memory map was stored so that all subsequent shearing tests could be started from the same reference state. Each test consisted of linearly raising the principal compressive strain to 2% (i.e. e_{11} = -0.02, e_{12} = e_{21} = 0) and maintaining constant mean stress using the MODE 3 boundary control (G = 1.0E-7). During tests printed

particle quantities and the boundary stress and strain-increment tensors, together with plots of contact forces (options 1 and 5) and linear particle velocities (options 1 and 6), were output for examination.

The effect of the loading rate was examined first. Two tests were carried out, the first raised the compressive strain at a rate of 1%/40,000 cycles and the second at a rate of 1%/20,000 cycles. For both tests the fraction of the critical timestep was set to 0.1 thus giving minor principal strain-rates of $\dot{e}_1$ =-0.34363E-4 and $\dot{e}_1$ = -0.68726E-4 respectively and for both tests the fraction of critical damping was set to 0.05. Printed and plotted output showed that results were in almost exact agreement with the exception of particle velocities and out of balance forces. These quantities were higher (approximately double) for the higher loading rate. For the lower loading rate used in the first test typical out of balance forces were of the order of 1.0E4 whereas the typical contact force was in the order of 1.0E7. The ratio of the average out of balance force to the average contact force (0.1% for the lower loading rate) is a direct measure of the suitability of the loading rate.

The effect of damping was examined by carrying out another test wherein the damping parameter was set to 0.1 of its critical value. For this test the loading rate and fraction of the critical timestep were identical to those used in the first loading rate test above. Results could now be compared to the first loading rate test where the fraction of critical damping applied was 0.05. This comparison showed that results appeared completely independent of damping as output from both tests was in almost exact agreement. Bearing in mind that damping is only incorporated to eliminate oscillations it appears that this is achieved with very low damping.

Finally the effect of the critical timestep was investigated by conducting a further test using a timestep of 0.2 of its assumed critical value. Once again the lower rates of damping and loading rate were used. Results were in agreement with the first of the loading rate tests which employed a fraction of critical timestep of 0.1. Results for this test therefore suggest that numerical instability was absent.

Based on the above 50 disc test, control parameters were set for the 1000 disc test. Critical fractions were set for the timestep and damping of 0.2 and 0.05 respectively, and for the selected timestep the loading rate was set to 1% compressive strain/20,000 cycles. However, because the critical timestep (based on the minimum mass-stiffness ratio) is less for the 1000 disc test the actual timestep will be less than that used in the 50 disc test. This means that the loading rate will be higher with respect to time. Nevertheless the loading rate is within the limits used for the 50 disc tests. A summary of the control parameters to be set for the 1000 disc test is given below.

BOUNDARY CONTROL	DAMPING	TIMESTEP	LOADING RATE
MODE 3	BETA=0.05	$0.2\ \Delta t_{crit}$	$\dot{e}_{11} = \Delta e_{11}/\Delta t$
G = 1.0E-7			$= \pm 0.63080E-4$

These control parameters, based on the 50 disc test, suggest that the results from the 1000 disc test are reliable. They do not provide sufficient results to describe the effects of the control parameters. Future large scale tests are required to set an allowable parameter range based on result accuracy, i.e. limits should be set wherein results are acceptably independent of these control parameters. This work could prove that the loading rate and timestep may be raised in

order to minimise calculation effort.

For the above 50 disc tests all stress-strain curves were identical and hence Figure 4.5 shows the curves for only one of the tests. No comments are given at this stage concerning the shape of these curves as discussion of results is reserved until after the 1000 disc tests has been described in detail.

4.2.4 Compaction and Consolidation

The method suggested in section 3.7.2 was chosen in order to isotropically compact and consolidate. However, as a dense assembly was sought compaction was carried out with the surface friction of all particles set to zero. After compaction the coefficient of friction was set to 0.4. High damping (BETA=0.5) was used throughout both the compaction and consolidation stages.

4.2.5 Boundary Control

All three phases of deformation were to be controlled by boundary MODE 3. The form of the servomechanism to be used was

$$\dot{e}^{t}_{11} = \mp 0.63080E\text{-}4$$

$$\dot{e}^{t}_{12} = \dot{e}^{t}_{21} = 0$$

$$\dot{e}^{t}_{22} = \dot{e}^{t-\Delta t}_{22} + G(\bar{\sigma}^{t-\Delta t/2}_{o} - \bar{\sigma}^{t-\Delta t/2}_{o}) \qquad (4.7)$$

The reasons for choosing MODE 3 were

a) It is the only boundary control that is capable of following a desired stress path when stresses are approaching those at peak assembly strength. This is because MODE 2 control can lead to rapid readjustment of the boundary which often causes explosive velocities to be generated. Even with boundary velocity control boundary readjustments would still occur, which is undesirable.

b) Consideration of the number of particle constraints and degrees of

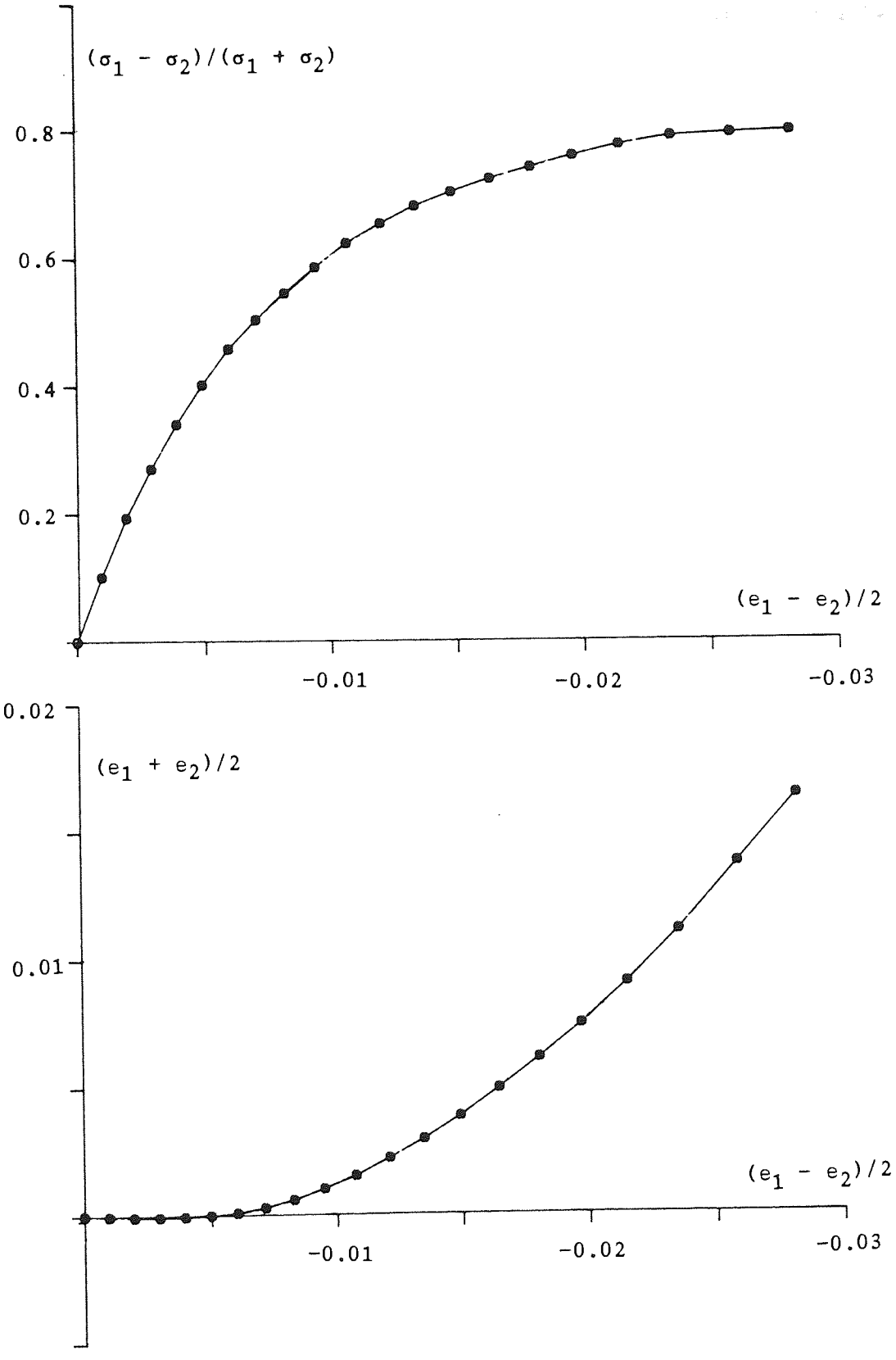

Figure 4.5 Stress/strain plots for the 50 disc test

freedom for internal regions of the assembly have been reported by Cundall et al (1982). By extracting a small sample from a large assembly, tests were performed using stress and strain controlled boundary modes to determine how closely each related to the undisturbed regional behaviour when the small sample remained embedded in the large assembly. Results from these tests showed that strain controlled boundaries produce assembly behaviour which is more closely related to that of an element embedded within a large assembly.

c) The possibility of extending the deformation past peak strength could only be contemplated if a strain controlled boundary was employed.

4.2.6 Output of Results

In order to carry out the suggested checks in section 3.7.3 and to obtain printed and plotted information the following list was to be output every 2000 cycles (i.e. $\Delta e_{11} = \mp 0.001$).

a) All particle quantities (forces, velocities, etc).

b) All plotting options in various combinations (e.g. overlayed options 1 and 5).

c) The stress and strain-increment tensors for the boundary and for a given central internal region containing about 500 particles.

d) Special plotted and printed results from analyses. Some of these will be discussed later in this chapter and others will be given in Chapter 7.

e) Output of the memory map onto magnetic tapes. A single 9-track magnetic tape can store up to 61 test reference states for the 1000 disc test at an information density of 1600 bpi. Running tests using magnetic tape is however very tedious from remote

terminals. Hence only selected reference states could be permanently stored and it was decided to store the reference state for the assembly as consolidated together with phase one and phase two unloading from $e_1 = -0.03$ every 2000 cycles.

4.2.7 Units

None of the three basic units, namely mass, length and time are to be related to any commonly used measures. Hence, for example, the magnitude of a contact force will be given in undefined force units. The reader may however attribute any compatible set of dimensions to the physical parameters in order to relate these units to standard quantities, e.g. SI units. On the other hand the numerical values of the physical parameters could be changed. Forces, stresses etc. could then be recalculated by simple dimensional analysis.

4.3 TEST DETAILS

Figure 4.6 shows the assembly as generated and after consolidation. In this figure the discs are numbered (although not clearly due to scale and reproduction) to show the order in which they were automatically generated, and also to show their subsequent position within the dense consolidated assembly. The grid that is overlayed on the assembly shows the location of the boxes used by 'Ball' to map particles and contacts. In addition Figure 4.6(b) shows an internal circular boundary of radius 180 units, which contains about 500 discs. This boundary is transparent to assembly behaviour and is only used for the calculation of macroscopic quantities, that are assumed to be free of boundary effects.

The cycle count at the end of consolidation was 34,000 and at this stage the assembly was in almost perfect equilibrium with typical

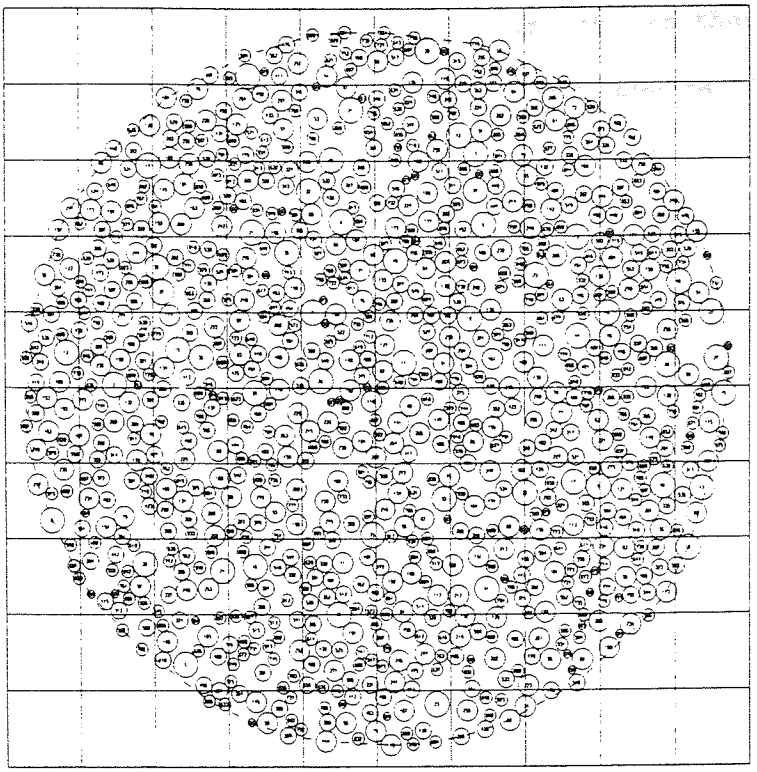

(a) Assembly as generated

(b) Assembly after compaction and consolidation

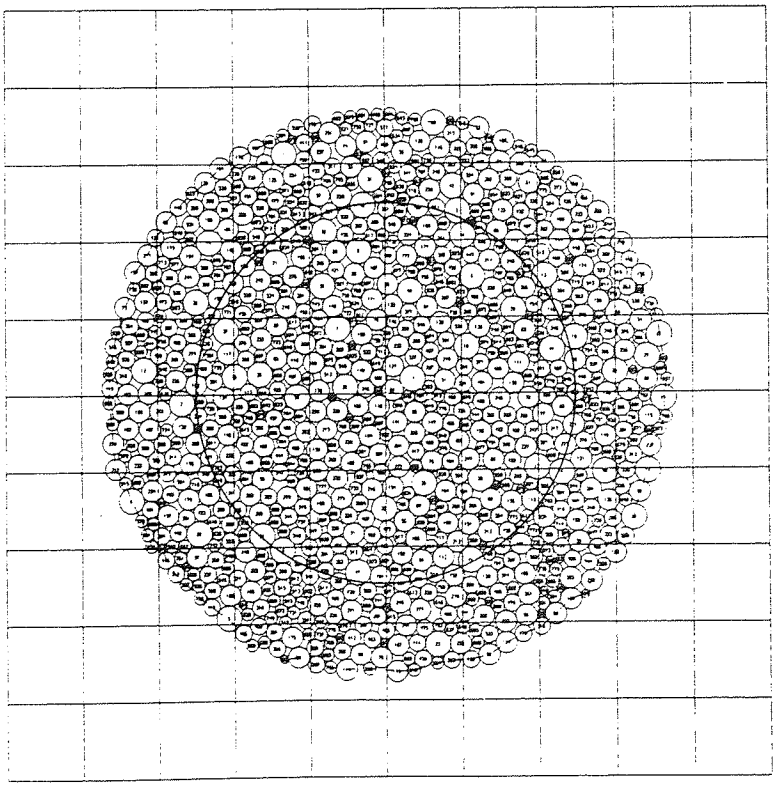

Figure 4.6 The 1000 disc assembly

particle forces and velocities being approximately 1.0E0 and 1.0E-7 respectively. The reference state at 34,000 cycles was then dumped to the magnetic tapes. All particle velocities were then set to zero and the boundary strain-rate $\dot{e}_{11}$ was set to -0.63080E-4 with all other components equal to zero. Phase 1 of shear was then executed by performing 60,000 cycles (15 successive jobs) such that the cycle count at the end of phase 1 was 94,000. During this phase the memory map was dumped consecutively to the magnetic tapes every 2000 cycles (i.e. every 0.1% compressive strain-increment) such that at the end of phase 1 a magnetic tape contained 31 test memory map dumps. Phase 2 was then executed by reloading the memory map with information from magnetic tape dumps. Phase 2a consisted of restoring tape dump 11 (54,000 cycles) to memory, zeroing velocities to minimise momentum changes, setting $\dot{e}_{11}$ = 0.63080E-4 with all other components zero and performing 20,000 cycles. Then, phase 2b and phase 2c were executed similarly by restoring tape dumps 21 (74,000 cycles) and 31 (94,000 cycles) and performing 40,000 and 60,000 cycles respectively. At the end of phase 2a, 2b and 2c the total cycle counts were 74,000, 114,000 and 154,000 respectively. During phase 2c the memory map was dumped consecutively to the magnetic tapes every 2000 cycles and hence, this identically filled the tapes with 61 memory map dumps. In addition, during phase 2b the memory map at a total cycle count of 94,000 cycles (e_{11} = -0.01) was dumped to an online hard-disc file. This file was subsequently used to reload the memory map at the start of phase 3. Once again velocities were zeroed, $\dot{e}_{11}$ = 0.63080E-4 (with all other components zero) and 40,000 cycles were performed to give a total cycle count of 134,000 cycles.

At increments of 2000 cycles throughout all three phases printed and plotted output was obtained. This was essential not only to observe microscopic and macroscopic behaviour but also to check that

results were representative of slow progressive deformation. These checks showed that oscillations were absent and that the assembly remained, throughout testing, close to equilibrium. Typical particle force to contact force ratio was 0.1% whereas the magnitude of particle velocities were in general less than those at the boundary.

4.4 RESULTS

The description and quantification of the mechanisms that describe the material response to deformation is given in detail in Chapter 5. However, to give the reader an insight into the overall behaviour of the assembly, macroscopic stress-strain data are provided below. To ensure that the definition of plotted quantities is clear the following notes are provided:-

a) Any quantity relating to a particular phase will be plotted with a unique symbol type. The symbols chosen to represent quantities of each phase are listed below.

   Phase 1 ○

   2 ▽

   3 △

b) When dealing with instantaneous tensor quantities, e.g. σ_{ij}, the following should be noted

   i) σ_1 is equal to the principal stress whose direction is closest to that of the x_1-axis (i.e. not necessarily the minor principal stress).

   ii) θ_σ defines the inclination of the minor principal stress to the x_1-axis, in degrees.

c) When dealing with incremental tensor quantities, e.g. Δe_{ij}, the following should be noted:

   i) Δe_1 and $\theta_{\Delta e}$ are defined as for b) above

ii) Because Δe_{ij} is incremental $\theta_{\Delta e}$ is plotted at $\Delta e_{ij}/2$

Figures 4.7 and 4.8 are dimensionless plots representing the properties of the stress and strain tensors calculated at both the boundary (assembly as a whole) and for the boundary of an internal circular region (shown in Figure 4.6(b)). In these plots boundary quantities are plotted with solid symbols and interior quantities plotted with hollow or outline symbols. From these plots it can be seen that there is a significant difference between boundary and interior quantities. This is due to boundary effects, the reasons for which will be given in Chapter 5. From this point it is assumed that the internal circular region behaves more closely to a sample within an infinite assembly. Hence, boundary stresses will no longer be plotted.

Figures 4.9, 4.10 and Figures 4.11 and 4.12 give the equivalent plots for phases 2 and 3 respectively. On these plots previous phases have been indicated by short dashed lines. Qualitatively, the shape of these curves resemble those which describe the global deformation of naturally occurring granular elements. Quantitatively, the gradients of these curves show that the modulus of the numerical assembly is much lower than typical moduli for sand. In addition, the magnitude of the maximum deviatoric stress is considerably less than would be expected for sand.

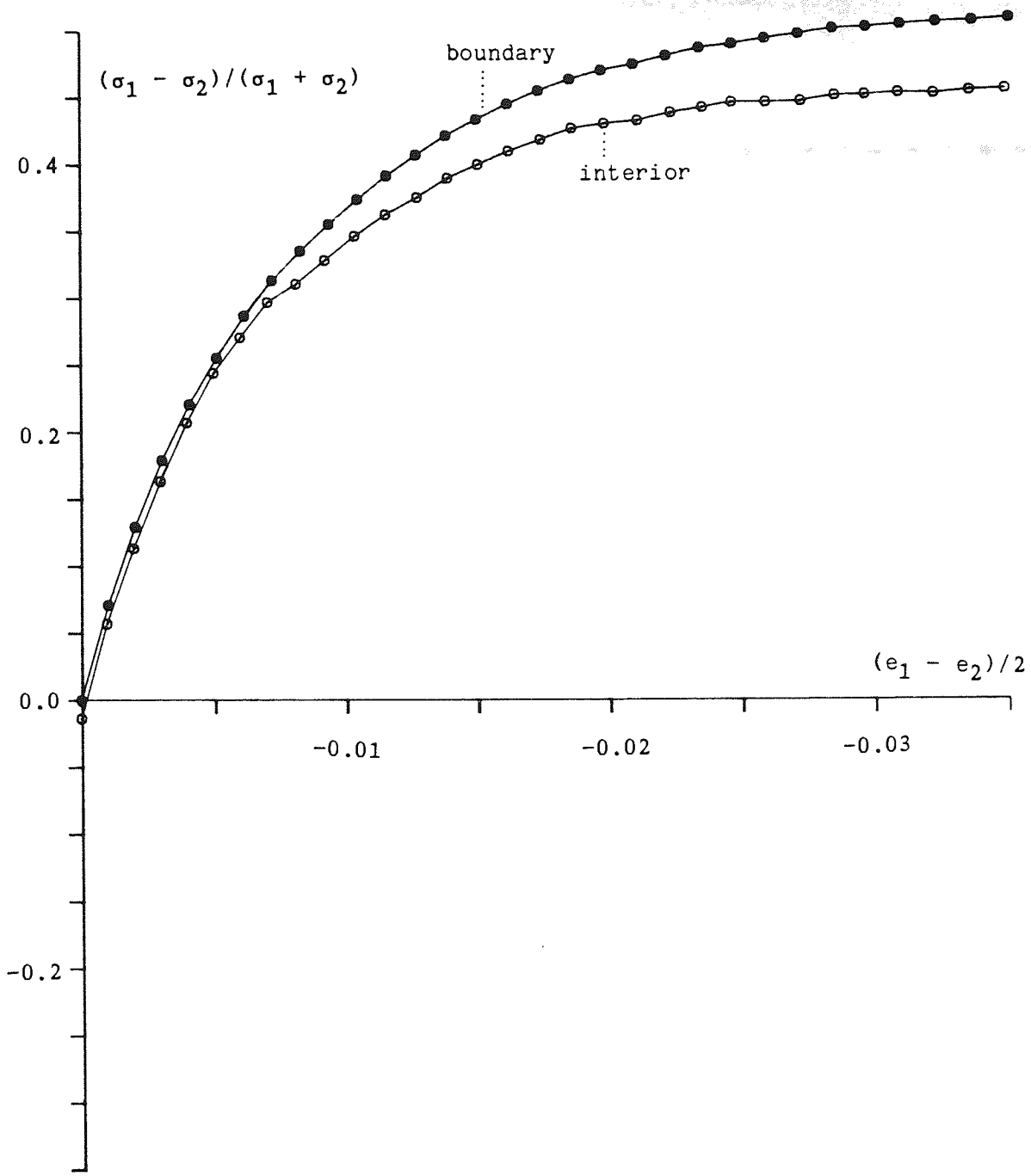

(a) Deviatoric stress against deviatoric strain

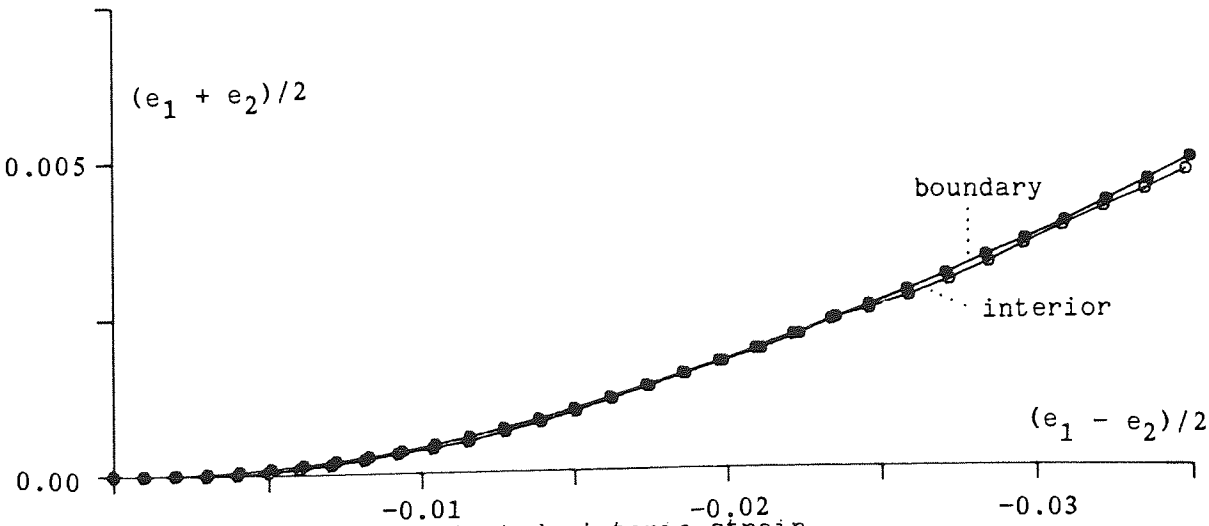

(b) Volumetric strain against deviatoric strain

Figure 4.7 Stress/strain plots for phase 1 - part 1

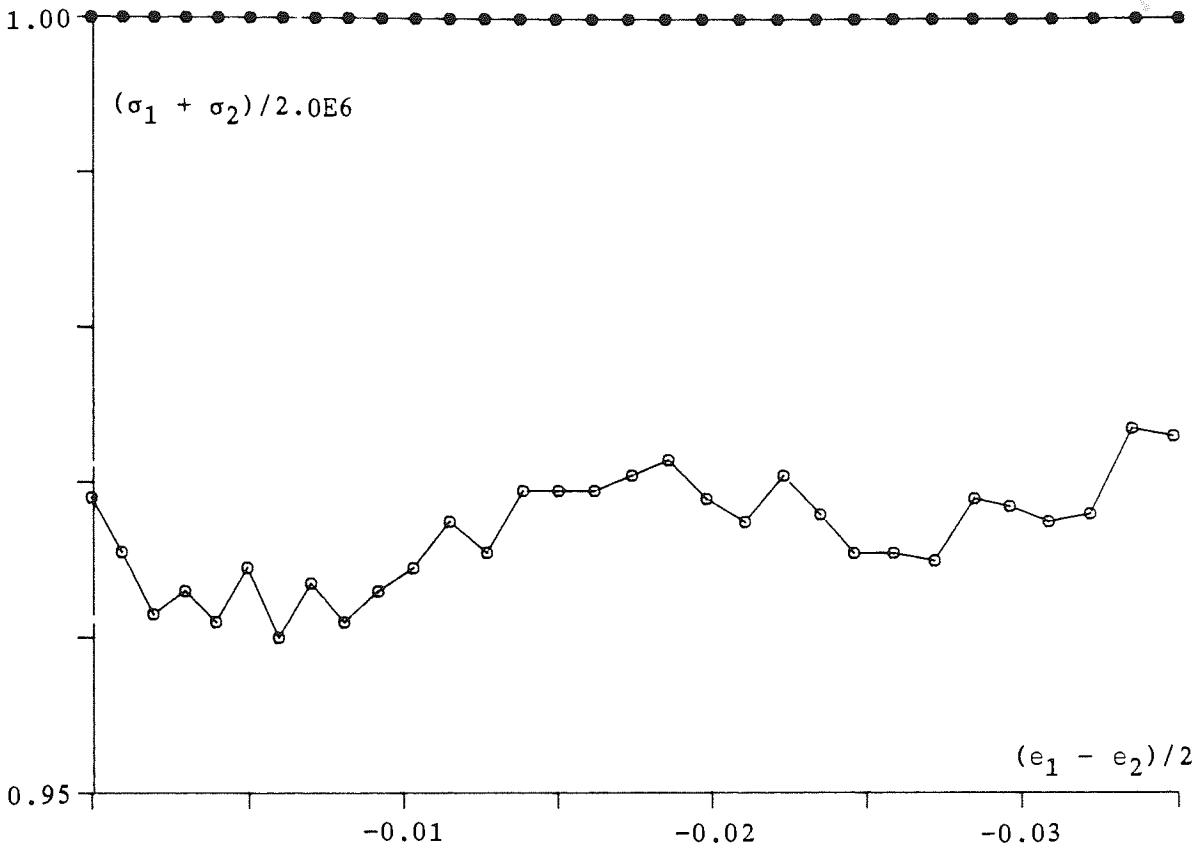

(c) Inner boundary mean stress normalised to boundary mean stress

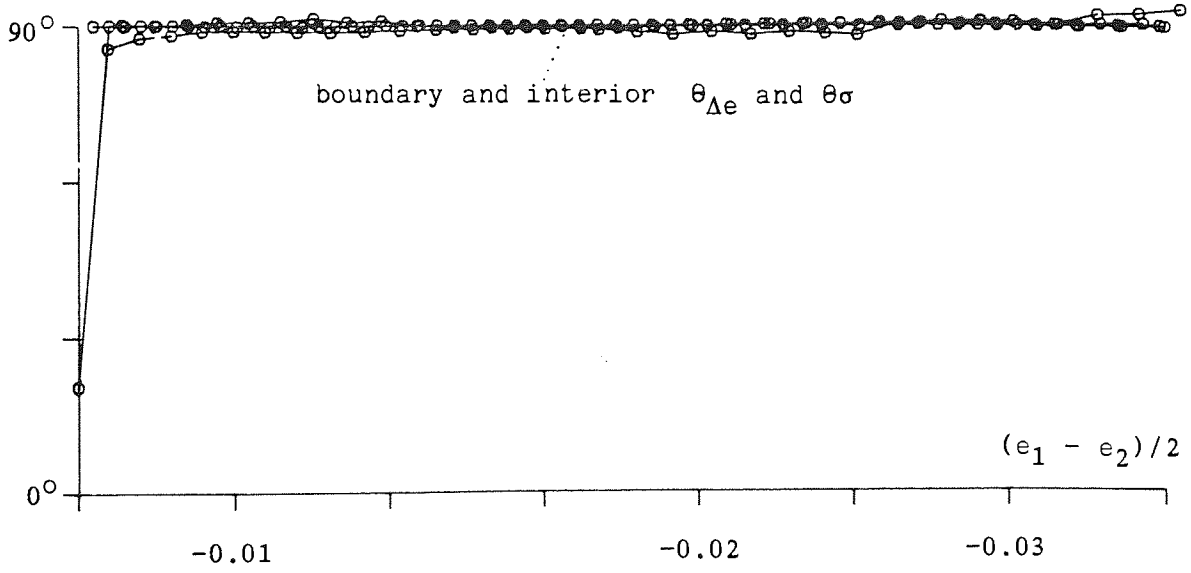

(d) Principle stress and strain-increment directions

Figure 4.8 Stress/strain plots for phase 1 - part 2

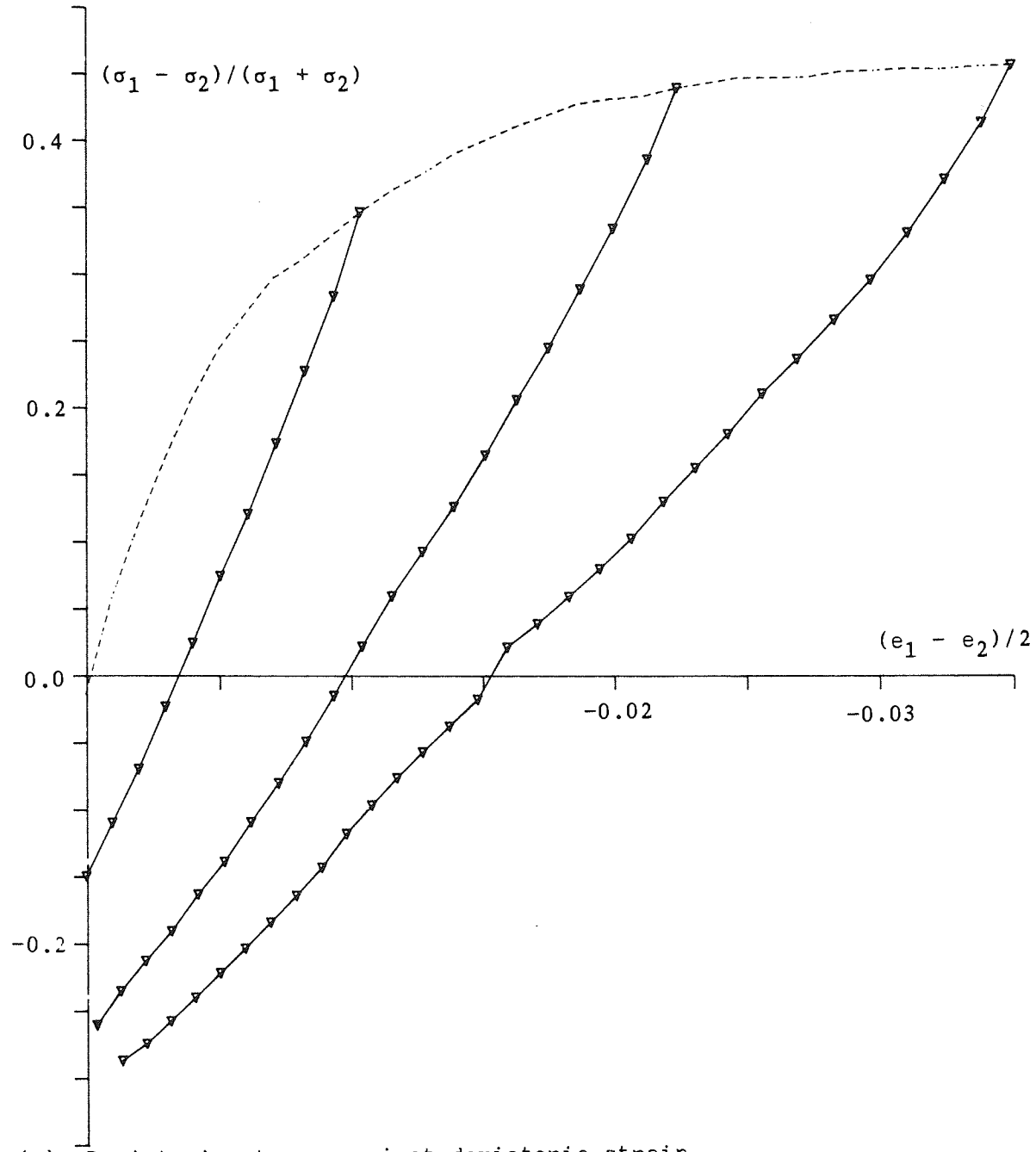

(a) Deviatoric stress against deviatoric strain

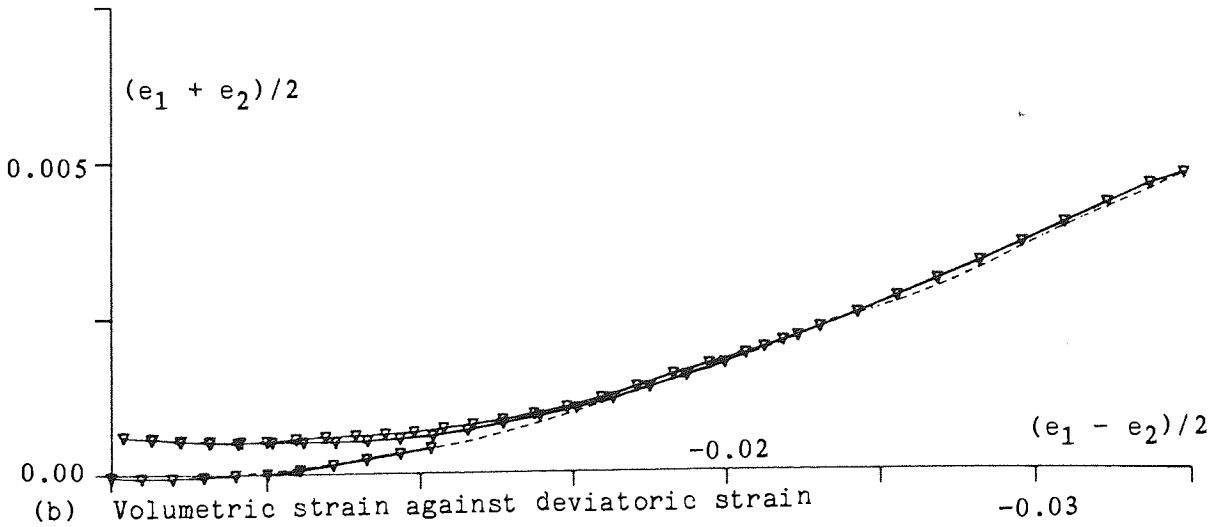

(b) Volumetric strain against deviatoric strain

Figure 4.9 Stress/strain plots for phase 2 - part 1

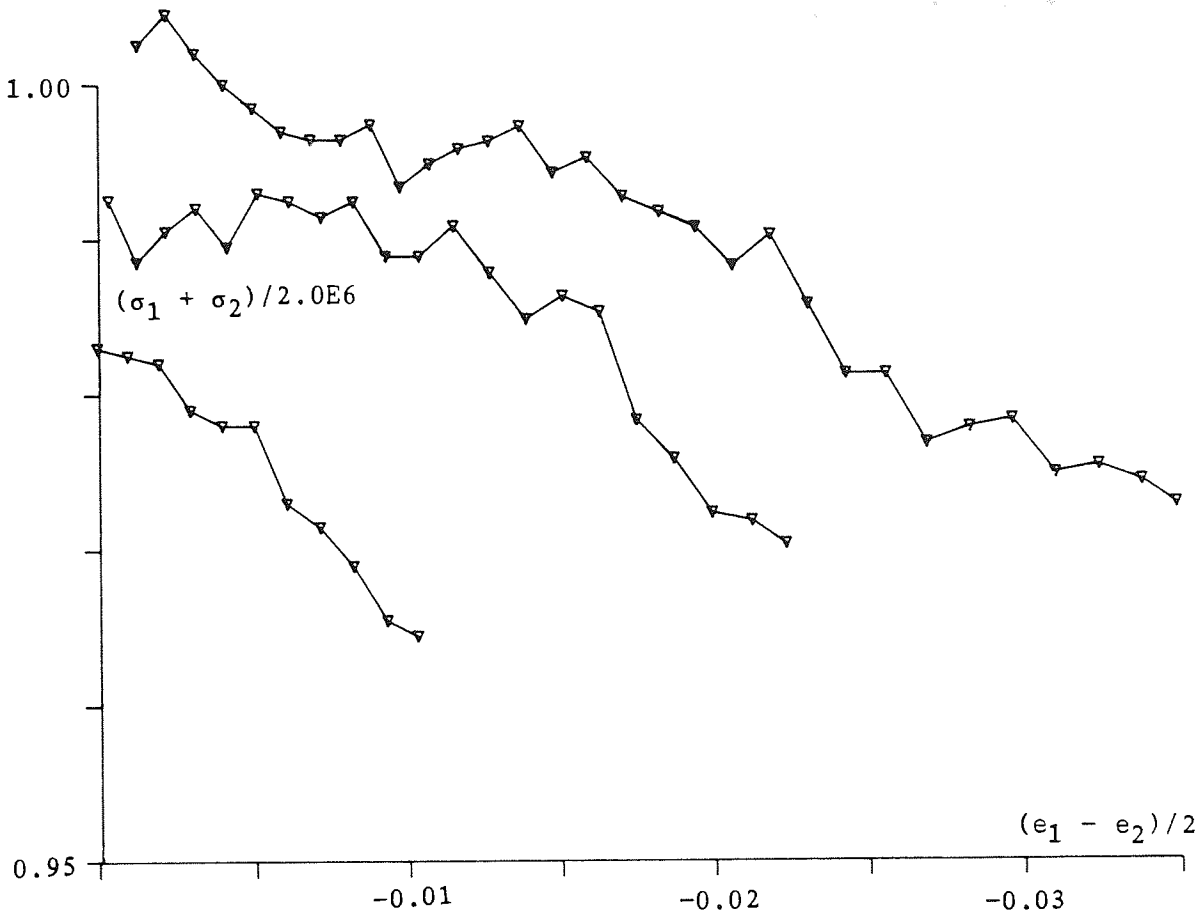

(c) Inner boundary mean stress normalised to boundary mean stress

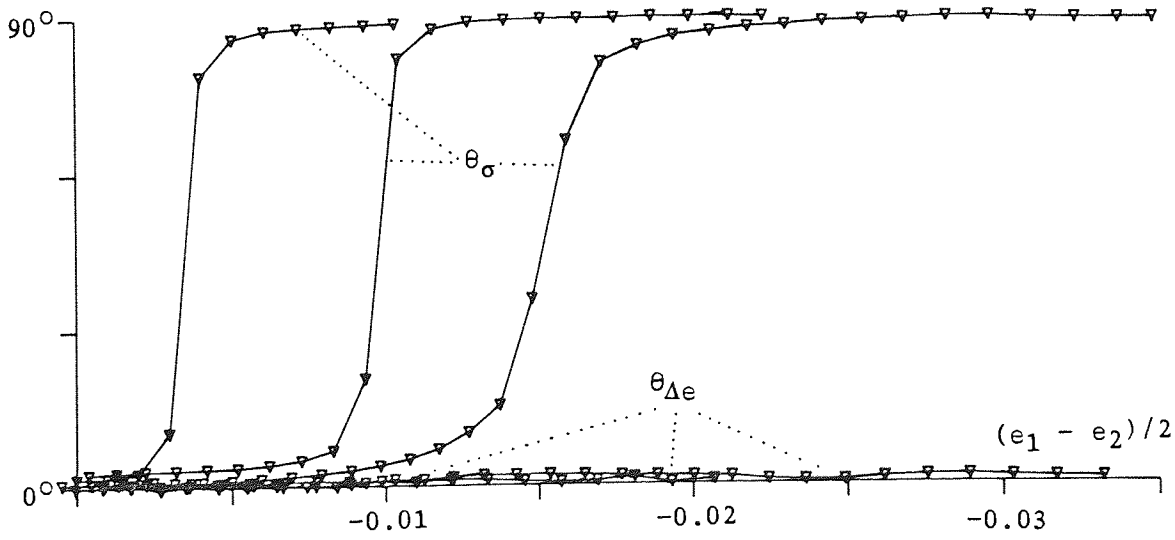

(d) Principle stress and strain-increment directions

Figure 4.10 Stress/strain plots for phase 2 - part 2

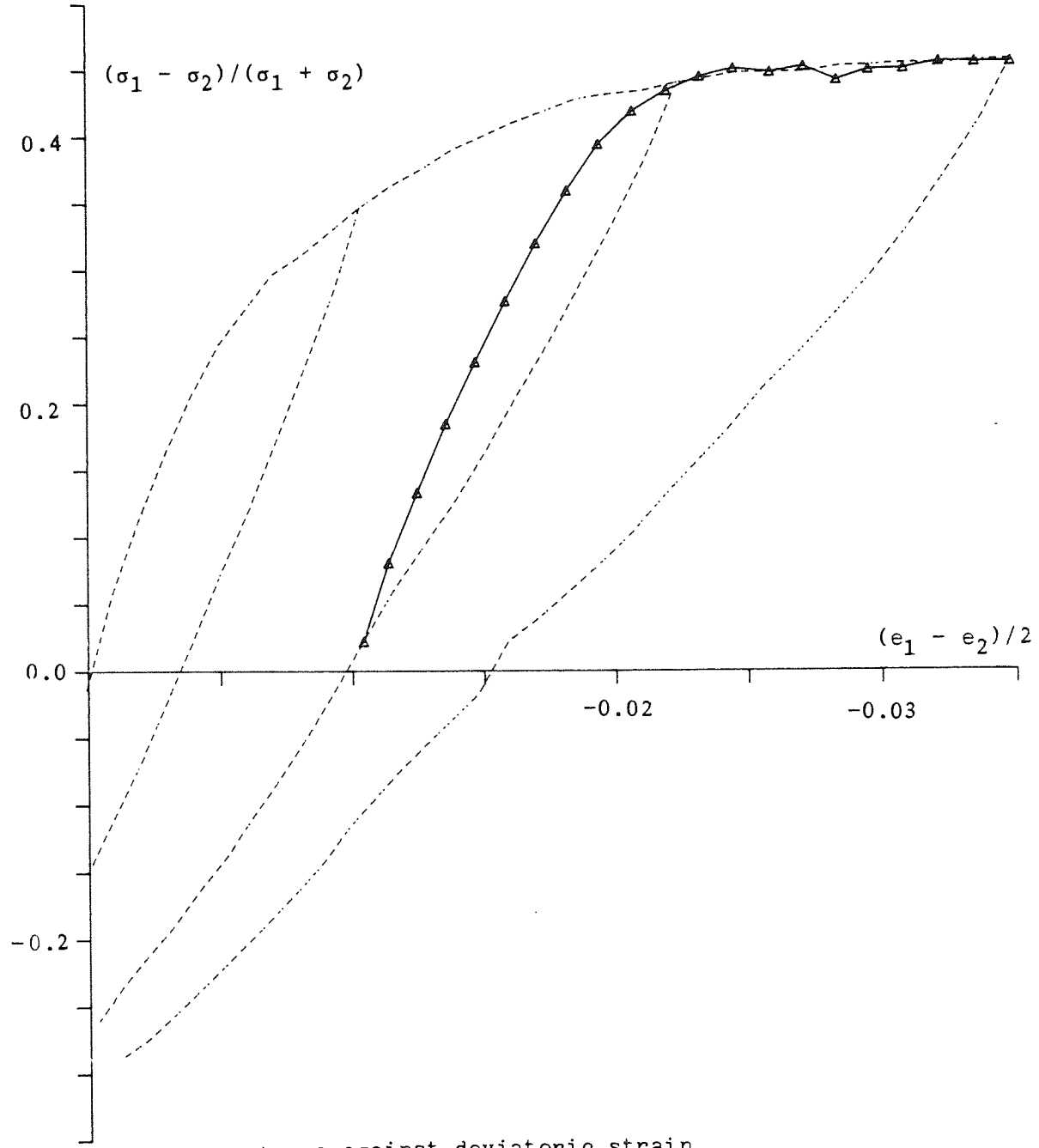

(a) Deviatoric stress against deviatoric strain

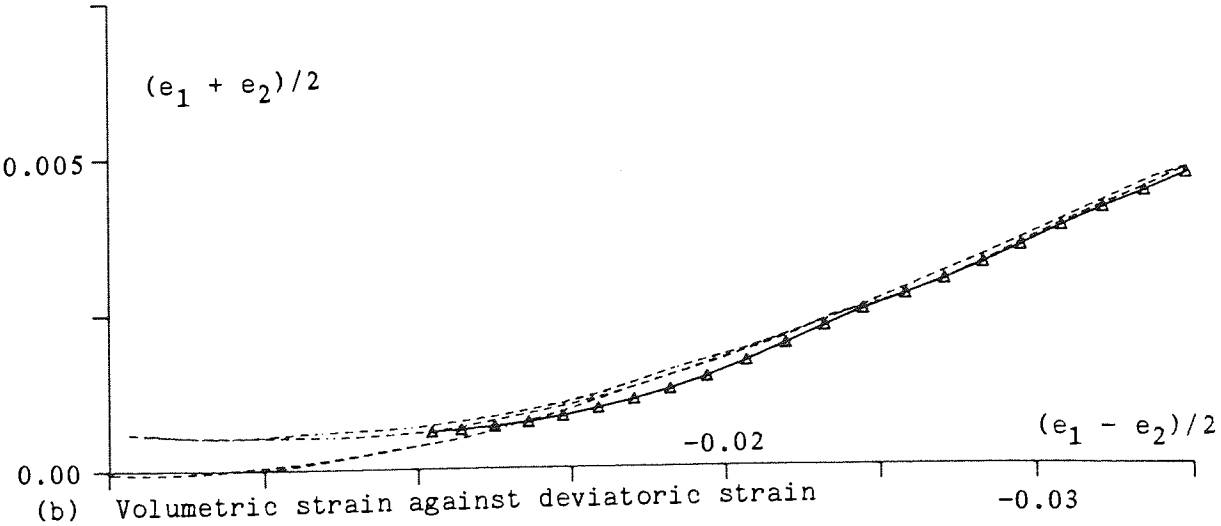

(b) Volumetric strain against deviatoric strain

Figure 4.11 Stress/strain plots for phase 3 - part 1

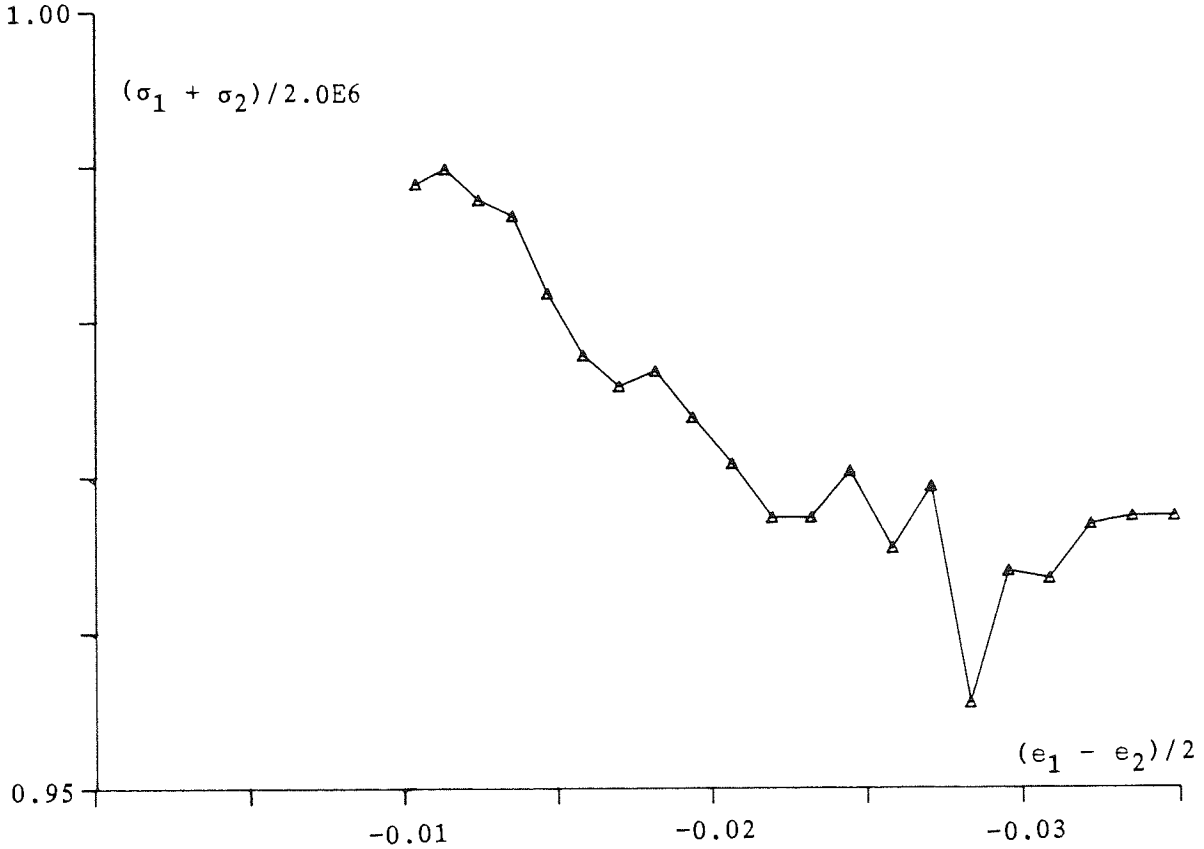

(c) Inner boundary mean stress normalised to boundary mean stress

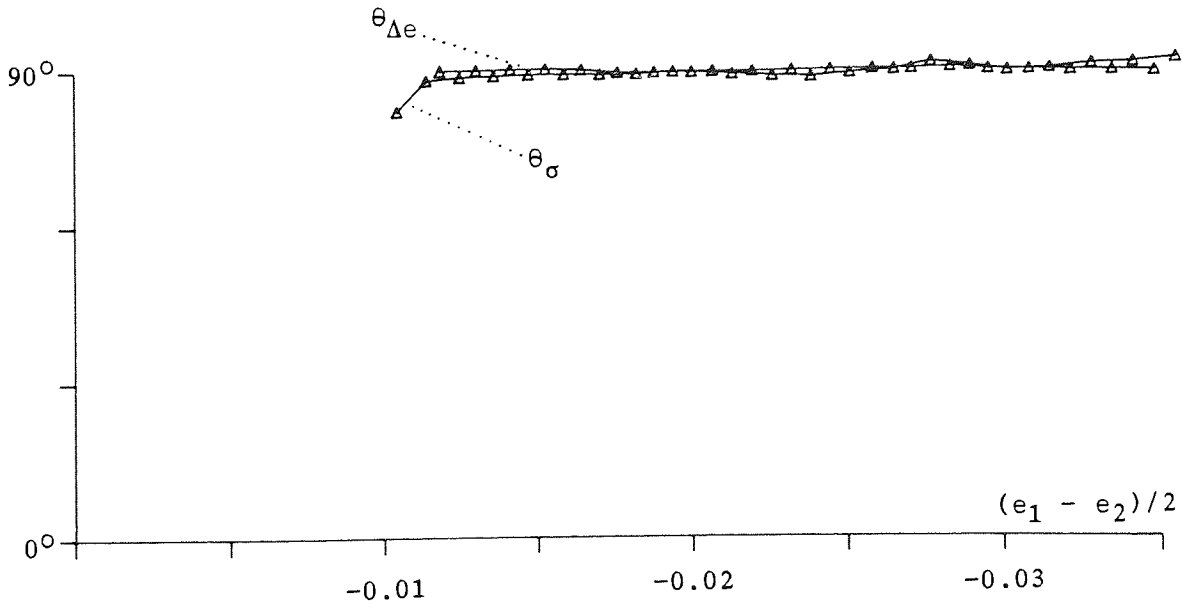

(d) Principle stress and strain-increment directions

Figure 4.12 Stress/strain plots for phase 3 - part 2

5 OBSERVED INTERNAL MECHANISMS OF DEFORMATION

5.1 INTRODUCTION

There is a vast quantity of information held in the memory map. The representation of extracted microscopic data is almost impossible in numerical form and hence graphical representation is essential. Standard plotting options 1 to 9 (section 3.5.1) have been used to achieve this. Every 2000 cycles during testing all plotting options were used but unfortunately the photographic quality of each set of microfische varied considerably. In an attempt to overcome this problem several 'plot-only' program runs were made. Each of these runs produced a complete set of plots for all 61 reference dumps held on magnetic tape. The best of these sets was then used to obtain consistent quality prints, a selection of which are presented in Appendix B.

Although the standard plotting options display the microscopic mechanisms which describe the assembly response to deformation, the problem of interrelating this information is not simple from visual inspection. In order to aid the collection of such data, further analyses and plotting routines were developed. Each will be explained in detail later.

Within this chapter section 5.2 describes the empirical observations which come directly from the plots in Appendix B. An attempt is then made in section 5.3 to find empirical relationships between the various mechanisms outlined in section 5.2. Finally guidelines are set for the development of a constitutive model although this is not attempted within this chapter. Chapters 6 and 7 are reserved for the theoretical development of these models.

5.2 DIRECT OBSERVATIONS FROM PLOTS

Each group of plots within Appendix B was taken one at a time and the following observations were noted.

5.2.1 Kinematics - General Observations

Figures B.2 - B.14 show particle positions and rotations without the use of any special scaling. During phase 1 of deformation the assembly as a whole changes from being circular to being elliptical in shape. This is visible by comparing relative locations of the assembly to the grid defining the static box positions. Unloading reverses this process and Figure B.14 shows that the shape of the assembly boundary is once again circular. This was, of course, expected when the type of boundary control mode is considered along with the test plots representing the strain tensor. However, although the assembly movements as a whole are visible, it is very difficult to detect relative linear movements of particles. This can be demonstrated by attempting to follow the relative movements of particles that map into a particular box. From this it becomes clear that the determination of whether a particle contact exists or not is virtually impossible. Particle rotations, on the other hand, are more clearly identifiable. During phase 1 many particles experience rotation and for a few the amount of rotation is large. Some of these rotations are, to some extent, recovered during unloading but many are not.

5.2.2 Force Transmission

Figure B.15 shows the fully consolidated assembly wherein contact forces have been allowed to develop naturally. It is clear from this figure that contact forces are by no means equal, as some contacts

transmit several times that of others. Macroscopically the orientation and distribution of the contact forces is both homogeneous and isotropic, i.e. by visual inspection there appears to be no regional preference regarding concentrations and there appears to be no preferred contact force orientation. Nevertheless, microscopically the distribution is inhomogeneous. Large forces tend to be transmitted along particle chains. These chains are positioned such that they form part of the boundary of enclosed, approximately circular, regions inside which there are relatively unloaded particles. It can be noted that force obliquities are very small (i.e. $\delta \approx 0$) and that large forces disperse near the boundary. This is due to the method used for compaction and consolidation. Strack and Cundall (1978) and Cundall and Strack (1979a) prepared a 1000 and 1001 disc assembly respectively, in an almost identical way to that described for the test reported here. Hence the equivalent plots were very similar to B.15, except that the forces between boundary particles have been suppressed from being plotted here. This suppression was required for plot scaling purposes. Early 1000 disc tests had revealed that boundary particle forces can be very large when using strain controlled modes, and therefore a better interior force scaling is obtained when they are excluded from plotting calculations. Indeed, problems regarding scaling also arose when interior particles became trapped between boundary particles. To overcome this a check was carried out in the plotting routine to identify such a situation. When this occurred the contact force was set to the value of the maximum internal contact force. This action was carried out for plotting purposes only.

Following the development of the force transmission pattern during phase 1 (Figures B.15 to B.21) it can be seen that there is a rapid and distinct change in the force distribution. Macroscopically

the distribution becomes progressively more and more anistropic. The circular patterns formed by the large force chains rapidly change to form the boundary of enclosed regions that are elongated in the x_1-direction (see Figures B.15 - B.18). Large forces now reach the boundary and force obliquities are apparent. However, the obliquity of contact forces along high force chains is low whereas the force obliquity is much higher in the unloaded regions. This indicates that slip is more likely to occur at contacts that carry small forces. Low force obliquity also indicates that the force distribution by no means mobilises full friction and hence tangential forces must provide only a minor contribution to the overall stress tensor. This will be clearly demonstrated in Chapter 7. Later during phase 1 (see Figures B.19 - B.21) the pattern made by the large force chains tend to straighten and hence the trend of forming closed loops is not so apparent. In addition the number of contacts within the assembly as a whole decreases and therefore the forces transmitted by the remaining contacts are required to increase in order to maintain constant mean stress.

All research workers who have conducted experiments on particle assemblies, wherein a provision for measuring contact forces was made, have noted that during the application of deviatoric stress there has been a preferred orientation of contact force towards the minor principal stress direction. These include: Drescher and de Josselin de Jong (1972), Oda and Konishi (1974), Konishi (1978), Strack and Cundall (1978), Cundall and Strack (1979a, 1979b, 1982), Cundall, Drescher and Strack (1982), Konishi, Oda and Nemat-Nasser (1982), Oda, Konishi and Nemat-Nasser (1982) and Cambou (1982). However, when the mathematical expression for the stress tensor within a granular assembly (c.f. eqn. 3.7) is examined it becomes clear why there must be a preferred orientation of force. Although force distributions

which were very similar to the ones shown here were illustrated in many of the above references, only Cundall and Strack (1982) attempted to describe its shape and evolution. This was done by considering the granular assembly to be split into a phase A and phase B material. Here phase A represents the stiff columns of material that carry high forces and phase B is the relatively unloaded regions. Observations from tests wherein stress and strain rate tensors were coaxial yielded the following conclusions. Phase A material aligns by chance in the direction of the major compressive strain rate. During deformation the columns that constitute phase A become kinked and shorter as strain is applied. This distortion was said to be analogous to column buckling or folding and required neighbouring particles to spin in opposite directions without slip. According to Cundall and Strack (1982) phase A material dissipates no energy, but due to buckling imposes deformation on deforming determining phase B.

This description of material response to increasing strain is certainly very useful and would apply to phase 1 of the test reported here. Nevertheless it does not mention or account for the enclosed loops (of phase B material) which are clearly obvious at low deviatoric stress. The author has therefore attempted to reinterpret the material response in order to more closely define the visual distribution of force.

By observing Figure B.2 it can be seen that there are many possible paths through the random assembly (i.e. contact to contact routes) which could be used to achieve the transmission of stress from one part of the boundary to another. Depending of the state of stress certain stiff chains are more suitably positioned to carry forces than others. By considering chains to be analogous to struts it can be said that a short straight chain is stiffer than a long, bent or kinked chain. Hence short chains require less lateral support from

neighbouring low stressed particles. Under isotropic stress (Figure B.15) the assembly is required to carry an equal amount of force in all directions. It is therefore a requirement that there is no directional preference to the layout of force chains within the assembly. To achieve this, many short chains develop high forces. These short chains merge with others to form a pattern of closed loops. The chosen particle where chains merge carries very high forces and would be most susceptible to crushing if a particle fracture criterion was employed. From a strength point of view it is beneficial for the force chains to form the boundary of convex loops. Hence, near circular low stressed regions are bounded by a network of short high force chains.

During phase 1 of shear the induced stress tensor demands that the average force inclination at contacts become more aligned towards the direction of minor principal stress. Chains of particles that carried high forces which were aligned in the direction of the major principal stress must reduce their load transmission. Conversely, for the constant mean stress test under consideration, force chains must increase transmission when aligned in the direction of the minor principal stress. From Figures B.15 - B.21 the mechanism for achieving this increase appears to be as follows: existing chains of particles that align in the minor principal stress direction maintain and increase their load transmission. In addition, new chains are formed which link together the existing ones. The overall result is that the distribution of high force carrying chains forms a network which although aligned in the direction of σ_1, is constructed of longer, more kinked chains. Although the network still forms closed convex loops, these loops are elongated and larger such that they enclose larger regions of relatively low stressed particles. The total linear length of the highly loaded particle chains must be

reducing. Consequently, the individual chains of particles which carry these high forces are less stiff and require more lateral support. The implication of this is that the respective particle chains are more susceptible to buckling.

It has already been observed that force obliquity at contacts in chains carrying high forces is small. An explanation of this is found by considering the normal contact forces which act on a typical high force transmission chain. Figure 5.1 shows an extract from a force transmission plot which provides a typical example of the microscopic details associated with the large force chains. Because forces plotted by solid lines are so much larger than those plotted by dashed lines, it becomes apparent that even if minor forces developed maximum obliquity in an attempt to rotate the high load carrying particle in a single direction (worst case) this would be counteracted by small force obliquities at major load carrying contacts. This becomes clear when considering the moment equilibrium of the particle, bearing in mind the large differential in normal force magnitudes. In fact, as moment equilibrium applies to all particles it is very difficult to envisage slip occuring at contacts carrying high forces, especially when the proximity of stiff particle chains is considered. Apart from elastic deformation the only mechanism for chains to deform must be rolling. Cundall and Strack (1982) describe the mechanism of particle chain deformation as buckling involving pure rotation of particles, i.e. neighbouring particles in the chain rotate in opposite directions without slip. The reader is invited to simulate this by deforming columns of coins on a smooth surface. By doing this axial force is applied by the two end coins whereas the lateral resistance which simulates that offered by low stressed particles is given by the friction between coins and the smooth surface.

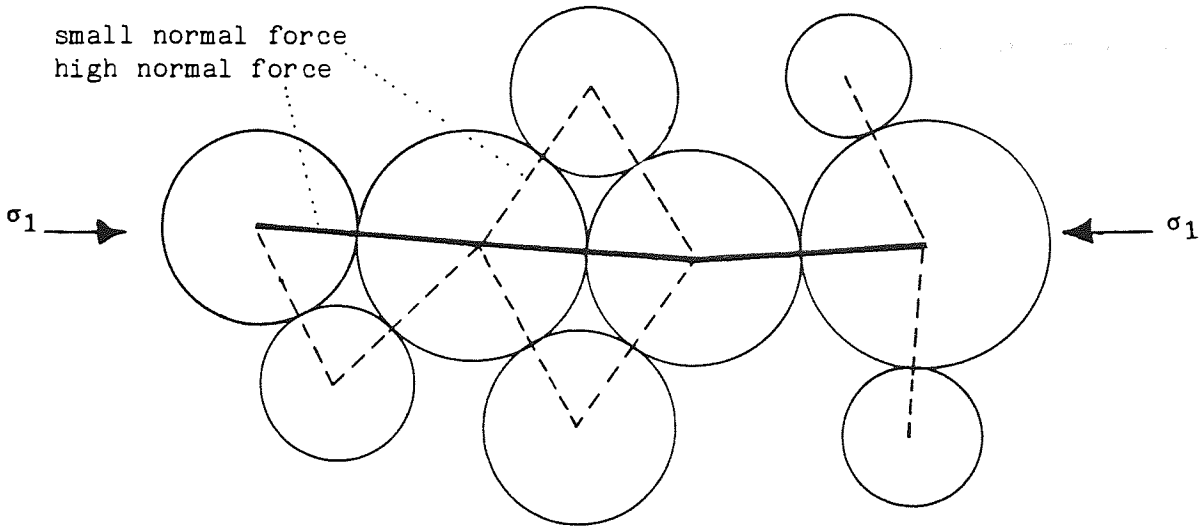

Figure 5.1 Normal forces acting on particle chains which carry very high forces

Furthermore during phase 1 the total number of contacts in the assembly decreases from 2099 to 1812. This means that the total number of contacts deleted minus the total number of contacts created is 287. All this activity must have occured in the instantaneously low stressed regions (c.f. Cundall's phase B).

Unloading the assembly during the early part of phase 2c (Figures B.22 - B.24) shows how the high force network changes to become more like the consolidated assembly. Figure B.24 which corresponds to the stress tensor being approximately isotropic shows how chains have shortened and arranged such that they bound near circular stressed regions. There nevertheless appears to be two fundamental differences between Figures B.15 and B.24. Firstly, the pattern of the force distributions are not identical. Presumably this is due to non-elastically induced structural changes which also accounts for the number of contacts being substantially different (1930 compared to 2099). Secondly contact force obliquity is visible at many contacts in Figure B.24. In the low stressed regions some force obliquities appear high enough to suggest slip. Cundall and Strack (1982) and Oda

and Konishi (1974) have also reported similar observations regarding obliquity. Cundall and Strack (1982) have explained the observation in terms of locked-in shear forces.

Further shearing during phase 2c alters the high force network such that it reflects its relationship with the induced stress tensor, i.e. high force transmitting chains of particles lengthen and tend to align in the direction of the minor principal stress. Phase 3 subsequently changed the force network from being similar to that shown in Figure B.24, at the start of the phase, to that shown in B.21 at the end of the phase. No new observations were made regarding the development of the force distribution.

It may be noted that during all phases of deformation a small minority of particles have less than two contacts. These particles are redundant. They could be removed from the assembly and instantaneous behaviour would be unaltered. Nevertheless these dormant particles often become active as deformation proceeds.

Finally, it should be pointed out that at no time during deformation was there a continuous highly loaded chain of particles spanning the boundary such that it became a direct bridge for the transmission of force. Had this been the case very high deviatoric stresses and volumetric strain would have resulted. This suggests that the assembly contains a sufficiently large number of particles to avoid such a situation. The 50 disc test did not contain a sufficient number of particles and hence misleading material behaviour resulted. This means that, with the present boundary control modes, small assemblies cannot represent the regional behaviour within larger assemblies.

5.2.3 Velocity Distributions

Figures B.28 - B.39 show that at all stages of the test the velocity field is smooth. Regional particle flow conforms to the overall strain-rate tensor. The only exception to the above can be seen in Figures B.33 and B.34 where the velocities of some particle groups appear to violate the general smoothness of flow. This is probably due to high force columns of particles buckling, as by this stage of deformation the chains are long and twisted, and therefore unstable. Nevertheless the magnitude of these vectors is not sufficiently large to suggest that catastrophic structural changes are occurring.

Figure 5.2 shows typical locations of neighbouring particles in the assembly. Superimposed on the assembly boundary are typical velocity vectors which have been calculated from the instantaneous strain-rate tensor at some time during phase 1. As, in general, the velocity field is smooth then the contact force between particle A and particle B will decrease, and between particle C and particle D will increase. With further strain the contact between A and B may break and a new contact may be developed between particles E and F. The above behaviour is, nevertheless, not rigidly adhered to for interior particles, i.e. not all AB type contacts are broken. Due to stability requirements some contacts will remain aligned in the x_2 direction. However, the boundary particle contact GH must increase its force and IJ must decrease its force as directed by the strain-rate tensor. This means that when sufficient strain has been induced all IJ type contacts will be deleted. The higher deviatoric stresses at the boundary (Figure 4.7) are thus accounted for.

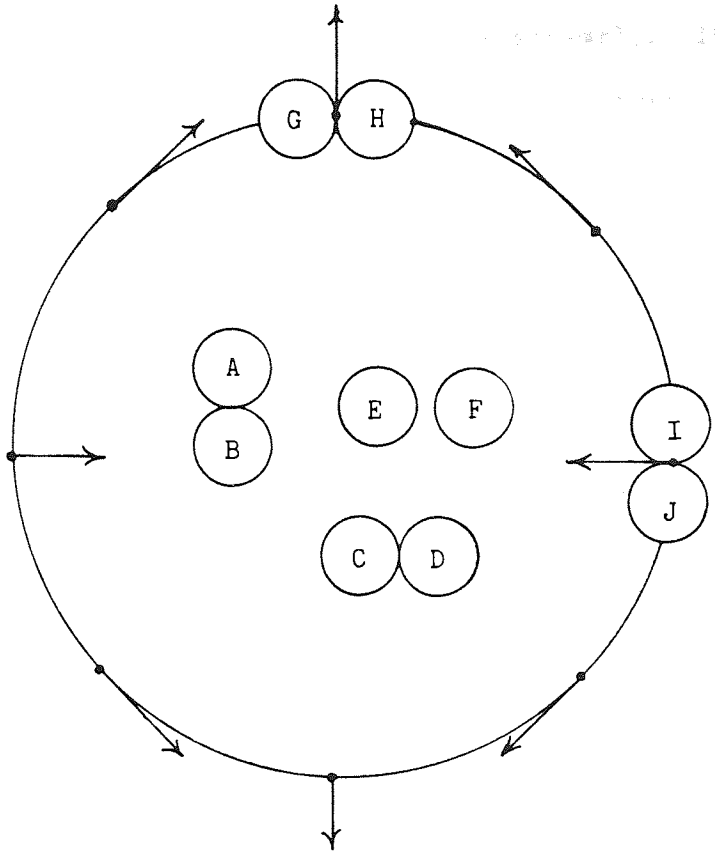

Figure 5.2 Neighbouring particles and boundary velocities during phase 1

5.2.4 Internal Deformation Mechanisms

Throughout the test particles can be seen to rotate and contacts can be seen to slip. This is true even for the early stages of phase 1 and for the whole of the unloading, phase 2c. Macroscopically there appears to be no fixed patterns of slip or rotation. Microscopically, however, small clusters of particles can be seen to have rotations without the occurrence of slip. Cundall, Drescher and Strack (1982) describe these clusters as 'hinge' regions. Perhaps these hinge regions are associated in some way with column buckling and hence account for discontinuities in particle centroid velocity plots. From the plots it is difficult to estimate what percentage of contacts have experienced slip. It is also difficult to firmly establish a preferred orientation for slipping contacts. There is certainly no

large discontinuity due to slip within the assembly. In section 5.2.2 it was noted that slip is unlikely to occur at contacts carrying large forces. During phase 1 large forces tend to concentrate in the x_1-direction. This suggests that the low forces are more likely at contacts whose normals tend to concentrate in the x_2-direction. As slip must occur in the low stressed regions, then it is likely that the respective contact normals should have a preference towards the x_2-direction. A further examination will be carried out later.

Oda, Konishi and Nemat-Nasser (1982) have classified the possible non-elastic activity at particle contact into four groups:

i) Pure slip - contact slip without particle rotation, see Figure 5.3(a)

ii) Pure roll - rolling at contacts without slip, e.g. Figure 5.3(b)

iii) Slip and roll - spin and slip occurs at the contact, e.g. Figure 5.3(c). The branch between particle centres does not need to change orientation if slip compensates for rolling

iv) Rigid - neither slip nor rolling occurs at the contact e.g. Figure 5.3(d)

By carrying out simple geometric calculations using stored particle data relative to two points in the test, it is possible to classify contact activity, provided a constant check has been carried out to detect branch deletion and creation. Figures B.40 - B.51 offer a visual alternative wherein a measure of contact slip and particle spin is plotted. It must be noted however, that these plots only show the slip that occured between particles that were in contact at the end of the increment. Even so, increments were small and the overall structural rearrangement was not great.

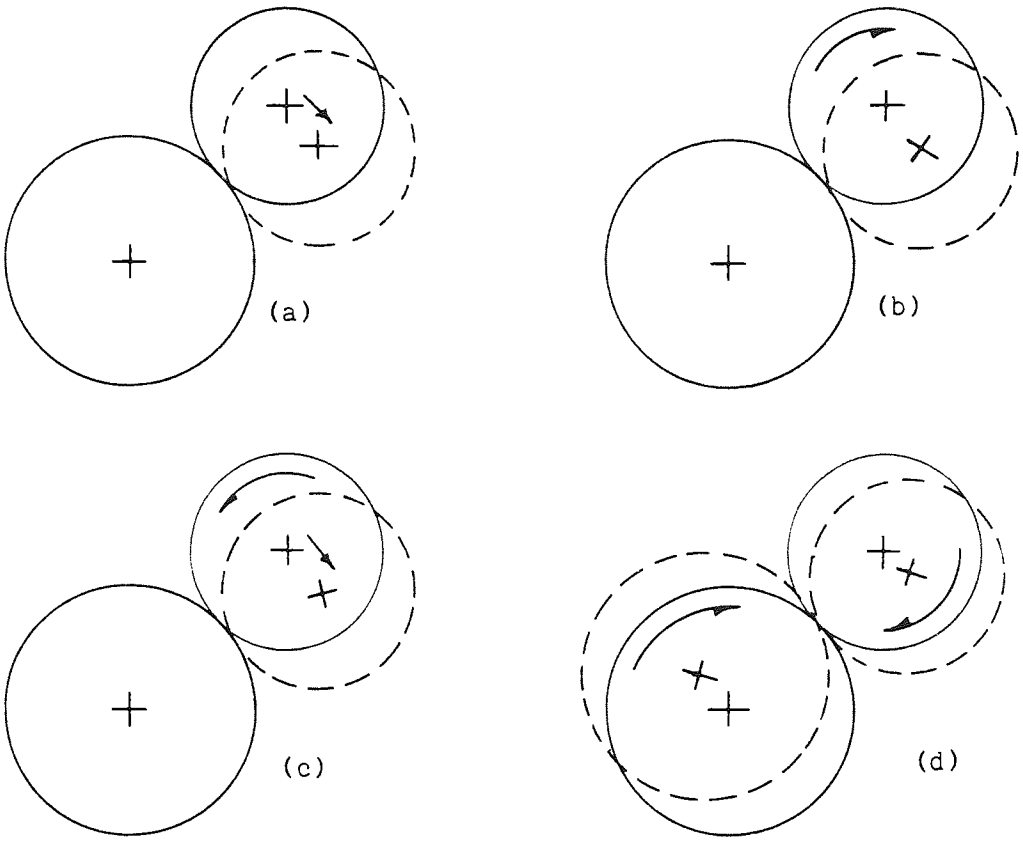

Figure 5.3 Possible contact activity

Slip virtually never occurs without at least one of the respective particles rotating. Large slips occur at contacts between particles which have had the same direction of rotation. The occurrence of slip at contacts where particle centres have rotated in opposite directions is very rare. Cundall and Strack (1982) and Oda, Konishi and Nemat-Nasser (1982) state that rolling is the major cause of deformation. From the plots provided here this appears to be true as most contact activity is associated with particle rotation. Rigid (i.e. non slipping) regions, which include 'hinge' regions, were also noted by the above two references.

5.2.5 Space Lattice Analogy

From Figures B.2 - B.14 it was noted that the relative positions of particle centroids change very little during the test. In fact, microscopic structural changes could not be observed and hence induced differential directional stiffnesses (or induced structural anisotropy) was not apparent. Figures B.52 - B.63 show that quite considerable changes do occur to the overall distribution of contact branches, where a branch is defined as the line joining particle centroids. It can be seen that many branches have been deleted or have been created. The information alongside these plots gives the number of contacts which exist between respective particles at both considered stages. The number of new or created contacts is given together with the number of contacts deleted from a given point in the test. Hence the total number of contacts is given by EXISTING + NEW and EXISTING + DELETED is a constant giving the number of contacts at the reference point, e.g. for Figures B.52 - B.57 EXISTING + DELETED = 2099, which is the number of contacts for the consolidated assembly.

For phase 1 (Figures B.52 - B.57) it is clear that the distribution of contact normals becomes more concentrated in the x_1-direction. This observation is in agreement with Oda (1974), Oda, Konishi and Nemat-Nasser (1982), Konishi, Oda and Nemat-Nasser (1982), Cundall and Strack (1982) and others. The major mechanism which accounts for this is contact deletion and creation. In agreement with the observations of Cundall (1980) contact deletion occurs mainly in the maximum tensile strain direction (x_2-direction). In addition many new contacts are created whose inclinations are biased towards the maximum compressive strain direction (x_1-direction). More contacts are deleted than created and hence the total number of contacts decreases, i.e.

$$(\text{EXISTING} + \text{DELETED}) > (\text{EXISTING} + \text{NEW})^{t1} > (\text{EXISTING} + \text{NEW})^{t2} \quad (5.1)$$

where t refers to time and $t2 > t1$.

Figures B.58 - B.63 give the corresponding plots for the unloading phase, 2c. For these plots the reference state at the end of phase 1 (NCYC = 94,000) was used for comparing the relative positioning of particles. It can be seen that the average contact normal inclination gradually rotates away from the x_1-direction. In general, contacts are created in the x_2-direction and lost in the x_1-direction. In fact many of those contacts that were deleted during phase 1 are now regained and vice versa. From information given alongside these figures contact creation appears to be the main mechanism that accounts for this. Hence

$$(\text{EXISTING} + \text{DELETED}) < (\text{EXISTING} + \text{NEW})^{t1} < (\text{EXISTING} + \text{NEW})^{t2} \quad (5.2)$$

but even when the strain in the x_1-direction has returned to zero the total number of contacts (EXISTING + NEW) is considerably less than that of the consolidated assembly (1992 compared to 2099). This result means that a considerable structural change must have occurred. Boundary effects are most evident in these plots. Due to the control mode used all boundary contacts which initially aligned in the x_2-direction were deleted by $e_1 = -0.015$ and were all regained during unloading, this is not representative of internal behaviour.

Nemat-Nasser (1982) has outlined that there are two basic quantities associated with each active contact, namely, the branch between particle centroids and the inclination of the contact normal. Oda (1978) has explained granular structure by defining two concepts, packing and orientation. Packing is associated with the number of contacts per particle (coordination number) and by the inclination of contact normals. Orientation is given by the inclination of the

apparent long axis of non-spherical particles. However, since we are only concerned with disc assemblies the orientation aspect is not relevant. Cundall (1980) has introduced a visual description of structure directly from plots similar to those described in this section. By considering the connection of branches at particle centres the whole assembly can be divided into microscopic elements termed 'domains'. Each domain is locally the smallest enclosed region that can be bounded by branches.

Figure 5.4 shows a typical extract from the plots considered here. Instantaneous domains are given by the smallest polygons that can be constructed by considering solid and double solid branch lines. In addition, the original domain pattern can be identified from the arrangement of single solid and dashed lines. Problems do occur in domain construction in local regions where redundant particles exist. As noted in section 5.2.2, redundant, non load bearing particles get captured in voids. Nevertheless these particles often have one, or perhaps even two, weak contacts with the particles surrounding them. These contacts should be ignored in domain construction, the result being that some domains will contain a redundant particle completely. Then, for any stage of the test the instantaneous assembly can be seen as a continuous mosaic of domain elements.

It is interesting to note that the size and shape of domains reflects the definitions of structure given by Oda (1978) and Nemat-Nasser (1982). Domain shape is directly related to the inclination of contact normals and domain size is a function of the coordination number. The relationship between domain size and coordination number is explained by bearing in mind that the coordination number is related to the total number of contacts. As the number of contacts decreases domains must enlarge in order to maintain the continuous mosaic. This will become clearer later.

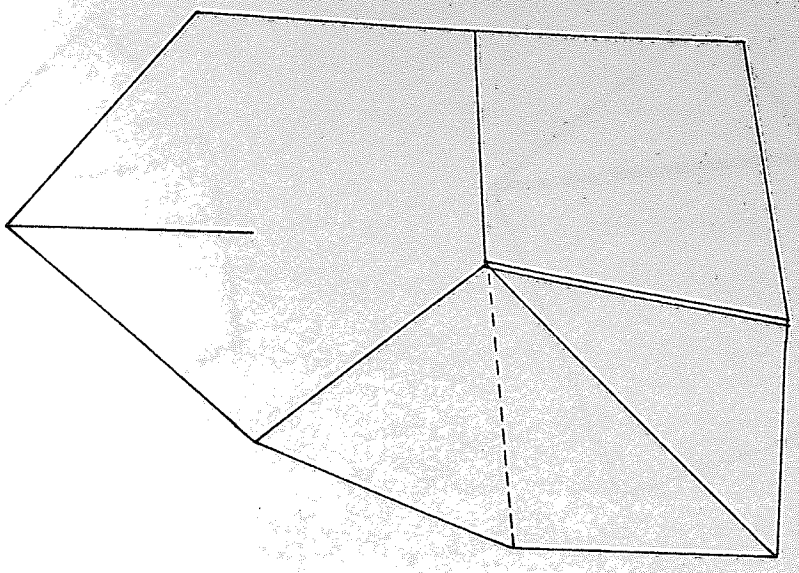

Figure 5.4 Typical extraction from Figure B.56

At the end of consolidation (consider the single solid and dashed branches shown in Figures B.52 - B.57) domains are irregular shaped polygons which possess a small number of sides. Very few domains have more than five sides and many have a minimum of only three sides. In addition, the overall shape of the domains is such that there is no directional preference for the orientation of their apparent long axis. This is of course due to the random assembly generation and isotropic compaction and consolidation. Subsequent assembly deformation leads to branches being deleted and created. By observing the plots it can be seen that contact deletion has the effect of forming one domain out of two domains which share the respective branch. Conversely, contact creation forms two domains out of one where each of the new domains share the newly created branch. This is shown clearly in Figure 5.5.

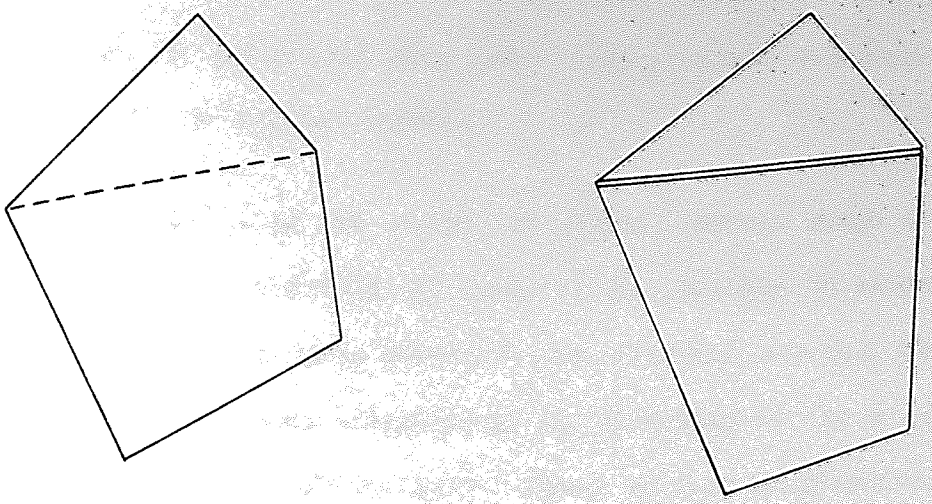

a) Deletion b) Creation

Figure 5.5 Domain creation and deletion

Figure 5.5 shows that domains resulting from contact deletion and creation change both their size and inclination. Therefore, if contact deletion and creation have preferred orthogonal directions respectively then the overall shape of domains becomes elongated in the direction of contact creation. In addition, if contact deletion is more dominant than contact creation then the average domain will enlarge. The converse is also true. As creating contacts raises the overall coordination number average domain size is associated with the coordination number. If the total number of contacts at any moment t equals C then

$$2C^t = P\bar{n}^t = D^t\bar{S}^t \tag{5.3}$$

where P is the total number of particles, $\bar{n}$ is the average coordination number, D is the total number of domains and $\bar{S}$ is the average number of sides per domain. If m equals the number of contacts gained minus the number deleted from time t_1 to time t_2, then

$$\bar{S}^{t_2} = (P\bar{n}^{t_1} + 2m)/(D^{t_1} + m) \tag{5.4}$$

It must be noted that only small displacements are required in order to create or delete contacts.

By utilising the average or overall domain shape to describe the instantaneous assembly structure it is possible to explain structural evolution. During phase 1 the overall domain shape becomes progressively more elongated in the direction of the major compressive strain-rate (x_1-direction). Phase 2c then progressively changes the domains such that they become smaller and less inclined towards the x_1-axis. In fact, at the end of phase 2c domains are slightly elongated towards the x_1-axis. It may also be noted that the size of the average domain, during the latter stages of phase 2, never reduces such that it is equivalent in size to that at the end of consolidation. This is of course due to the inability of the assembly to regain all deleted contacts.

5.2.6 Contact Normal Distribution and Contact Force Obliquity

Figures B.64 - B.76 have been produced in order to give an overall picture of instantaneous contact quantities that are free from boundary effects.

Figures B.64a - B.76a give polar histograms to show the distribution of contact angles. In order to construct this plot each contact that mapped into the inner circular region was interrogated to find out which of the 18 10^o bands between 0^o and 180^o (contact normal direction) its inclination belonged to. The program counter for that band was then incremented by one. After all contacts had been scanned each band counter was divided by NCON, the total number of contacts, and multiplied by 100%. The upper half (i.e. above horizontal axis) was then plotted such that the sum of radial ordinates was equal to

100%. The part of the histogram below the horizontal axis is skew-symmetrical to that above the horizontal axis, i.e. the radial ordinate of the band 40-50° is identical to that of 220-230°. This is simply because a contact inclination of 45° is equivalent to an inclination of 225°. Hence the total sum of radial coordinates from 0-360° is 200%.

The shape of this distribution is near circular for the consolidated assembly. During phase 1 it becomes more and more elongated in the x_1-direction. This is of course due to contact deletion and creation, as described in section 5.2.5. Later, during phase 2c the distribution changes gradually to eventually become slightly elongated towards the x_2-direction.

Using the identical method of construction Figures B.64b - B.76b give the distribution of contact angles weighted to the magnitude of the contact normal force, i.e.

$$r = \sum_{1}^{n} \hat{F}_N / \sum F_N \cdot 100\% \qquad (5.5)$$

where r is the radial coordinate of the unique bands between 0° and 180° and n is the number of contacts mapping into the respective band. In fact, as equation (5.5) suggests, these plots could be interpreted as the distribution of normal forces. It can be seen from these histograms that the weighted structure changes much more rapidly in order to reflect the evolution of load carrying contacts. Further reference to these figures will be made in Chapter 7.

Figures B.64c and B.64d - B.76c and B.76d have been constructed to investigate force obliquity. The histogram gives an unweighted distribution of contact obliquity. Positive values are associated with tangential forces which attempt to turn the respective particle in an anti-clockwise direction. The plot of force against obliquity

considers all obliquities as positive and a point is given for each contact force mobilised to the instantaneous maximum.

Due to the method of compaction and consolidation force obliquities are very low. Even so, although few, some contacts appear to have obliquities equal to the maximum. During deformation high contact obliquities develop very quickly, even during unloading. However, high obliquity is in general associated with low force. Very few contacts are slipping that have forces greater than $F_{max}/2$. From additional information given regarding contact numbers and the number of slipping contacts it can be seen that the percentage of slipping contacts is always less than 25%.

In order to more clearly give the number of contacts and the number of slipping contacts, three further plots have been produced which give information for all phases. Figure 5.6 shows a plot of the number of contacts, Figure 5.7 plots the number of slipping contacts and Figure 5.8 gives the percentage of slipping contacts. Each of these plots is against deviatoric strain.

5.3 INTERRELATED MECHANISMS

In this section an attempt is made to interrelate the mechanisms already observed in the previous section. In order to aid this task a special plot is required that can somehow represent the main features of the plots shown in Figures B.2 - B.63. It is desirable to superimpose plotting options 1, 5, 7, 8 and 9 in order to find relationships between contact slip, particle rotation, structure and force tranmission. However, if this was done the resulting plot would undoubtedly be of little use due to overplotting.

A new plot has been developed which plots particles with dashed

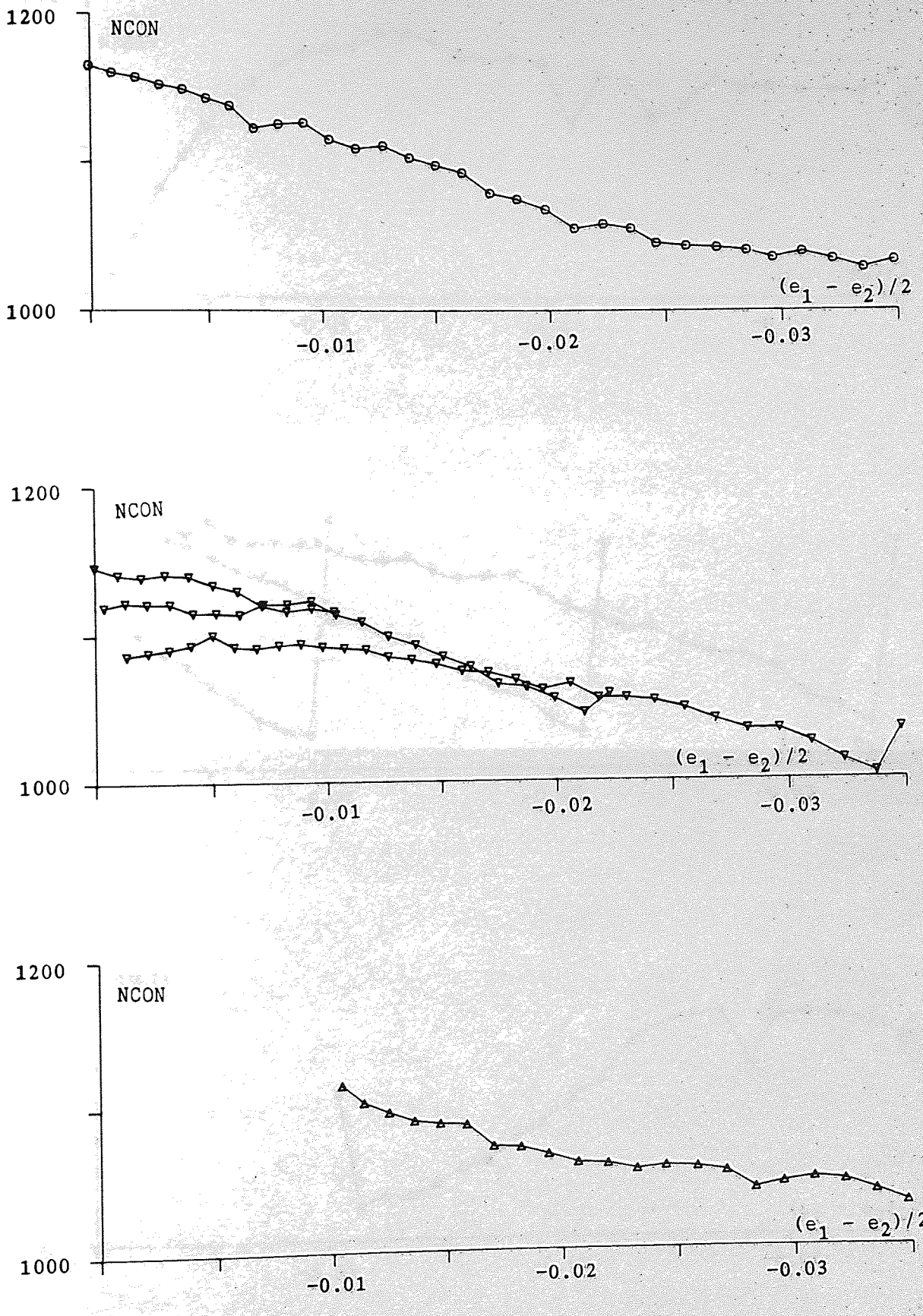

Figure 5.6 Contact numbers against deviatoric strain

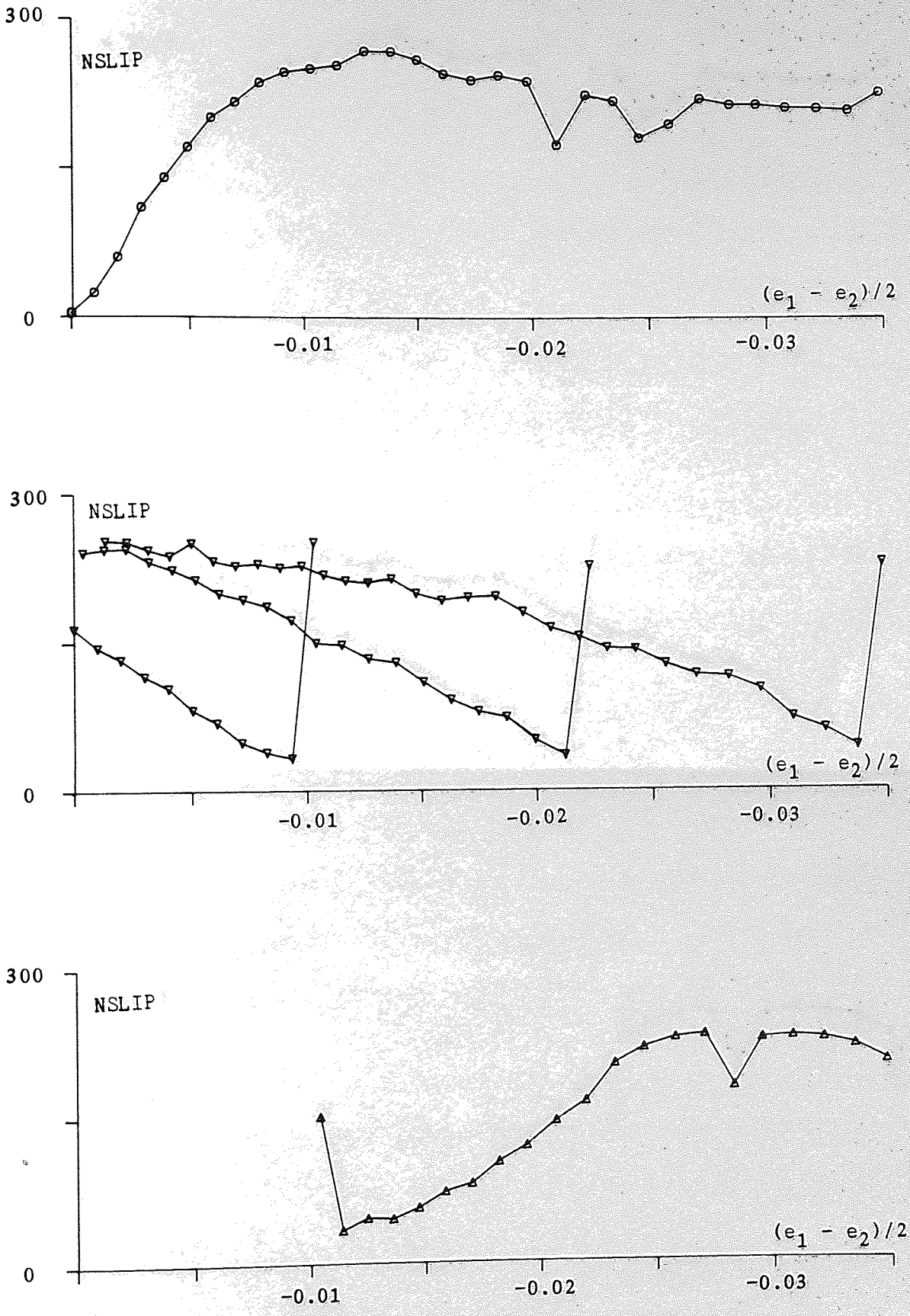

Figure 5.7 Slipping contact numbers against deviatoric strain

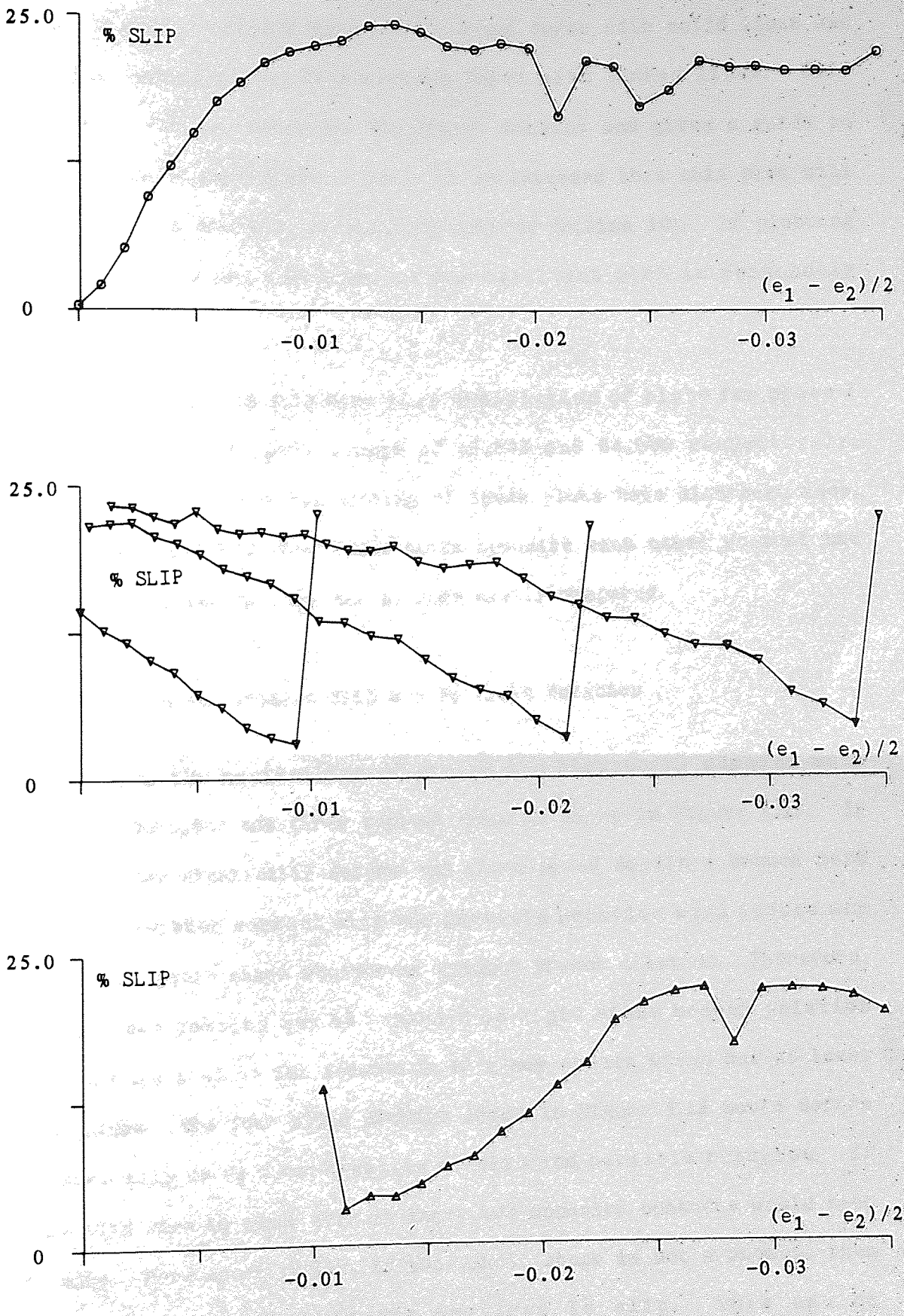

Figure 5.8 Percentage of contacts slipping against deviatoric strain

lines, branches carrying more than average force with solid lines and branches carrying less than average force with dashed lines. This plot shows the instantaneous structural domains and gives a guide to the location of high force chains. It is intended that this plot will be included in the list of plotting options (option 10). If plotting options 7 and 8 are superimposed the resultant plot is reasonably clear.

Figures 5.9 and 5.10 show this combination of plots for phase 1 of deformation at cycle counts of 44,000 and 84,000 respectively. Enlargements from the top portion of these plots have also been made. Figures 5.11 and 5.12 show these plots opposite each other so that the information given by them can be more easily compared.

5.3.1 Structure, Contact Slip and Particle Rotation

During the application of strain the structural domains must deform. Consider the three typical domains shown in Figure 5.13. In order to non-elastically deform the three sided domain a branch must delete. Neither contact slip nor particle rotation will induce any change in domain shape whatsoever without branch deletion. Therefore, three sided domains may be regarded as rigid since branch deletion will always lead to the formation of a new domain which has at least four sides. The four sided domains shown in Figure 5.13 could deform by pure slip or by a combination of slip and particle rotation. If pure slip were to occur then at least two opposite contacts would need to slip. More specifically, if the domain shape is not a rhombus then at least three contacts are required to slip. This can be demonstrated by deforming a pin-jointed irregular quadrilateral, from which it can be shown that at least three sides are subsequently rotated. Branch rotation without particle rotation necessitates

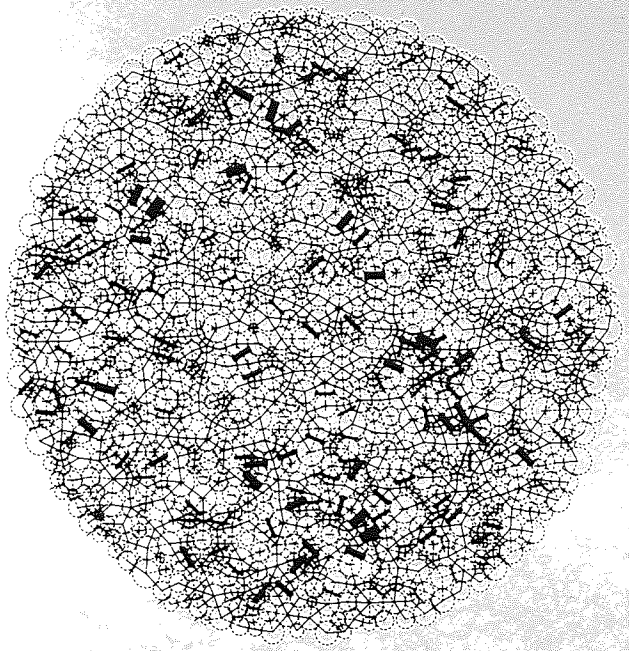

Figure 5.9 Superimposed mechanisms - phase 1 (44,000 cyles)

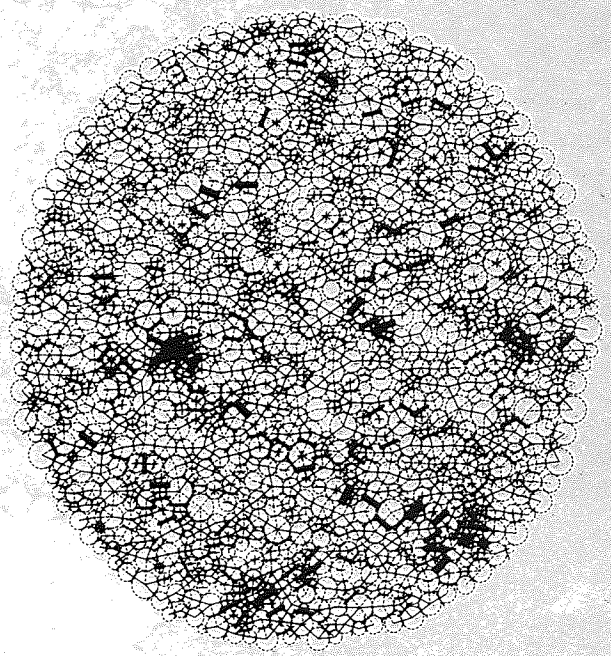

Figure 5.10 Superimposed mechanisms - phase 1 (84,000 cycles)

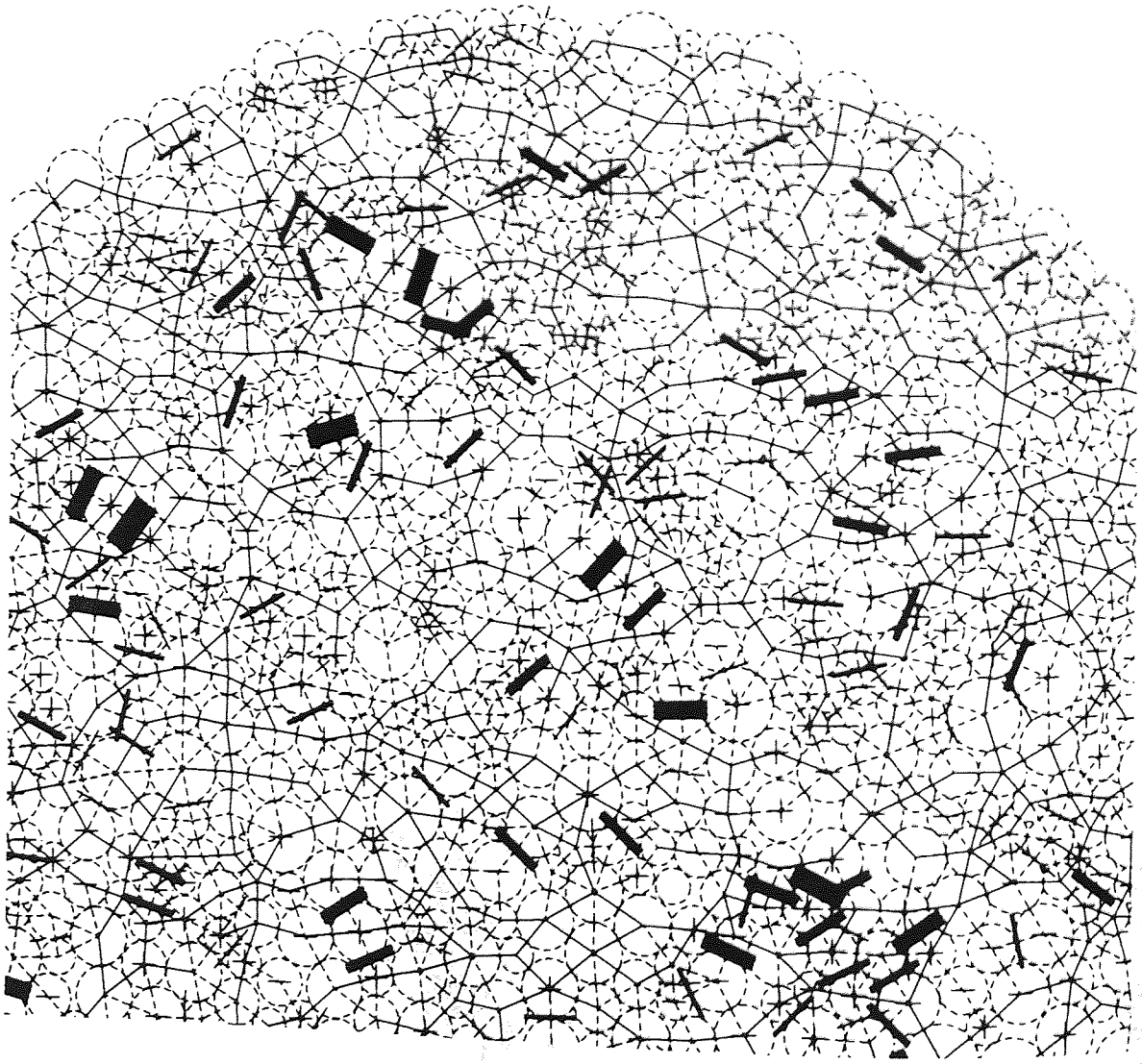

Figure 5.11 Enlargement from Figure 5.9

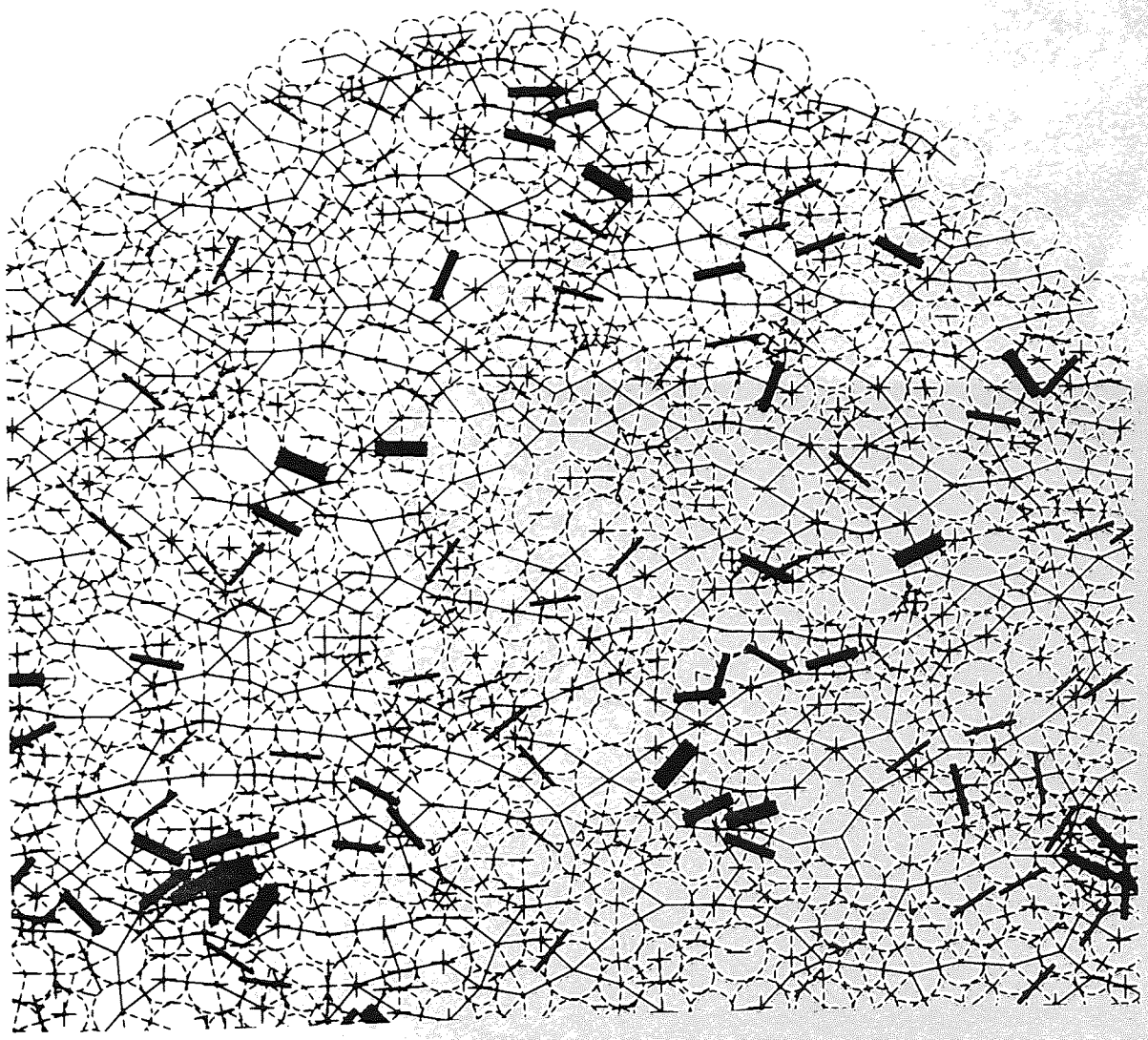

Figure 5.12 Enlargement from Figure 5.10

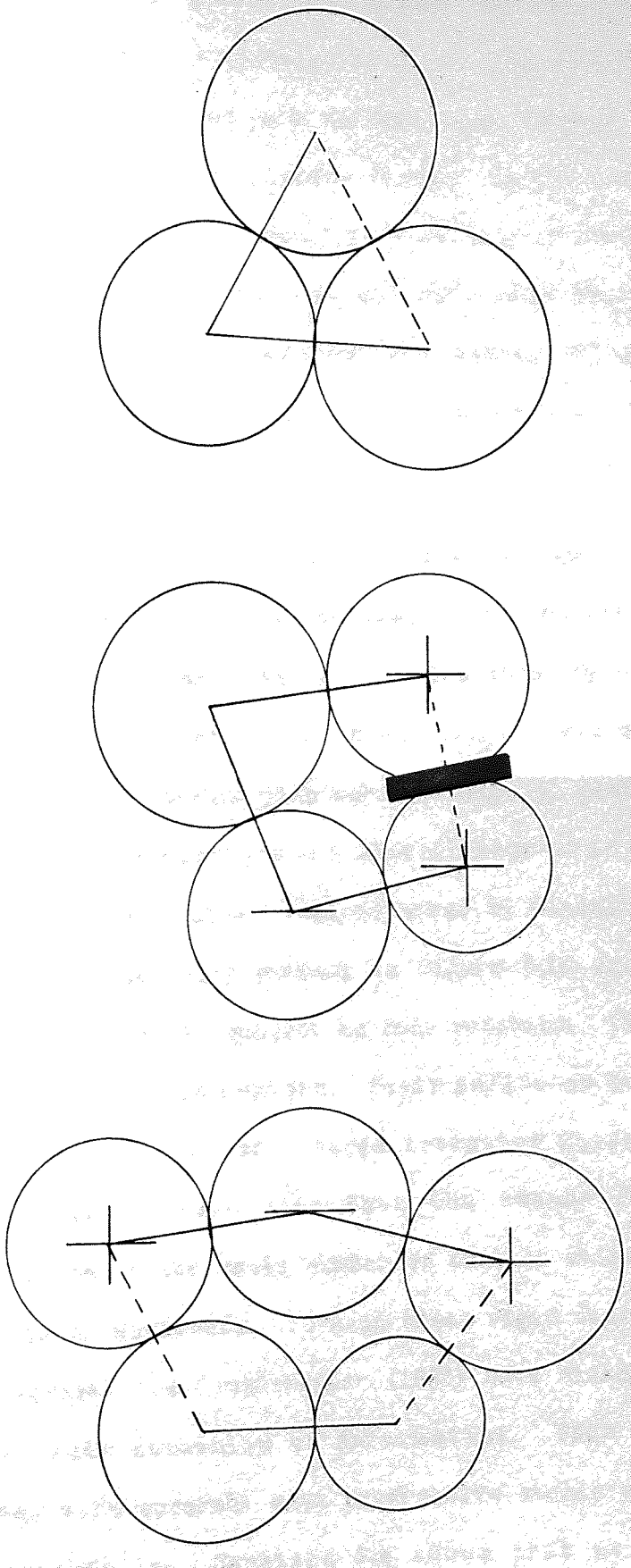

Figure 5.13 Domains of three, four and five branches

contact slip. In the interest of minimum energy dissipation contact rolling is preferable to contact slip. Rolling at contacts dissipates no energy but for a four sided domain deformation cannot occur by this mechanism alone. A combination of rolling with at least one slipping contact is required and to minimise energy dissipation, it is preferable that the slipping contact is the one that transmits the minimum normal force. Finally, domains with five or more sides do not require any contact slip at all to change shape. Deformation can therefore take place without any energy being dissipated. These domains have the potential for high deformation but are restrained by their neighbours.

In Figures 5.11 and 5.12 many slips and particle rotations can clearly be seen. If studied along with the structure of the domain then it can be seen that it is rare that more than one branch per domain experiences slip. Many local regions can be seen to be inactive, i.e. neither slip nor differential particle rotation occurs. These particle clusters are usually made up of domains of three and four sides. The 'hinge' regions noted by Cundall, Drescher and Strack (1982) are especially evident in Figure 5.12 and are merely clusters like these that are subject to body rotation. These clusters could be envisaged as solid regions. Their influence on the assembly is not dissimilar to that of a large irregular shaped particle. Oda and Konishi (1974) have said that the reason for their unexpected observation of the small number of contact slips, was probably due to rigid block movements. Perhaps these rigid clusters account for this. Oda, Konishi and Nemat-Nasser (1982) have claimed that particle spin is the main mechanism of deformation. This is probably true and becomes more apparent with progressive strain as the total number of contacts falls. Equation 5.4 shows that as contacts delete the average number of sides for domains increases and, hence, rotation is

likely to become more dominant than slip in domain deformation.

Figure 5.7 shows the number of contacts slipping throughout all three phases of the test. It is postulated here that when the shear elastic displacements have settled then the number of slipping contacts is related to the number of contacts. This idea is based on the fact that when contact numbers are low particle spin becomes the major mechanism of domain deformation. Due to the low friction method of compaction and consolidation, then the greatest contact force obliquity ($\bar{\delta}$) is mobilised early during phase 1, because $\bar{\delta} = 0$ when $e_{ij} = 0$. Contact slip will be a maximum at this point as the coordination number is still relatively high. Subsequently the number of slipping contacts decreases as the number of contacts decreases. Phase 2 initially involves a reversal in the direction of contact shear forces, and hence the number of contacts slipping probably falls to zero. This is not quite so evident in Figure 5.7 because not enough data was extracted during the first few cycles of unloading. The number of contacts slipping then increases due to shear reversal at contacts and due to the recovery of contact numbers. Phase 3 involves a further reversal of the shear force direction of contacts. At the end of this phase contact numbers and the number slipping are similar to those at the end of phase 1.

Further tests are required in order to prove the ideas given above. One of these tests could be to carry out further unloading, into extension, for phase 2c. During this test it would be expected that the number slipping would decrease. Another test could be to carry out a similar 1000 disc test but using a less dense assembly. Density and coordination number are linked and hence a less dense assembly should have a lower coordination number, and therefore the average domain would have a greater number of sides.

5.3.2 Force Distribution, Contact Slip and Particle Rotation

Observations from Figures 5.11 and 5.12 once again confirm that slip rarely occurs at contacts carrying high forces. This is quite clear as slip is usually associated with dashed branches. Perhaps, at an initial glance slip directions do not appear to be biased towards any particular direction. A closer examination reveals otherwise, especially for Figure 5.11. In fact, the direction of slip has a definite tendency to align in the x_1-direction. The reason for this is that high force transmitting contacts tend to align in the x_1-direction and small contact forces tend to align in the x_2-direction. Slip is far more likely to occur at contacts carrying low forces. The direction of slip is at right angles to the respective branch. Hence the direction of slip is likely to be biased towards the x_1-direction.

High force transmitting chains of particles can be seen to buckle by pure particle rotation. This mechanism is directly related to the inability of slip to occur at high force transmitting contacts.

5.3.3 The Relevance of Structure

Whatever the previous contact and particle activity the domain structure is the result. This structure mediates both the stress and strain-rate tensors and therefore is a most relevant stepping stone towards gaining a relationship between stress and strain. Structural anisotropy is reflected by the shape and orientation of domains.

The force distribution uses the structure. Forces are transmitted along domain boundaries but domain sides that align in the direction of maximum compressive stress are required to carry greater loads.

5.4 CONSTITUTIVE MODELLING

The ideal model to represent the behaviour of homogeneous granular elements would be required to predict the 3-dimensional response to deformation under all possible stress states. In order to achieve this the mathematical model would require equations that describe the microscopic mechanisms of deformation. In addition particle shape and grading would have to be accommodated during the model construction. Until these model ingredients, that relate to the microscopic material response, have been fully identified existing constitutive models that claim to be accurate will always be subject to criticism. A great deal of testing still remains to be carried out.

The work carried out here, clearly, only scratches the surface of what is involved in understanding the complete material response. From this limited amount of data an attempt will nevertheless be made to gain relationships between stress and structure and also strain-rate and structure. To carry out this task two separate approaches have been adopted. Firstly, in Chapter 6, a continuum model is developed to fully describe the deformation of 2-dimensional and 3-dimensional regular packings. Secondly, in Chapter 7, an attempt is made to quantify structural anisotropy for random assemblies in tensorial form and then to relate this tensor to the stress and strain-rate tensors.

6 ANALYSIS OF REGULAR PACKINGS

6.1 INTRODUCTION

Program Ball has been used, as an alternative to experimental testing, to identify the phenomena observed within granular material, from which it is hoped to deduce a corresponding, physically sound, constitutive model. In the formulation of such a model the macroscopic stress and strain-rate tensors must in some way relate to the internal structure. It is clear from the work presented in Chapter 5 that even for idealised non-regular disc assemblies the structure is complex. It is therefore instructive to examine the behaviour of simpler structures, e.g. regular packings. A complete review of previous work on regular packings is not included, for this the reader is directed to Thornton (1975) and Blackburn (1983).

The analysis presented within this chapter is concerned with the mechanics of regular arrays of rigid spheres, and extends the previous work of Thornton (1979) on the face-centred cubic array, Thornton and Blackburn (1981) on body-centred tetragonal arrays, to the analysis of body-centred orthorhombic assemblies. The essential features of the analysis have been presented elsewhere by Thornton and Barnes (1982). Here, as an addition to that work, results will also be presented for the analysis of the equivalent two-dimensional assemblies of rigid discs.

6.2 THE PHYSICAL MODEL

In order to obtain a complete solution of the mechanics of any system it is necessary, first of all, to identify the physical model. For the body-centred orthorhombic array under consideration the structural geometry must be defined as well as the physical properties of the individual particles.

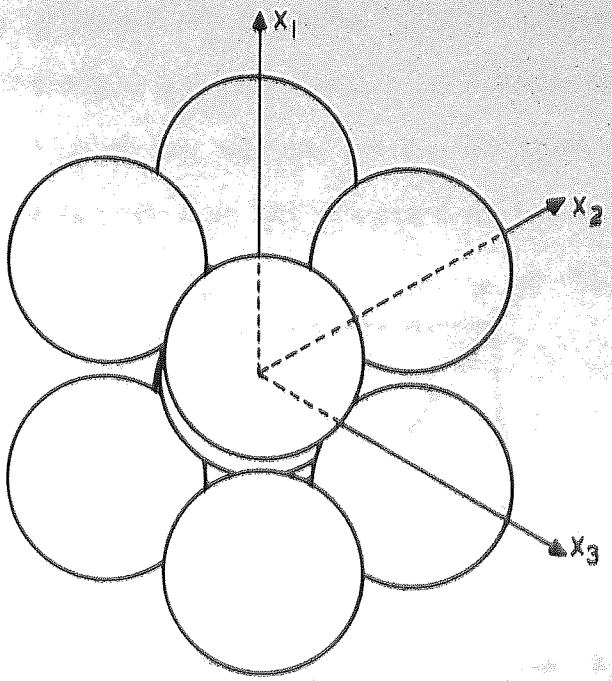

Figure 6.1 The body-centred orthorhombic array

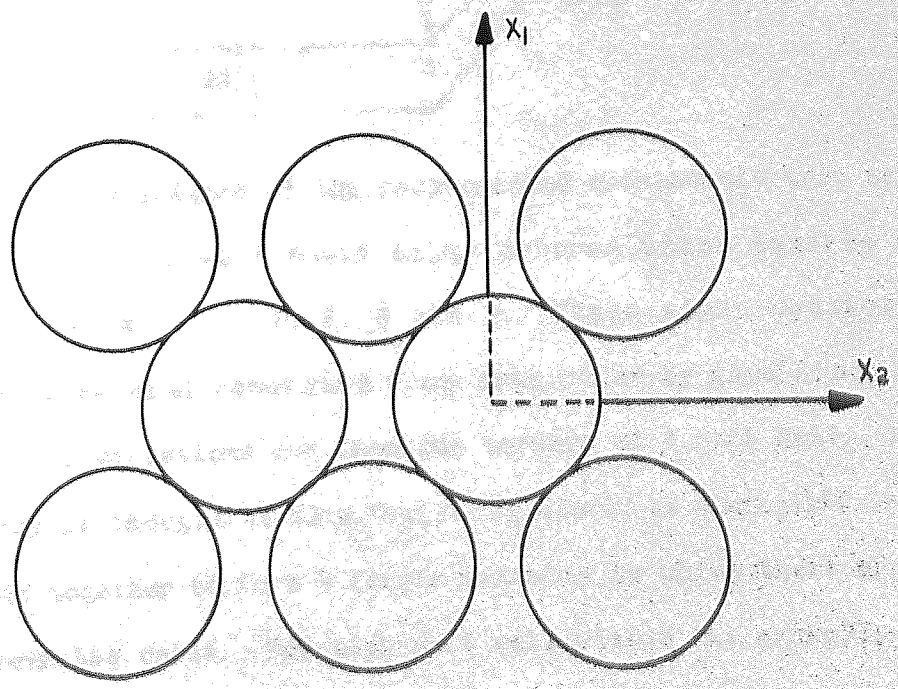

Figure 6.2 A typical two-dimensional array

Figures 6.1 and 6.2 show typical examples of the arrays under consideration. The structure of the body-centred orthorhombic array is illustrated by the space lattice, shown in Figure 6.3, which has been constructed by joining the centres of the spheres. The central sphere has its centre situated at the origin O of the cartesian axes

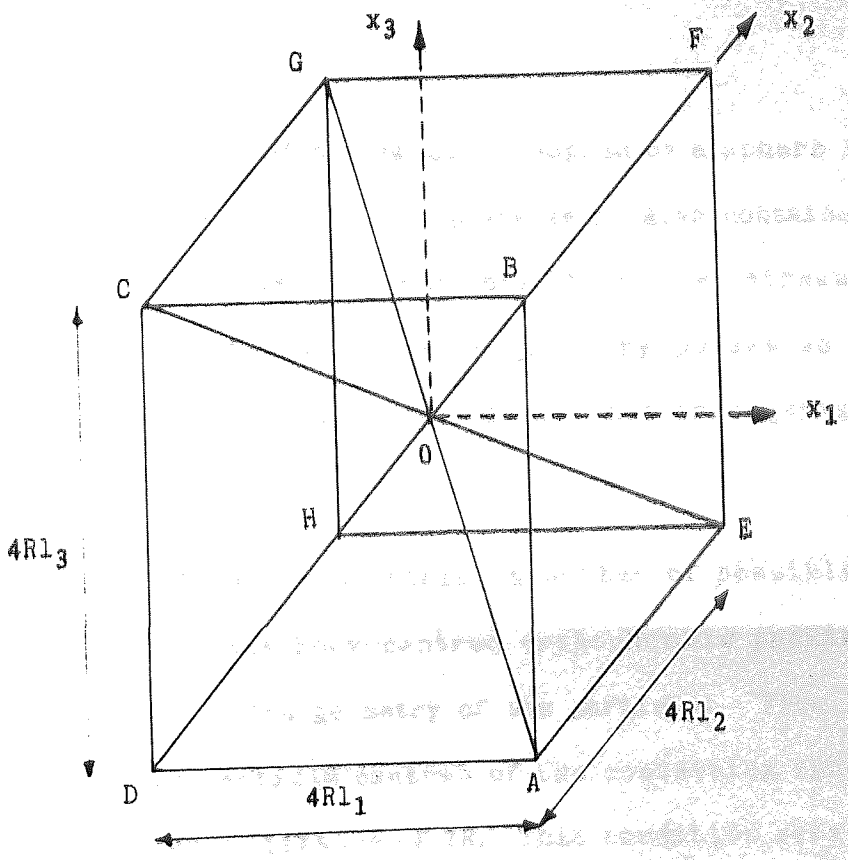

Figure 6.3 Space lattice of the body-centred orthohombic unit cell

x_i and is in contact with eight other spheres whose centres are positioned at A, B, C, D, E, F, G and H. These eight contacting spheres are in general separated from each other by gaps along the three orthogonal directions and form the corners of a unit cell. This unit cell may be thought of as a 'building block' as many unit cells may be fitted together to form a larger assembly in which there are no spaces between the cells. For each unit cell within the assembly the coordinate distances between the centres of contiguous spheres are given by

$$L_j = 2Rl_j \qquad (6.1)$$

where R is the radius of the sphere and l_i are the direction cosines of the line joining their centres. From this, the dimensions of the unit cell are $2L_i$ or $4Rl_i$ (all components of l_i positive) and within each cell the equivalent solid volume of two spheres is contained. Therefore, as all spheres are identical, the volume occupied by each sphere in an infinite assembly must be half that of the unit cell, i.e.

$$V_o = 32 l_1 l_2 l_3 R^3 \qquad (6.2)$$

It should be noted that the volume occupied by a sphere is not equal to the solid volume (V_s) of the sphere as it also contains voids. The shape of the volume (V_o) is in general that of a tetrakaidecahedron (polyhedron with 14 faces) whose geometry possesses orthotropic symmetry and is dependant upon the spacial arrangement of sphere centres.

Although there are an infinite number of possible structural arrangements for the body-centred orthorhombic packing there are restrictions due to the geometry of the particles. From Figure 6.3 it can be seen that particle centres of the contacting spheres may not come closer than a distance of 2R. This condition sets the minimum dimension of the unit cell to 2R and hence the minimum value of l_i equal to 1/2. In addition as $l_i l_i$, by definition, equals unity then there is a maximum value of l_i equal to $\sqrt{1/2}$, this condition being applicable when two values of l_i are equal to the permissible minimum. By changing the dimensions of the unit cell any valid assembly geometry can be obtained and therefore l_i may be regarded as a measure of the structural anisotropy. Furthermore, the solid volume density (V_s/V_o) becomes a function of the structural anisotropy, although there is no one-to-one relationship between the solid volume density and the structural anisotropy.

Figure 6.4 illustrates the two-dimensional equivalent unit cell

from which similar observations to those made above may be established.

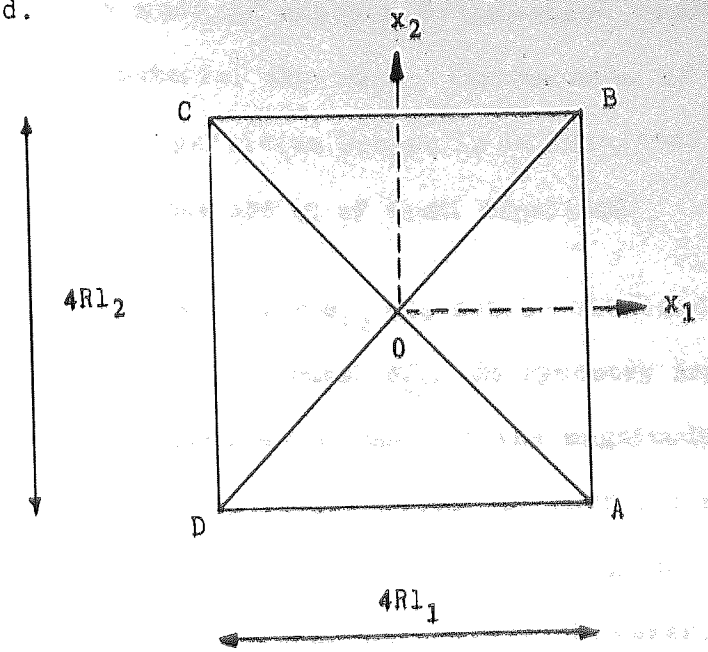

Figure 6.4 The two-dimensionally equivalent unit cell

For this structure the area occupied by each disc in an infinite assembly is given by

$$A_o = 8l_1l_2R^2 \tag{6.3}$$

The shape of A_o is in general that of a hexagon and as the particle geometry restricts the minimum value of l_i to 1/2 then by implication l_i maximum is restricted to $\sqrt{3/4}$.

Finally, in order to fully explain the physical model the physical properties of the particles themselves need to be defined. However as the assumption of rigid particles has been made only the limit on contact force obliquity need be given. For simplicity the Coulomb type friction law is used which limits this obliquity to a constant, i.e the coefficient of friction, μ (c.f. Eqn. (2.9)).

6.3 ASSEMBLY KINEMATICS

Having established the physical model, the various kinematical possibilities must be considered before the stress tensor can be

determined. Within the work presented here attention has been restricted to a mode of uniform deformation wherein there is no rotation of the material axes (x_i). Furthermore, if particle spin is prevented then all particles behave in an identical manner and slip occurs at all contacts and is of equal magnitude.

The strain-rate tensor $\dot{e}_{ij}$ may now be obtained by defining the average velocity gradient tensor $\dot{d}_{ij}$. By symmetry arguments, Thornton and Barnes (1982) demonstrated that as the magnitude of the relative velocity $\dot{\Delta}$ is the same at all contacts, then the average velocity gradient tensor may be derived from considering the relative velocity between only two contiguous particles. However, in order to be consistent with the method of calculating the average displacement gradient tensor (d_{ij}, Chapter 3) the deformation of the unit cell will be considered and the average velocity gradient tensor defined as

$$\dot{d}_{ij} = \partial \dot{u}_i / \partial x_j = \frac{1}{V} \int_S u_i v_j ds \qquad (6.4)$$

where u_i gives the velocity at the surface S (c.f. Eqn. (3.13)). For the three-dimensional assembly V represents the volume bounded by surface S, whereas for the two dimensional assembly V represents the area bounded by perimeter S. Figure 6.5 shows the surface of the body-centred orthorhombic unit cell where the vectors superimposed at the corners represent the velocities of the sphere centres relative to the centre of the central sphere. Due to the considered mode of deformation the magnitude of these vectors is $2\dot{\Delta}$ and their direction is restrained to be normal to the line joining sphere centres, i.e. $m_j l_j = 0$ where m_j are the direction cosines of the velocity vectors. In the case of body-centred orthorhombic arrays equation (6.4) is equivalent to

$$\dot{d}_{ij} = \frac{1}{2V_c} \sum_{k=1}^{6} \hat{u}_i \hat{v}_j A^k S \qquad (6.5)$$

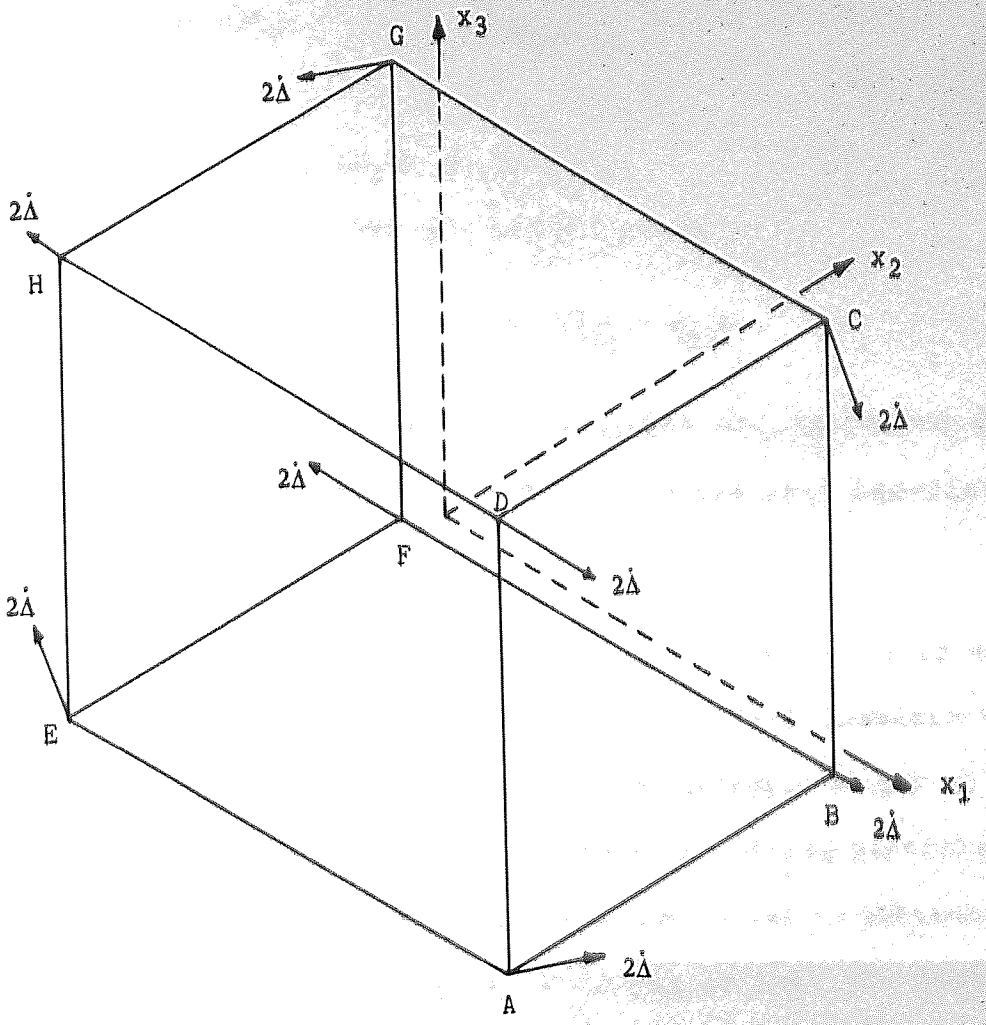

Figure 6.5 Kinematics of the body-centred orthorhombic unit cell

where $\hat{u}_i$ and $\hat{v}_j$ are the average velocity vector and outward unit normal for the rectangular surface $\dot{\Delta}S$. When considering plane ABCD the average velocity vector for the surface is obtained from the u_1 components of particle centres A, B, C and D. The plane has zero velocity components in directions 2 and 3 and its unit normal is in the x_1-direction. In addition $\Delta S/2V_0$ is equivalent to the linear x_1-dimension. Hence, the contribution of planes ABCD and EFGH to $\dot{d}_{ij}$ are

$$\dot{d}_{11} = 2(2\dot{\Delta}m_1)/4l_1R = \dot{\Delta}m_1/Rl_1$$

where all other component contributions are zero. Similarly by

considering surfaces EADH and FBCG, and ABFE and DCGH

$$\dot{d}_{\bar{2}\bar{2}} = \dot{\Delta}m_2/Rl_2 \qquad \dot{d}_{\bar{3}\bar{3}} = \dot{\Delta}m_3/Rl_3$$

Therefore

$$\dot{e}_{\bar{i}\bar{j}} = \dot{d}_{\bar{i}\bar{j}} = \dot{\Delta}m_i/Rl_j \ (= 0, \text{ if } i \neq j) \tag{6.6}$$

since the strain-rate and spin tensors are given by

$$\dot{e}_{\bar{i}\bar{j}} = \frac{1}{2}(\dot{d}_{\bar{i}\bar{j}} + \dot{d}_{\bar{j}\bar{i}}) \text{ and } \dot{w}_{\bar{i}\bar{j}} = \frac{1}{2}(\dot{d}_{\bar{i}\bar{j}} - \dot{d}_{\bar{j}\bar{i}}) \tag{6.7}$$

and $\dot{d}_{\bar{i}\bar{j}}$ has no off-diagonal components and therefore $\dot{w}_{\bar{i}\bar{j}} = 0$. Equation (6.6) also holds true for the equivalent two-dimensional assembly.

Equation (6.6) shows that the strain-rate tensor is dependent upon the micro-mechanics at the interparticle contacts and is a function of the assembly structure. The velocity vector at contacts may be in any direction normal to the line joining particle centres and therefore general states of deformation may be obtained for any assembly geometry. It is for this reason that the body-centred orthorhombic (and two-dimensionally equivalent) array was chosen to model granular media.

Finally, it should be noted that if the derivation of the strain-rate tensor had been carried out by considering the surface integral of an assembly consisting of many unit cells then $\dot{e}_{ij} \rightarrow \dot{e}_{\bar{i}\bar{j}}$. In the case of an infinite assembly $\dot{e}_{ij} = \dot{e}_{\bar{i}\bar{j}}$.

6.4 THE STRESS TENSOR

Since the tractions acting on the surface of a typical sphere are discrete forces acting at the contact points the state of stress within the particle is not homogeneous. However, due to the regular arrangement of particles, the average stress tensor will be identical for all particles and will be equivalent to the macroscopic stress

state when considering an infinite assembly. Thus, for the body-centred orthorhombic assembly

$$\sigma_{ij} = \frac{1}{V_o}\sum_{n=1}^{8} \hat{F}_i \hat{x}_j \quad \text{(c.f. Eqn. (3.7))} \tag{6.8}$$

where $\hat{F}_i$ represents the force acting at contact coordinates $\hat{x}_j$, which have their origin at the sphere centre. Due to force equilibrium and symmetry, however, contact forces on a common diameter are of equal magnitude and contribute equal amounts to the stress tensor. Hence

$$\sigma_{ij} = \frac{2}{V_o}\sum_{n=1}^{4} \hat{F}_i \hat{x}_j \tag{6.9}$$

Also, as slip occurs at all contacts, forces $\hat{F}_i$ may be divided into normal forces $\hat{N}_i$ and shear forces $\hat{T}_i$ where $\hat{T}$ is in the direction of slip and has magnitude $\mu\hat{N}$. Coordinates $\hat{x}_j$ may be represented by $R\hat{l}_j$, normal forces $\hat{N}_i$ by $-\hat{N}\hat{l}_i$ and shear forces $\hat{T}_i$ by $\mu\hat{N}\hat{m}_i$, to give

$$\sigma_{ij} = \frac{-2R}{V_o}\sum_{n=1}^{4} \hat{N}(\hat{l}_i\hat{l}_j - \mu\hat{m}_i\hat{l}_j) \tag{6.10}$$

The relationship for forces $\hat{N}$ may be obtained by considering particle moment equilibrium. Each contact force contributes to the moment sum of the particle by an amount

$$M_k = \varepsilon_{ijk}F_i x_j \quad \text{(c.f. Eqn. (3.3))} \tag{6.11}$$

where M_k gives the contribution to the moment about axis k and ε_{ijk} is the third order alternating (or permutation) tensor. Therefore, since particles are spherical and force F may be divided into normal and shear components

$$\begin{aligned} M_k &= -NR\varepsilon_{ijk}(l_i l_j - \mu m_i l_j) \\ M_k &= \mu NR\varepsilon_{ijk} m_i l_j \end{aligned} \tag{6.12}$$

as normal forces pass through the sphere centre. From equation (6.12) the moment sum for the particle is then given by the summation of contributions from each contact force.

$$\sum_{n=1}^{8} M_k = 2\mu R\sum_{n=1}^{4} \hat{N}\varepsilon_{ijk}\hat{m}_i\hat{l}_j \tag{6.13}$$

Therefore due to the structural symmetry and the restriction that $\sum M_k = 0$ it can be shown that the magnitude of forces $\hat{N}$ must be equal. If in Eqn. (6.10) N is substituted for $\hat{N}$ then

$$\sigma_{ij} = \frac{-2RN}{V_o} \sum_{n=1}^{4} \hat{l}_i \hat{l}_j - \mu \hat{m}_i \hat{l}_j \qquad (6.14)$$

which due to symmetry of the structure becomes

$$\sigma_{ij} = \frac{-8RN}{V_o} (l_i l_j - \mu m_i l_j) \quad (= 0, \text{ if } i \neq j) \qquad (6.15)$$

where the direction cosines l_j are taken positive and m_i is given by the direction of $\mathring{A}$.

An identical analysis may be performed for the equivalent two-dimensional assembly from which the resulting stress tensor is given by

$$\sigma_{ij} = \frac{-4RN}{V_o} (l_i l_j - \mu m_i l_j) \quad (= 0, \text{ if } i \neq j) \qquad (6.16)$$

From equations (6.15) and (6.16) it can be seen that σ_{kk} depends only on the normal forces and equals $-8RN/V_o$ and $-4RN/V_o$ respectively. Hence, the stress tensor may be written as

$$\sigma_{ij} = \sigma_{kk} (l_i l_j - \mu m_i l_j) \quad (= 0, \text{ if } i \neq j) \qquad (6.17)$$

As both the strain-rate and stress tensors have no off-diagonal components it may be concluded that the assumed mechanism is associated with co-axiality.

6.5 ENERGY DISSIPATION

Due to the assumption of rigid particles the strain-rate tensor has no elastic components and the rate of energy dissipation per unit volume may be written

$$\sigma_{ij} \dot{e}_{ij} = (a_{ij} + S_{ij}) \dot{e}_{ij} \qquad (6.18)$$

where a_{ij} and S_{ij} are the normal force contribution and the shear

force contribution to the stress tensor, i.e.

$$a_{ij} = \sigma_{kk} l_i l_j \tag{6.19a}$$

$$S_{ij} = -\sigma_{kk} \mu m_i l_j \tag{6.19b}$$

and from equations (6.6) and (6.19) it is found that

$$a_{ij}\dot{e}_{ij} = 0 \quad (\text{since } m_i l_i = 0) \tag{6.20a}$$

and $$S_{ij}\dot{e}_{ij} = -\sigma_{kk}\mu\dot{\Delta}/R \quad (\text{since } l_i l_i = 1) \tag{6.20b}$$

which demonstrates that the normal force contribution a_{ij} is the non-dissipative stress and the shear force contribution is the dissipative stress. Also by substituting for $\sigma_{kk} = -8TR/\mu V_o$ (for the body-centred orthorhombic assembly) in equation (6.20b)

$$S_{ij}\dot{e}_{ij} = 8T\dot{\Delta}/V_o = 8\mu N\dot{\Delta}/V_o \tag{6.21}$$

which confirms that the rate of energy dissipation per unit volume is provided by the product of the contact shear force T and velocity $\dot{\Delta}$ at each of the eight contacts as a result of overcoming the interparticle friction μ. Further examination of equation (6.20b) shows that for a given mean stress and interparticle friction the rate of energy dissipation is only dependent upon the magnitude of the contact velocity and is independent of the structural anisotropy.

6.6 YIELD SURFACES

The stress tensor, equation (6.17), defines the states of stress which will cause yield, the yield mechanism being defined by the strain-rate tensor, equation (6.6). Thus, having specified the physical properties of the array (structure and interparticle friction) it is possible for a given mean stress to identify the complete range of stress states which will cause yield by varying the components m_i which give the direction of the relative velocity $\dot{\Delta}$ at contacts.

Yield conditions are conventionally represented in principal

stress space (σ_i) by yield surfaces. Due to the dependence on mean stress it is convenient to depict the yield conditions on the deviatoric plane (i.e. σ_{kk} = constant) of the principal stress space.

If the body-centred cubic array ($l_i = 1/\sqrt{3}$) is considered then the yield conditions are defined by a circle centred on the space diagonal, as shown in Figure 6.6a, and according to equation (6.6) all the stress points on this locus are associated with zero rate of volumetric strain. The yield conditions for body-centred tetragonal arrays (e.g. $l_1 \neq l_2 = l_3$) are defined by ellipses, Figure 6.6b, which are symmetric about one of the axes and whose centres are displaced from the space diagonal. Figure 6.6c shows the yield locus for a body-centred orthorhomic array which has an arbitrary permissible structure ($l_1 \neq l_2 \neq l_3$).

It follows from the geometry of the deviatoric yield loci that the shape of the yield surface is in general that of an oblique elliptical cone with base planes parallel to the deviatoric planes. The inclination of the cone is given by the structural anisotropy of the array, and from the stress tensor (equation 6.17), the size of the deviatoric yield locus is linearly proportional to the product of meanstress and the coefficient of friction. Likewise, the yield surface for the two-dimensionally equivalent structure is defined by two straight lines passing through the origin as shown in Figure 6.7, where $l_1 > l_2$.

The yield locus shown in Figure 6.6c is redrawn in Figure 6.8a and a three dimensional view of the corresponding yield surface is shown in Figure 6.8b. These figures show how the total stress vector σ is divided into its non-dissipative and dissipative components. It can be seen that the non-dissipative stress vector a remains constant and therefore the deviatoric yield locus is coincident with the base

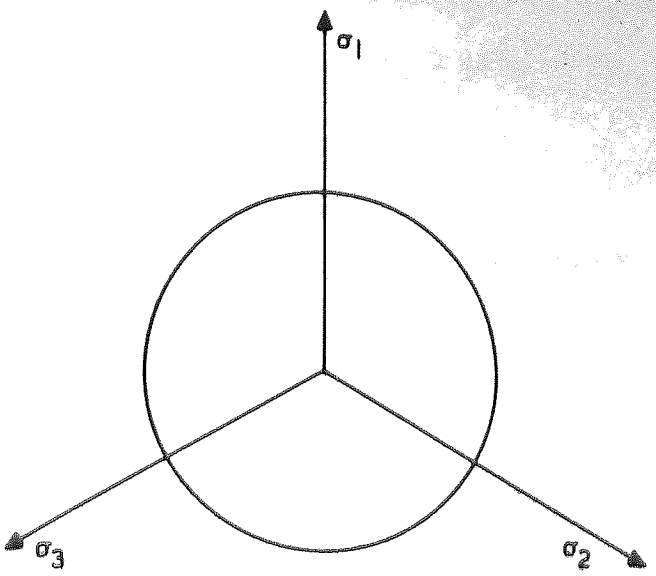

(a) body-centred cubic

(b) body-centred tetragonal

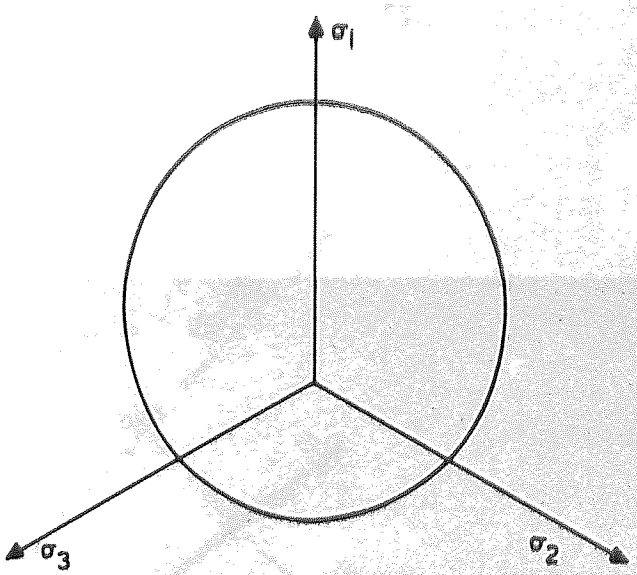

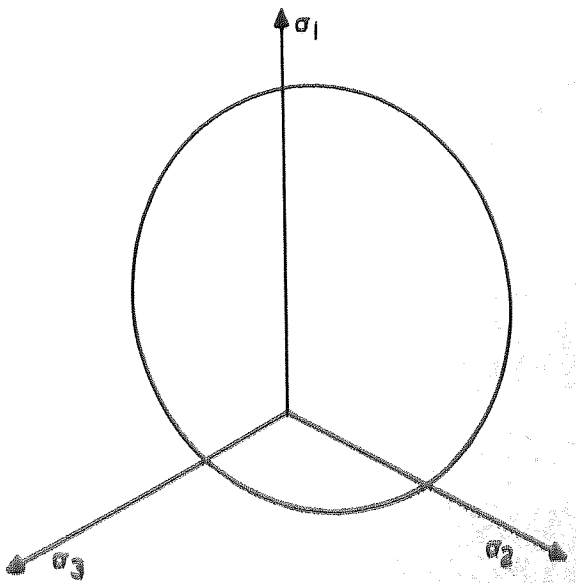

(c) body-centred orthorhombic

Figure 6.6 Yield loci

planes of the conical yield surface. Figure 6.8a shows the corresponding components of α and S on the deviatoric plane which illustrates that only part of the deviatoric stress is dissipative since

$$s_{ij} = a_{ij} + S_{ij} \qquad (6.22)$$

where the deviatoric stress tensor $s_{ij} = \sigma_{ij} - \sigma_{kk}\,\delta_{ij}/3$ and $a_{ij} = \alpha - \alpha_{kk}\delta_{ij}/3$ where α is the total translation of the centre of the deviatoric yield locus from the origin.

Although there are an infinite number of possible structural arrangements there are restrictions due to the geometry of the particles themselves in that, for the body-centred orthorhombic array, direction cosines l_i must lie in the range $1/2 < l_i < 1/\sqrt{2}$.

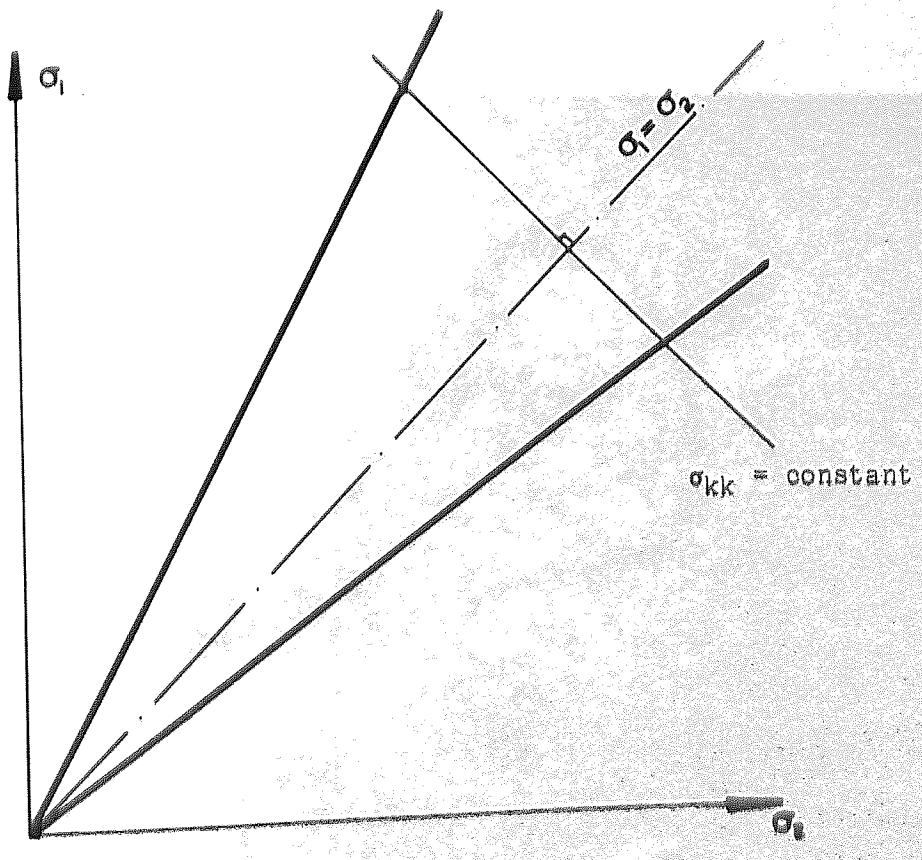

Figure 6.7 Yield surface of the two-dimensionally equivalent array

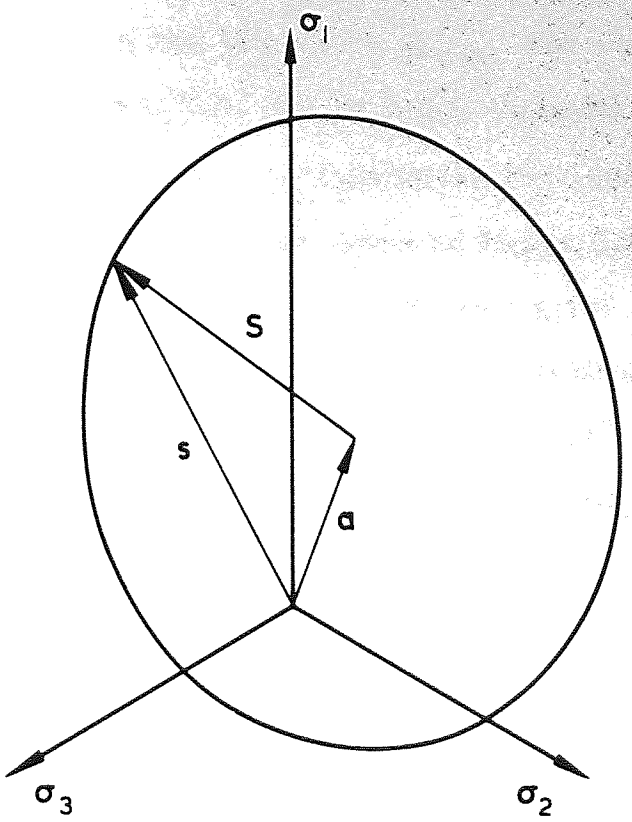

(a)

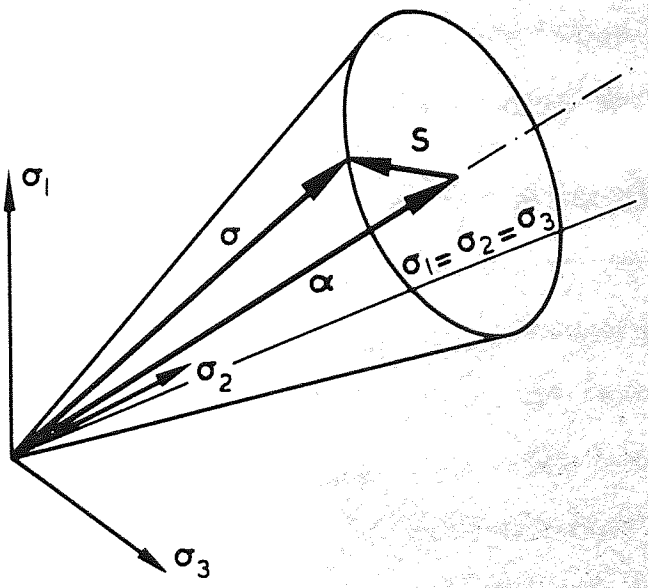

(b)

Figure 6.8 Yield surface geometry

Consequently there is a limit to the possible locations of the centre of the yield locus on the deviatoric plane. Two deviatoric limiting envelopes can be identified, one of which circumscribes the possible loci centres and the second circumscribes the limiting yield loci. The shape of these envelopes are shown in Figure 6.9 for body-centred orthorhombic arrays where the dashed envelope gives the limit on loci centres. Both envelopes show the expected orthotropic symmetry, the envelope bounding loci centres being an equilateral triangle. Furthermore it is interesting to note that the shape of the envelope bounding the limiting yield loci is geometrically similar to the experimentally observed failure envelope for dense sand, see for example Lade (1972).

Yield surfaces for three body-centred tetragonal arrays $l_1 > l_2$, $l_1 = l_2$ and $l_1 < l_2$ are shown in Figure 6.10 with strain rate vectors $\dot{e}$ superimposed. It is clear that the normality rule of classical plasticity theory does not apply. Instead, the strain-rate vectors are normal to the axis of the yield surface. This is a physical requirement imposed by equation (6.20a) which states that the strain-rate (plastic) and non-dissipative stress vectors are orthogonal.

From the yield surface geometry already presented it follows that the base planes of the yield surfaces may be referred to as the 'dissipative stress planes'. Adopting this terminology, it is found that normality of the strain-rate vector to the yield surface is only observed when the dissipative stress planes are examined by looking along the direction of the non-dissipative stress vector. This is illustrated in Figure 6.11a for the case of the body-centred orthohombic locus shown in Figure 6.6c. The implication of this view is that the non-dissipative stress components α_{ij} are eliminated and only the dissipative stress components S_{ij} are seen. Hence, viewed in this way the yield locus (or surface) is that of a completely

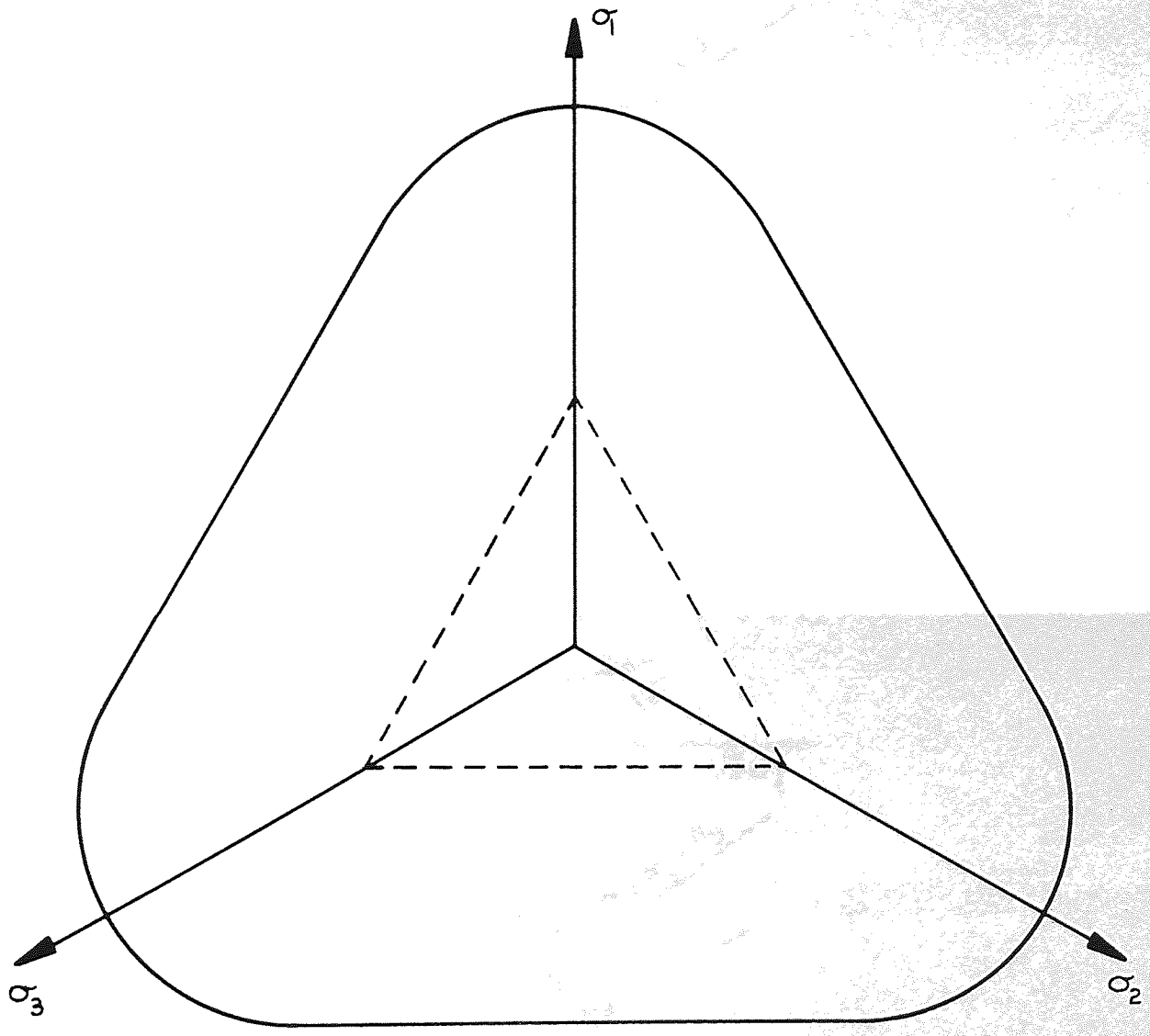

Figure 6.9 Limiting envelopes for the body-centred orthorhombic array

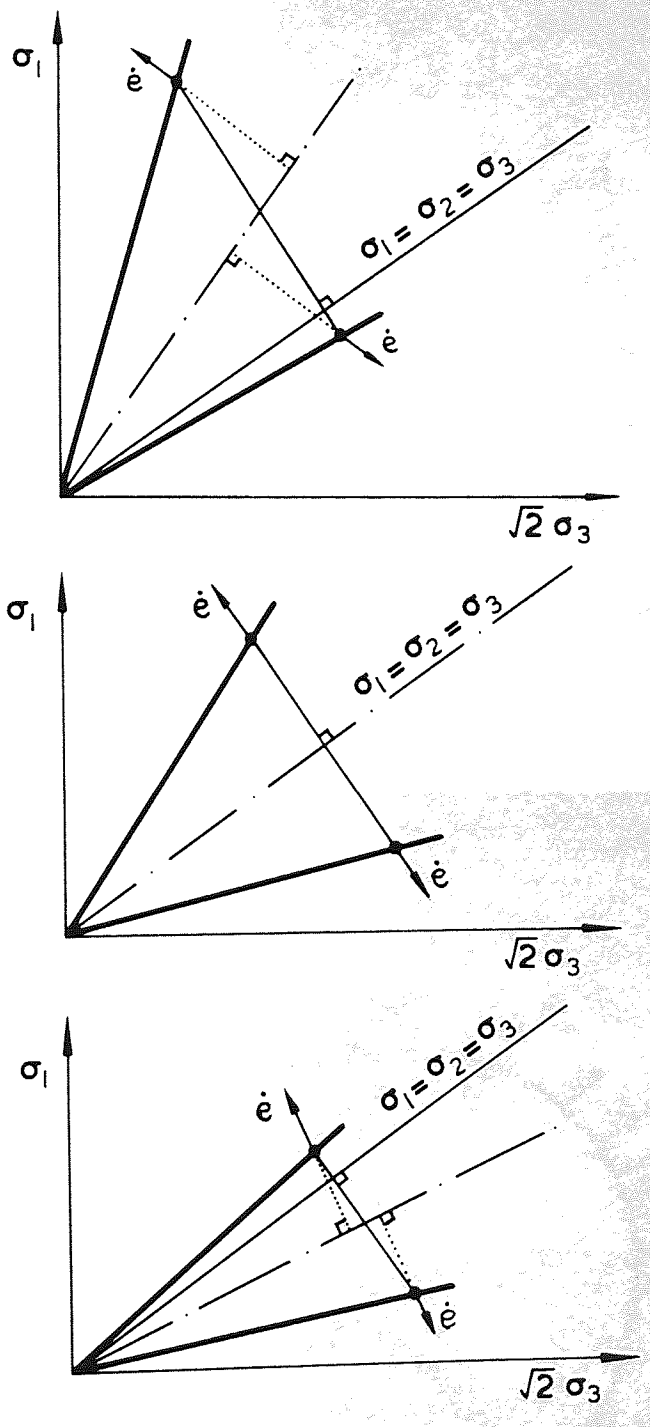

Figure 6.10 Strain-rate vectors superimposed onto the yield surfaces of body-centred tetragonal arrays

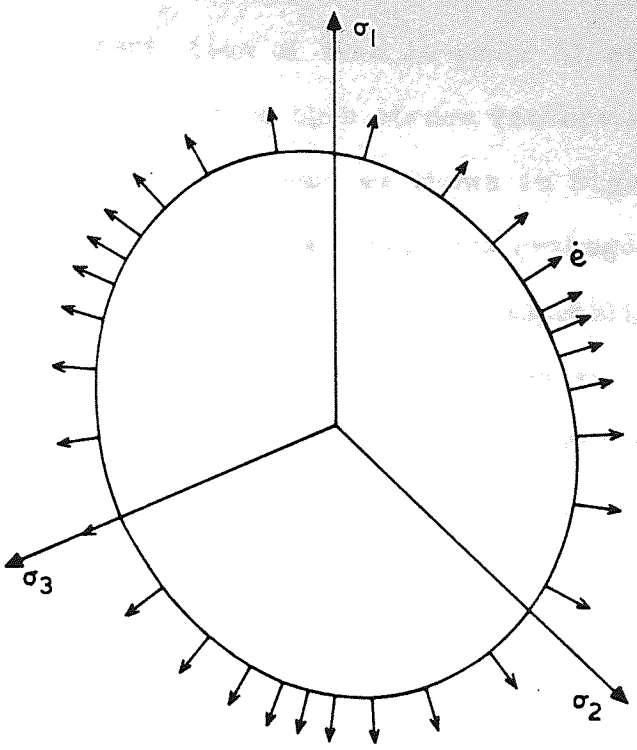

(a)

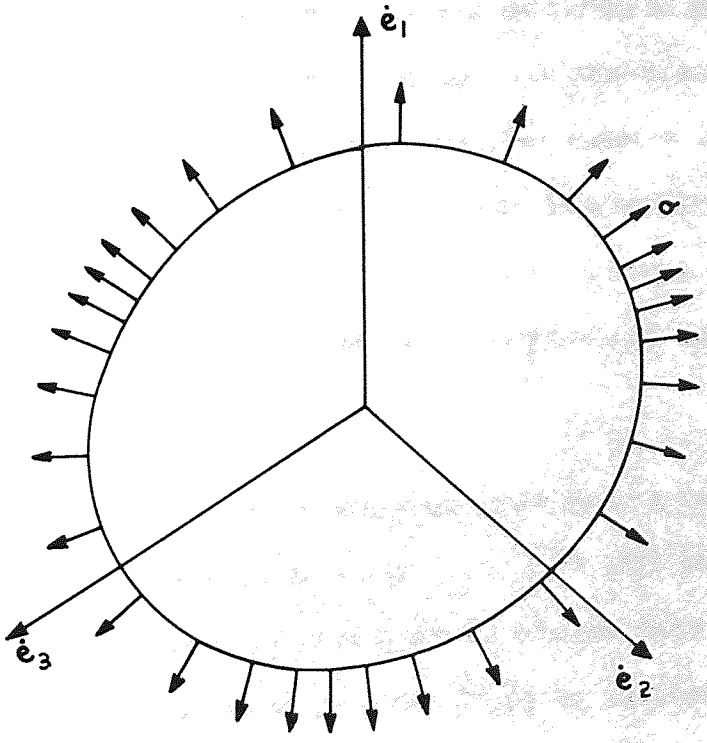

(b)

Figure 6.11 The orthoganality condition

dissipative system. According to Ziegler (1977) the condition of orthogonality applies when considering a purely dissipative system. The geometric interpretation of this is that, if strain-rate vectors are normal to the yield locus then stress vectors are normal to the corresponding strain-rate locus as shown in Figure 6.11b. For a constant value of $\dot{\Lambda}/R$ (Eqn. 6.6) Ziegler's orthogonality condition holds for the deformation of the considered assemblies when principal stress and strain-rate spaces are superimposed and the corresponding surfaces viewed in such a way that the non-dissipative stress components are eliminated. Figure 6.11 gives an example of the orthogonality condition when applied to an arbitrary body-centred orthorhomic array.

As shown in Figures 6.6 the location and shape of the deviatoric yield loci depend on the structure of the array. Yield results in a change in structure, but, for irrotational deformation, the general body-centred orthorhombic description remains valid throughout the deformation process. Consequently it can be inferred from the figures already shown that, during deformation, the non-dissipative stress vector α (i.e. the axis of the yield surface) rotates about the origin of principal stress space. Hence, for the body-centred orthorhombic array the deviatoric yield loci translate, distort and rotate in a manner which reflects the changes in the structural anisotropy of the array.

Figure 6.12 illustrates the evolution of the deviatoric yield locus for a face-centred cubic array ($l_2 = l_3 = 1/2$) which is deformed at constant mean stress in an arbitrary manner into a body-centred cubic arrangement. The initial yield locus is centred at A with the stress state defined by the point 1. During deformation the centre of the yield locus follows the trajectory ABCDE with the corresponding

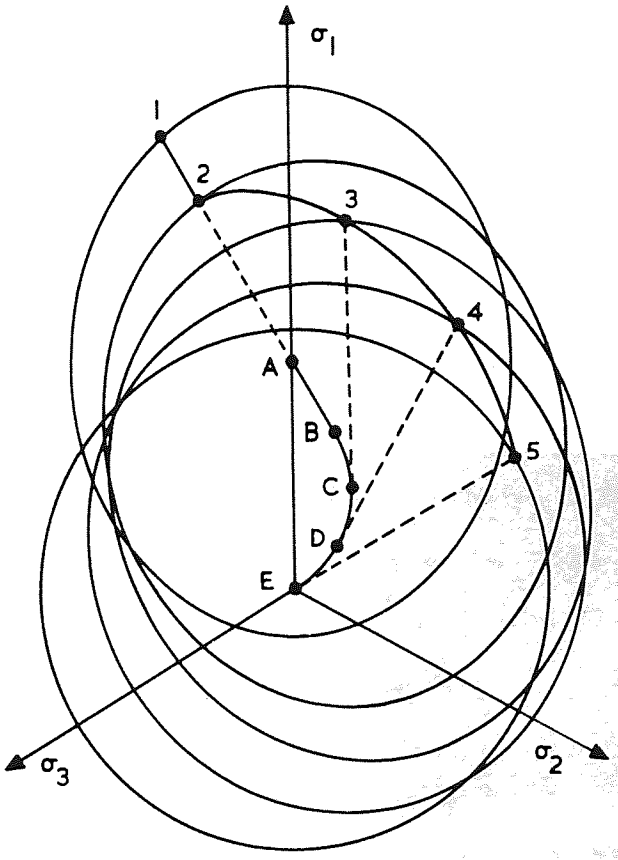

Figure 6.12 Evolution of the deviatoric yield locus during deformation

stress path defined by points 12345. The lines A1.....E5 correspond to the instantaneous dissipative stress vectors and it can be seen that they are tangential to the trajectory ABCDE of the centre of the yield locus. Therefore, the motion of the deviatoric yield locus may be defined as follows

$$\dot{a}_{ij} = -hS_{ij} \tag{6.23}$$

which, it is interesting to note, corresponds to Ziegler's (1959) modification to Prager's (1955) kinematic hardening rule.

The geometry described in this section can immediately be identified with the geometry used to describe the essence of classical plasticity models. All the fundamental properties have been examined and as a result it is reasonable to expect that the solution to the particle mechanics problem may be expressed in terms of a plasticity theory. Equations describing this plasticity model are expected to have the same form as those of classical theories due to the geometric representation of the model showing clear similarities. The derivation of this theory is presented in the following section.

6.7 THE CONTINUUM MECHANICS MODEL

Firstly, two 'characteristic measures' of plastic behaviour may be defined, one of which is termed the 'characteristic strain-rate'

$$\dot{e} = \dot{\Delta} / R \tag{6.24}$$

which is a measure of the magnitude of slip, relative to particle size, at the contacts. The second is defined as the 'characteristic stress'

$$\sigma = -\sigma_{kk} \tag{6.25}$$

which is a measure of the magnitude of the stress-field and dictates the size of the yield locus, for any given value of interparticle friction. Equations (6.6) and (6.19) may now be rewritten as

$$\dot{e}_{ij} = \dot{e}m_i/l_j \tag{6.26}$$

$$\alpha_{ij} = -\sigma l_i l_j \tag{6.27}$$

$$S_{ij} = \mu\sigma m_i l_j \tag{6.28}$$

Using equations (6.26), (6.27) and (6.28) it may then be shown that

$$\dot{e} = (C_{ijkl}\ \dot{e}_{ij}\ \dot{e}_{kl})^{1/2} \tag{6.29}$$

where $C_{1111} = l_1^2$, $C_{2222} = l_2^2$, $C_{3333} = l_3^2$ with all other components equal to zero.

$$\sigma = (B_{ijkl}\ \alpha_{ij}\alpha_{kl})^{1/2} \tag{6.30}$$

where $B_{1111} = 1/l_1^2$, $B_{2222} = 1/l_2$, $B_{3333} = 1/l_3^2$ with all other components equal to zero.

$$\mu\sigma = (B_{ijkl}S_{ij}S_{kl})^{1/2} \tag{6.31}$$

The relevance of the characteristic measures is made clear in the definition of the dissipation function. From equations (6.18), (6.20), (6.24) and (6.25)

$$D = \sigma_{ij}\dot{e}_{ij} = S_{ij}\ \dot{e}_{ij} = \mu\sigma\dot{e} \tag{6.32}$$

which shows that the rate of energy dissipation per unit volume is given by the coefficient of interparticle friction multiplied by the product of the two characteristic measures.

If equation (6.29) is substituted into equation (6.32) the dissipation function may be defined in terms of the strain-rate tensor

$$D = \mu\sigma(C_{ijkl}\dot{e}_{ij}\dot{e}_{kl})^{1/2} \tag{6.33}$$

Alternatively, the dissipation function may be defined by the dissipative stress tensor by substituting equation (6.31) into equation (6.32)

$$D = \dot{e}\ (B_{ijkl}S_{ij}S_{kl})^{1/2} \tag{6.34}$$

Now according to Euler's identity for homogeneous equations it may be shown that for any homogeneous function $F(x_i)$

$$x_j.\partial F(x_i)/\partial x_j = nF(x_i) \tag{6.35}$$

where n is a constant giving the order of $F(x_i)$. Hence, using Euler's

identity in conjunction with the dissipation function (equation (6.32) it can be shown that

$$S_{ij} = \partial D/\partial \dot{e}_{ij} \text{ as } n = \dot{e}_{ij}(\partial D/\partial \dot{e}_{ij})D^{-1} = 1 \tag{6.36}$$

$$\text{or} \quad \dot{e}_{ij} = \partial D/\partial S_{ij} \text{ as } n = S_{ij}(\partial D/\partial S_{ij})D^{-1} = 1 \tag{6.37}$$

Thus the flow rules are found by differentiating equations (6.33) and (6.34) to give

$$S_{ij} = (\mu\sigma/\dot{e})C_{ijkl}\dot{e}_{kl} \tag{6.38}$$

$$\text{and} \quad \dot{e}_{ij} = (\dot{e}/\mu\sigma)B_{ijkl}S_{kl} \tag{6.39}$$

Yield occurs when the ratio of the shear and normal contact forces reach a critical value, i.e. when

$$T - \mu N = 0 \tag{6.40}$$

However, as N is proportional to σ (e.g. $\sigma = 8NR/V$ for spheres) then by using equations (6.30) and (6.31) the yield function can be obtained from equation (6.40)

$$Y = B_{ijkl}S_{ij}S_{kl} - \mu^2 B_{ijkl}\alpha_{ij}\alpha_{kl} = 0 \tag{6.41a}$$

which clearly distinguishes between the dissipative and non-dissipative parts of the stress tensor. Equation (6.41a) can be rearranged to give

$$Y = B_{ijkl}(\sigma_{ij} - \alpha_{ij})\ (\sigma_{kl} - \alpha_{kl}) - \mu^2 B_{ijkl}\alpha_{ij}\alpha_{kl} = 0 \tag{6.41b}$$

or expanded, leading to

$$Y = B_{ijkl}\sigma_{ij}\sigma_{kl} - (1 + \mu^2)\sigma_{ii}\sigma_{jj} \tag{6.41c}$$

The form of equations (6.41) are very similar to those given by Baltov and Sawczuk (1965) and Mroz (1967) when an allowance for the dependency of yield on mean stress is given.

In order to complete the continuum mechanics model it is necessary to describe the motion of the yield surface during plastic deformation. In section 6.6 it was identified from Figure 6.12 that the translation rule corresponds to Ziegler's (1959) modification to

Prager's (1955) kinematic hardening rule, and is given by equation (6.23). Substituting the flow rule, equation (6.38), into equation (6.23)

$$\dot{a}_{ij} = -h(\mu\sigma/\dot{e})C_{ijkl}\dot{e}_{kl} \tag{6.42}$$

in which the hardening parameter h needs to be identified.

Let i = j = k = l = 1, then

$$\dot{a}_{11} = -h(\mu\sigma/\dot{e})C_{1111}\dot{e}_{11} \tag{6.43}$$

Now by definition

$$a_1 = \alpha_1 + \sigma/3 \quad \text{(for spheres)} \tag{6.44a}$$

$$a_1 = \alpha_1 + \sigma/2 \quad \text{(for discs)} \tag{6.44b}$$

and from equation (6.27)

$$\alpha_1 = -\sigma l_1^2 \tag{6.45}$$

Adopting natural strains then, since orthotropic symmetry is maintained during deformation, l_1 is related to e_1 by

$$l_1^2 = (l_1)_0^2 \exp(2e_1) \tag{6.46}$$

where $(l_1)_0^2$ gives the initial value of l_1^2. Substituting equations (6.45) and (6.46) into (6.44) gives

$$a_1 = -\sigma((l_1)_0^2\exp(2e_1) - 1/3) \tag{6.47a}$$

$$a_1 = -\sigma((l_1)_0^2\exp(2e_1) - 1/2) \tag{6.47b}$$

Equations (6.47) may now be differentiated with respect to e_1 to obtain

$$\dot{a}_1 = -2\sigma l_1^2\dot{e}_1 \quad \text{(for both equations)} \tag{6.48}$$

which may be compared to equation (6.43) to give

$$h = 2\dot{e}/\mu \tag{6.49}$$

This is confirmed by considering i = j = 2,3. Substituting for h in equation (6.42)

$$\dot{a}_{ij} = -2\sigma C_{ijkl}\dot{e}_{kl} \tag{6.50}$$

in which C_{ijkl} defines the structural anisotropy and is clearly a function of the total strain e_{ij}. Therefore equation (6.50) may be

integrated to obtain the translation rule.

$$a_{ij} = (a_{ij})_0 - 2\sigma \int C_{ijkl} de_{kl} \qquad (6.51)$$

where $(a_{ij})_0$ is the initial value of a_{ij} which corresponds to the initial array structure.

Hence, the complete mathematical theory of plasticity, corresponding to the particle mechanics solution, is given by the yield function (equation (6.41)), the flow rules (equations (6.38) and (6.39)) and the translation rule (equation (6.51)).

6.8 ELASTIC COMPLIANCE

The theory presented in the previous sections is applicable to rigid arrays of particles wherein a force displacment law for interparticle contact was absent. Therefore, any change in array structure was associated with plastic deformation, which occurred when the contact force obliquity reached a critical value (μ). The region within the yield surface may therefore be considered a 'rigid region' and any stress state within this region is indeterminate. Furthermore stress states associated with yield may not be obtained from the strain-rate tensor as the magnitude of the stress field (σ) is unknown. Hence, only the stress ratios (σ_{ij}/σ_{kk}) are available. Thus, in order to define all states of stress it becomes apparent that some kind of force displacement law is required at interparticle contacts.

It is not the object of this work to identify the true particle deformation, for which it would be necessary to consider the stress-state within particles. Attention will therefore be restricted to an elastic force displacement law at interparticle contacts.

Provided elastic displacements are small, such that they do not affect the structural geometry of the array, then any elastic force

displacement law may be incorporated. For simplicity, if linear elasticity is assumed at interparticle contacts then contact forces may be determined from elastic contact displacements and stiffnesses (c.f. force displacement law incorporated within 'Ball'). Normal contact forces then dictate the magnitude of the stress field (σ) and for any given structure fix α_{ij}. Shear contact forces give the magnitude and direction of S_{ij}, and hence the stress tensor becomes determinate.

By setting constant the magnitudes of the normal and shear contact forces, for a given array structure, then a deviatoric locus may be constructed by varying the direction of the shear contact forces. The shape of this deviatoric locus is identical to that of the yield locus (had $T = \mu N$). Each point on this locus corresponds to a constant value of stored energy. Hence, for a fixed value of normal force

$$T/N = \delta \qquad (\delta \leq \mu) \tag{6.52}$$

dictates the amount of stored energy. By varying δ the size of the deviatoric locus changes and in so doing accommodates the change in stored energy. The deviatoric locus may be interpreted as an 'elastic potential', the limiting size of which is given by the yield locus (i.e. $\delta = \mu$).

It is interesting to note that the deviatoric yield locus associated with the body-centred cubic array is circular (as shown in Figure 6.4) and all points on it are associated with zero rate of volume change provided the mean stress remains constant. The normal force contribution to the stress tensor α_{ij} has no deviatoric components a_{ij} and therefore S_{ij} may be considered to be the 'distortional' part of the stress tensor. Yield occurs when the magnitude of S_{ij} reaches a maximum constant value and is associated

with maximum distortional strain energy and, hence, is in exact agreement with the interpretation of von Mises yield criterion.

6.9 DISCUSSION OF RESULTS

The mathematical theory of plasticity presented above was developed from the initial considerations of the load-deformation relationship at interparticle contacts. By using this approach to the problem a physically sound base has been constructed for the rational development of a microstructural soil plasticity theory.

The theory shows that yield conditions for regular, but anisotropic, granular assemblies are defined by oblique elliptical cones whose axes do not coincide with the space diagonal of principal stress space. Plastic deformation results in a rotation of the yield cone axis and the induced anisotropy is reflected in the translation, distortion and rotation of the yield locus on the deviatoric plane. The model clearly identifies the effect of friction and structure. For a given mean stress the coefficient of interparticle friction dictates the size of the yield locus. The structure, which is defined by both the shape and the spacial arrangement of the particles, dictates the orientation of the non-dissipative stress vector (axis of the cone) and also the shape of the deviatoric yield locus.

Several features of the phenomenological behaviour of more complex granular media, such as sand, are exhibited by the model. The so-called 'Bauschinger' effect is accounted for by the yield function and the translation rule incorporates a memory effect in that the current yield state is dependent on the previous strain history. Both volumetric expansion and contraction are accommodated by the model which is of the non-associated flow type as a result of the physical requirement that the plastic strain-rate vectors are orthogonal to the

non-dissipative stress vector.

By comparing the results of the above analysis to those given in Chapter 5 for the 1000 disc test it becomes apparent that the theory of regular arrays is of limited use when trying to model the behaviour of random assemblies. For the considered mode of deformation all contact forces are of equal magnitude in the regular assembly and structural anisotropy is completely defined by the relative positions of particle centroids. Deformation of the regular assembly occurs without any loss or gain of contact numbers and is always accompanied by interparticle slip at every contact point. Clearly this is not typical of the behaviour of irregular assemblies where the structure is used in a biased way by the force distribution. Indeed, the force distribution is microscopically very inhomogeneous and the magnitude of contact forces becomes very much direction dependent. Hence, regular arrays fail to reflect this induced mechanical anisotropy which is superimposed on structure. Structural evolution can not be accounted for as the major mechanism for structural change in random assemblies is contact creation and deletion. Finally, from test results, the number of slip locations never exceeds 25% of the total number of contacts and, in addition, slip is much more likely at contacts carrying small forces. Therefore, the rate of energy dissipation would be greatly overestimated by the dissipation function for regular arrays (equation 6.32).

Statistical analyses are therefore required in order to quantify the mechanisms that occur in random assemblies. This could make possible the extension of the above plasticity theory to more complex granular media. Statistical analyses of this type are undertaken in Chapter 7.

7 THE RELEVENCE OF MICROSTRUCTURE IN GRANULAR MEDIA

7.1 INTRODUCTION

In Chapter 5 a qualitative description was given of the observed microscopic response of granular media to deformation. The observed microscopic mechanisms gave rise to progressive changes in the overall structure, force distribution and velocity distribution. It was suggested that a description of the structure could well serve as an effective link between the stress and strain-rate tensors, since both force and velocity distributions are mediated by the assembly structure. Adopting this approach, a constitutive model for granular media requires a mathematical expression to describe structure which can subsequently be used in flow equations.

Chapter 6 gives the analysis that leads to the derivation of a continuum model for regular assemblies of spherical particles subjected to an assumed mode of deformation. The microstructure for the regular assembly is simple and can be completely described by considering the relative positions of any two contiguous particles. Under the given mode of deformation simple force and velocity distributions result that can be directly related to the instantaneous structure. Although the analyses of regular arrays help to understand the behaviour of random assemblies, comments given in section 6.9 outline the inability of regular structures to fully account for the microscopic mechanisms observed in the deformation of random assemblies.

The purpose of this chapter is, first of all, to identify all the geometric parameters which must be considered to provide a full description of granular material structure. Then the evolution of structure for the 1000 disc test will be quantified by examining test

data using statistical analyses. Finally, an attempt will be made to relate the derived structural parameters to the stress and strain-rate tensors. No attempt will be made to develop a constitutive model for random granular assemblies as the amount of relevant test data is, to date, far from sufficient. Results from analyses presented here will hopefully stimulate the further work required to achieve this.

7.2 DEFINITION AND EVOLUTION OF MICROSTRUCTURE

Cowin (1978) posed the question: 'Given that porosity is the first measure of local granular structure or fabric, what is the best second measure of local granular structure or fabric?'. Here 'fabric' is a word chosen to mean the spatial arrangement of particles and hence, completely defines the structure of a granular assembly. The question implies that porosity is of most importance. This will later be shown to be not entirely true. A better question would be: 'Which geomtric parameters should be considered in order to more fully describe granular fabric?'. Oda (1978) explained granular fabric by employing two concepts, namely packing and orientation. Packing consists of both a scalar part and a directional part. The scalar part should account for the average coordination number, a measure of the particle size distribution and the assembly porosity. The directional part relates to the distribution of contact normal inclinations which describes structural anisotropy. Orientation is relevant only for non-spherical particles and imposes a further anisotropic component due to the preferred orientation of the particles. Although orientation may be of importance for describing material such as sand, attention will be restricted to two-dimensional disc assemblies where orientation is not relevant.

The solid density is often characterised by the void ratio (e), or alternatively, may be defined by the specific volume $v = 1 + e =$

Total sample volume/solid volume

$$v = \frac{V}{P\pi\langle R^2\rangle} \tag{7.1}$$

where V is the volume of the assembly, P is the total number of particles within V, R is the radius of a disc and $\langle\ \rangle$ means statistical average. The average coordination number $\bar{n}$ and the total number of contacts C can be substituted into equation (7.1) by using the definition $\bar{n} = 2C/P$

$$v = \frac{\bar{n}V}{2C\pi\langle R^2\rangle} \tag{7.2}$$

In order to explain structural anisotropy, Nemat-Nasser (1982) has introduced various local contact quantities such as $n_i n_j$, $l_i l_j$, $n_i l_j$ and higher order terms, where n_i defines the contact normal vector and l_i defines the unit vector which gives the direction of the line joining particle centres. In the case of spherical particle assemblies vectors n_i and l_i are coincident and hence only the distribution of contact normals need be considered in order to describe structural anisotropy.

The variation in the shape of the distribution of contact normals during the 1000 disc test is shown in Figures B.64a - B.76a. Changes in the shape of this polar histogram have already been discussed in section 5.2.6. The above discrete distributions may be approximated by continuous distributions which are described by the probability density function $E(\theta)$ satisfying the equation

$$\int_0^{2\pi} E(\theta)\, d\theta = 1 \tag{7.3}$$

where $E(\theta)$ is the probability density function of a contact normal

existing at an inclination of θ. If the distribution is random and can therefore be approximated by a uniform distribution then the structure is, in effect, isotropic. For a uniform distribution $E(\theta)$ is constant and hence equals $1/2\pi$. Anisotropy is indicated by a non-uniform distribution and can be characterised by the non-zero moments of the distribution. The moments of the distribution are given by the following tensors

$$\mu_0 = \int E(\theta)d\theta = 1 \tag{7.4a}$$

$$\mu_1 = \int E(\theta)n_i d\theta = \phi_i = \langle n_i \rangle \tag{7.4b}$$

$$\mu_2 = \int E(\theta)n_i n_j d\theta = \phi_{ij} = \langle n_i n_j \rangle \tag{7.4c}$$

plus higher order moments.

At each contact point there are two contact normal vectors which are equal and opposite. Hence, only even ordered moments of the distribution are non-zero. The second order tensor ϕ_{ij} corresponds to the so-called 'fabric tensor' used by Satake (1978, 1982). This is incorrectly named and should be renamed the structural anisotropy tensor. This tensor alone is not capable of describing fully the structural details of the packing. For example, both the regular packings shown in Figure 7.1 can be considered to be isotropic.

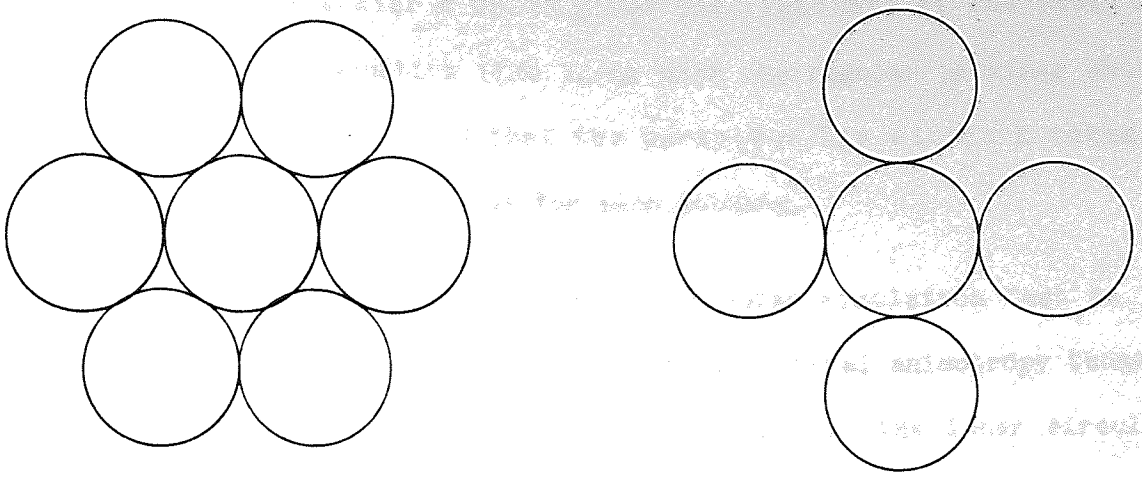

a) Dense regular packing b) Loose regular packing

Figure 7.1 Regular packings with equivalant values of ϕ_{ij}

Both packings have equivalent structural anisotropy tensors where $\phi_{11} = \phi_{22} = 0.5$ and $\phi_{12} = \phi_{21} = 0$. However, packing a) is the densest regular packing with a coordination number of 6 whereas packing b) is the loosest possible regular packing with a coordination number of 4.

Oda, Nemat-Nasser and Mehrabadi (1982) have provided an alternative equation to describe fabric, also described as a fabric tensor, which may be written as

$$F_{ij} = \frac{2\bar{R}C}{V} \langle n_i n_j \rangle \qquad (7.5)$$

where $2\bar{R}$ is the average branch length.

By substituting for C/V from equation (7.2) this may be rewritten as

$$F_{ij} = K \langle n_i n_j \rangle \text{ where } K = \frac{\bar{n}\bar{R}}{v\pi\langle R^2 \rangle} \qquad (7.6)$$

Equation (7.6) would appear to be a most satisfactory description of

structure as it combines both the structural anisotropy tensor $\phi_{ij} = \langle n_i n_j \rangle$ and the scalar K which gives the tightness of the packing. When considering equation (7.6) along with the regular packings shown in Figure 7.1 it is noted that the parameter $\bar{n}/v$ within K takes a significantly different value for each packing.

Using the data obtained from the computer simulation test it is possible to examine the evolution of the structural anisotropy tensor. By only considering contact points which map into the inner circular boundary (i.e. those used to produce the polar histograms B.64a - B.76a) it is possible to calculate ϕ_{ij} by

$$\phi_{ij} = \frac{1}{2C} \sum_{c=1}^{2C} \hat{n}_i \hat{n}_j = \langle n_i n_j \rangle \qquad (7.7)$$

This calculation was made at every 2000 cycles and results are shown graphically in Figure 7.2. From Figure 7.2a it can be seen that the consolidated assembly was not quite isotropic. Although the deviation from $\phi_1 = \phi_2$ is very small, it is an indication that the consolidated assembly was either not truly random or did not contain a sufficient number of contacts within the region considered for statistical averages to exactly represent averages for an infinite assembly. During phase 1 it can be seen that $\phi_1 - \phi_2$ increases almost linearly and during the unloadng phase 2 decreases linearly but not along the path traced by phase 1. For phase 3 it can be seen that the anisotropy is regained and $\phi_1 - \phi_2$ follows that given by phase 1. For all phases Figure 7.2b shows that ϕ_{ij} is coaxial with the applied strain-rate tensor.

There must, of course, be a limit to the degree of anisotropy that can be induced during loadng. This limit must be a function of the rate of contact creation and deletion. It has been stated in

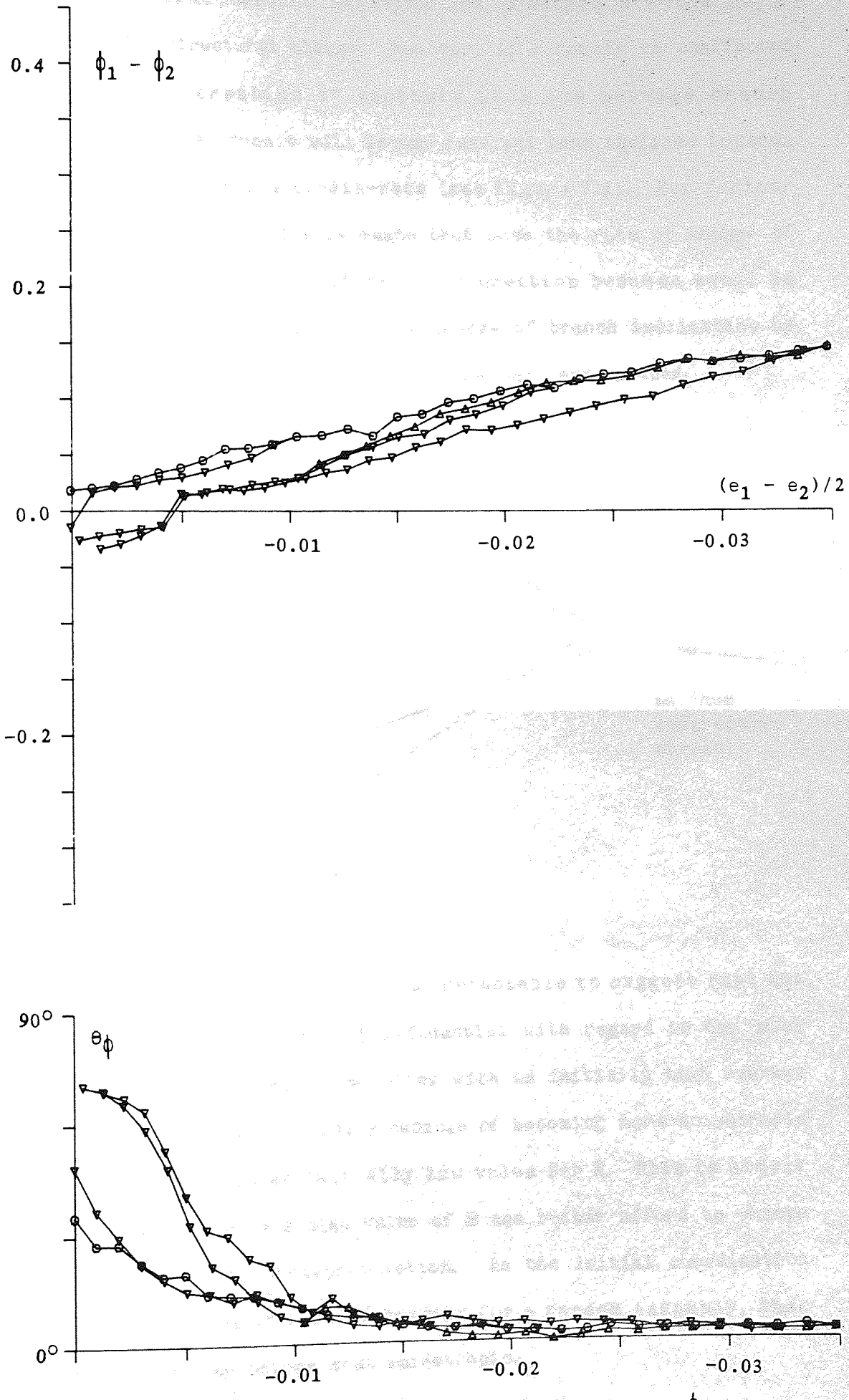

Figure 7.2 Evolution of the structural anisotropy tensor ϕ_{ij}

section 5.2.5 that contact deletion and creation are the major mechanisms for structural change. However, if a domain is unaffected by deletion or creation of contacts then the average branch inclination for that domain will become less and less inclined towards the maximum compressive strain-rate (see Figure 7.3). For further deformation during phase 1 this means that once the rate of change of branch inclination by contact deletion/creation becomes equal in magnitude and opposite to the rate of change of branch inclination by domain deformation, then maximum anisotropy has been induced.

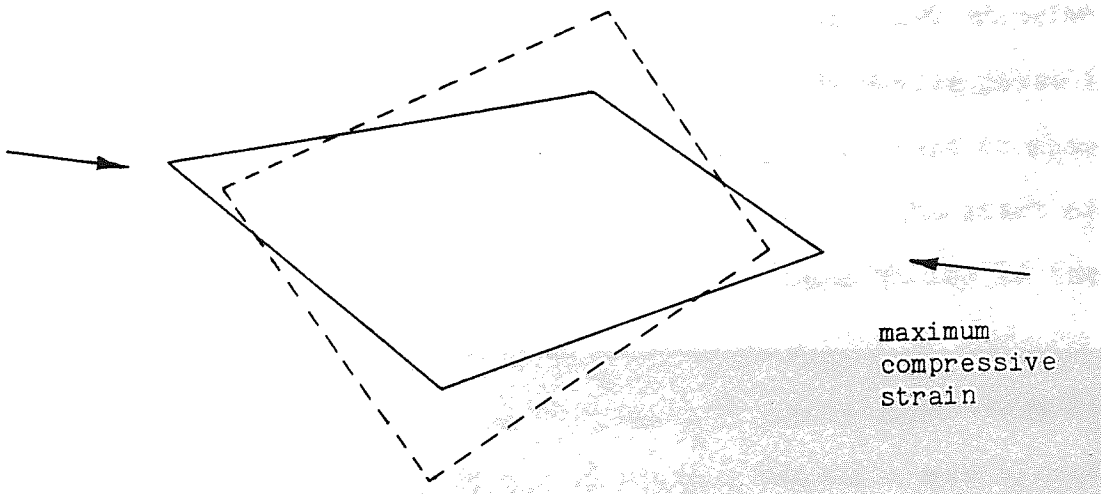

Figure 7.3 Domain deformation

In general it would appear to be reasonable to suggest that the coordination number may be very influential with regard to how much anisotropy can be induced. Assemblies with an initially high average coordination number are generally capable of becoming more anisotropic than those possessing an initially low value for $\bar{n}$. This is simply because assemblies with a high value of $\bar{n}$ can better afford to change branch inclination by contact deletion. As the initial coordination number is a function of initial density for a random assembly, then dense assemblies can become most anisotropic.

For random assemblies the scalar K in equation (7.6) is very sensitive to changes in the coordination number. It is reasonable to assume that contact creation/deletion is uncorrelated to the average branch length, i.e. long branches are not more readily deleted than shorter ones, and vice versa. Consequently the variation of K is linearly related to $\bar{n}/v$. However, volume changes are very small (not greater than 1% for the test reported here) in comparison to the change in $\bar{n}$ and hence K is almost proportional to $\bar{n}$. Figure 7.4 shows how $\bar{n}$ for each particle type (1-5, large to small) varies during phase 1 and phase 2c. The analysis used to derive plotting quantities was restricted to particles whose centres mapped into the inner circular region ($X_c = Y_c = 390$, $R = 180$). Clearly, $\bar{n}$ decreases during phase 1 as contact deletion is dominant and increases during phase 2c when contact creation is dominant. Initial values of $\bar{n}$ at the start of phase 1 are greater than those at the end of phase 2c due to the inability of the assembly to recover the initial number of contacts. This plot is also useful to show that contact creation/deletion is independant of R . For example, if contact deletion was biased towards long branches then the rate of decrease of $\bar{n}$ would be greater for large particles than for small ones. There is no apparent rate of decrease difference between plots. Plots for particle types 1 and 5 could possibly be disregarded from examination as only a few particles of this type mapped into the region.

7.3 RELATIONSHIP BETWEEN STRESS AND STRUCTURE

Oda (1978) has proposed the following relationship between stress and structural anisotropy from tests using specimens of Soma sand.

$$\sigma_1/\sigma_3 = \text{const.}\ S_1/S_3 \qquad (7.8)$$

where S_i gives the areas of the principal planes of the 'fabric

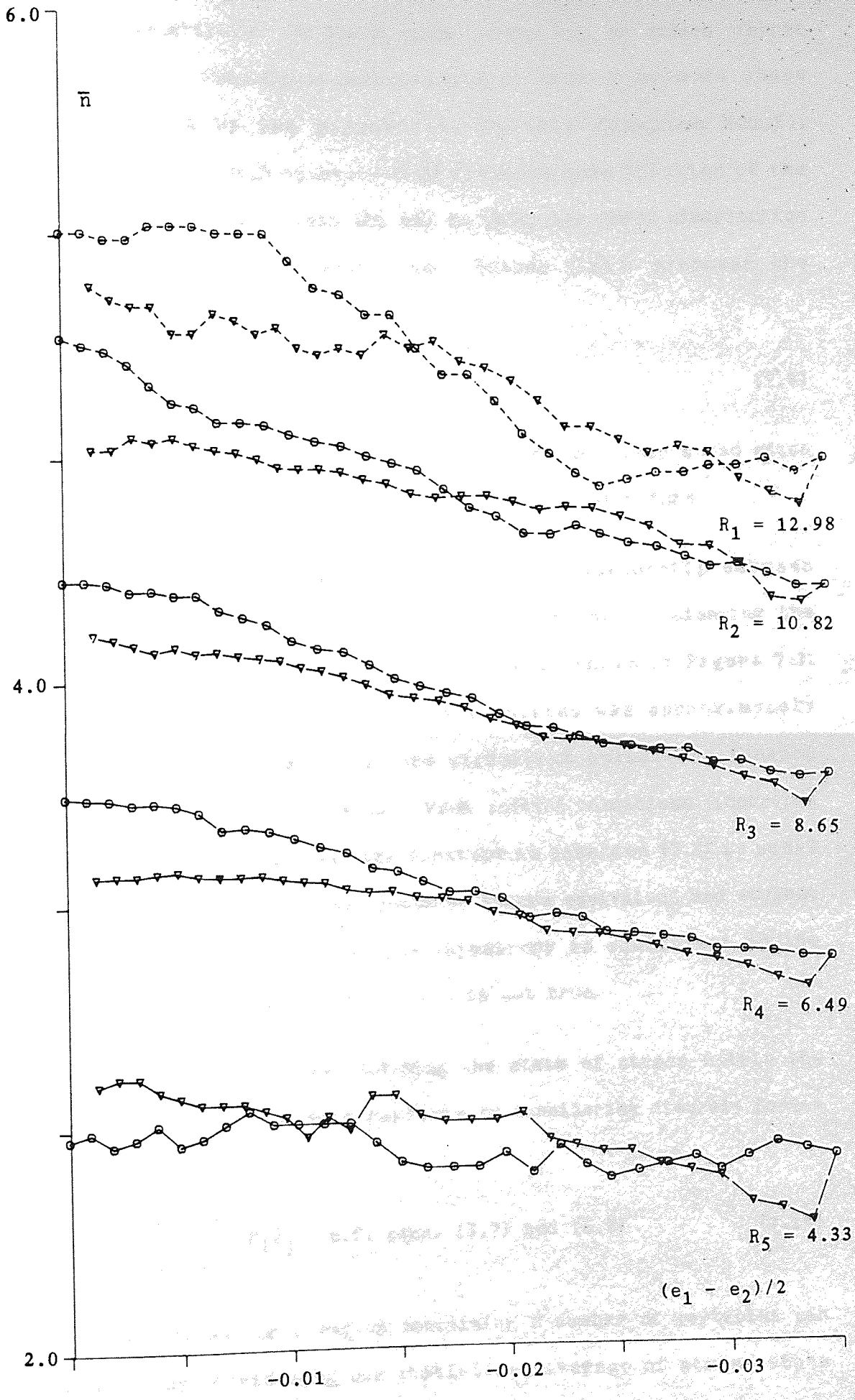

Figure 7.4 Average coordination numbers for particle types

ellipsoid' perpendicular to the x_i axes. Here, the so called 'fabric ellipsoid' is a 3-dimensional distribution of contact normals whose shape is given by the probability density function $E(\alpha,\beta)$. Nevertheless, although equation (7.8) includes some function of the structure it does not explain the way in which the force distribution uses it in order to transmit load. Satake (1982) proposed the relationship

$$\sigma_{ij} = \sigma_{kk}\phi_{ij} \tag{7.9}$$

but concluded that the degree of stress-induced anisotropy would often be much greater than was allowable by the granular structure.

Both the above attempts at providing a relationship between stress and structure are clearly unsatisfactory when considering the evolution of the structural anisotropy tensor shown in Figure 7.2. For the test carried out here the mean stress was approximately constant and the stress tensor and structural anisotropy tensors remained approximately coaxial. From initial conditions (isotropic stress, isotropic structure) the constant in equation (7.8) is equal to unity. Thus, the above relationships become equivalent and suggest that the amount of induced stress anisotropy is equivalent to the amount of structural anisotropy. This is not true.

Returning to basics and defining the state of stress within the volume occupied by a single particle by considering discrete forces acting at the contact points

$$\bar{\sigma}_{ij}{}^{P} = \frac{1}{V^P} \sum_{c=1}^{n} \overset{c}{F}_i \overset{c}{x}_j \quad \text{c.f. eqns. (3.7) and (6.8)} \tag{7.10}$$

The overall stress for a region containing P number of particles can be obtained by considering the statistical average of stress state within the particles weighted to the volume occupied by each particle.

$$\bar{\sigma}_{ij} = \frac{1}{V} \sum_{p=1}^{P} V^p \bar{\sigma}_{ij}^p \qquad (7.11)$$

Combining equations (7.10) and (7.11) the macroscopic stress tensor is defined as

$$\bar{\sigma}_{ij} = \frac{1}{V} \sum_{p=1}^{P} \sum_{c=1}^{n} F_i^c x_j^c \qquad (7.12)$$

noting that for each particle the coordinates x_j are referenced to the particle centre.

As in section 6.4, which dealt with the stress analysis of regular arrays, the total force at a contact can be separated into its normal component (N) and shear component (T) to give

$$\bar{\sigma}_{ij} = \frac{1}{V} \sum_{p=1}^{P} \sum_{c=1}^{n} N_i^c x_j^c + \frac{1}{V} \sum_{p=1}^{P} \sum_{c=1}^{n} T_i^c x_j^c \qquad (7.13)$$

Restricting attention to disc assemblies

$$N_i = -Nn_i \quad T_i = Tm_i \quad x_j = Rn_j \quad m_i = \varepsilon_{ij} n_j \qquad (7.14)$$

where n_i define the contact normal, m_i is a unit vector at -90° to n_i and R is the particle radius. Substituting equations (7.14) into equation (7.13)

$$\bar{\sigma}_{ij} = \frac{-1}{V} \sum_{p=1}^{P} R^p \sum_{c=1}^{n} N^c n_i^c n_j^c + \frac{1}{V} \sum_{p=1}^{P} R^p \sum_{c=1}^{n} T^c m_i^c n_j^c \qquad (7.15)$$

If it is now assumed that R^p is uncorrelated with $N^c n_i^c n_j^c$, and using the relation $2C = P\bar{n}$

$$\bar{\sigma}_{ij} = \frac{-\bar{R}}{V} \sum_{c=1}^{2C} N^c n_i^c n_j^c + \frac{\bar{R}}{V} \sum_{c=1}^{2C} T^c m_i^c n_j^c \qquad (7.16)$$

This assumption has been validated by showing that

$$\frac{\sum_{c=1}^{2C} R^c N^c n_i^c n_j^c}{\sum_{c=1}^{2C} R^c N^c} = \frac{\sum_{c=1}^{2C} N^c n_i^c n_j^c}{\sum_{c=1}^{2C} N^c} \qquad (7.17)$$

for all stored data relating to the inner boundary of the test. This means that the average shape of the distribution of normal forces around each type of particle is identical. Equation (7.16) can be rewritten

$$\bar{\sigma}_{ij} = \frac{-2\bar{R}C}{V} \langle N n_i n_j \rangle + \frac{2\bar{R}C}{V} \langle T m_i n_j \rangle \qquad (7.18)$$

Multiplying top and bottom by $\bar{N}$, which is the average normal force for any considered region gives

$$\bar{\sigma}_{ij} = \frac{-2\bar{R}\bar{N}C}{V} \left\langle \frac{N}{\bar{N}} n_i n_j \right\rangle + \frac{2\bar{R}\bar{N}C}{V} \left\langle \frac{T}{\bar{N}} m_i n_j \right\rangle \qquad (7.19)$$

From equation (7.19) two dimensionless tensors can be defined

$$A_{ij} = \left\langle \frac{N}{\bar{N}} n_i n_j \right\rangle = \frac{\sum_{c=1}^{2C} \hat{N}^c \hat{n}_i^c \hat{n}_j^c}{\sum_{c=1}^{2C} \hat{N}^c} \qquad A_{ii} = 1 \qquad (7.20)$$

and

$$B_{ij} = \left\langle \frac{T}{\bar{N}} m_i n_j \right\rangle = \frac{\sum_{c=1}^{2C} \hat{T}^c \hat{m}_i^c \hat{n}_j^c}{\sum_{c=1}^{2C} \hat{N}^c} \qquad B_{ii} = 0 \qquad (7.21)$$

Equation (7.20) is in fact the second moment of the distribution of contact normals weighted to the magnitude of normal contact forces. Such distributions are displayed in Figures B.64b - B.76b. As m_i are, by definition, related directly to n_i then equation (7.20) and equation (7.21) show how the force distribution uses the structure. Figure 7.5 shows the evolution of the weighted structural anisotropy tensor A_{ij} which was calculated using equation (7.2) for only those contact points which mapped into the inner circular boundary. If Figures 7.2 and 7.5 are compared then it can be seen that ϕ_{ij} is not linearly related to A_{ij}. In fact normal contact forces must rearrange their overall direction quickly in order to transmit the required load and hence the structure is utilised in the most efficient way. High normal forces therefore choose contact inclinations that align in the

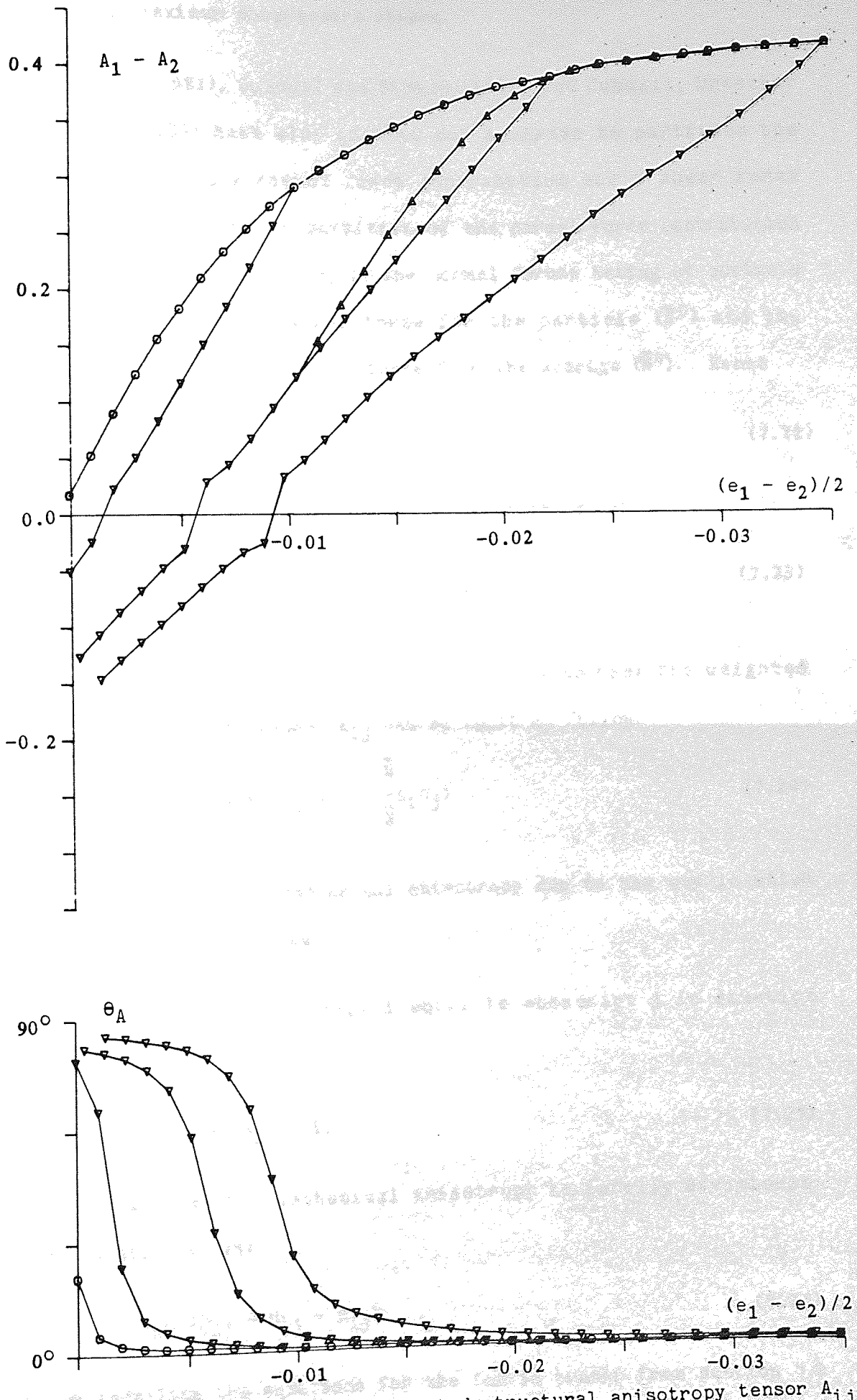

Figure 7.5 Evolution of the weighted structural anisotropy tensor A_{ij}

direction of maximum compressive stress.

Cundall (1981), Cundall and Strack (1982) and Cundall, Drescher and Strack (1982) have also carried out analyses to partition the stress tensor into a normal force contribution and a shear force contribution. A further partition of the normal force contribution was suggested. This was to split the normal forces acting at contacts (N^c) into the average normal force for the particle ($\bar{N}^p$) and the variation of the normal contact force from the average ($\tilde{N}^c$). Hence

$$N^c = \bar{N}^p + \tilde{N}^c \tag{7.22}$$

Substituting equation (7.22) into equation (7.19) gives

$$\sigma_{ij} = \frac{-2R\bar{N}C}{V} \left[\langle n_i n_j \rangle + \langle \frac{\tilde{N}}{\bar{N}} -n_i n_j \rangle - \langle \frac{T}{\bar{N}} -m_i n_j \rangle \right] \tag{7.23}$$

Introducing a new tensor C_{ij} then it can be seen that the weighted structural anisotropy tensor A_{ij} can be split as follows

$$A_{ij} = \phi_{ij} + C_{ij} = \langle n_i n_j \rangle + \langle \frac{\tilde{N}}{\bar{N}} -n_i n_j \rangle \tag{7.24}$$

B_{ij} and C_{ij} define the mechanical anisotropy due to the way in which forces utilise the structure.

Now by setting subscript i equal to subscript j in equation (7.23)

$$\bar{\sigma}_{ii} = \frac{-2R\bar{N}C}{V} \quad \text{as } \phi_{ii} = 1, \tag{7.25}$$

which shows that the mechanical anisotropy is totally deviatoric. Using equation (7.25)

$$\bar{\sigma}_{ij} = \sigma_{kk} (\phi_{ij} + C_{ij} - B_{ij}) \tag{7.26}$$

and by recalling the equations for the fabric tensor from section 7.2 it can be shown that

$$\bar{\sigma}_{kk} = \bar{N}F_{kk} = \bar{N}K \tag{7.27}$$

This shows that the mean stress is directly related to the scalar part of the fabric tensor and is a measure of force magnitude. It was earlier pointed out that K is most sensitive to the coordination number $\bar{n}$, and hence, $\bar{n}\bar{N}$ will remain approximately constant for a constant mean stress.

By defining the implied stress partitions as

$$\bar{\sigma}_{ij}{}^{\bar{N}} = \bar{\sigma}_{kk}\,\phi_{ij} \tag{7.28a}$$

$$\bar{\sigma}_{ij}{}^{\tilde{N}} = \bar{\sigma}_{kk}\,C_{ij} \tag{7.28b}$$

$$\bar{\sigma}_{ij}{}^{N} = \bar{\sigma}_{ij}{}^{\bar{N}} + \bar{\sigma}_{ij}{}^{\tilde{N}} \tag{7.28c}$$

$$\bar{\sigma}_{ij}{}^{T} = -\bar{\sigma}_{kk}\,B_{ij} \tag{7.28d}$$

$$\bar{\sigma}_{ij} = \bar{\sigma}_{ij}{}^{N} + \bar{\sigma}_{ij}{}^{T} \tag{7.28e}$$

then Figures 7.2 and 7.5 should be equivalent to similar plots of $\bar{\sigma}_{ij}{}^{\bar{N}}$ and $\bar{\sigma}_{ij}{}^{N}$, normalised by $\bar{\sigma}_{kk}$, respectively.

All the data required to calculate the stress tensor partitions was available during testing and hence it was possible to monitor the evolution of each partition. Cundall (1981), Cundall and Strack (1982) and Cundall, Drescher and Strack (1982) give some results showing the evolution of these partitions for a similar simulation test to that reported here. The results are far from similar to those which will be presented later in this section. To ensure that the reader has confidence in results reported here, the numerical algorithm embodied within the computer program is described in Appendix D. This algorithm computes partitions within a circular boundary of radius D with centre coordinates X_i.

Figure 7.6 shows plots which represent $\bar{\sigma}_{ij}$, $\bar{\sigma}_{ij}{}^{N}$ and $\bar{\sigma}_{ij}{}^{T}$ normalised to $\bar{\sigma}_{kk}$ for phase 1. Figure 7.7 and 7.8 represent plots of

the same quantities for phase 2 and phase 3 respectively. In these plots earlier phases are shown by dashed lines. Figures 7.9, 7.10 and 7.11 are similar to the above and show the evolution of the two partitions $\bar{\sigma}_{ij}^{\bar{N}}$ and $\bar{\sigma}_{ij}^{\tilde{N}}$. The evolution of $\bar{\sigma}_{ij}^{N}$ is repeated on these plots for comparison.

From plots in Figures 7.6 - 7.11 it can be seen that all tensors are approximately coaxial. Observations on evolution of the deviatoric components show that the normal force contribution to the stress tensor is far more significant than the tangential force contribution. The representation of the deviatoric components of $\bar{\sigma}_{ij}^{N}$ closely resemble those plotted in Figure 7.5 for A_{ij}. Equivalent plots for $\bar{\sigma}_{ij}^{\bar{N}}$ closely resemble those shown in Figure 7.2 for ϕ_{ij}. This proves that the partitioning was carried out correctly within the program. Observations on the evolution of $\bar{\sigma}_{ij}^{T}$ show that it offers only a small contribution to the overall stress tensor. However, although the contribution is small it is quickly generated or reversed during initial loading, unloading or reloading respectively. In addition it also permits $\bar{\sigma}_{ij}^{\tilde{N}}$ to reduce during unloading or reloading without major structural changes. The deviatoric component of $\bar{\sigma}_{ij}^{T}$ is directly related to the force obliquity at contacts and therefore its magnitude could possibly be related to the number of contacts where slip is occurring. By observing Figures 5.6 - 5.8 it can be seen that the number of contacts that experience slip, after initial shear displacements have settled, is related to the total number of contacts (this has been postulated in section 5.3.1). This suggests that the number of slipping contacts reduces as the total contact number falls. If the number of slipping contacts can be considered a measure of obliquity then the evolution of $\bar{\sigma}_{ij}^{T}$ plotted here tends to support the above postulate. Finally Figure 5.8 indicates that there are never more than 25% of contacts slipping. Figures B.64d - B.76d show that

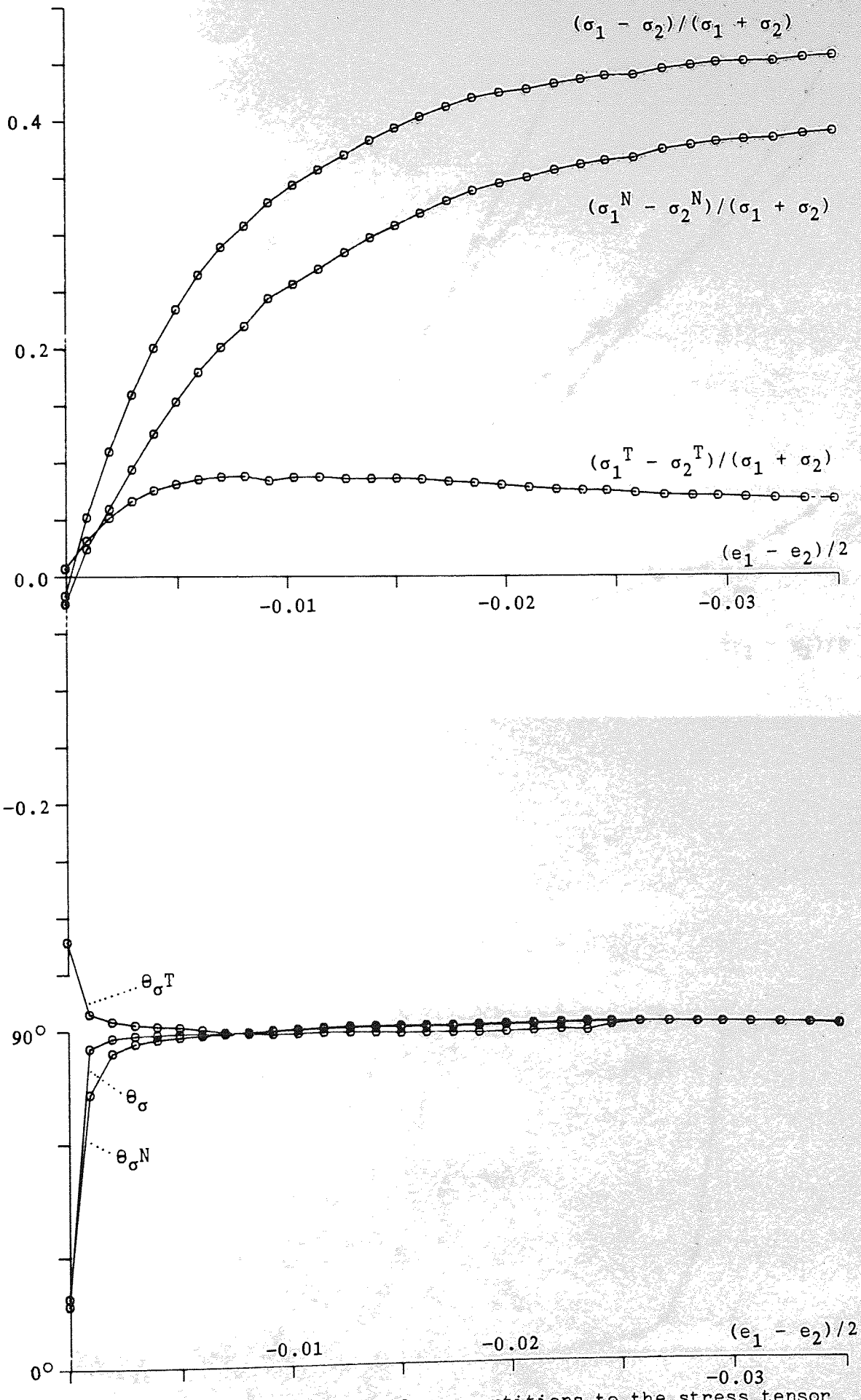

Figure 7.6 The normal and shear force partitions to the stress tensor (phase 1)

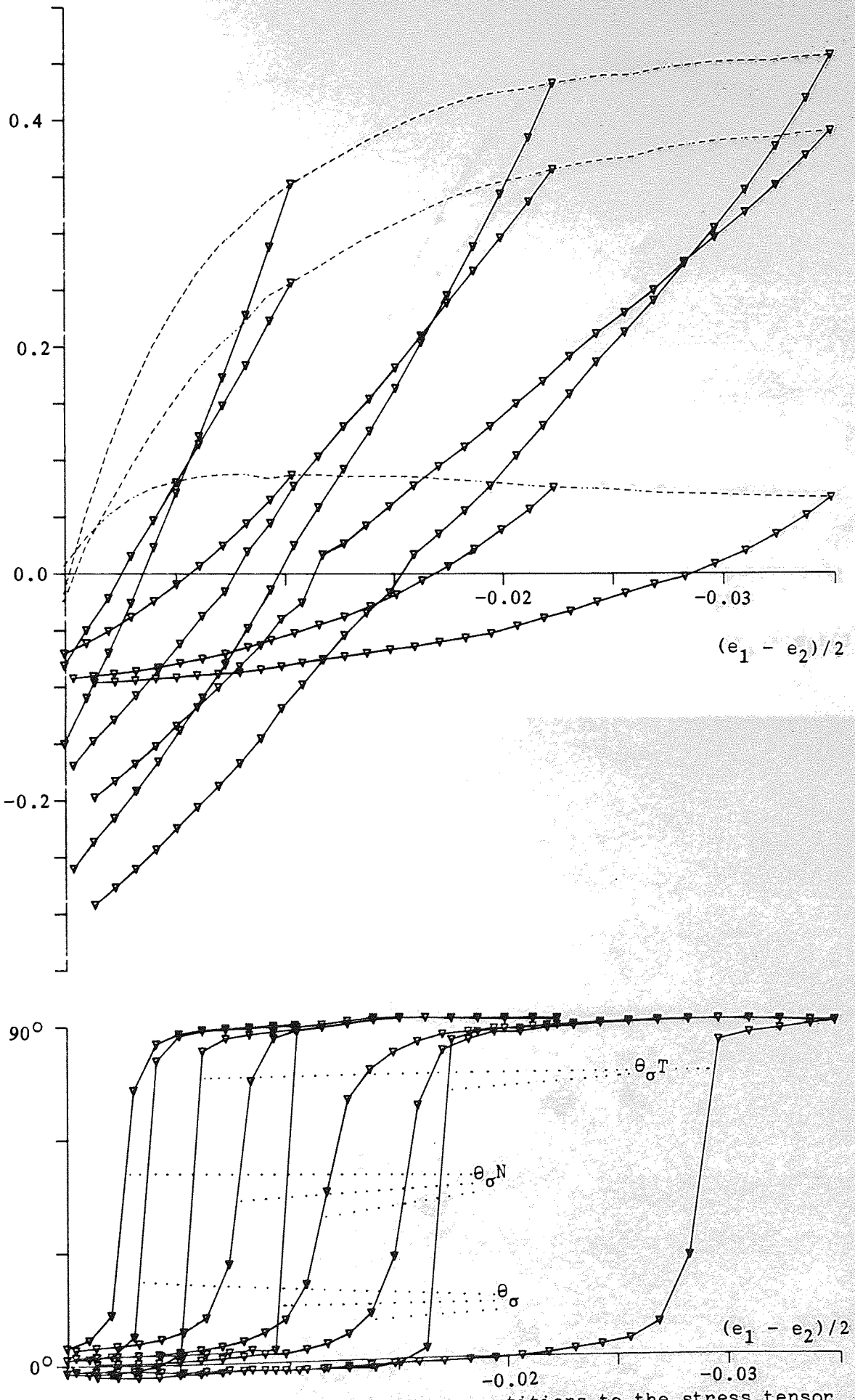

Figure 7.7 The normal and shear force partitions to the stress tensor (phase 2)

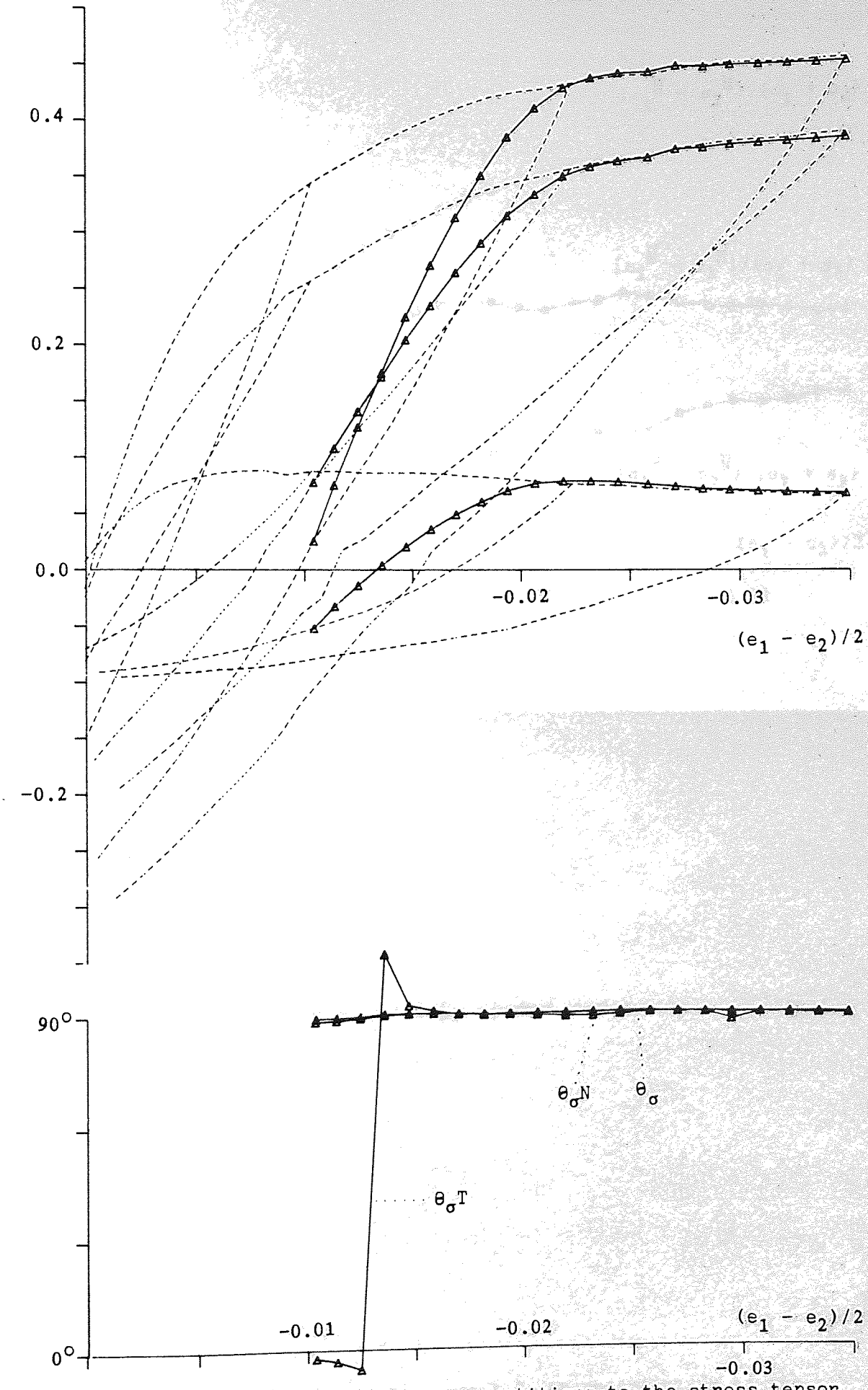

Figure 7.8 The normal and shear force partitions to the stress tensor (phase 3)

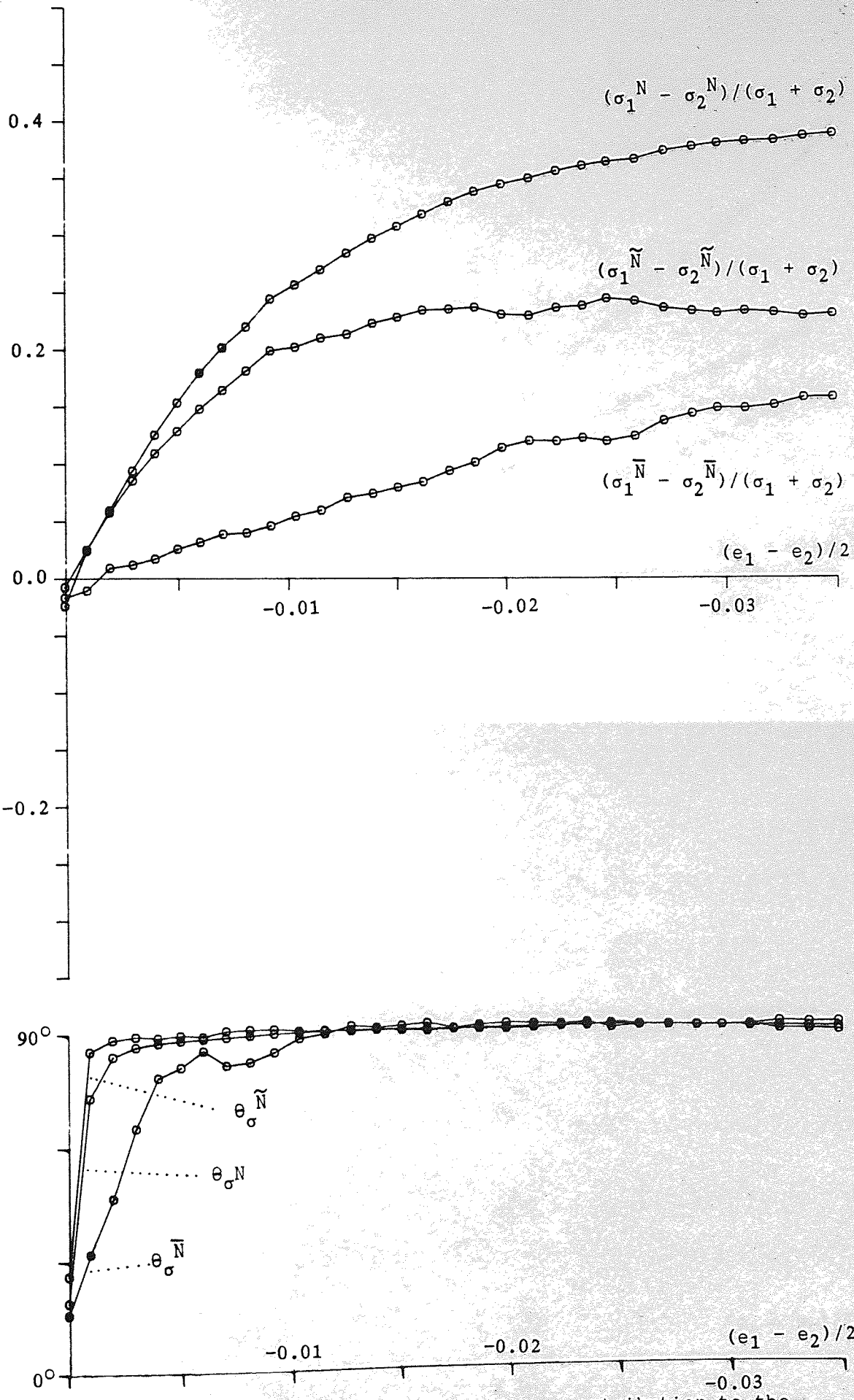

Figure 7.9 Sub-partitions of the normal force contribution to the stress tensor (phase 1)

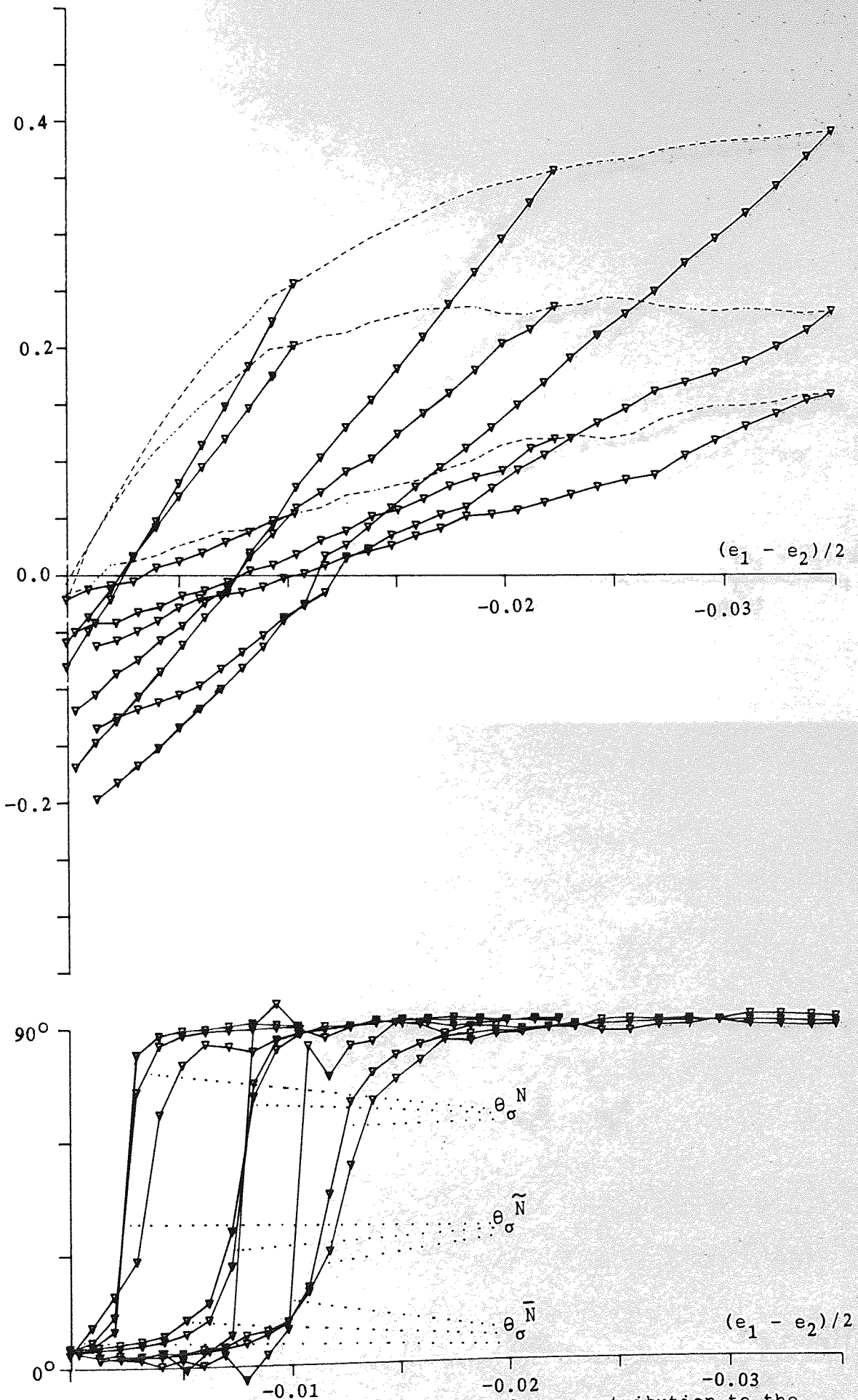

Figure 7.10 Sub-partitions of the normal force contribution to the stress tensor (phase 2)

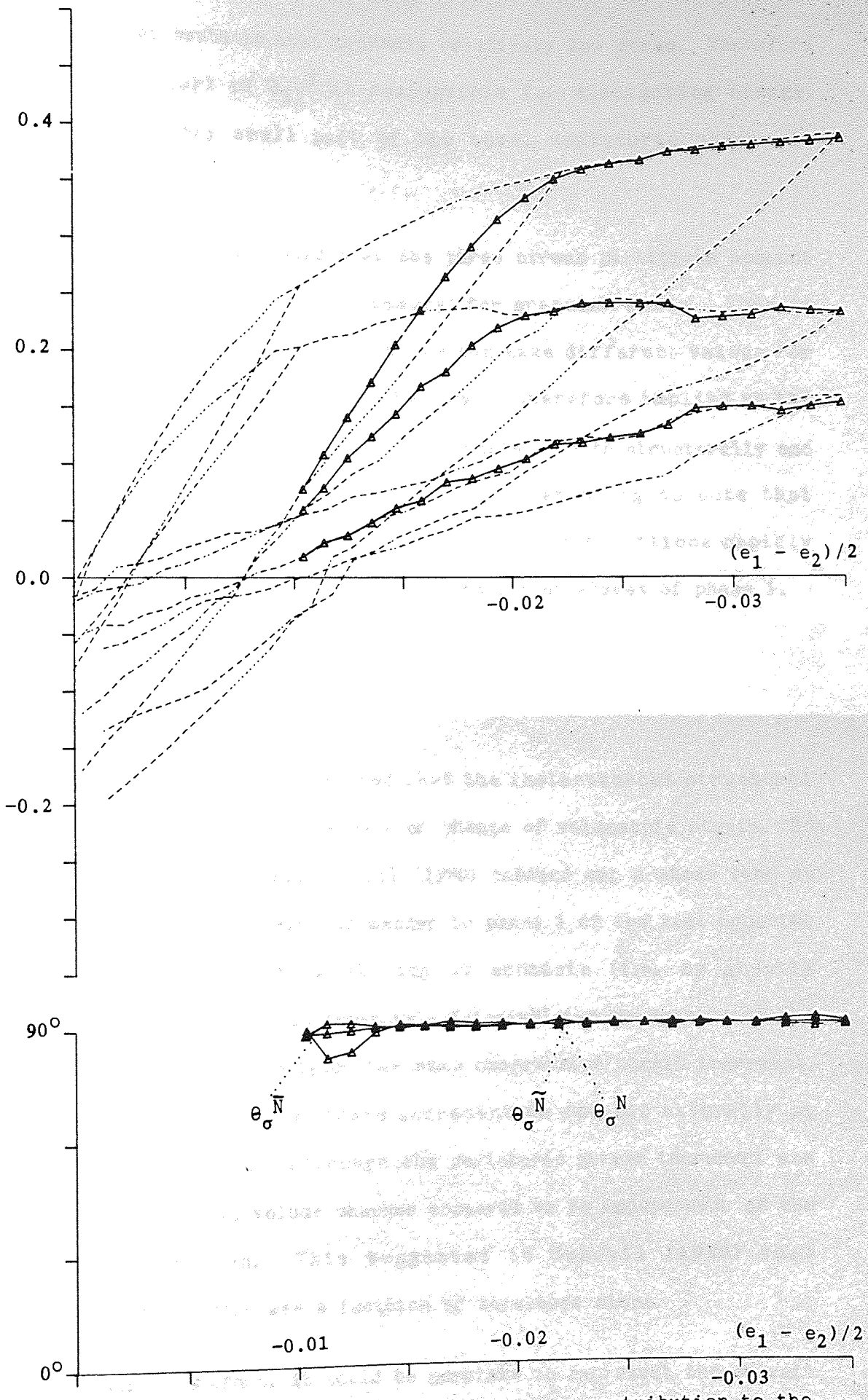

Figure 7.11 Sub-partitions of the normal force contribution to the stress tensor (phase 3)

slip occurs at contacts that transmit relatively low force. Therefore only a small part of $\bar{\sigma}_{ij}^{T}$ is responsible for dissipating energy. Hence only a very small part of the total deviatoric stress is dissipative.

Cundall (1981) has said that the three stress partitions account for the so called property of 'memory' for granular media. This is based on the fact that the partitions can take different values for the same overall stress tensor. Memory is therefore implied by the stress partitions as their evolution reflects both structurally and mechanically induced anisotropy. It is interesting to note that during phase 3 the deviatoric components of the partitions rapidly change to become equal to those during the latter stages of phase 1.

7.4 STRAIN-RATE AND STRUCTURE

Cundall (1980) has suggested that the instantaneous structural domain shape accounts for the rate of change of volumetric strain. To strengthen this hypothesis Cundall (1980) carried out a shear test on a 68 disc assembly in a similar manner to phase 1 of the test reported here. Then by preventing sliding at contacts (i.e. by greatly increasing the allowable interparticle friction) two increments of the test were repeated by applying the same compressive strain increment. This allowed the tensile strain increment to develop naturally at constant mean stress. Although the deviatoric stress increment was substantially higher, volume changes appeared to be independent of the force distribution. This suggested to Cundall (1980) that instantaneous dilation was a function of structure alone.

Perhaps, therefore, it could be possible to represent the overall deformation of a region of granular material by the deformation of a

single domain whose shape is given by the structural anisotropy tensor ϕ_{ij}. If it is assumed that a four-sided regular domain is capable of representing the overall structure then Thornton (1977), Cundall (1980) and Chapter 6 have proposed equations that can predict the domain dilation. Recalling equation (6.6) from the theory of regular arrays

$$\dot{e}_{ij} = \dot{\Delta}m_i/Rn_j \quad (= 0, \text{ if } i \neq j) \tag{7.29}$$

Because $\dot{e}_{ij}$ and ϕ_{ij} are approximately coaxial

$$\dot{e}_1/\dot{e}_2 = -n_2^2/n_1^2 = -\phi_2/\phi_2 \tag{7.30}$$

By knowing the evolution of the structural anisotropy tensor it is possible to predict an increment Δe_2 for a given increment Δe_1

$$\Delta e_2 = -\Delta e_1 \, (\phi_1^{t_1} + \phi_1^{t_2})/(\phi_2^{t_1} + \phi_2^{t_2}) \tag{7.31}$$

Using equation (7.31) a plot of $(e_1 + e_2)/2$ against a known deviatoric strain $(e_1 - e_2)/2$ has been produced to predict the volume changes during phase 1 of the 1000 disc test. This is shown in Figure 7.12 together with the actual relationship which was shown earlier in Figure 4.7b. It can be seen that although equation (7.31) correctly predicts the trend it underestimates the volumetric expansion. A detailed analysis, similar to that carried out for the stress tensor, is required for the strain-rate tensor. This new analysis has just been performed and details are given below.

Returning once again to basics the velocity gradient tensor for a single domain can be defined as

$$\dot{\underline{d}}_{ij}^{d} = \frac{1}{V^d} \sum_{s=1}^{S} \overset{s}{u}_i \overset{s}{v}_j \overset{s}{L} \quad \text{(c.f. eqn. (6.5))} \tag{7.32}$$

where V^d gives the domain volume, v_j give the direction of the outward

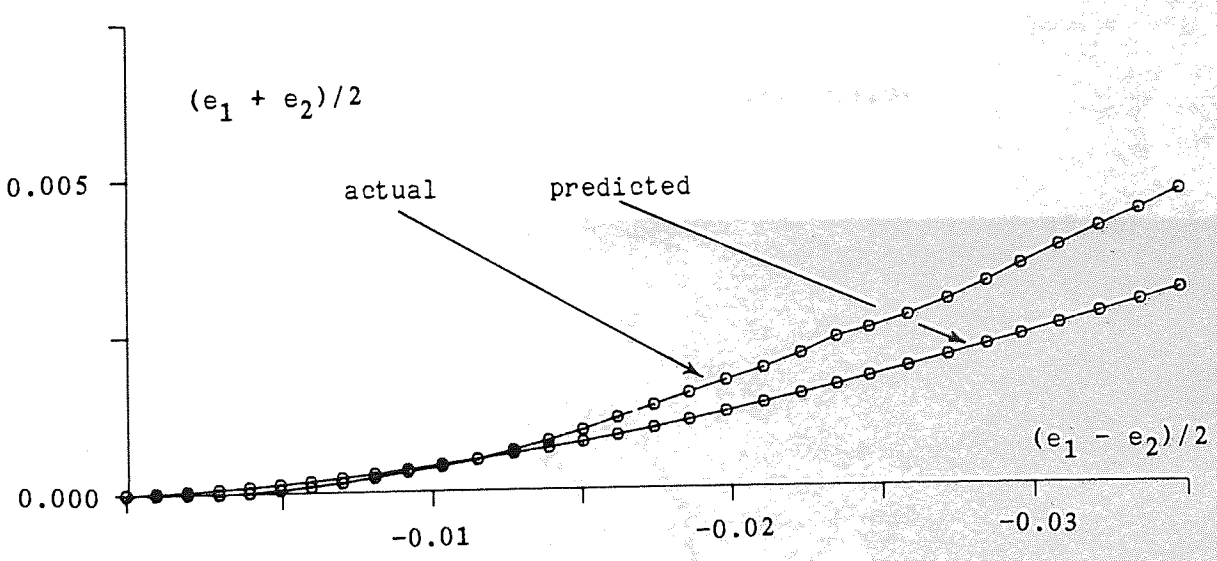

Figure 7.12 Actual and predicted volumetric expansions

unit normal to domain sides of length L and u_i give the average branch velocity, i.e. the velocity of the mid point of side L. If the summation over the domain branches is performed in an anti-clockwise manner then $v_j = m_j$, where $m_j = \varepsilon_{ji} n_i$ (defined as in section 7.3). Then by partitioning u_i into its normal (U_N) and parallel (U_P) to the branch direction (see Figure 7.13).

$$\dot{\bar{d}}_{ij}^{d} = \frac{1}{V^d} \sum_{s=1}^{S} L^s \left(U_N^s m_i^s m_j^s + U_P^s n_i^s m_j^s\right) \tag{7.33}$$

The overall velocity gradient tensor for a region containing many domains is given by

$$\dot{\bar{d}}_{ij} = \frac{1}{V} \sum_{d=1}^{D} \dot{\bar{d}}_{ij}^{d} V^d \tag{7.34}$$

Substituting equation (7.33) into equation (7.34) yields

$$\dot{\bar{d}}_{ij} = \frac{1}{V} \sum_{d=1}^{D} \sum_{s=1}^{S} L^s \left(U_N^s m_i^s m_j^s + U_P^s n_i^s m_j^s\right) \tag{7.35}$$

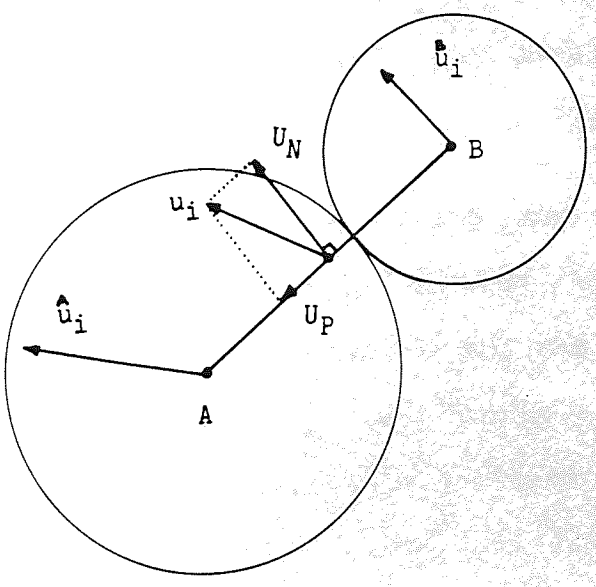

Figure 7.13 Normal and parallel components of branch velocity

The volumetric strain rate $\dot{e}_{ii} = \dot{d}_{ii}$ and hence

$$\dot{e}_{ii} = \frac{1}{V} \sum_{d=1}^{D} \sum_{s=1}^{S} L^{s} U_{N}^{s} \qquad (7.36)$$

and by assuming L is uncorrelated with U_N then

$$\dot{e}_{ii} = \frac{D\bar{S}\bar{L}\bar{U}_N}{V} \qquad (7.37)$$

The average branch length $\bar{L} = 2\bar{R}$ and using equation (5.3) $2C = D\bar{S}$ and therefore

$$\dot{e}_{ii} = \frac{4\bar{R}C}{V} \bar{U}_N \qquad (7.38)$$

and by comparing the equation for the fabric tensor, equation (7.5), with equation (7.38) the following relationship is noted

$$\dot{e}_{ii} = 2K\bar{U}_N = KU \qquad (7.39)$$

where U is a measure of a branch translation. As explained earlier, K is approximately linearly proportional to $\bar{n}$ and therefore $\dot{e}_{ii}$ becomes partly dependent on the coordination number. K is always positive which implies that expansion occurs when U is positive and contraction when U is negative.

At present there are no algorithms incorporated within 'Ball' to quantify the above analysis, and therefore, no results are available for presentation. Nevertheless the form of the equations above does suggest that the strain-rate tensor is related to a measure of structural anisotropy weighted to branch velocities.

8 CONCLUDING REMARKS

The Distinct Element Method is a most powerful tool, and testing with 'Ball' allows accurate and undisturbed measurements to be made that would be very difficult and tedious to make in physical experiments, e.g. the stress partitions (Chapter 7) extracted from test data could not have been produced from physical tests because of time constraints. Easy measurement and graphical representation of results mean that computational algorithms can be written to search for new microscopic mechanisms. These new algorithms can be thought of as enhancements to the numerical apparatus.

By making use of numerical simulation accurate results have been produced from the 1000 disc test reported in Chapter 4. From graphical output observations on internal microscopic mechanisms of deformation have been made. A detailed description of how forces are transmitted through the assembly is given in Chapter 5 along with a qualitative description of granular fabric and an explanation for induced anisotropy. The interrelation of observed mechanisms has also been discussed.

In Chapter 6 a mathematical theory of plasticity has been presented which was developed by considering the load deformation at the interparticle contacts within regular arrays of spheres. It has been noted, however, that this theory does not account for all the mechanisms that can occur in random assemblies. The theory could, nevertheless, form a valid base for the future development of more realistic microstructural soil plasticity theories.

A definition of granular fabric for random assemblies has been given in Chapter 7. From stress analyses it has been shown that it is

possible to partition the macroscopic stress tensor. Each partition plays a very definite role and together they show how the force distribution utilises the structure. An analysis to define the rate of volume change has also been presented which shows how the velocity distribution uses the structure.

Only one full scale test has been carried out here and therefore many more tests are required before a full understanding of deformation is obtained for even the idealised media considered here. These future tests could consider, varying the physical properties, different particle gradings, loose assemblies, and boundary servo control could be adjusted to produce constant volume conditions or to emulate cyclic loading and stress rotation conditions by progressively varying the desired stress tensor.

The above future work requires no adjustments to be made to the existing version of 'Ball'. The apparatus could, however, be modified to allow variable particle shape and to allow the extension into 3-dimensional testing. These modifications are feasible but require a complete re-think on how test results would be graphically output. Testing using the Distinct Element Method incorporated in 'Ball' is at present based upon simple assumptions regarding particle interactions. Hence results will not necessarily apply to sand etc. Providing the numerical apparatus was enhanced to accommodate testing 3-dimensional assemblies of irregular shaped particles then it is only the contact laws that require examination in order for the apparatus to be used to simulate the behaviour of naturally occuring granular media. Further developments in this direction require a literature search and further research on the fundamental behaviour of interparticle compliance. This work would give a better understanding of contact friction, contact cohesion, contact creep and particle crushing. In fact, a

study of this nature would attempt to reveal the deformation characteristics of interacting solids. Indeed, if solids can be thought of as lots of smaller particles bonded together, then Ball may be a very useful tool to investigate particle deformation. Tests similar to the Brazillian Test could be conducted on particle assemblies that have various simplified contact cohesion and creep laws. This system of one particle made of many others would be a complex system in its own right. Global particle force-displacements could be monitored as well as microscopic particle crack propagations etc.

There are of course innumerable problems regarding material behaviour where The Distinct Element Method could be used as an aid for study. These include even complex composite media like concrete and fast moving fluid flow of particles in transport. The method awaits only enthusiasm and increased computational support.

APPENDIX A

A qualitative and quantitative validation of the Distinct Element Method (Chapter 2) and the program 'Ball' (Chapter 3) has been carried out by comparing the results obtained in a test on a regular assembly to those predicted by the theory of regular arrays (Chapter 6). The initial structural arrangement of the assembly is shown in Figure A.1.

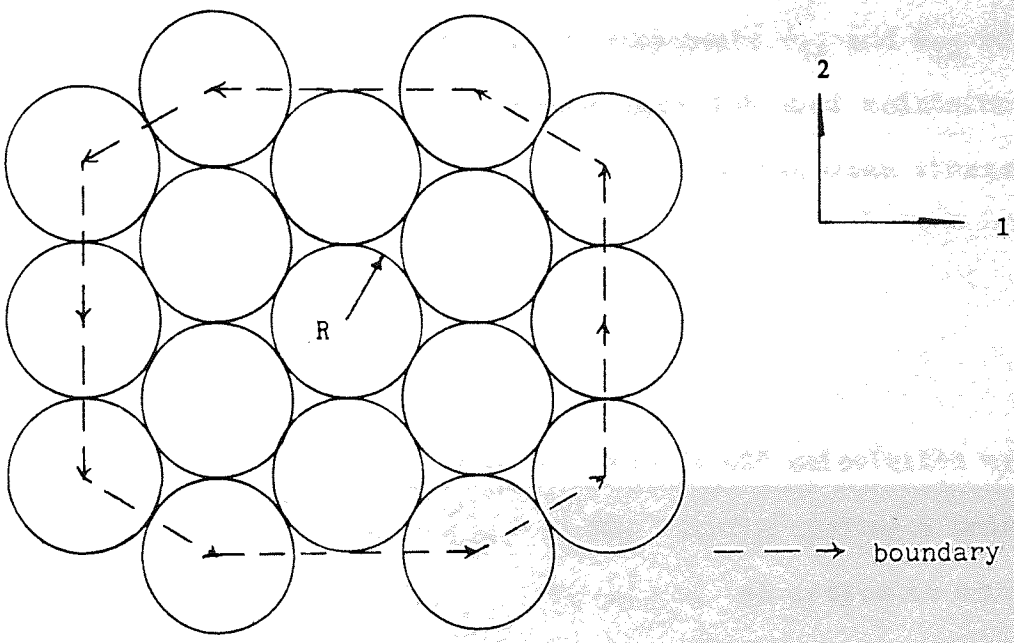

Figure A.1 The initial assembly

The dense packed assembly consists of 17 discs, the quantities describing the physical properties of the particles are listed below.

QUANTITY	VALUE
RADIUS (R)	70
DENSITY (ρ)	2000
FRICTION (μ)	0.4
NORMAL STIFFNESS (K_n)	1.0E9
SHEAR STIFFNESS (K_s)	1.0E9

The assembly was generated manually and the boundary automatically located. The following parameters were then set

FRACTION OF CRITICAL DAMPING	0.05
FRACTION OF CRITICAL TIMESTEP	0.2
GAIN OF SERVOMECHANISM (G)	0.1E-7

For the purpose of consolidation a variation on the general type of servo-controlled boundary, described by equation (3.8), was used. This form of MODE 3 attempts to adjust components $\dot{e}_{11}$ and $\dot{e}_{22}$ of the strain-rate tensor such that the stress path followed maintains the desired values of $\overset{*}{\sigma}_{11}$ and $\overset{*}{\sigma}_{22}$ and hence the desired mean stress $\overset{*}{\sigma}_0$, i.e.

$$\dot{e}_{11}^{t+\Delta t} = \dot{e}_{11}^{t} + G\,(\overset{*}{\sigma}_{11}^{t} - \bar{\sigma}_{11}^{t})$$

$$\dot{e}_{22}^{t+\Delta t} = \dot{e}_{22}^{t} + G\,(\overset{*}{\sigma}_{22}^{t} - \bar{\sigma}_{22}^{t})$$

e_{ij} was initially set to zero and then 50,000 calculation cycles were performed to raise $\overset{*}{\sigma}_{11} = \overset{*}{\sigma}_{22} = -1.0E6$. During cycling a printout of $\dot{e}_{ij}$, $\overset{*}{\sigma}_{ij}$ and $\bar{\sigma}_{ij}$ was given at intervals of 100 cycles to monitor the performance of the servo and to check for assembly oscillations which would be reflected in $\dot{e}_{ij}$. After completing the required number of cycles a printout of the memory map was given. From this it could be seen that particle velocities were low and that the assembly was in almost perfect equilibrium. All normal contact forces were equal and the force obliquity at contacts was zero. A printout of $\dot{e}_{ij}$, Δe_{ij}, $\overset{*}{\sigma}_{ij}$ and $\bar{\sigma}_{ij}$ was given, which revealed that $\overset{*}{\sigma}_{ij} = \bar{\sigma}_{ij}$, and that all printed tensors were isotropic.

Shearing of the assembly was then achieved by using a further form of MODE 3. This form maintains constant mean stress $\overset{*}{\sigma}_0$ whilst shearing the sample keeping $\dot{e}_{11}$ constant and adjusting $\dot{e}_{22}$ i.e.

$$\dot{e}_{22}^{t+\Delta t} = \dot{e}_{22}^{t} + G\,(\overset{*}{\sigma}_{0}^{t} - \bar{\sigma}_{0}^{t})$$

where the value of G remained unchanged.

Before cycling $\dot{e}_{11}$ was set so that it would increase e_{11} by 1% every 20,000 cycles. The minor principal strain rate, $\dot{e}_{22}$ was then initialised as $-3.\dot{e}_{11}$, a figure which is strictly applicable to regular arrays of rigid discs, in an attempt to obtain a quick start-up and thereby reduce transmission time. Then, 200,000 cycles were performed during which, at every 20,000 cycle count, a printout of the memory map and relevant tensors was given, and in addition a plot of the particles, boundary and force distribution was obtained. From this information it was found that the assembly was close to equilibrium and that contact forces and obliquities were equal throughout the test. It was also observed that $\overset{*}{\sigma}_0 = \bar{\sigma}_0$ and that $\overset{*}{\sigma}_{ij}$ remained coaxial with $\dot{e}_{ij}$ and therefore e_{ij}.

From the memory maps, printed during the test, calculations were made to obtain the inclination of branches joining particle centres. These were carried out in order to verify that the assembly remained, throughout the test, as a regular packing. The theory of regular arrays (Chapter 6) was then applied to predict the instantaneous stresses and strains from the extracted information on array structure (n_i). A plot of the numerical and predicted stress-strain curves is shown in Figure A.2 in order to quantitatively validate the Distinct Element Method and 'Ball'. From this it can be seen that the deviatoric stress against deviatoric strain curves are in perfect agreement. Discrepancies, however, occur in the curves of volumetric strain against deviatoric strain in that the regular array theory predicts a slightly higher increase in volume during deformation. This is explained by the fact that the regular array theory makes the assumption that the particles are rigid and hence the elastic displacements would affect the inclination of contact normals, and

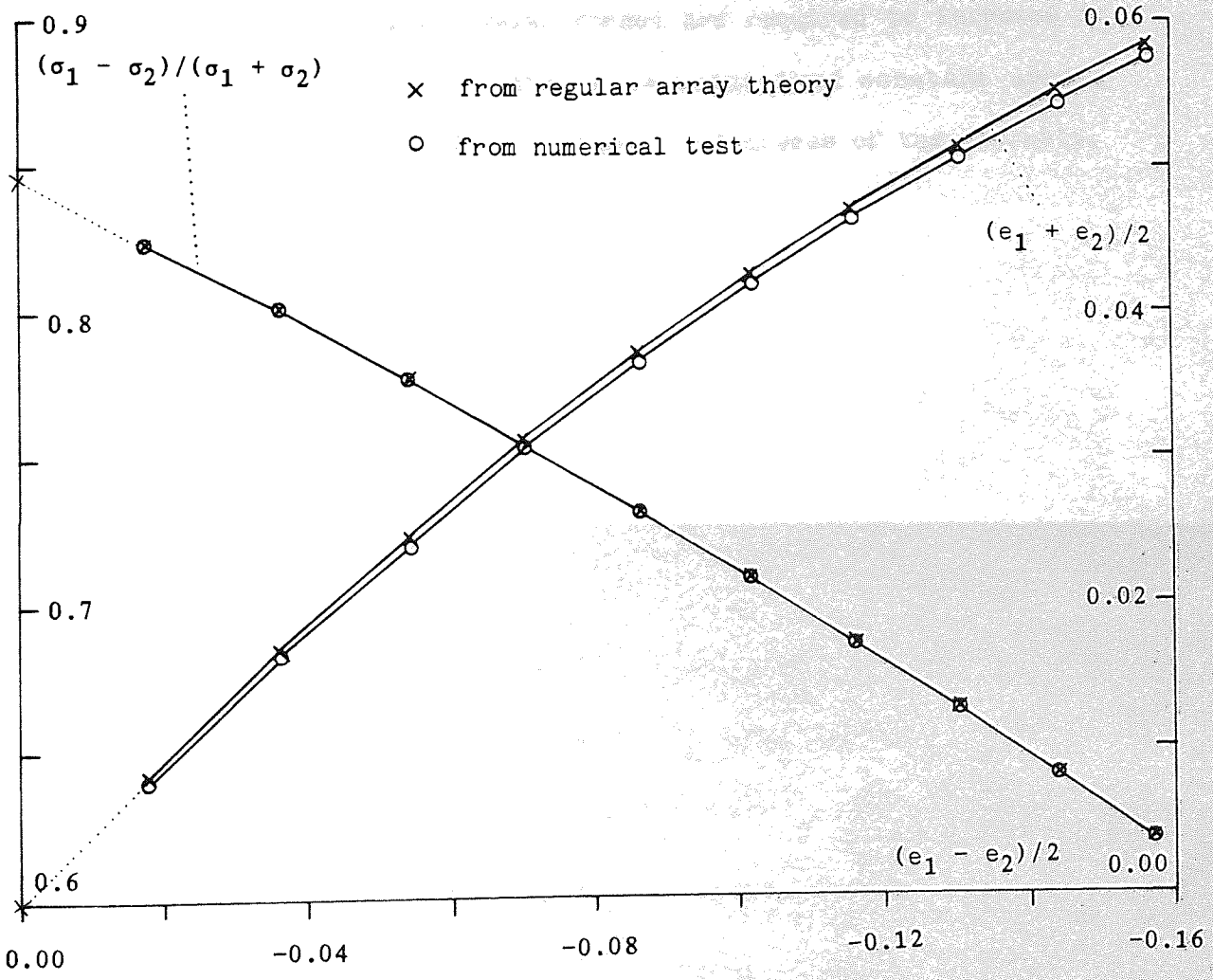

Figure A.2 Stress-strain plots during the shearing of the consolidated assembly

normal contact displacements would shorten the length of the branch joining particle centres. However, the shear elastic displacement has already been taken into account as contact inclinations were obtained from the memory maps. The discrepancies occurring in the plots are therefore due to the change in branch length which has not been accounted for. Hence, the difference between the numerical and calculated value of volumetric strain is due to the increase in normal forces during deformation. These forces are required to increase in order that the desired mean stress be maintained constant during contact deletion, and during the volumetric increase of the assembly.

APPENDIX B

During the 1000 disc test, reported in Chapter 4, the memory map holding information on particle and contact data (array A(I)) was permanently stored on magnetic tape at intervals of 2000 calculation cycles throughout phase 1 and phase 2c. Figure B.1, has been reproduced from Figure 4.7 to show, clearly, numbered points which locate the stored data with respect to the test stress/strain curves.

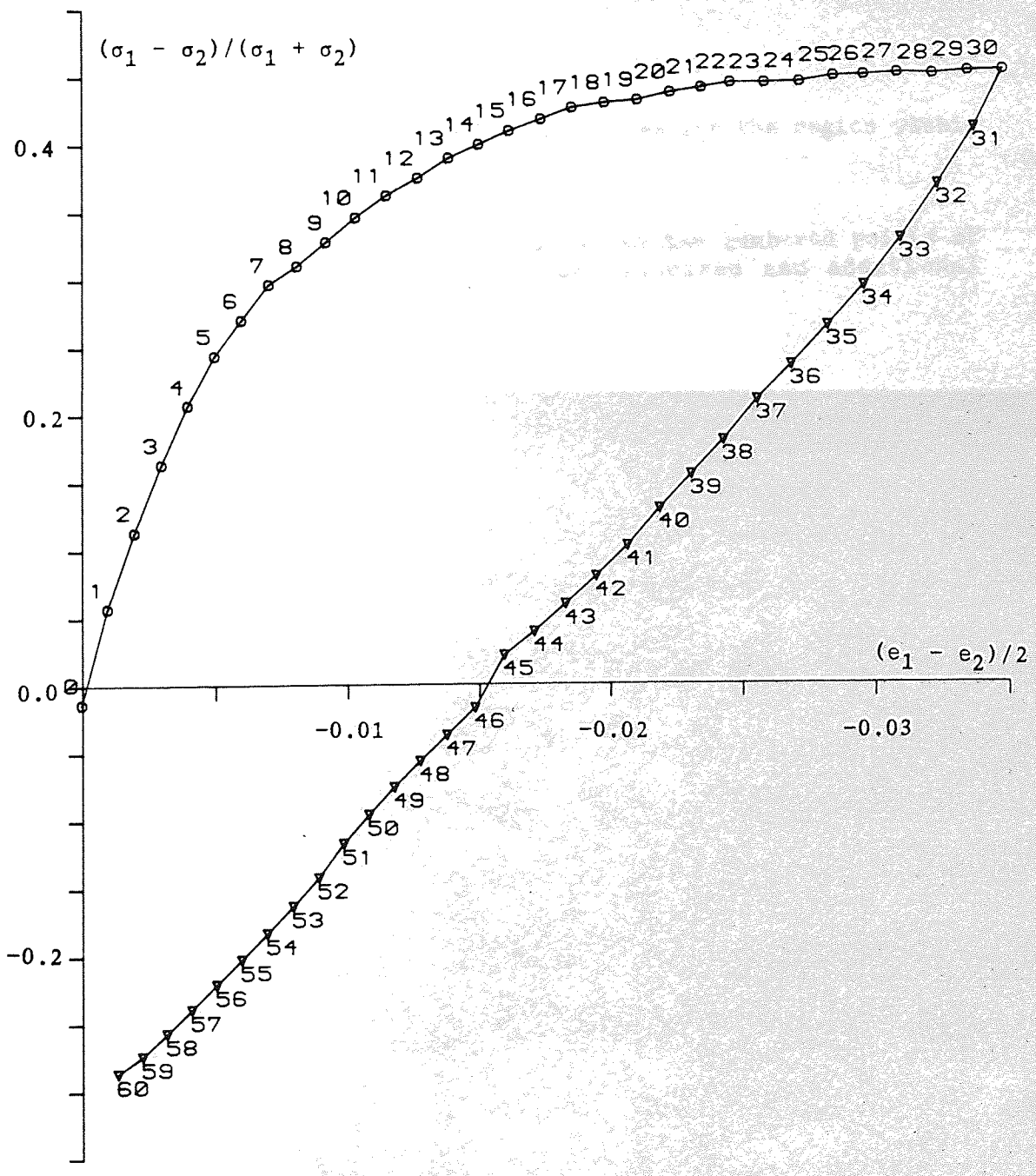

Figure B.1 Numbered points locating the permanently stored data

From the stored data the following plots have been produced

Figures B.2 - B.14
Discs, boundary, boxes and disc radius vectors (plot options 1,2,3 and 4)

Figures B.15 - B.27
Discs and contact forces (plot options 1 and 5)

Figures B.28 - B.39
Discs and linear disc centroid velocity vectors (plot options 1 and 6)

Figures B.40 - B.51
Discs, slip and rotation increments (plot options 1, 7 and 8)

Figures B.52 - B.63
Structure plots (plot option 9)

Figures B.64 - B.76
Plots giving information on contacts and forces for the region within the inner circular boundary

For all the above plots reference is given to the numbered points of Figure B.1. The plots are scaled where required and additional information is also given.

Plotting options 1,2,3,4

Cycles = 34,000

BNUM = 100

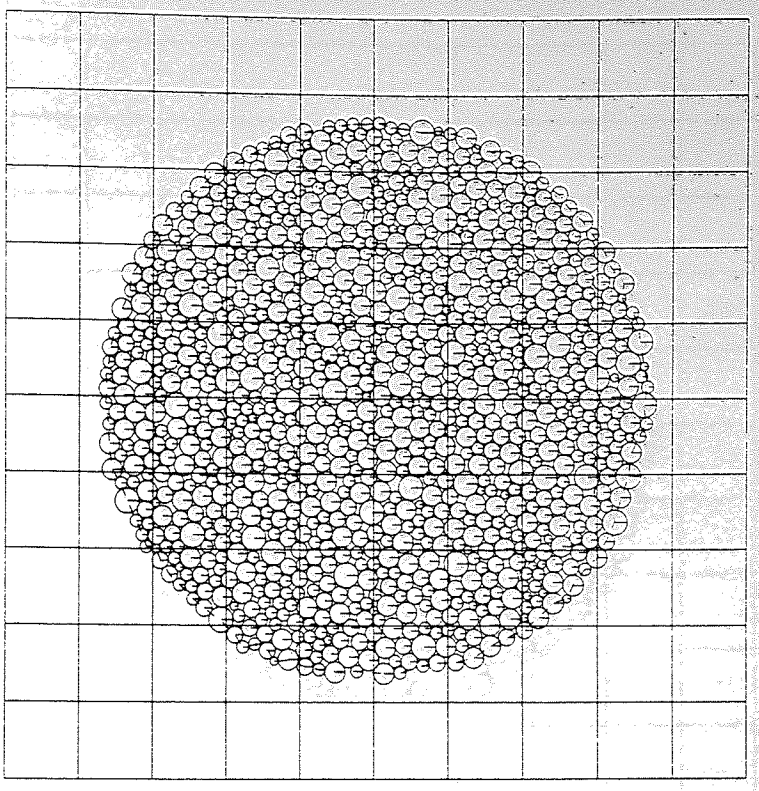

Figure B.2 Assembly at point 0

Plotting options 1,2,3,4

Cycles = 44,000

BNUM = 100

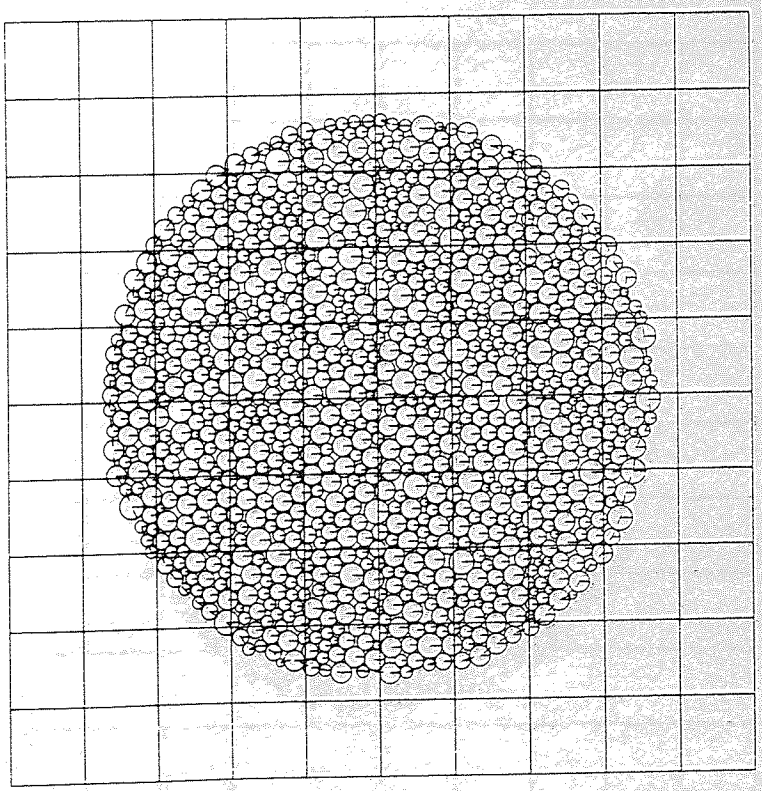

Figure B.3 Assembly at point 5

Plotting options 1,2,3,4

Cycles = 54,000

BNUM = 100

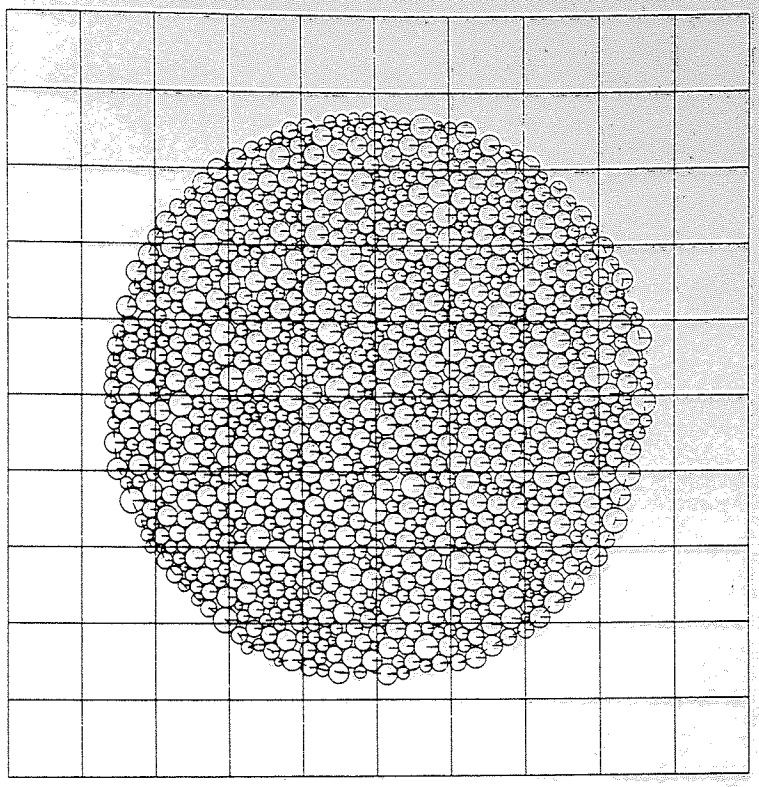

Figure B.4 Assembly at point 10

Plotting options 1,2,3,4

Cycles = 64,000

BNUM = 100

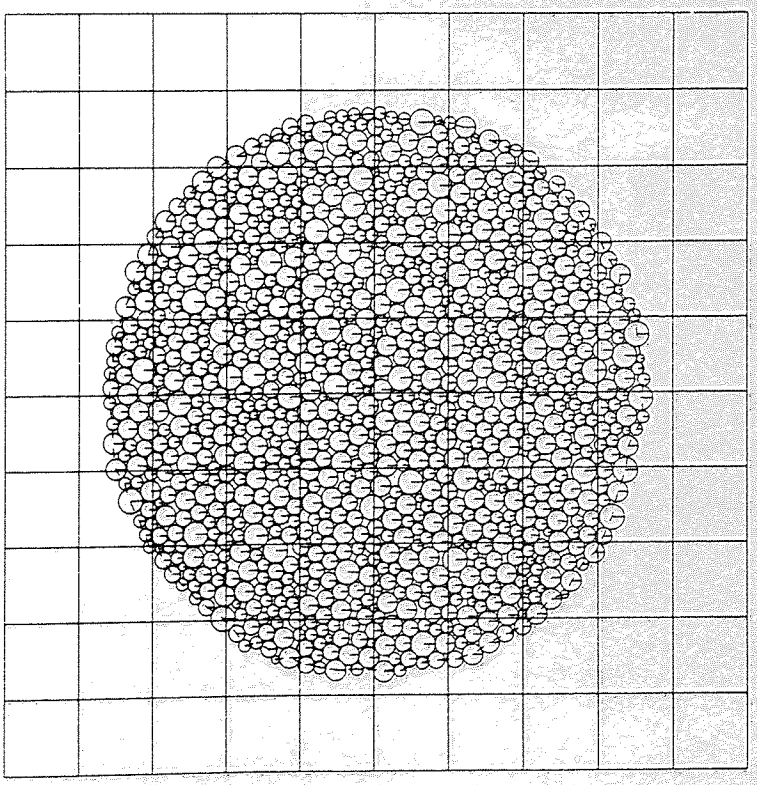

Figure B.5 Assembly at point 15

Plotting options 1,2,3,4

Cycles = 74,000

BNUM = 100

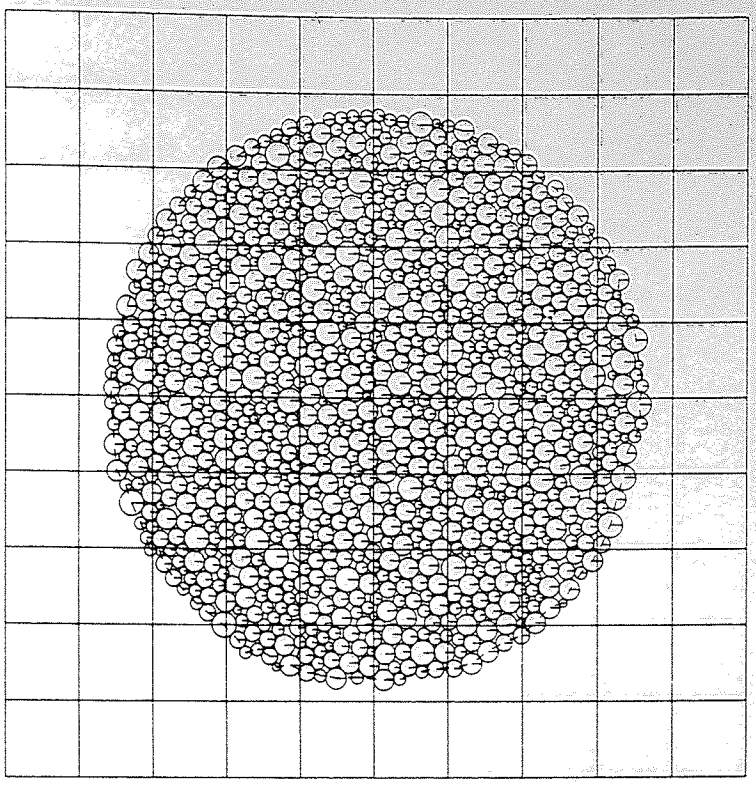

Figure B.6 Assembly at point 20

Plotting options 1,2,3,4

Cycles = 84,000

BNUM = 100

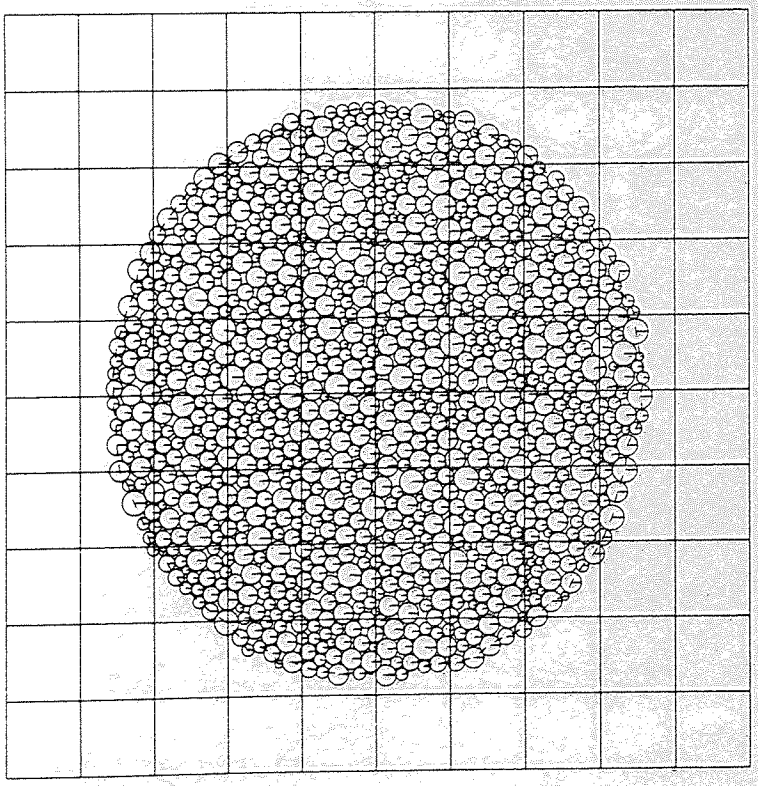

Figure B.7 Assembly at point 25

Plotting options 1,2,3,4

Cycles = 94,000

BNUM = 100

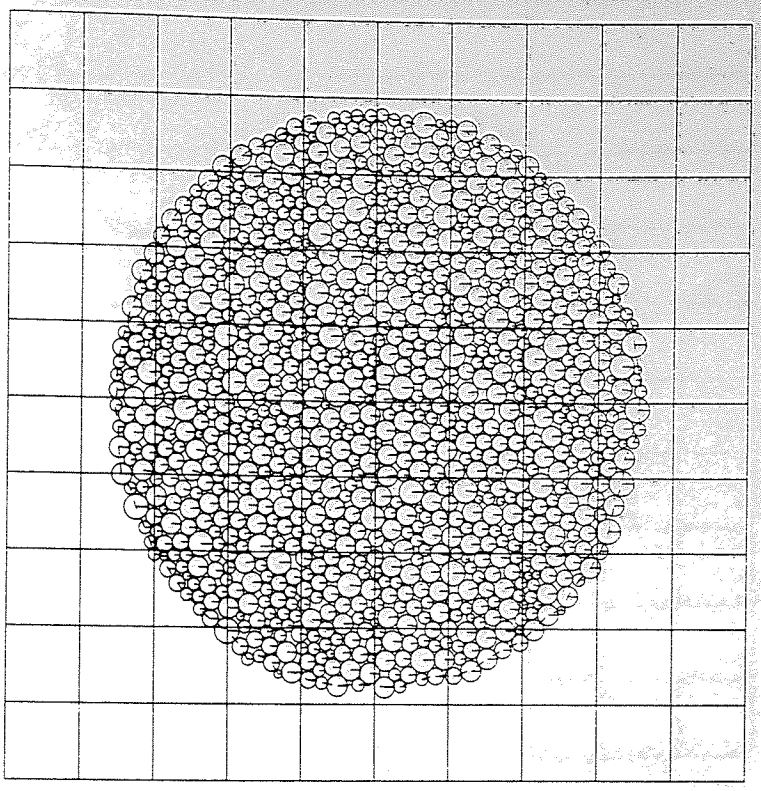

Figure B.8 Assembly at point 30

Plotting options 1,2,3,4

Cycles = 104,000

BNUM = 100

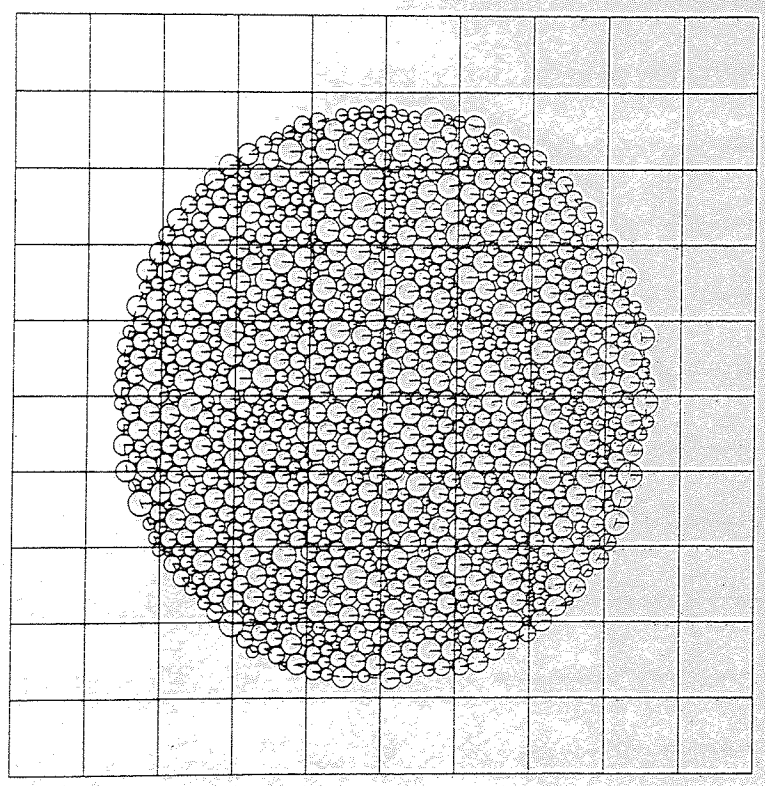

Figure B.9 Assembly at point 35

Plotting options 1,2,3,4

Cycles = 114,000

BNUM = 100

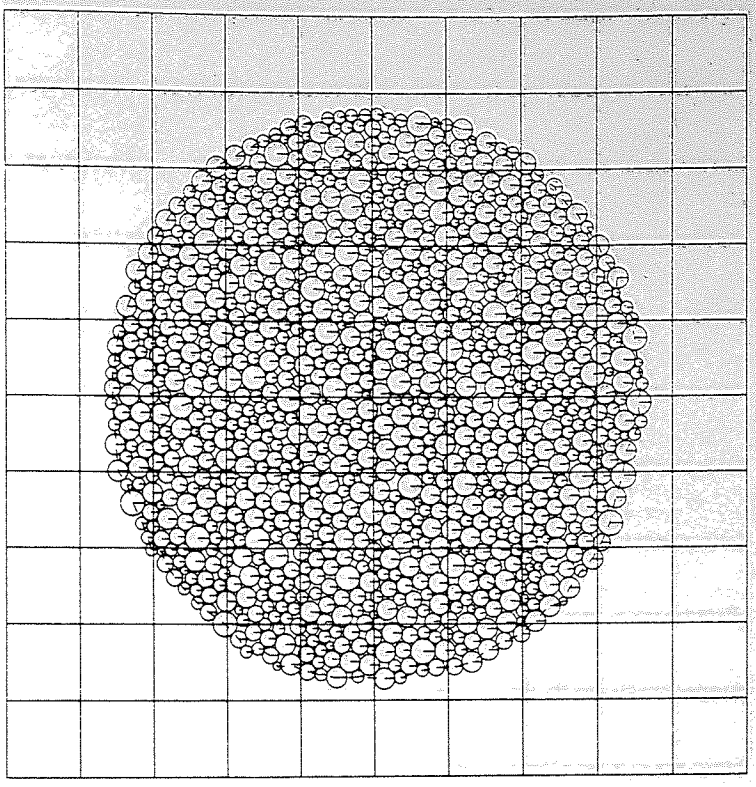

Figure B.10 Assembly at point 40

Plotting options 1,2,3,4

Cycles = 124,000

BNUM = 100

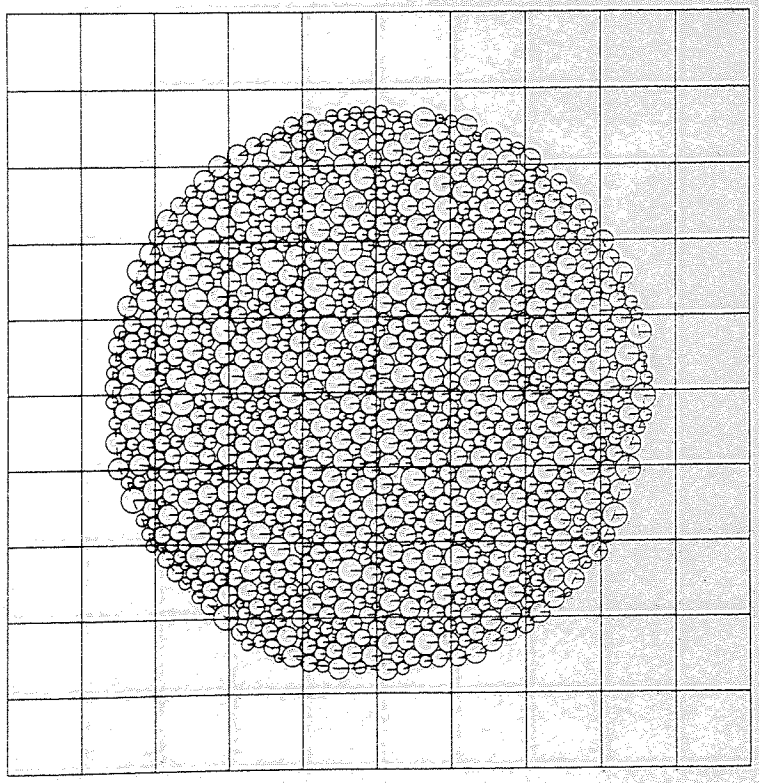

Figure B.11 Assembly at point 45

Plotting options 1,2,3,4

Cycles = 134,000

BNUM = 100

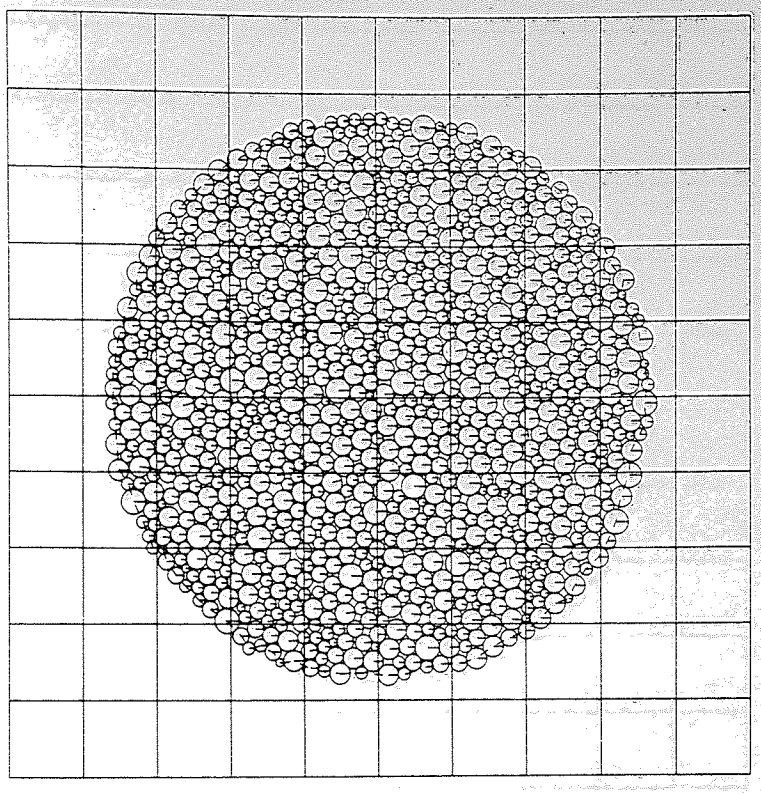

Figure B.12 Assembly at point 50

Plotting options 1,2,3,4

Cycles = 144,000

BNUM = 100

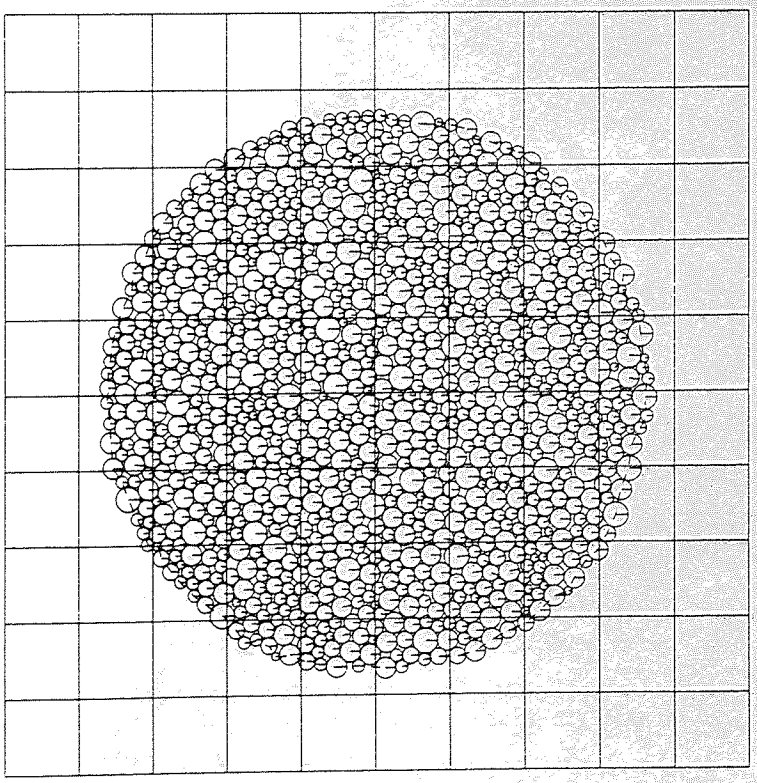

Figure B.13 Assembly at point 55

Plotting options 1,2,3,4

Cycles = 154,000

BNUM = 100

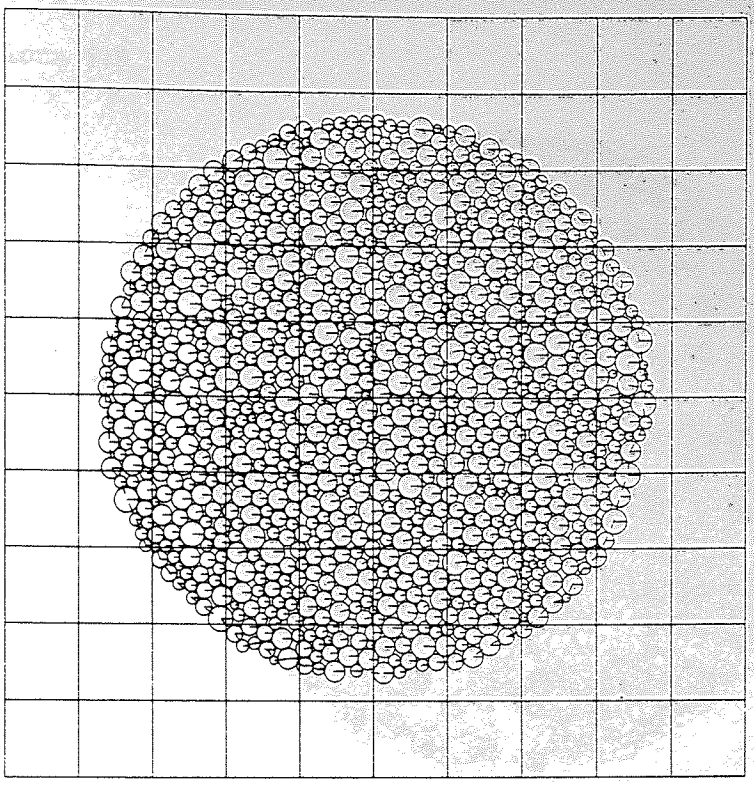

Figure B.14 Assembly at point 60

Plotting options 1,5

Maximum contact force = 4.8375×10^7

NCON = 2099

Cycles = 34,000

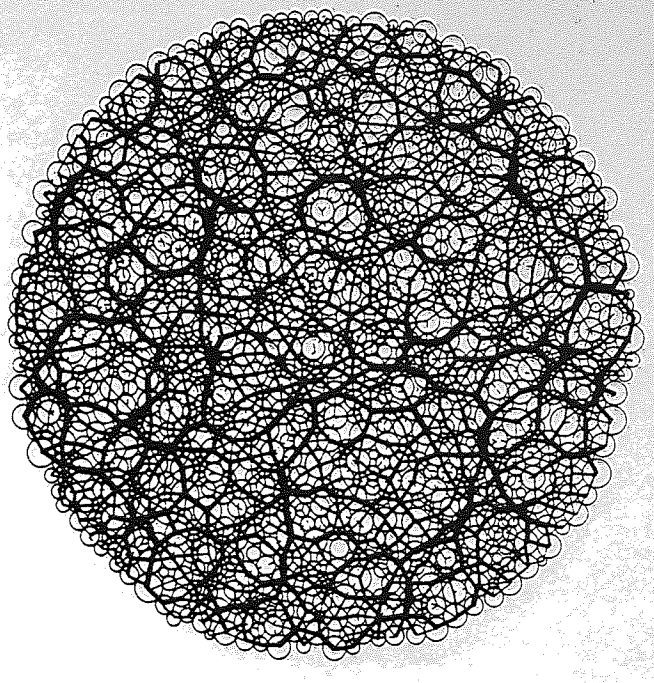

Figure B.15 Contact forces at point 0

Plotting options 1,5

Maximum contact force = 5.0461×10^7

NCON = 2066

Cycles = 44,000

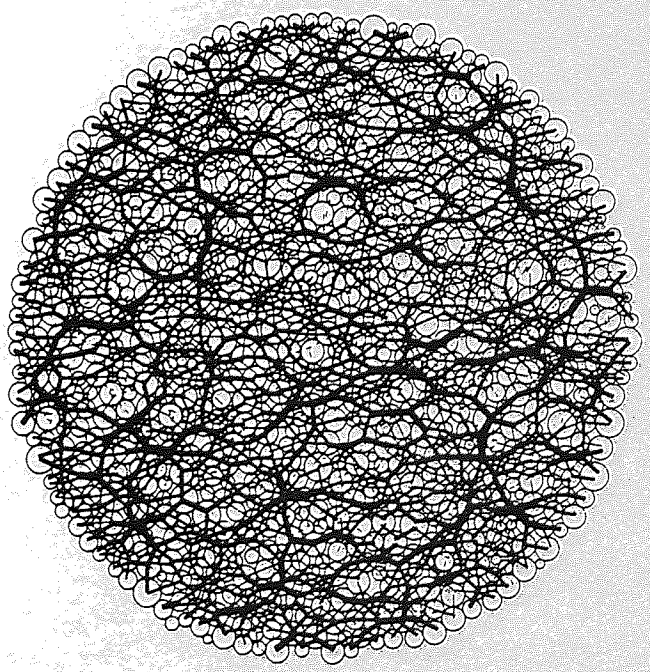

Figure B.16 Contact forces at point 5

Plotting options 1,5

Maximum contact
force = 5.5541 x 10^7

NCON = 2016

Cycles = 54,000

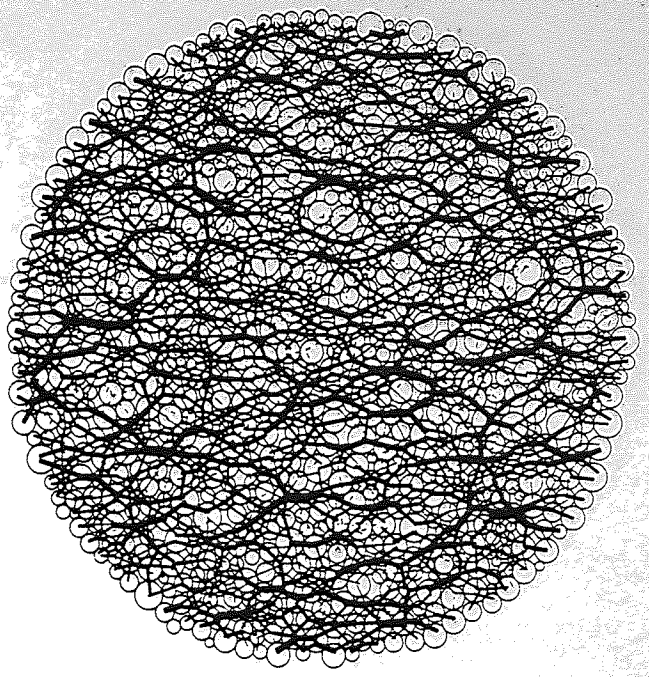

Figure B.17 Contact forces at point 10

Plotting options 1,5

Maximum contact
force = 6.0354 x 10^7

NCON = 1948

Cycles = 64,000

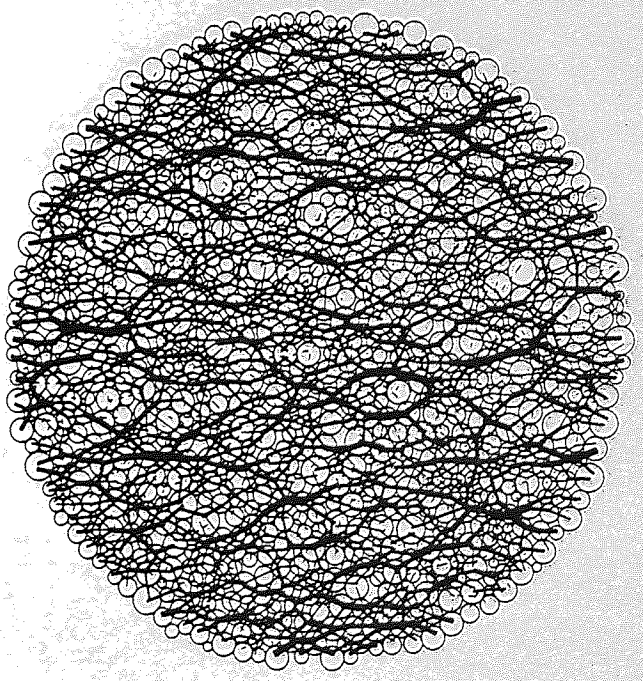

Figure B.18 Contact forces at point 15

Plotting options 1,5

Maximum contact
force = 6.8608 x 10^7

NCON = 1880

Cycles = 74,000

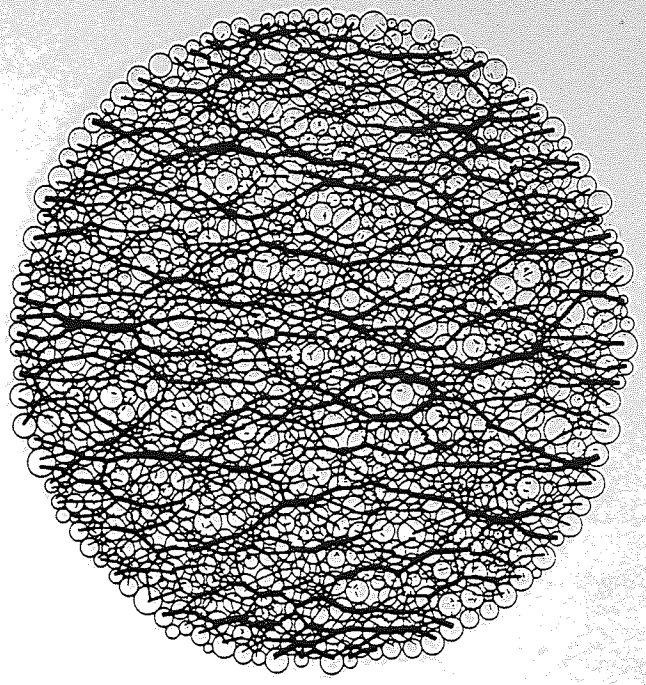

Figure B.19 Contact forces at point 20

Plotting options 1,5

Maximum contact
force = 7.1333 x 10^7

NCON = 1844

Cycles = 84,000

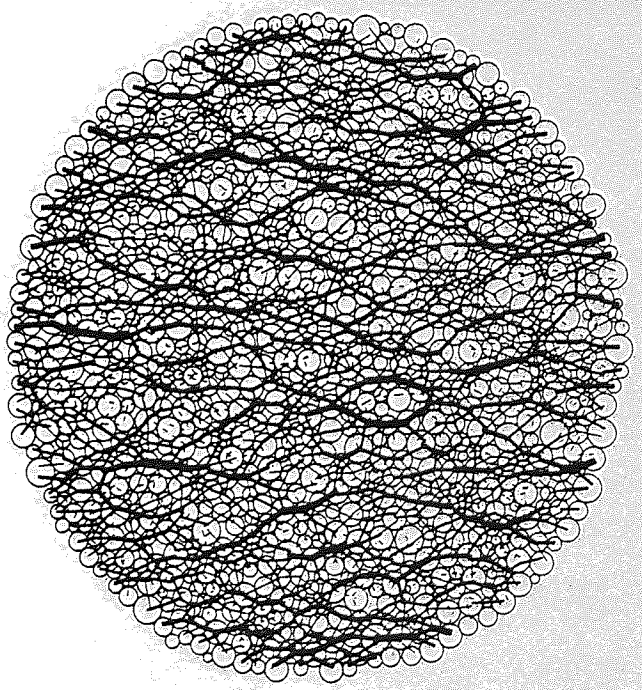

Figure B.20 Contact forces at point 25

Plotting options 1,5

Maximum contact
force = 6.7799 x 10^7

NCON = 1812

Cycles = 94,000

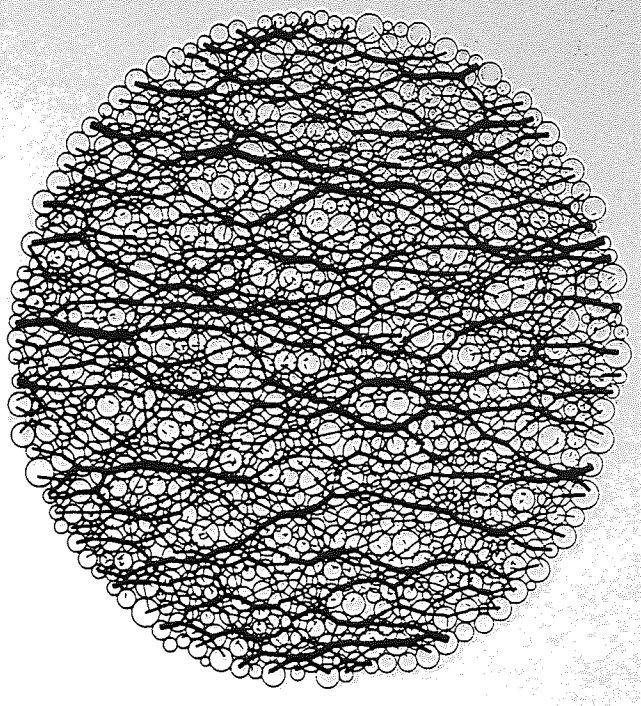

Figure B.21 Contact forces at point 30

Plotting options 1,5

Maximum contact
force = 6.3725 x 10^7

NCON = 1836

Cycles = 104,000

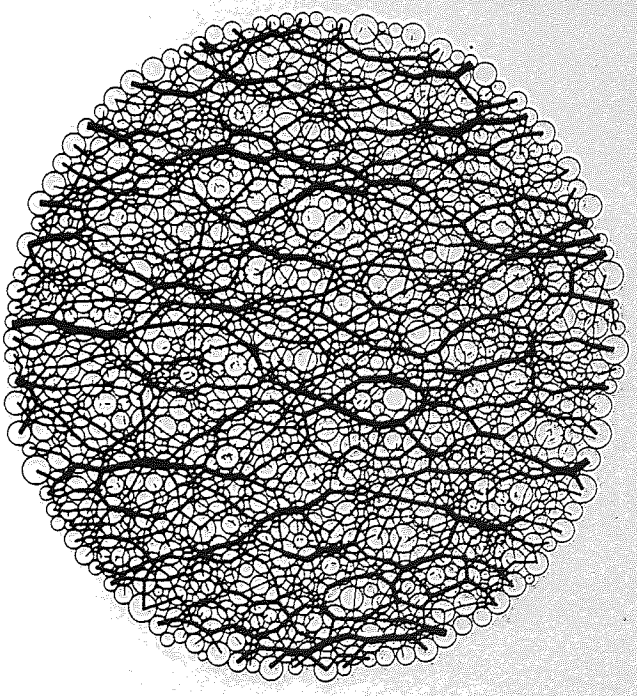

Figure B.22 Contact forces at point 35

Plotting options 1,5

Maximum contact
force = 5.9568×10^7

NCON = 1879

Cycles = 114,000

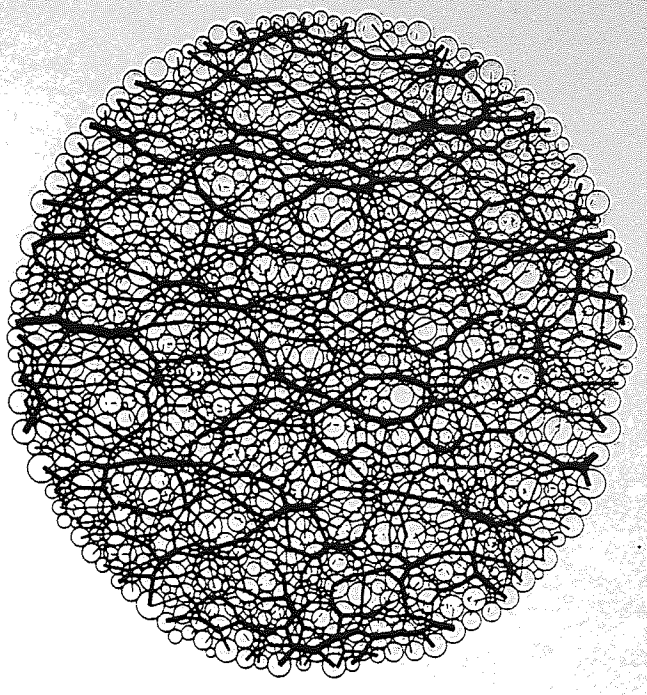

Figure B.23 Contact forces at point 40

Plotting options 1,5

Maximum contact
force = 5.6629×10^7

NCON = 1930

Cycles = 124,000

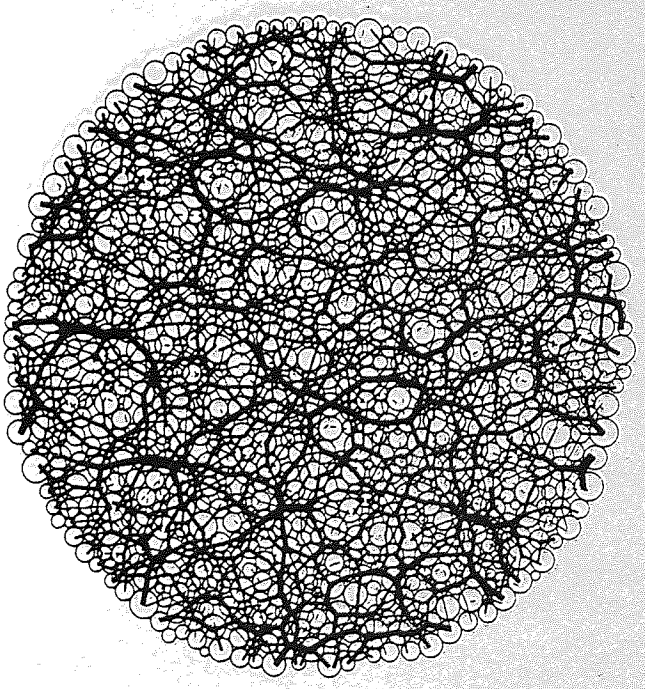

Figure B.24 Contact forces at point 45

Plotting options 1,5

Maximum contact force = 5.0942×10^7

NCON = 1960

Cycles = 134,000

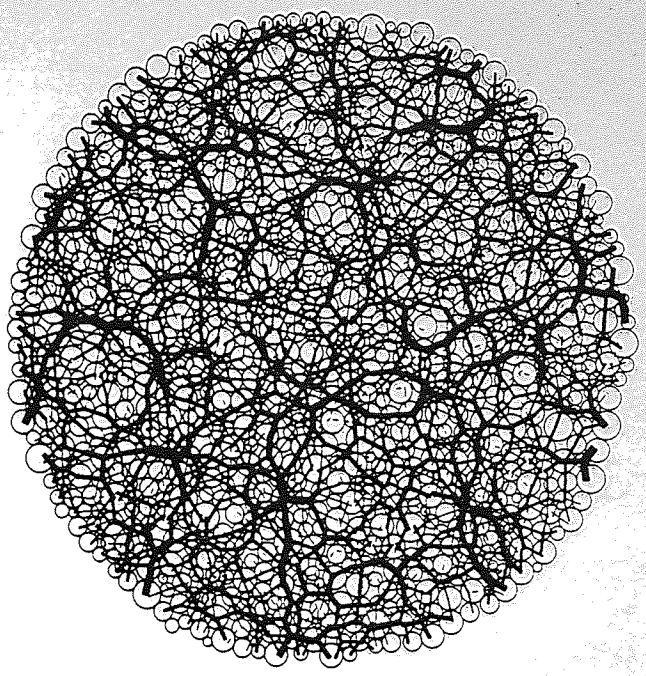

Figure B.25 Contact forces at point 50

Plotting options 1,5

Maximum contact force = 5.0470×10^7

NCON = 1981

Cycles = 144,000

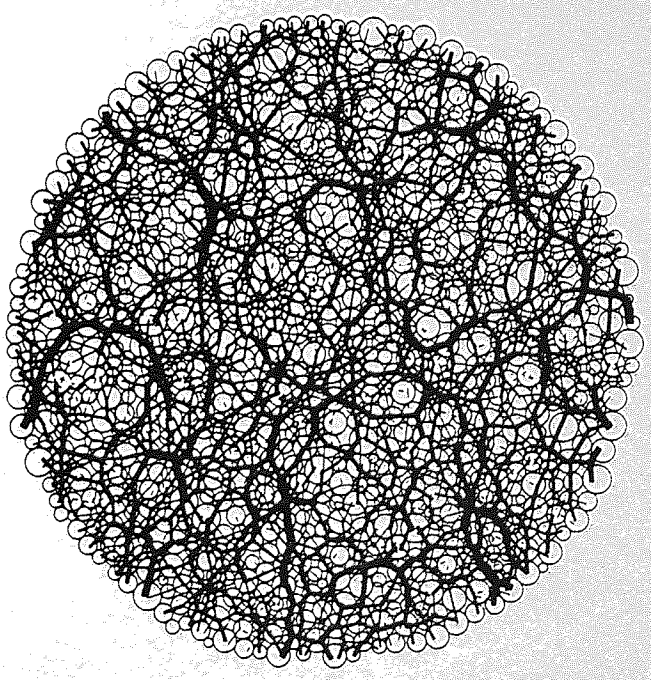

Figure B.26 Contact forces at point 55

Plotting options 1,5

Maximum contact
force = 5.7426 x 10^7

NCON = 1992

Cycles = 154,000

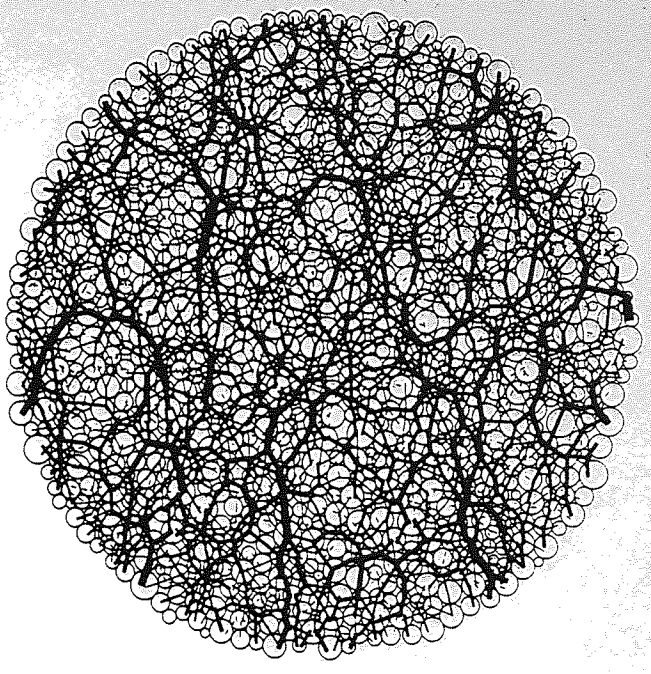

Figure B.27 Contact forces at point 60

Plotting options 1,6

Maximum velocity
= 2.1755 x 10^{-2}

Cycles = 44,000

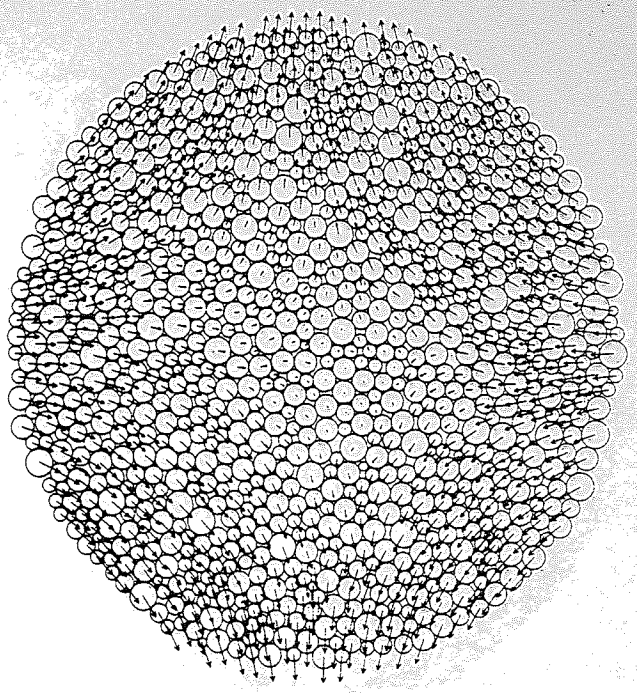

Figure B.28 Velocity of disc centroids at point 5

Plotting options 1,6

Maximum velocity
= 2.3211 x 10^{-2}

Cycles = 54,000

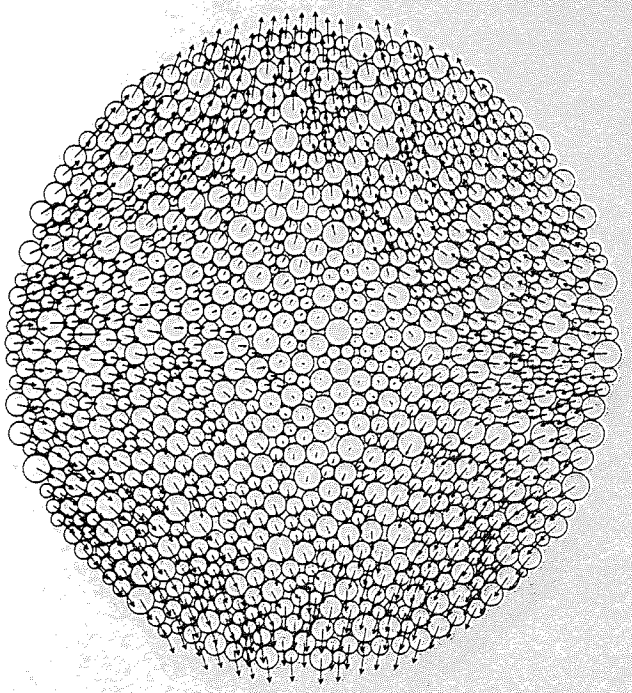

Figure B.29 Velocity of disc centroids at point 10

Plotting options 1,6

Maximum velocity
= 2.5279 x 10^{-2}

Cycles = 64,000

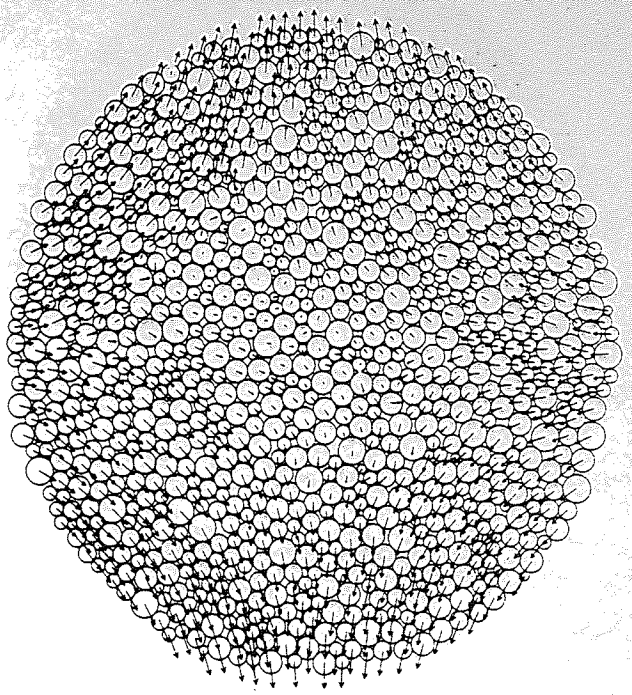

Figure B.30 Velocity of disc centroids at point 15

Plotting options 1,6

Maximum velocity
= 3.0729 x 10^{-2}

Cycles = 74,000

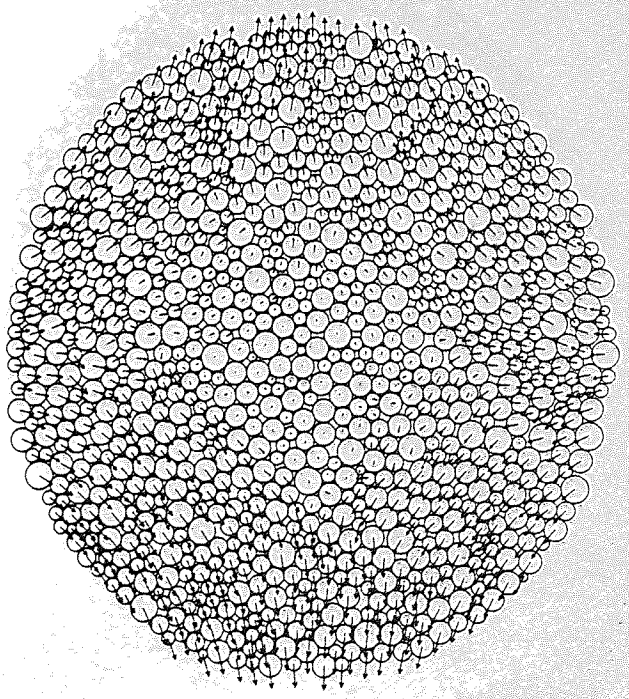

Figure B.31 Velocity of disc centroids at point 20

Plotting options 1,6

Maximum velocity
= 3.2728×10^{-2}

Cycles = 84,000

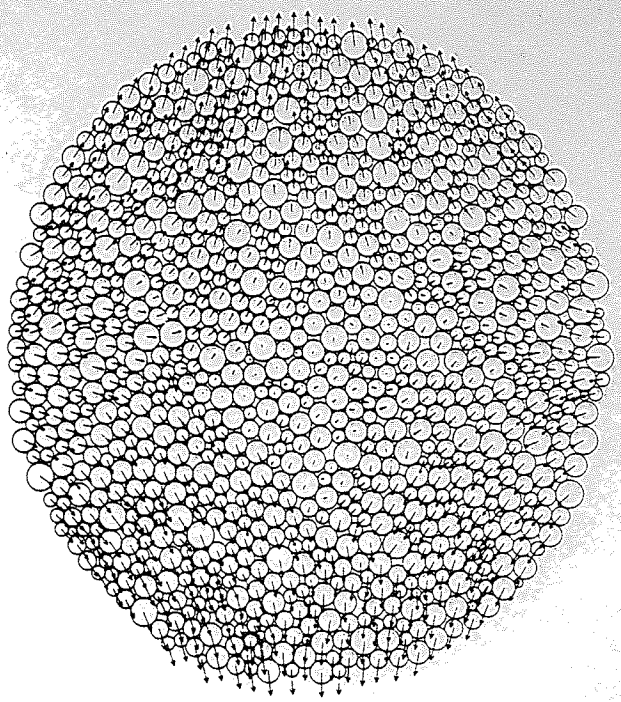

Figure B.32 Velocity of disc centroids at point 25

Plotting options 1,6

Maximum velocity
= 3.3514×10^{-2}

Cycles = 94,000

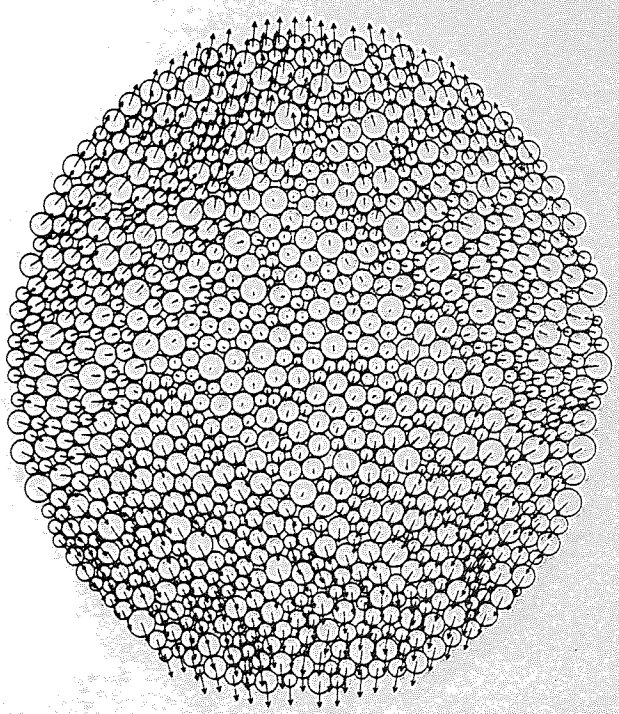

Figure B.33 Velocity of disc centroids at point 30

Plotting options 1,6

Maximum velocity
= 3.0725×10^{-2}

Cycles = 104,000

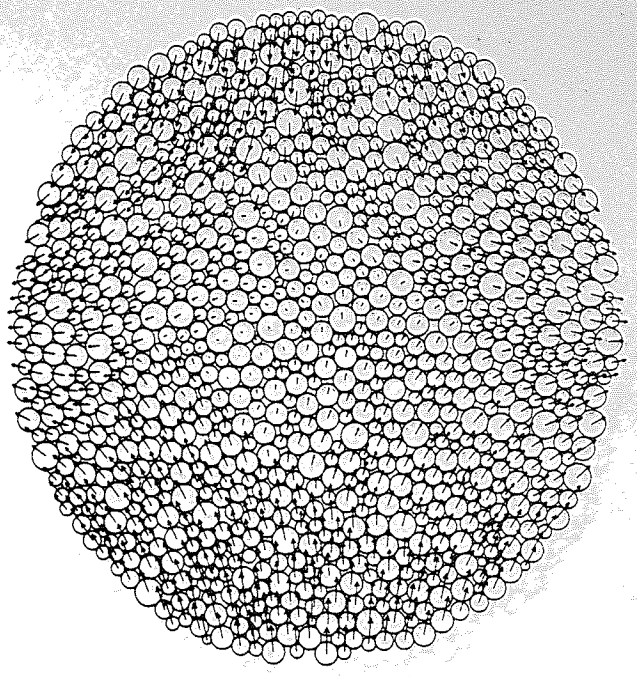

Figure B.34 Velocity of disc centroids at point 35

Plotting options 1,6

Maximum velocity
= 3.0784×10^{-2}

Cycles = 114,000

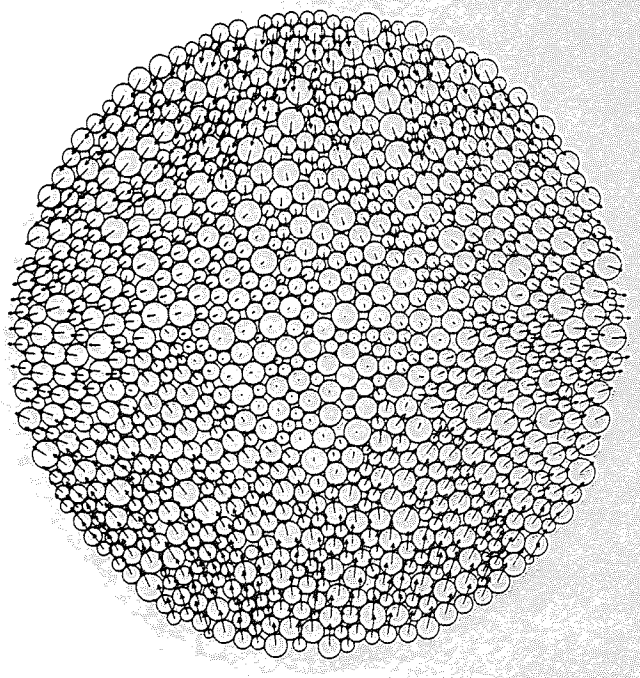

Figure B.35 Velocity of disc centroids at point 40

Plotting options 1,6

Maximum velocity
= 2.3805 x 10^{-2}

Cycles = 124,000

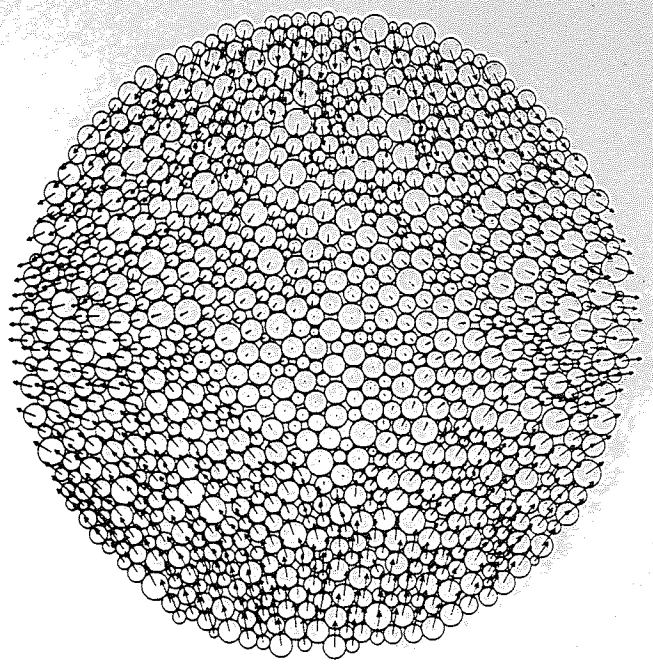

Figure B.36 Velocity of disc centroids at point 45

Plotting options 1,6

Maximum velocity
= 2.1506 x 10^{-2}

Cycles = 134,000

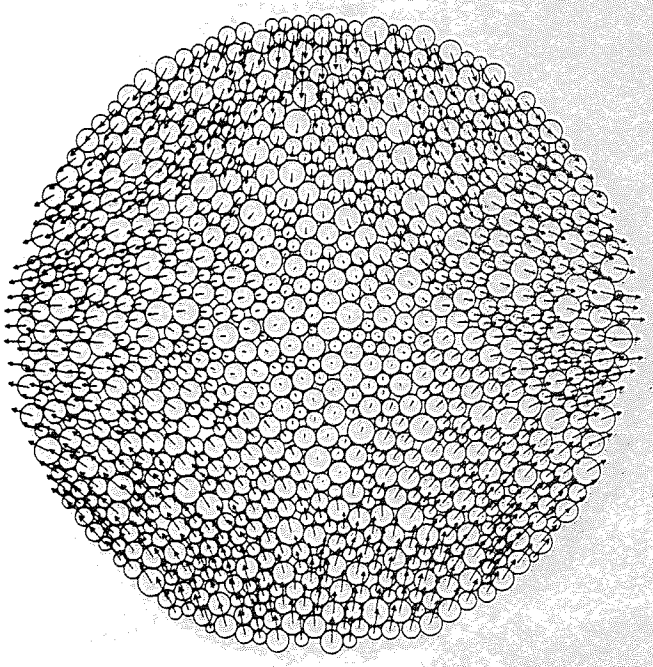

Figure B.37 Velocity of disc centroids at point 50

Plotting options 1,6

Maximum velocity
= 2.4253 x 10^{-2}

Cycles = 144,000

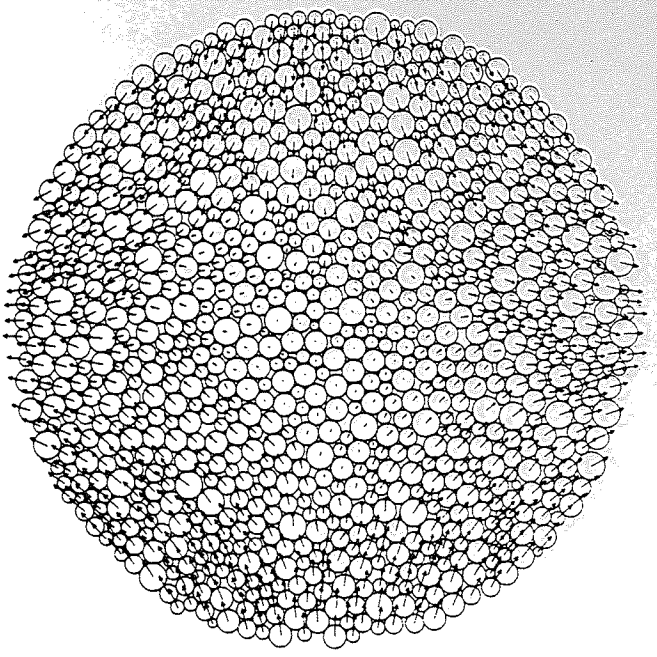

Figure B.38 Velocity of disc centroids at point 55

Plotting options 1,6

Maximum velocity
= 2.1444 x 10^{-2}

Cycles = 154,000

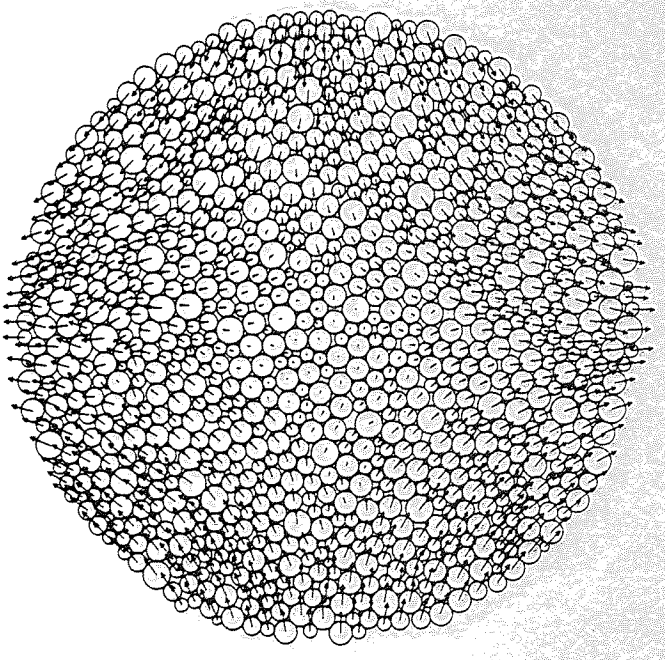

Figure B.39 Velocity of disc centroids at point 60

Plotting options 1,7,8

Maximum slip
increment = 0.2244

Maximum rotation
increment = 1.2970°

Cycles = 44,000

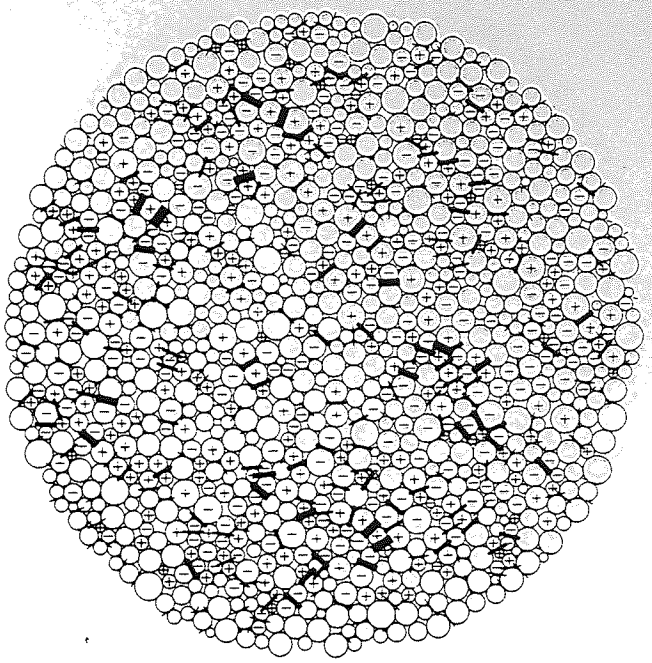

Figure B.40 Slip and rotation increments, point 4-5

Plotting options 1,7,8

Maximum slip
increment = 0.3247

Maximum rotation
increment = 1.6638°

Cycles = 54,000

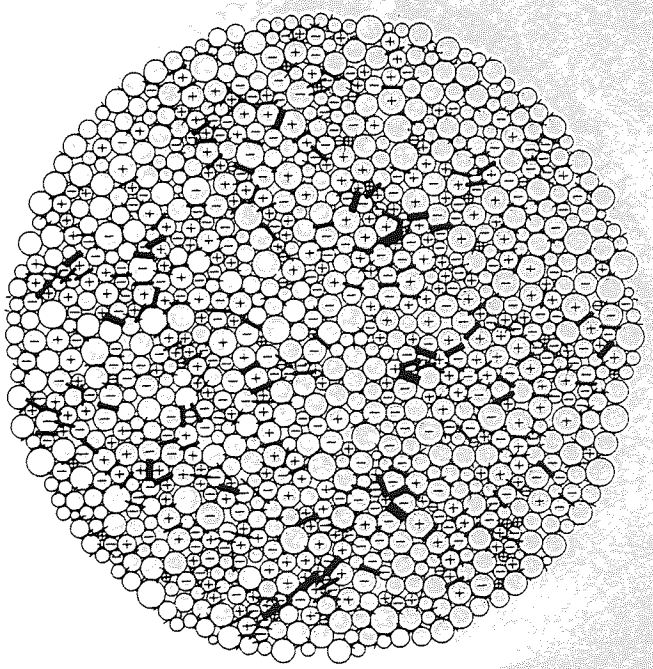

Figure B.41 Slip and rotation increments, point 9-10

Plotting options 1,7,8

Maximum slip
increment = 0.5108

Maximum rotation
increment = 2.4030°

Cycles = 64,000

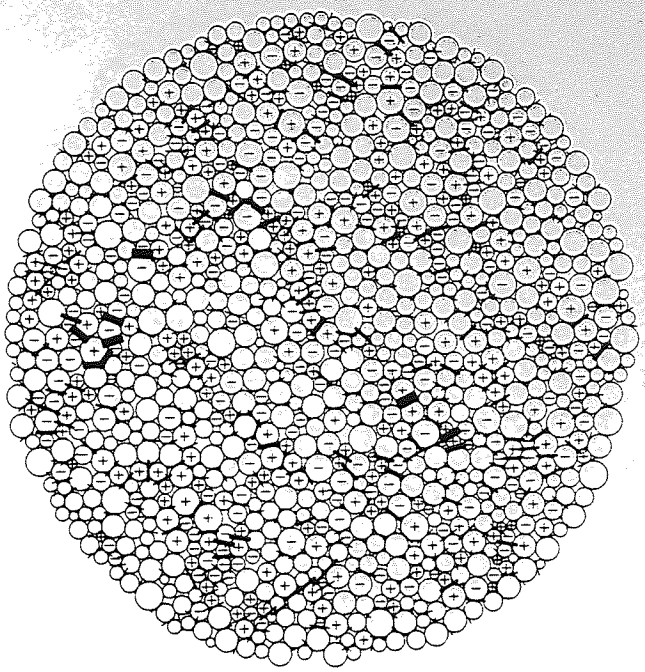

Figure B.42 Slip and rotation increments, point 14-15

Plotting options 1,7,8

Maximum slip
increment = 0.6124

Maximum rotation
increment = 2.8301°

Cycles = 74,000

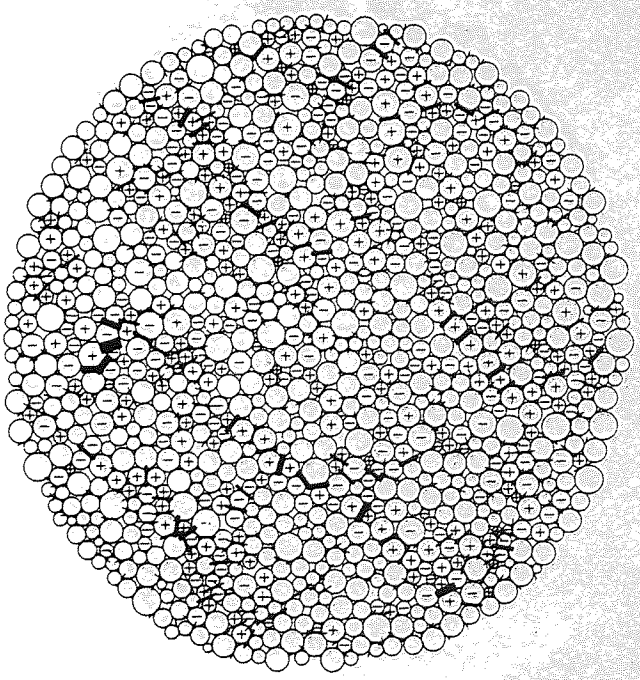

Figure B.43 Slip and rotation increments, point 19-20

Plotting options 1,7,8

Maximum slip
increment = 0.5422

Maximum rotation
increment = 2.7206°

Cycles = 84,000

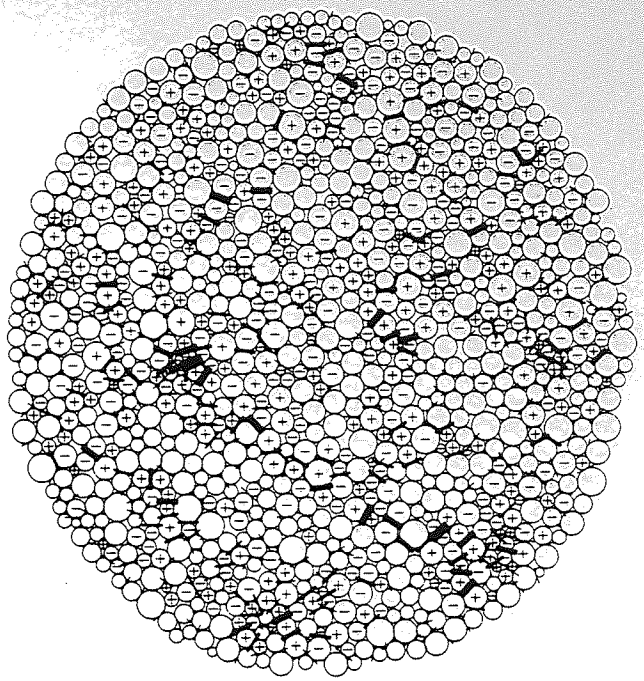

Figure B.44 Slip and rotation increments, point 24-25

Plotting options 1,7,8

Maximum slip
increment = 0.4948

Maximum rotation
increment = 2.8961°

Cycles = 94,000

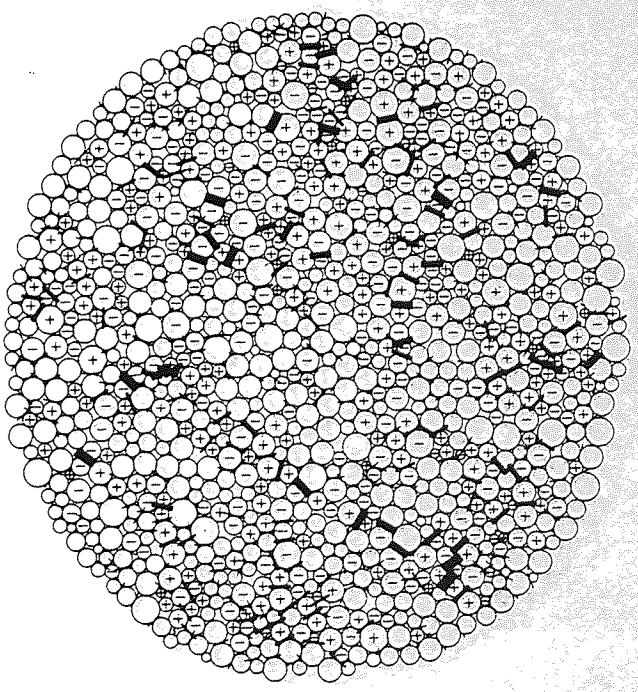

Figure B.45 Slip and rotation increments, point 29-30

Plotting options 1,7,8

Maximum slip
increment = 0.4950

Maximum rotation
increment = 2.8385°

Cycles = 104,000

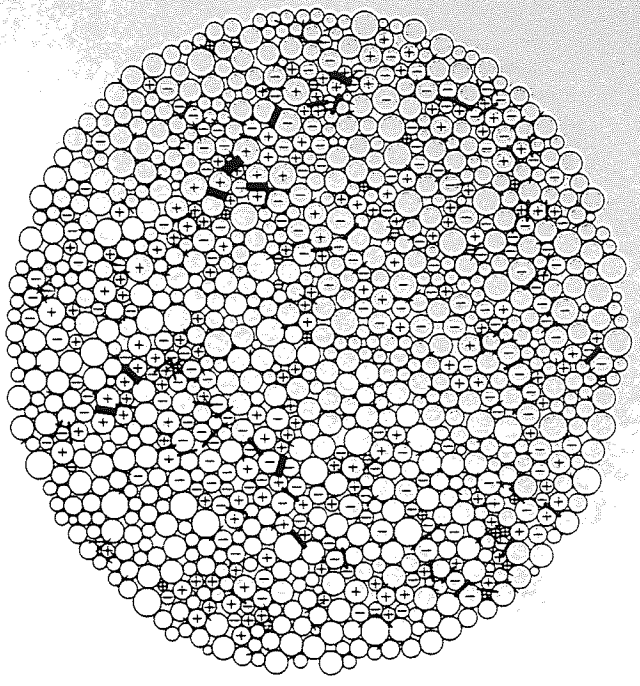

Figure B.46 Slip and rotation increments, point 34-35

Plotting options 1,7,8

Maximum slip
increment = 0.3763

Maximum rotation
increment = 2.2355°

Cycles = 114,000

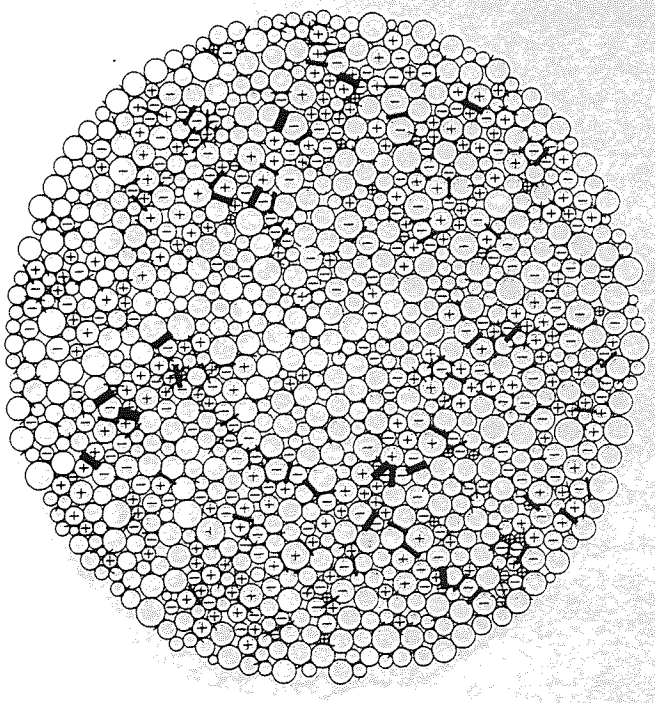

Figure B.47 Slip and rotation increments, point 39-40

Plotting options 1,7,8

Maximum slip
increment = 0.2612

Maximum rotation
increment = 1.8690°

Cycles = 124,000

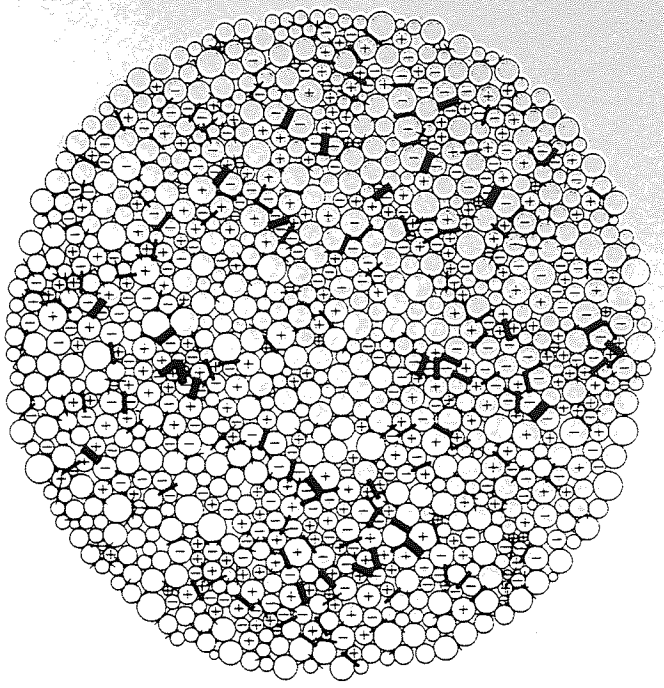

Figure B.48 Slip and rotation increments, point 44-45

Plotting options 1,7,8

Maximum slip
increment = 0.2692

Maximum rotation
increment = 1.4694°

Cycles = 134,000

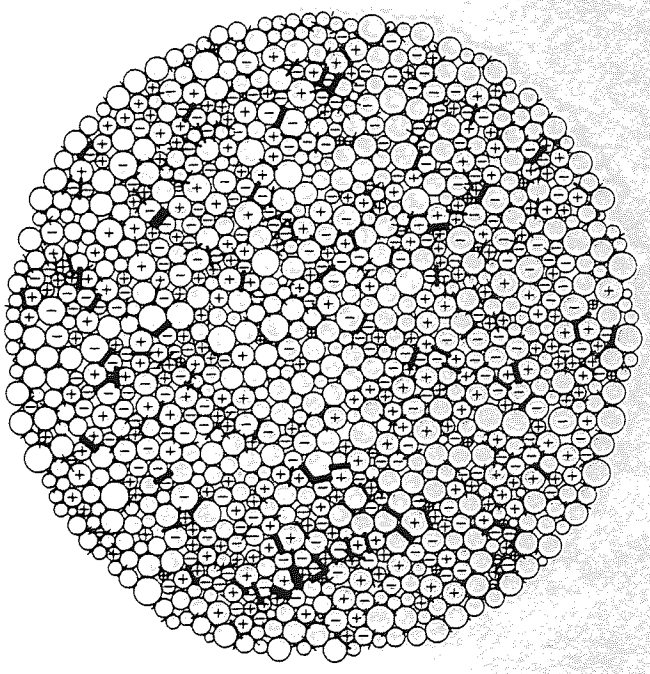

Figure B.49 Slip and rotation increments, point 49-50

Plotting options 1,7,8

Maximum slip
increment = 0.4271

Maximum rotation
increment = 2.2819°

Cycles = 144,000

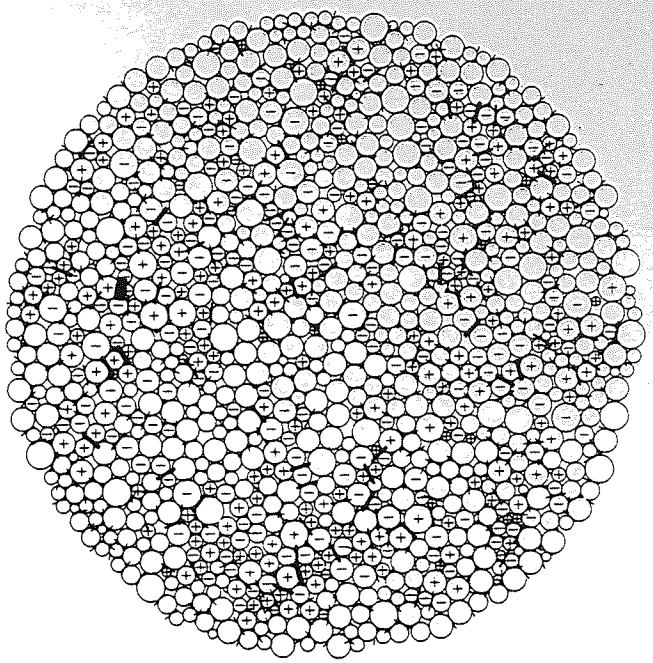

Figure B.50 Slip and rotation increments, point 54-55

Plotting options 1,7,8

Maximum slip
increment = 0.4787

Maximum rotation
increment = 2.0924°

Cycles = 154,000

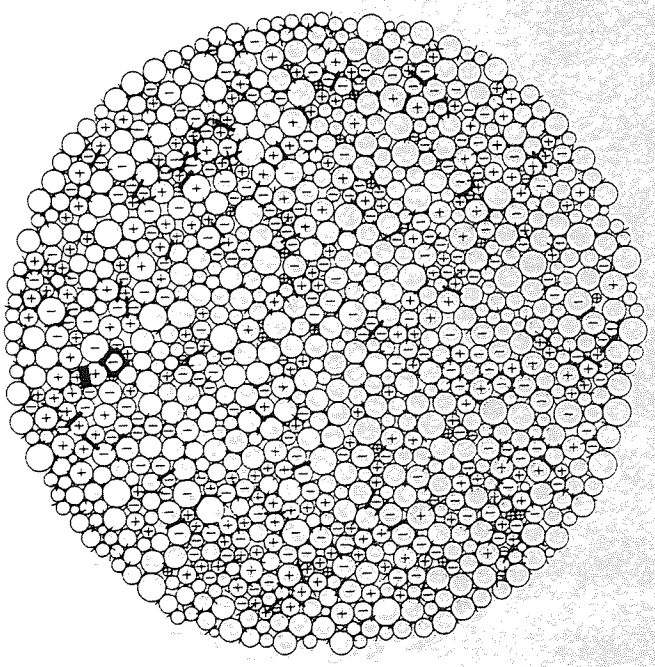

Figure B.51 Slip and rotation increments, point 59-60

Plotting option 9

Existing = 2020

New = 46

Deleted = 79

Cycles = 44,000

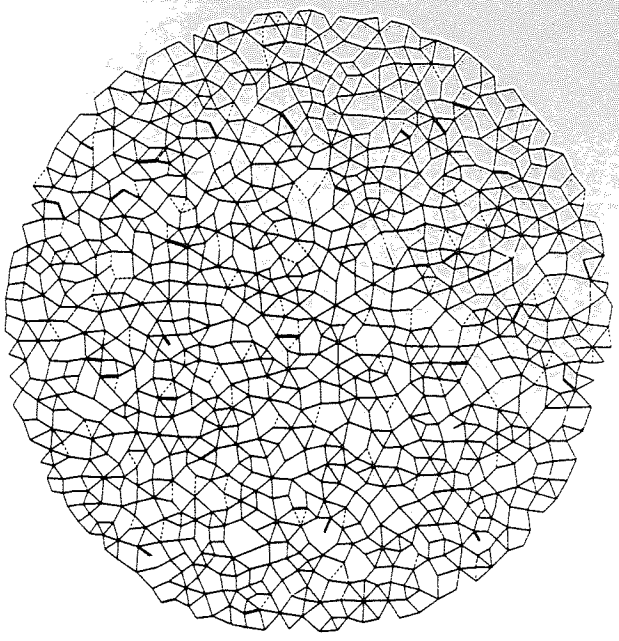

Figure B.52 Structure plot, point 5 relative to point 0

Plotting option 9

Existing = 1936

New = 80

Deleted = 163

Cycles = 54,000

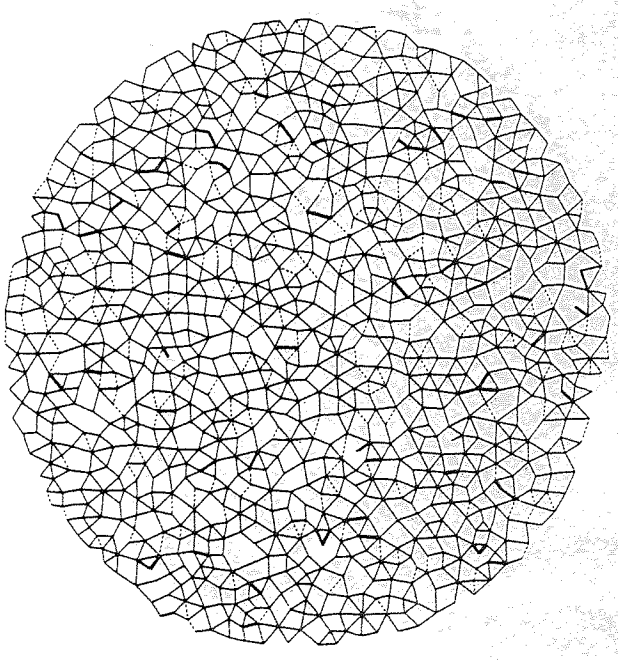

Figure B.53 Structure plot, point 10 relative to point 0

Plotting option 9

Existing = 1852

New = 96

Deleted = 247

Cycles = 64,000

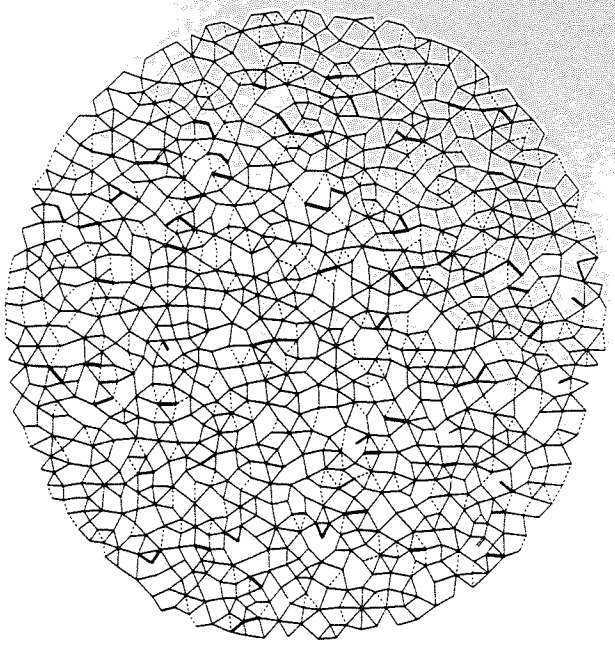

Figure B.54 Structure plot, point 15 relative to point 0

Plotting option 9

Existing = 1764

New = 116

Deleted = 335

Cycles = 74,000

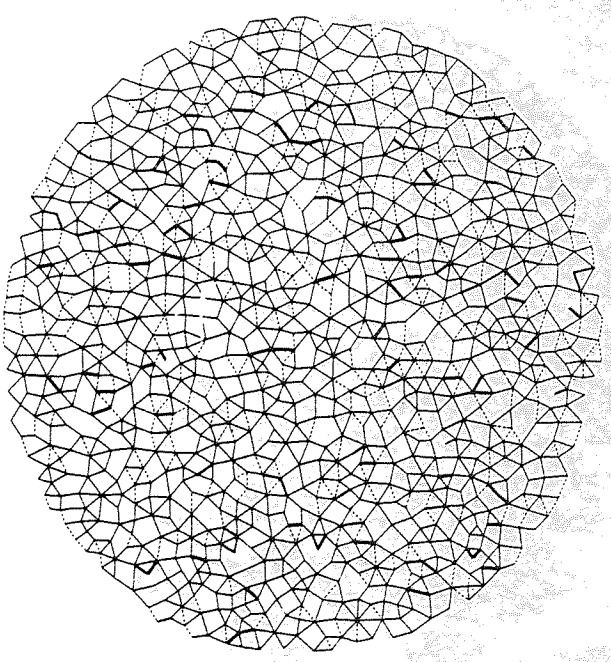

Figure B.55 Structure plot, point 20 relative to point 0

Plotting option 9

Existing = 1711

New = 138

Deleted = 388

Cycles = 84,000

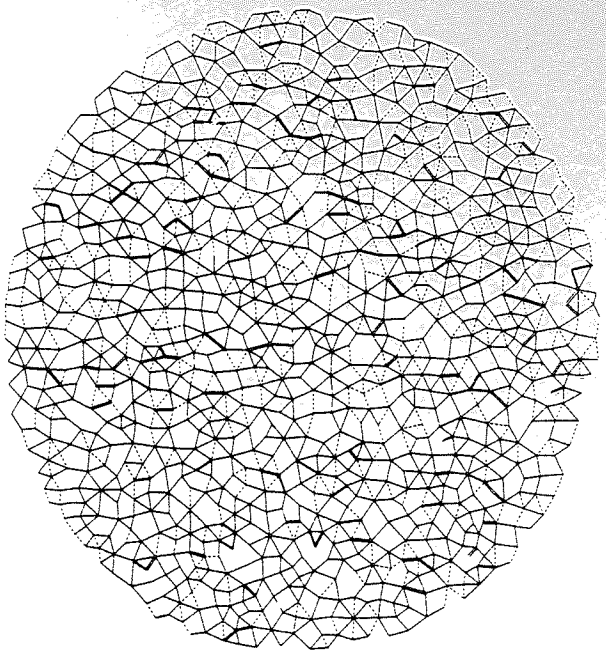

Figure B.56 Structure plot, point 25 relative to point 0

Plotting option 9

Existing = 1652

New = 160

Deleted = 447

Cycles = 94,000

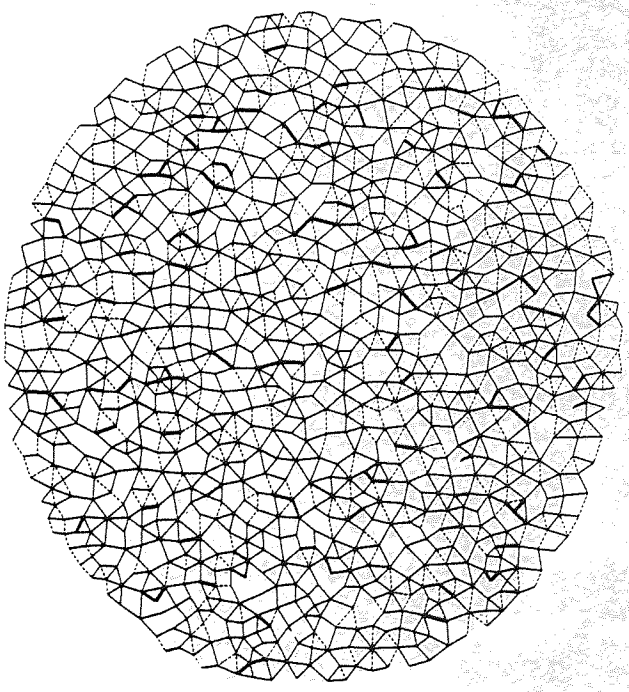

Figure B.57 Structure plot, point 30 relative to point 0

Plotting option 9

Existing = 1733

New = 103

Deleted = 79

Cycles = 104,000

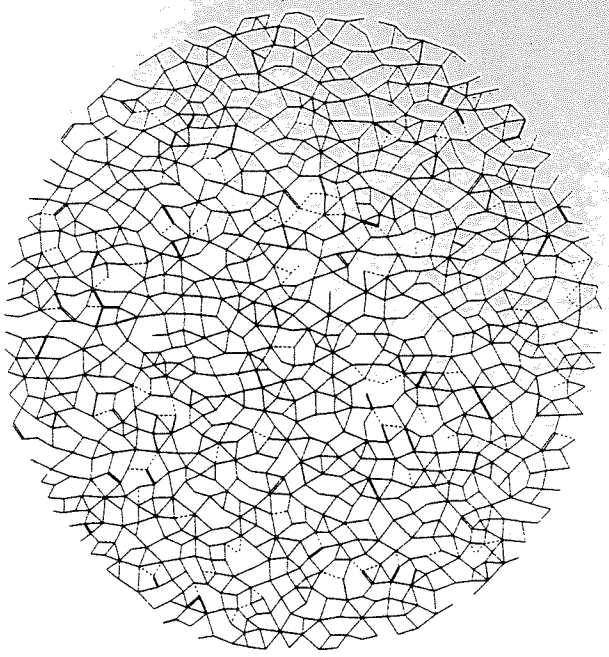

Figure B.58 Structure plot, point 35 relative to point 30

Plotting option 9

Existing = 1699

New = 180

Deleted = 113

Cycles = 114,000

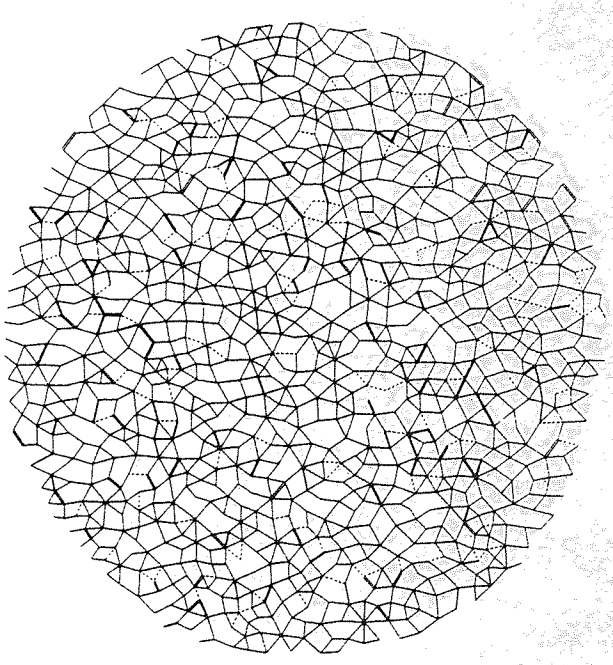

Figure B.59 Structure plot, point 40 relative to point 30

Plotting option 9

Existing = 1675

New = 225

Deleted = 137

Cycles = 124,000

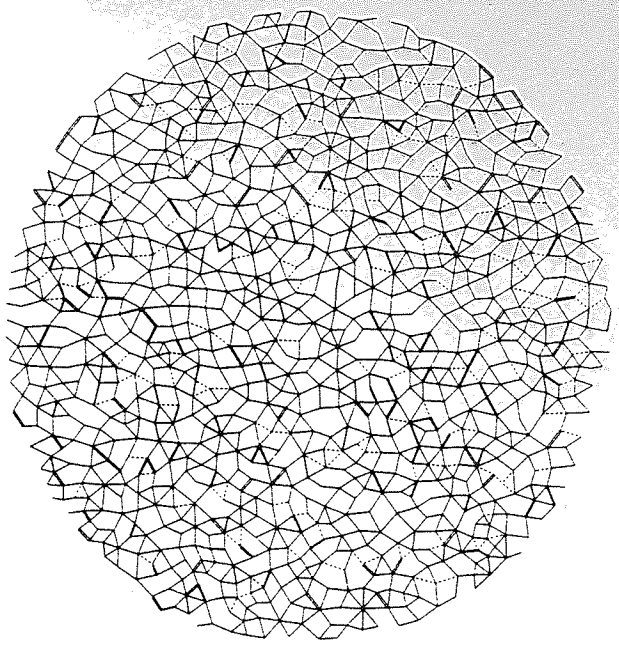

Figure B.60 Structure plot, point 45 relative to point 30

Plotting option 9

Existing = 1636

New = 324

Deleted = 176

Cycles = 134,000

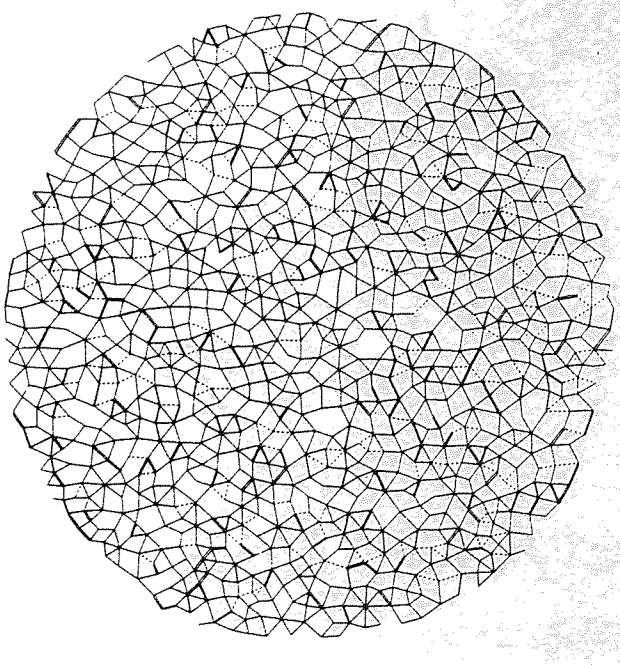

Figure B.61 Structure plot, point 50 relative to point 30

Plotting option 9

Existing = 1613

New = 368

Deleted = 199

Cycles = 144,000

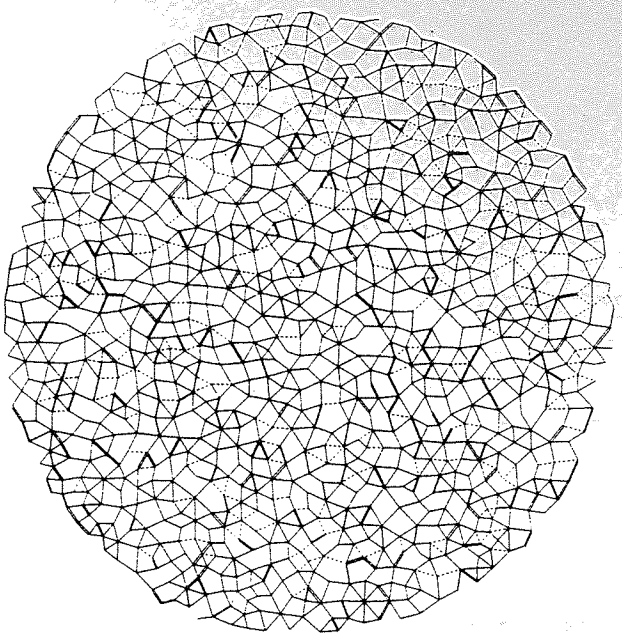

Figure B.62 Structure plot, point 55 relative to point 30

Plotting option 9

Existing = 1576

New = 416

Deleted = 236

Cycles = 154,000

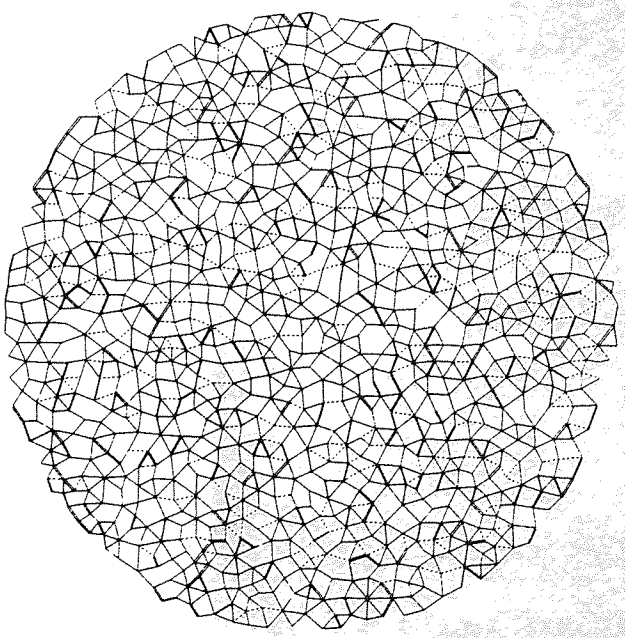

Figure B.63 Structure plot, point 60 relative to point 30

Figure B.64 Internal force and contact data at point 0

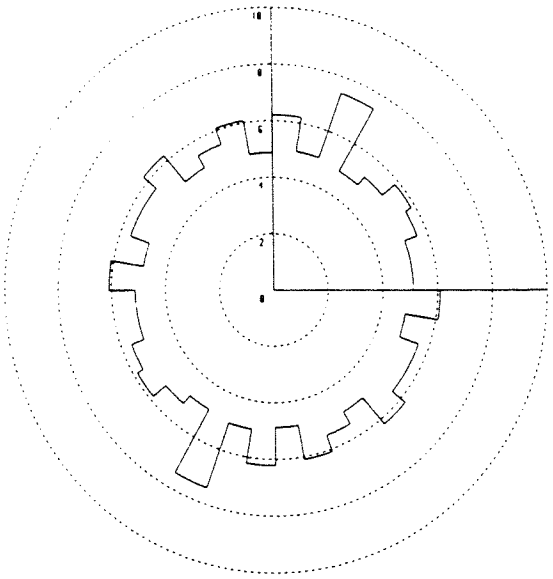

a) Contact angle distribution

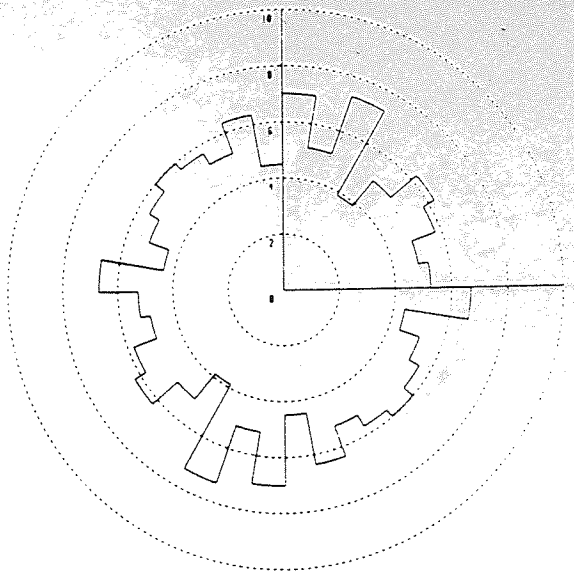

b) Contact angle distribution weighted to the magnitude of normal contact force

cycles = 34,000 NCON = 1165 NSLIP = 4

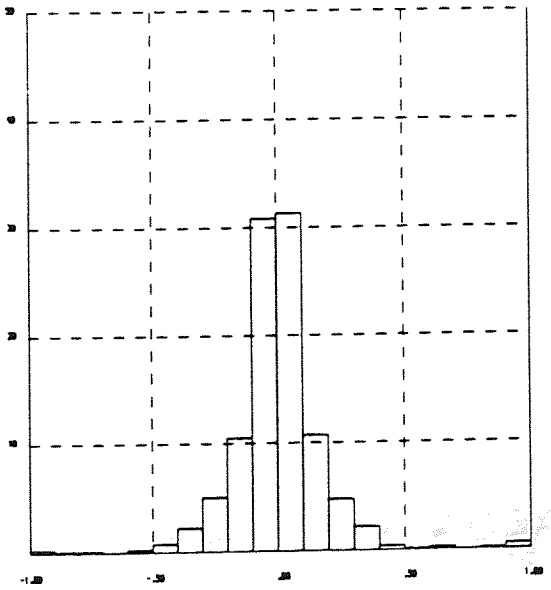

c) Contact force obliquity (normalised to maximum)

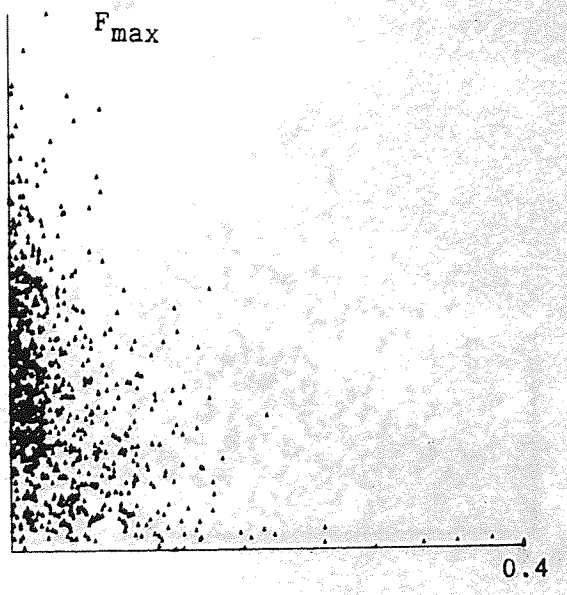

d) Plot of force against obliquity

Figure B.65 Internal force and contact data at point 5

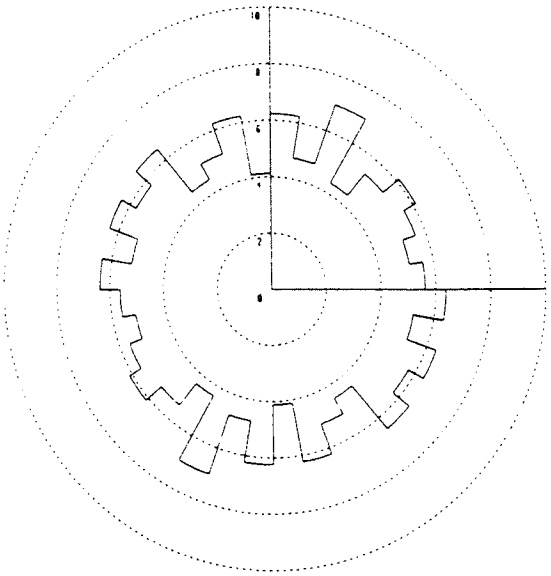

a) Contact angle distribution

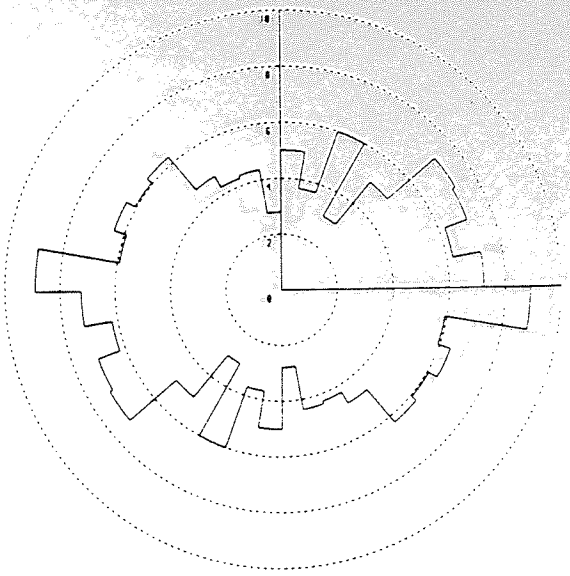

b) Contact angle distribution weighted to the magnitude of normal contact force

cycles = 44,000 NCON = 1143 NSLIP = 171

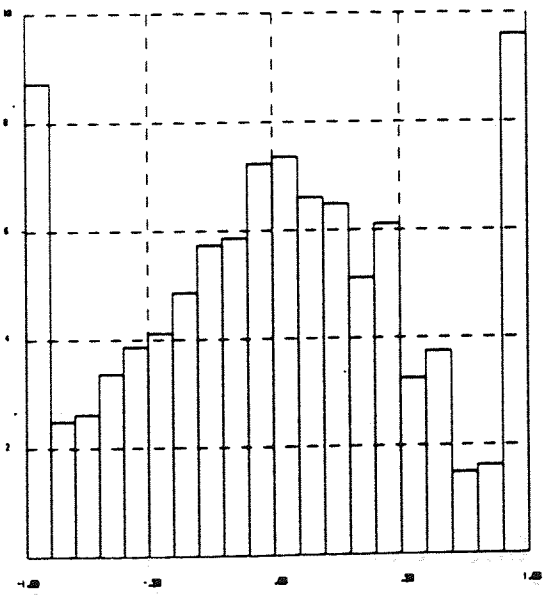

c) Contact force obliquity (normalised to maximum)

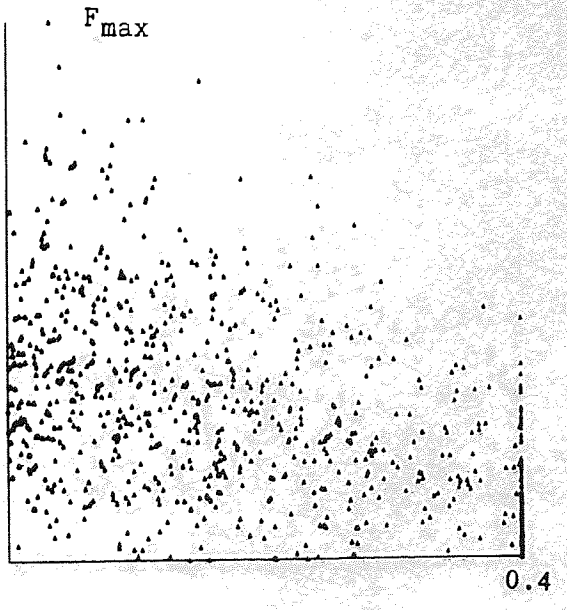

d) Plot of force against obliquity

Figure B.66 Internal force and contact data at point 10

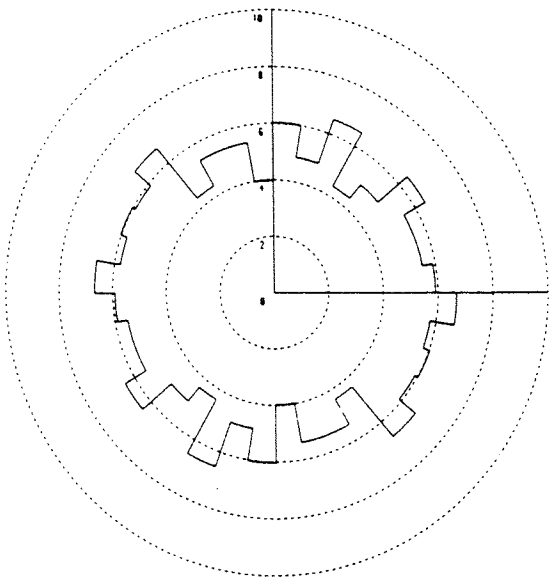

a) Contact angle distribution

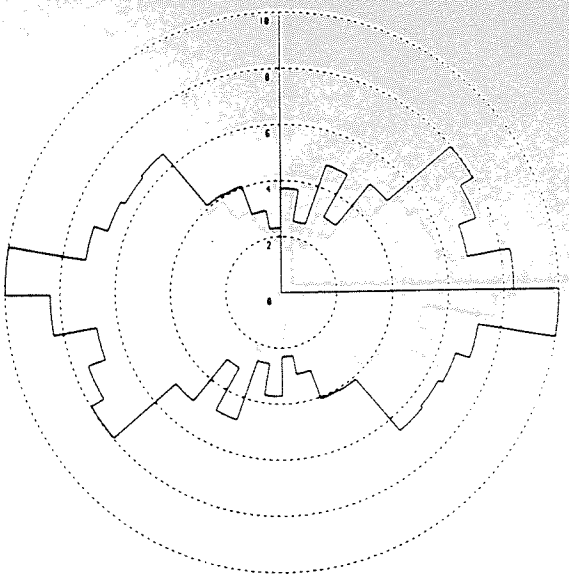

b) Contact angle distribution weighted to the magnitude of normal contact force

cycles = 54,000 NCON = 1116 NSLIP = 252

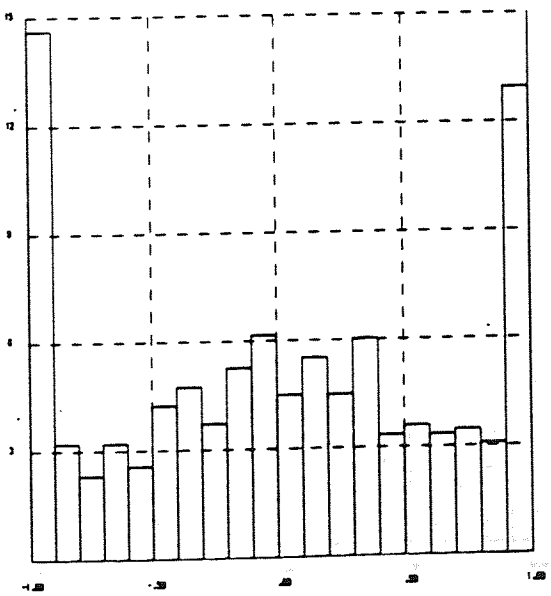

c) Contact force obliquity (normalised to maximum)

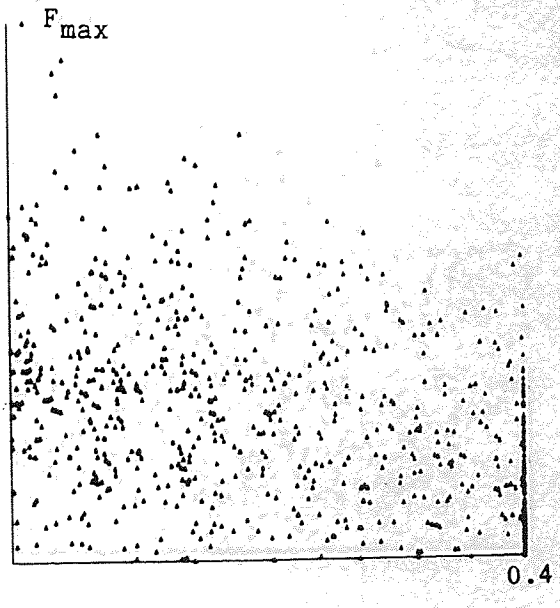

d) Plot of force against obliquity

Figure B.67 Internal force and contact data at point 15

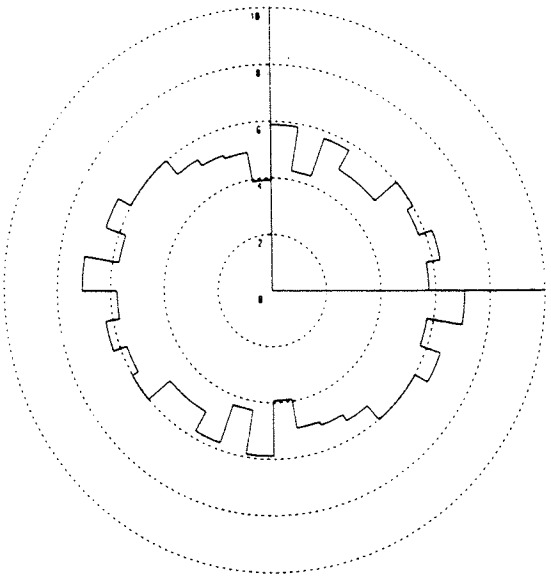

a) Contact angle distribution

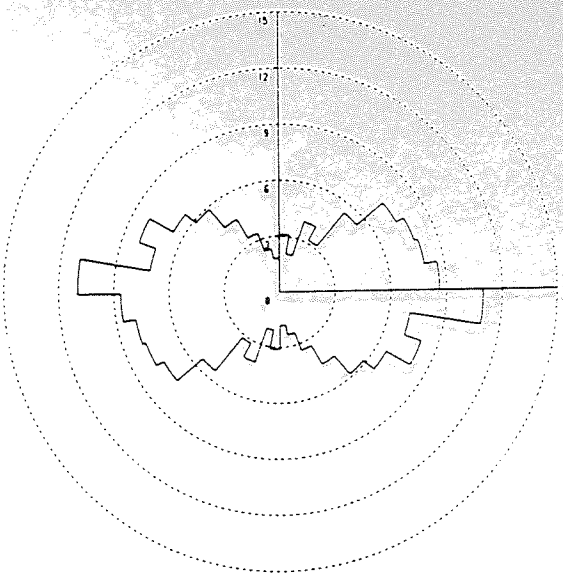

b) Contact angle distribution weighted to the magnitude of normal contact force

cycles = 64,000 NCON = 1094 NSLIP = 249

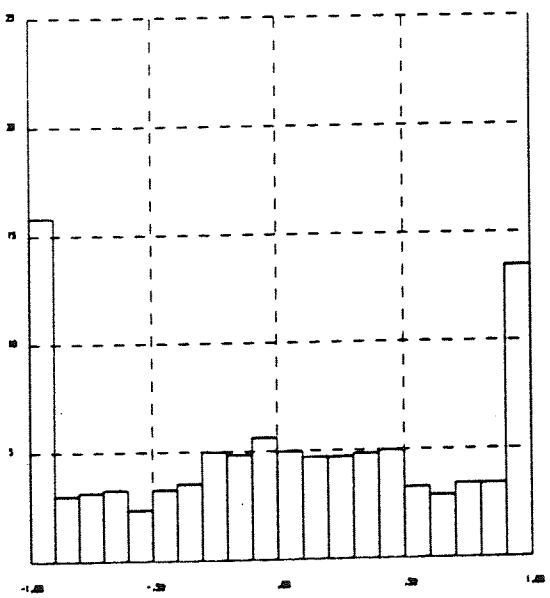

c) Contact force obliquity (normalised to maximum)

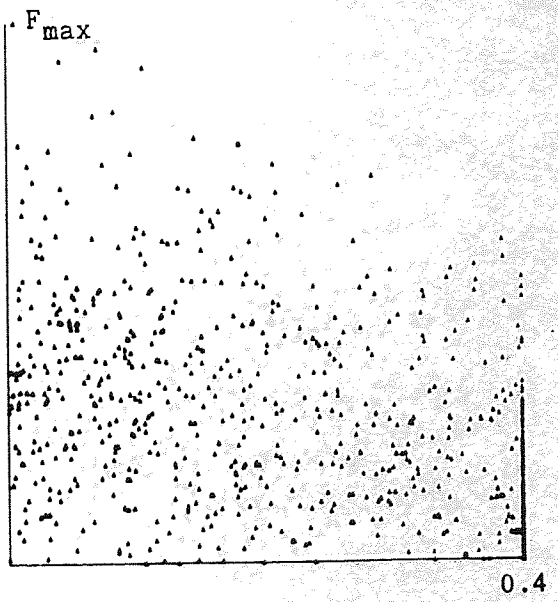

d) Plot of force against obliquity

Figure B.68 Internal force and contact data at point 20

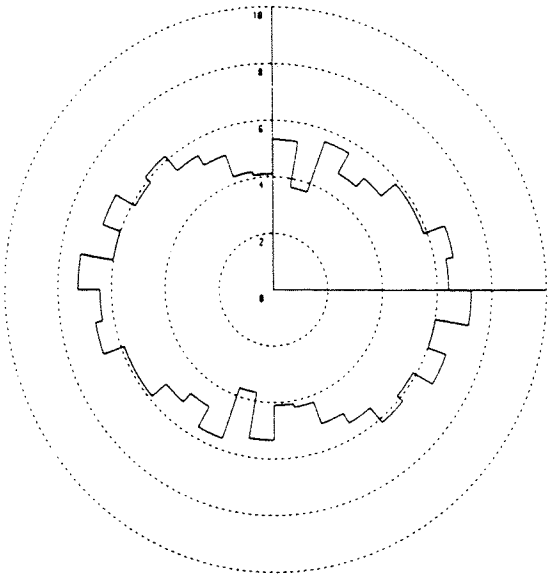

a) Contact angle distribution

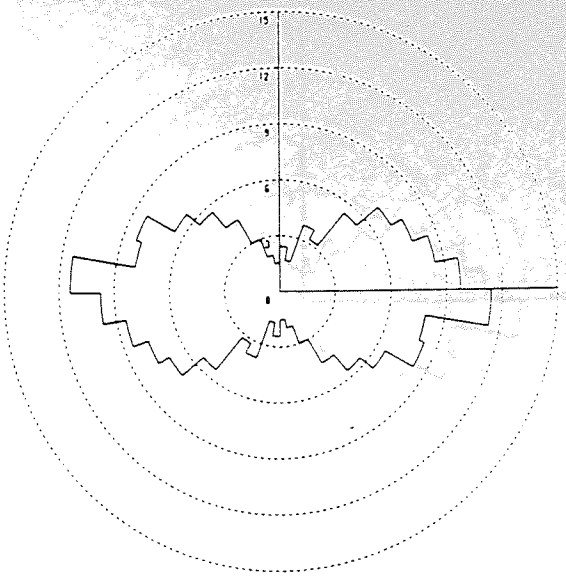

b) Contact angle distribution weighted to the magnitude of normal contact force

cycles = 74,000 NCON = 1059 NSLIP = 228

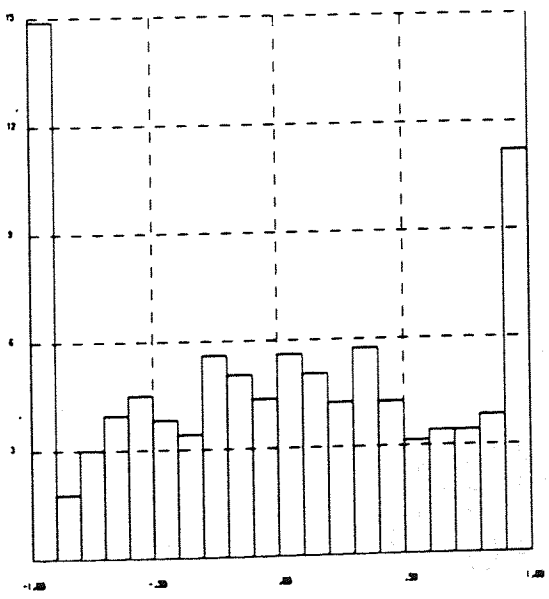

c) Contact force obliquity (normalised to maximum)

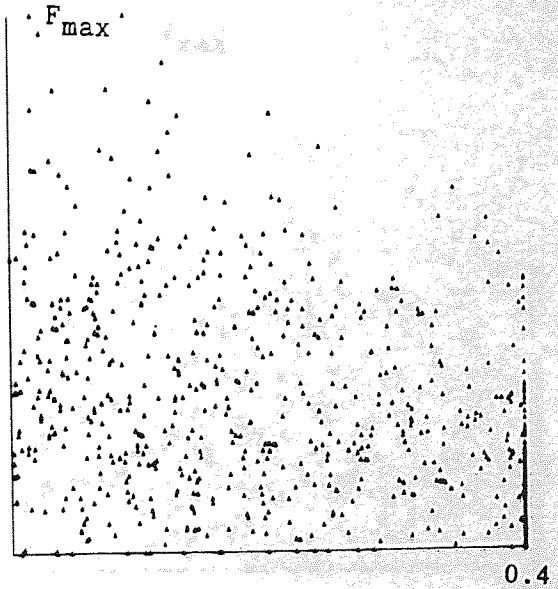

d) Plot of force against obliquity

Figure B.69 Internal force and contact data at point 25

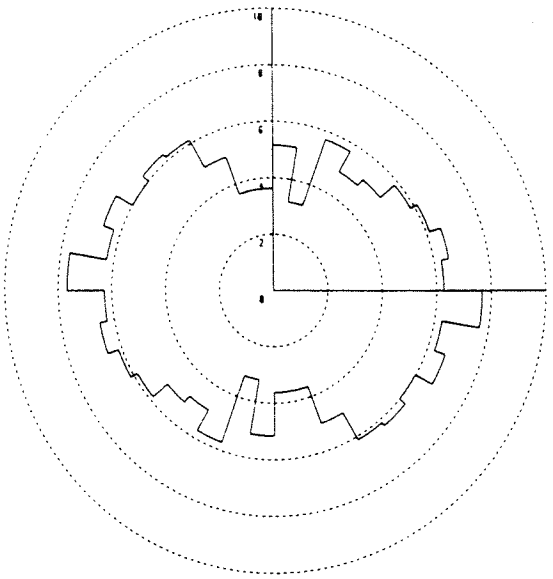

a) Contact angle distribution

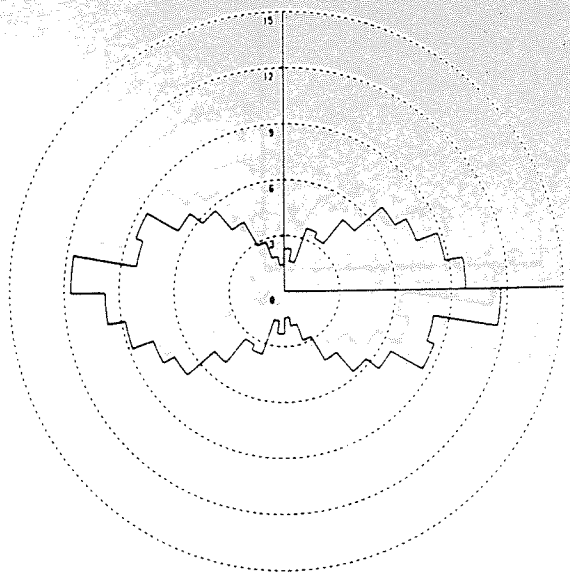

b) Contact angle distribution weighted to the magnitude of normal contact force

cycles = 84,000 NCON = 1041 NSLIP = 218

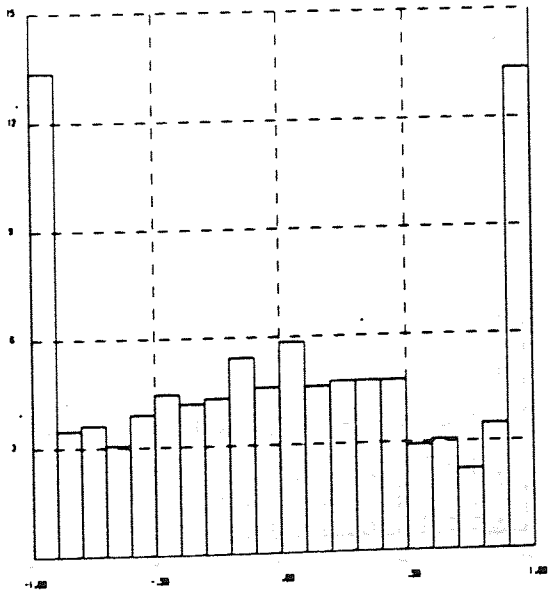

c) Contact force obliquity (normalised to maximum)

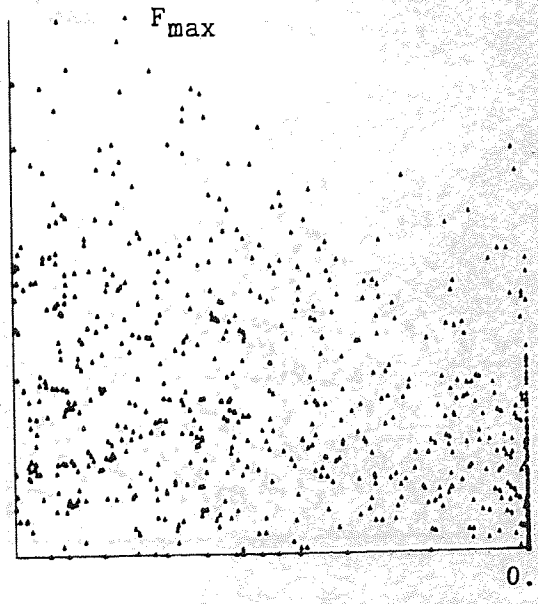

d) Plot of force against obliquity

Figure B.70 Internal force and contact data at point 30

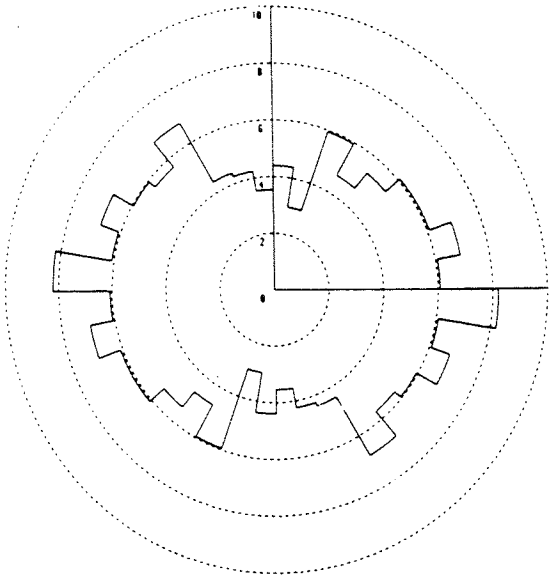

a) Contact angle distribution

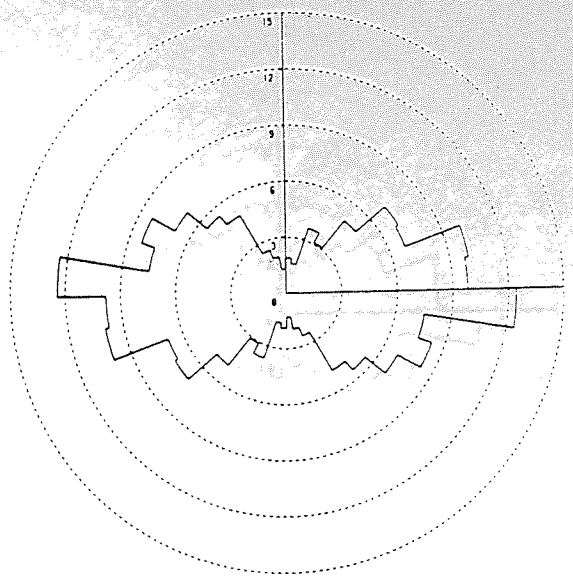

b) Contact angle distribution weighted to the magnitude of normal contact force

cycles = 94,000 NCON = 1034 NSLIP = 230

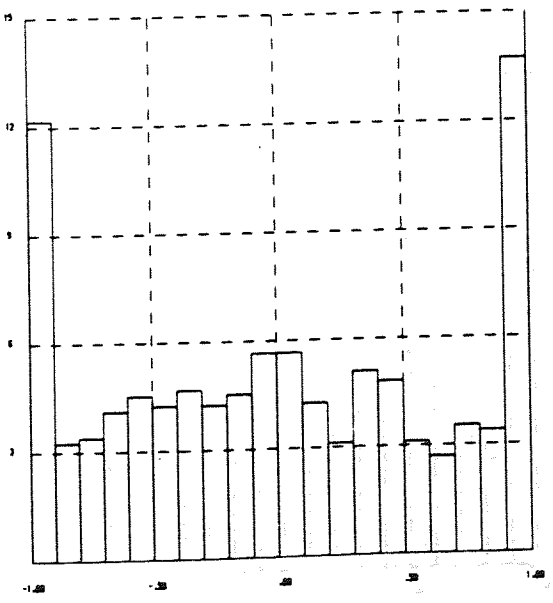

c) Contact force obliquity (normalised to maximum)

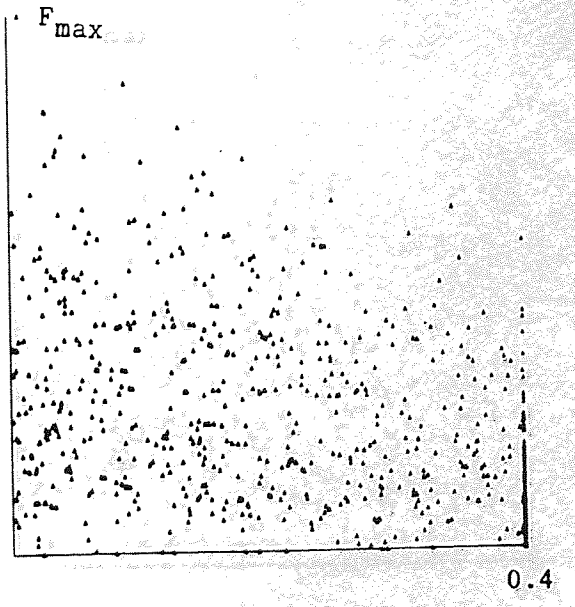

d) Plot of force against obliquity

Figure B.71 Internal force and contact data at point 35

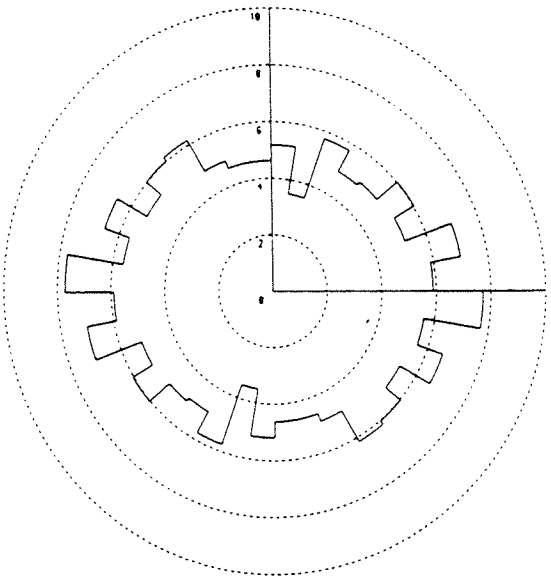

a) Contact angle distribution

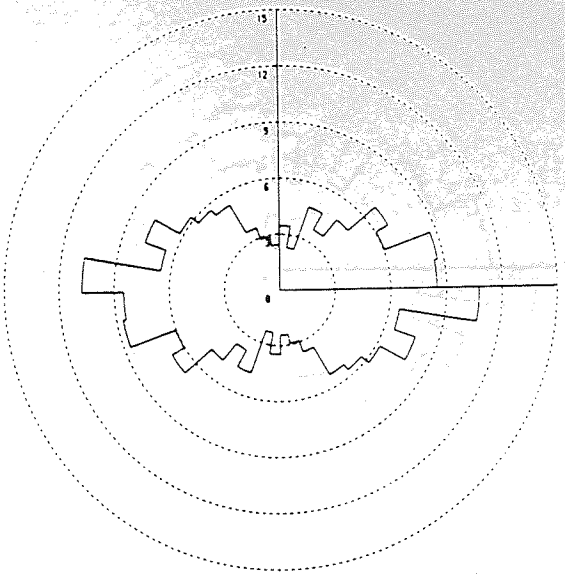

b) Contact angle distribution weighted to the magnitude of normal contact force

cycles = 104,000 NCON = 1034 NSLIP = 102

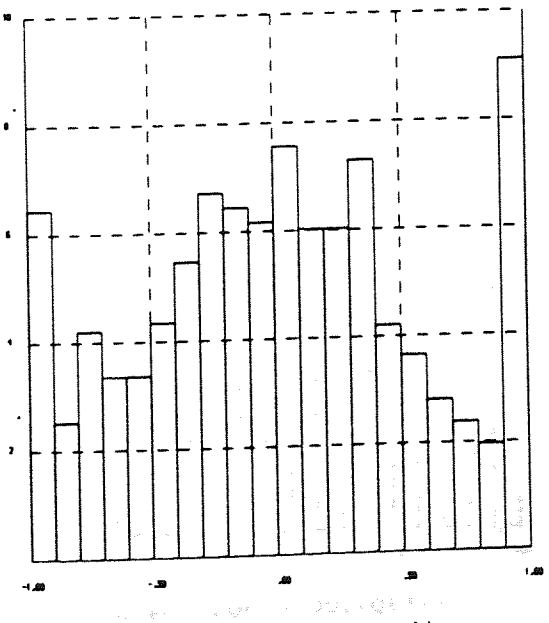

c) Contact force obliquity (normalised to maximum)

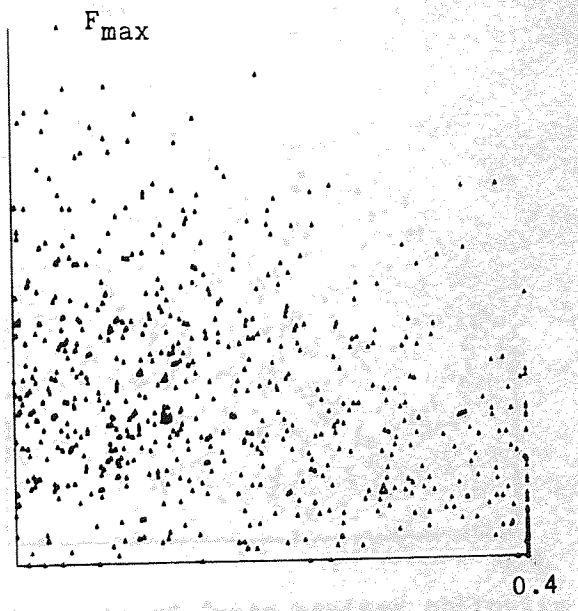

d) Plot of force against obliquity

Figure B.72 Internal force and contact data at point 40

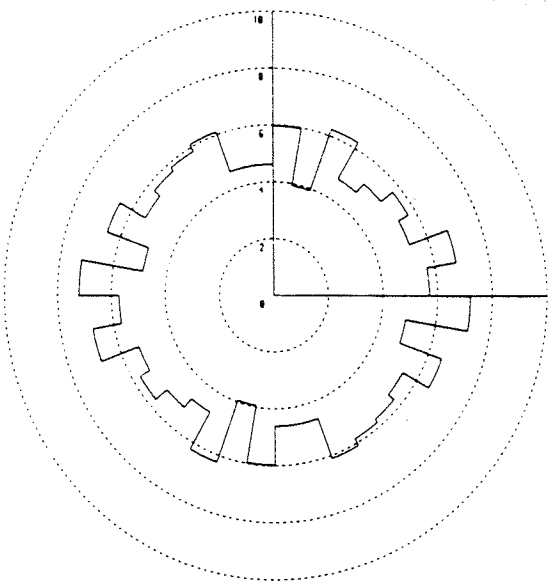

a) Contact angle distribution

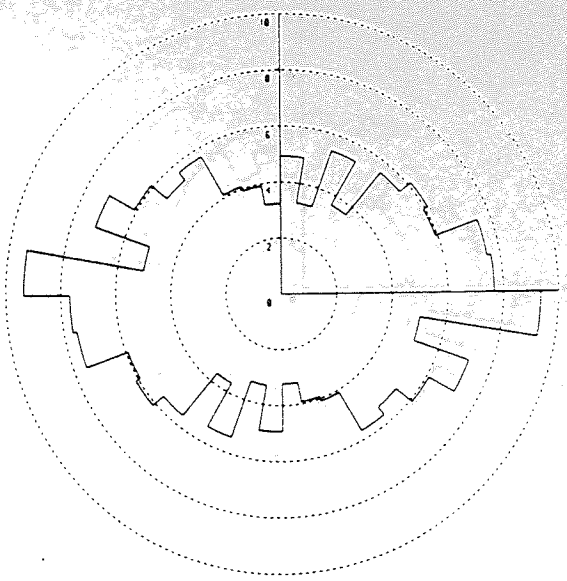

b) Contact angle distribution weighted to the magnitude of normal contact force

cycles = 114,000 NCON = 1056 NSLIP = 156

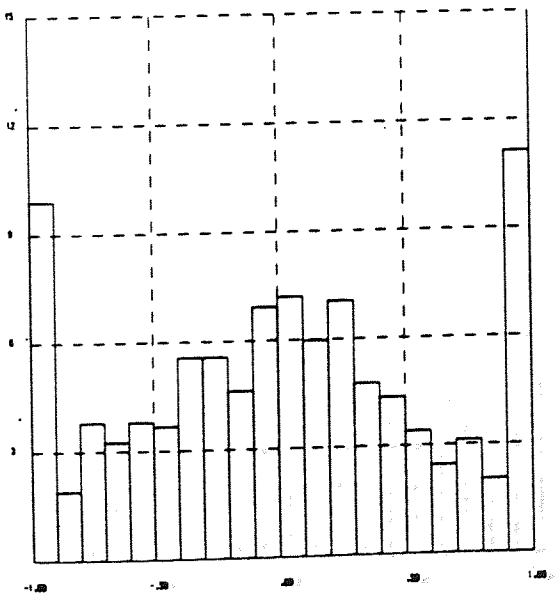

c) Contact force obliquity (normalised to maximum)

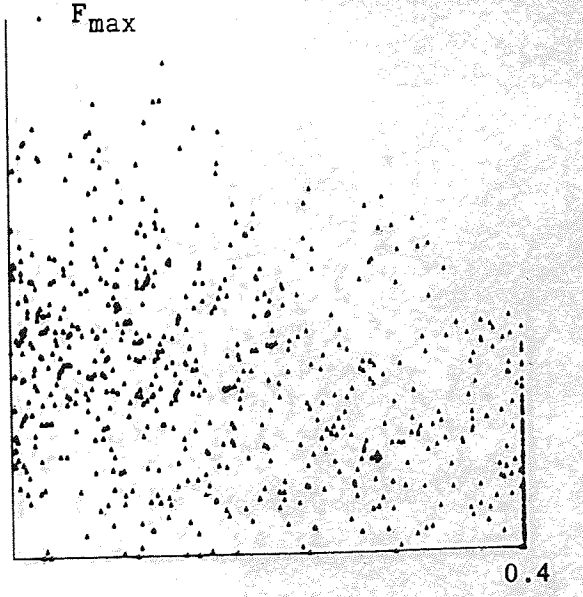

d) Plot of force against obliquity

Figure B.73 Internal force and contact data at point 45

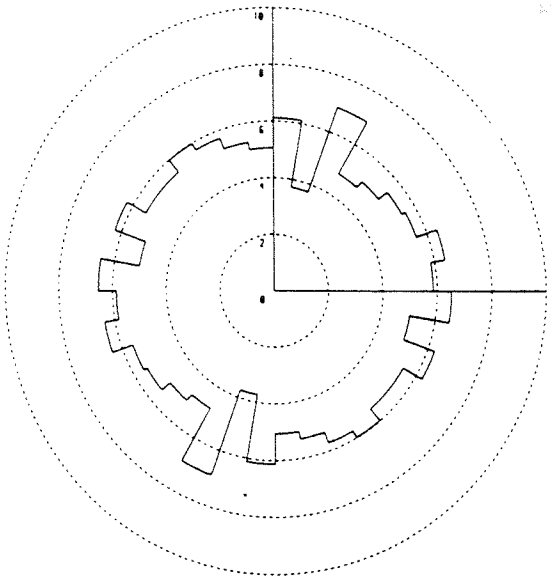

a) Contact angle distribution

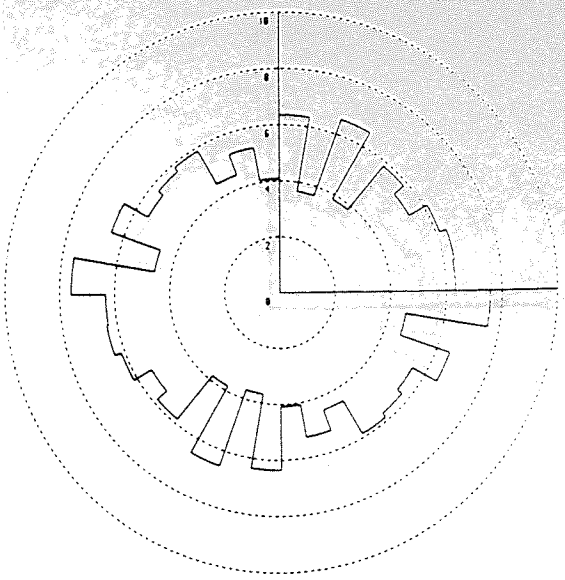

b) Contact angle distribution weighted to the magnitude of normal contact force

cycles = 124,000 NCON = 1075 NSLIP = 193

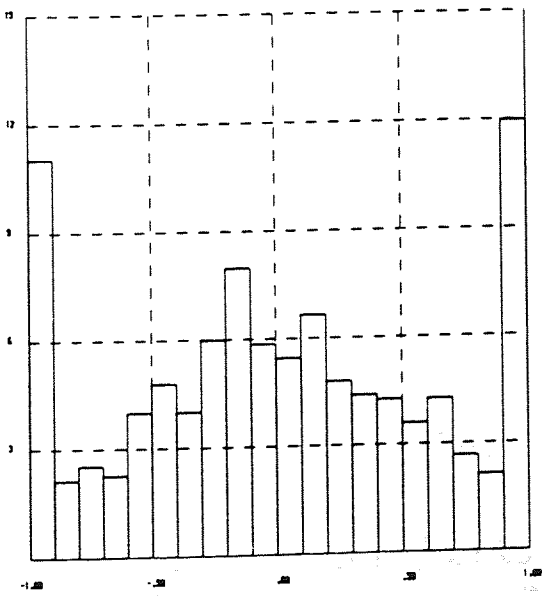

c) Contact force obliquity (normalised to maximum)

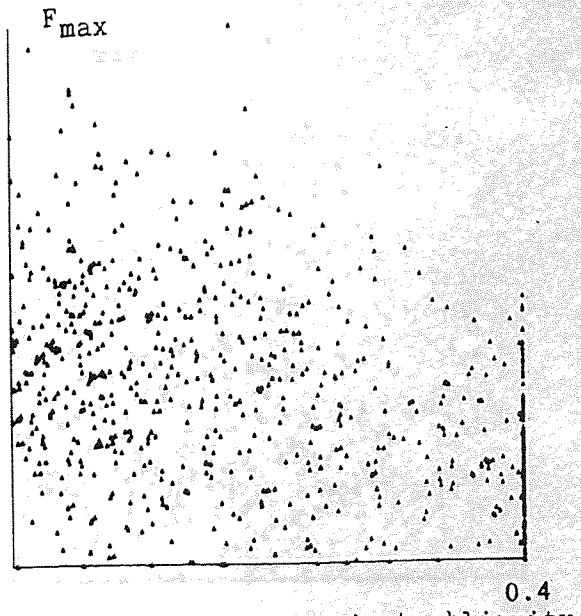

d) Plot of force against obliquity

Figure B.74 Internal force and contact data at point 50

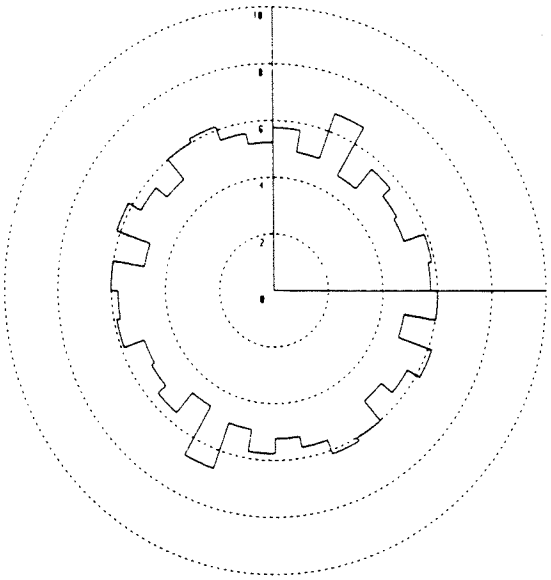

a) Contact angle distribution

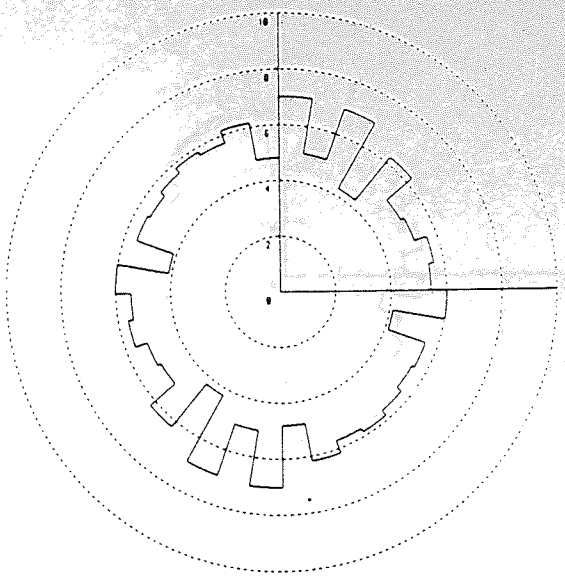

b) Contact angle distribution weighted to the magnitude of normal contact force

cycles = 134,000 NCON = 1091 NSLIP = 219

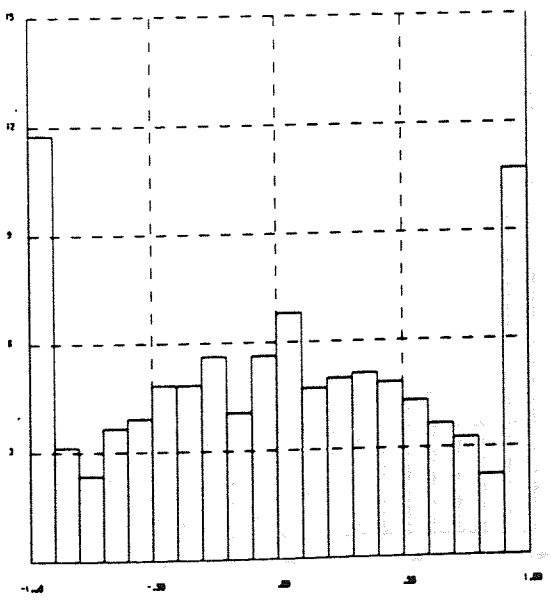

c) Contact force obliquity (normalised to maximum)

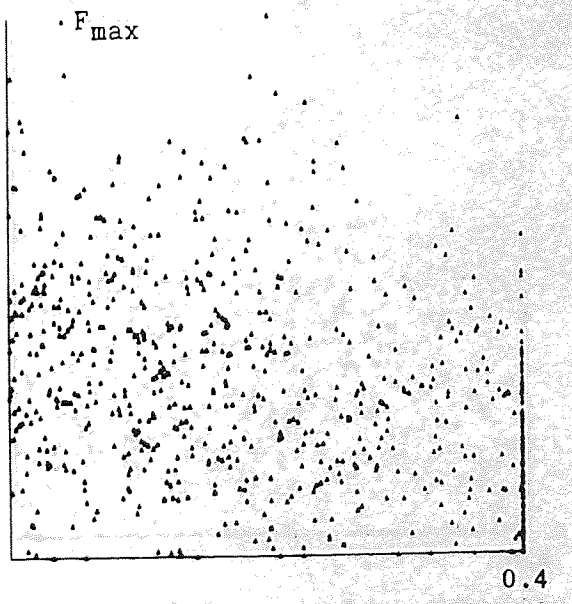

d) Plot of force against obliquity

Figure B.75 Internal force and contact data at point 55

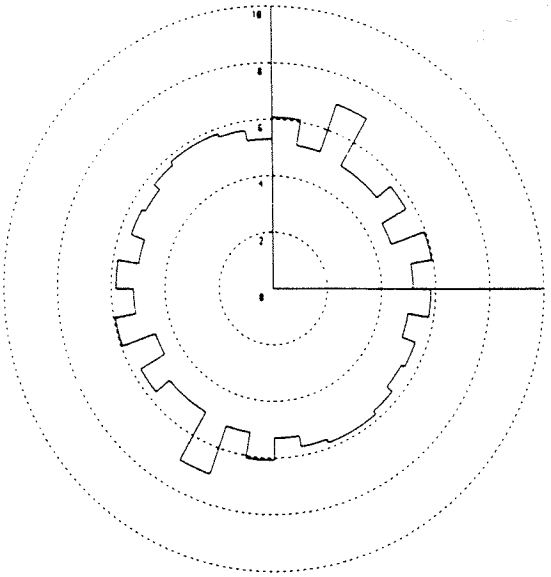

a) Contact angle distribution

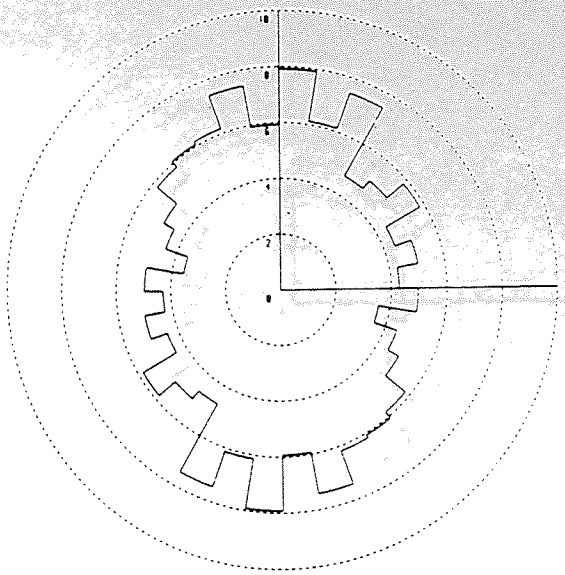

b) Contact angle distribution weighted to the magnitude of normal contact force

cycles = 144,000 NCON = 1092 NSLIP = 233

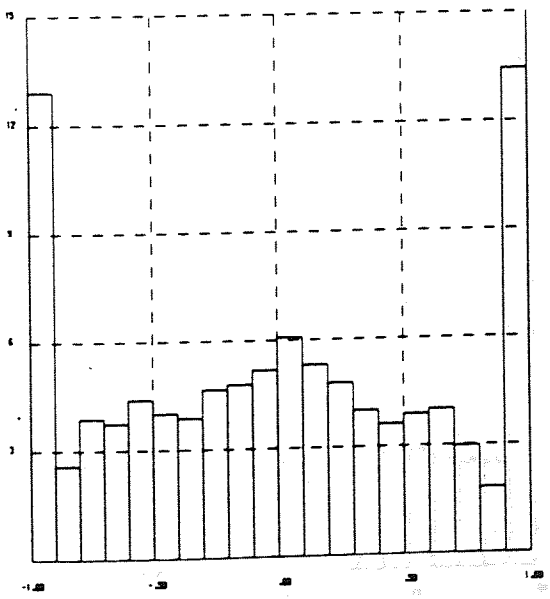

c) Contact force obliquity (normalised to maximum)

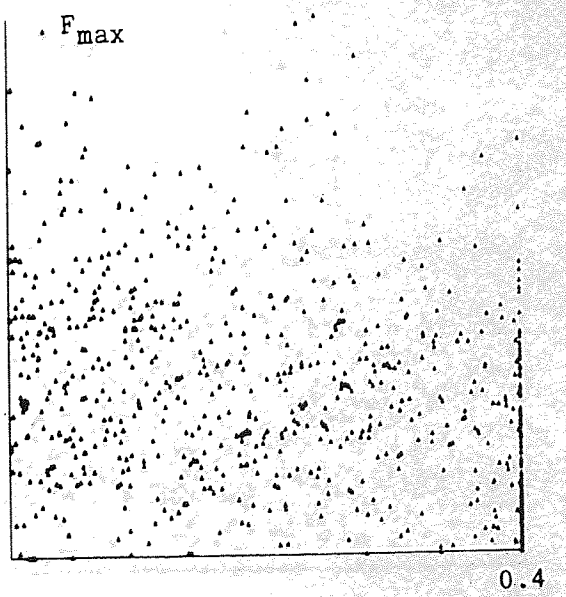

d) Plot of force against obliquity

Figure B.76 Internal force and contact data at point 60

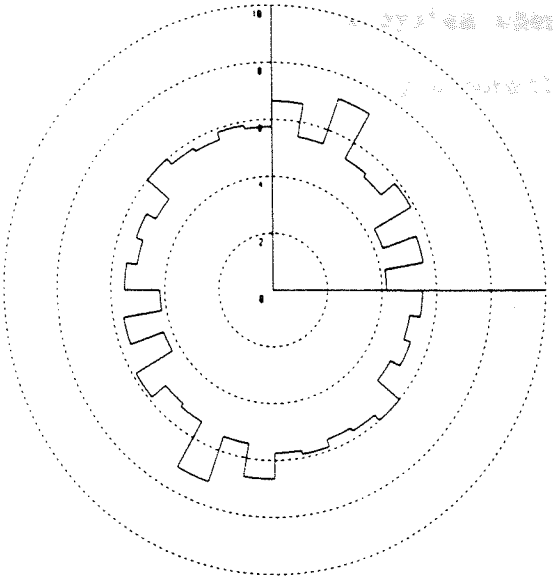

a) Contact angle distribution

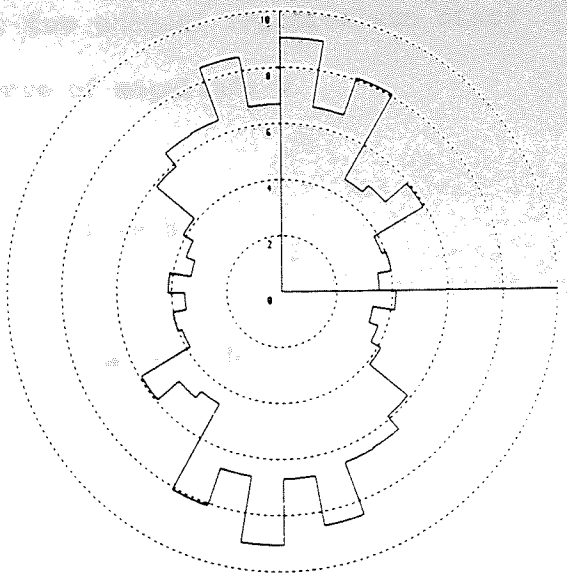

b) Contact angle distribution weighted to the magnitude of normal contact force

cycles = 154,000 NCON = 1086 NSLIP = 253

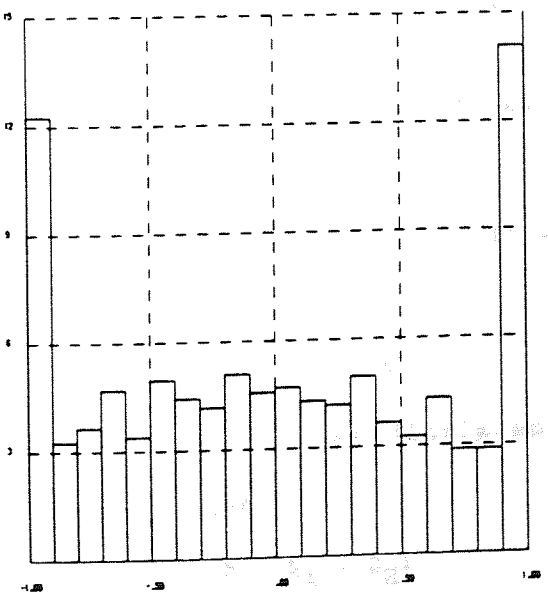

c) Contact force obliquity (normalised to maximum)

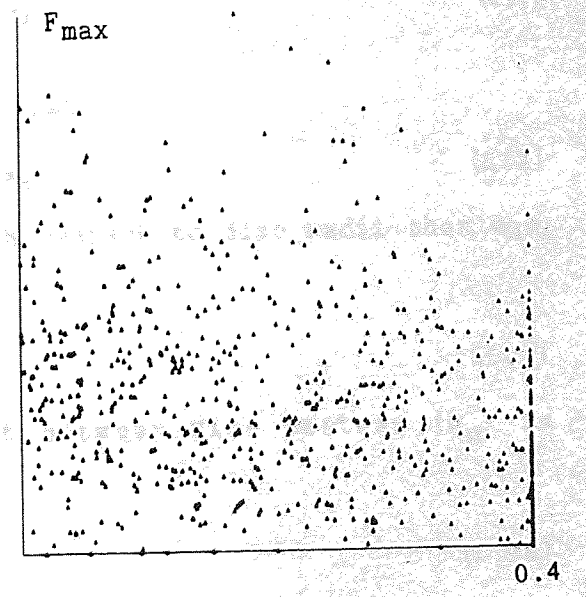

d) Plot of force against obliquity

APPENDIX C

CONTACT BETWEEN UNEQUAL FRICTIONLESS DISCS

Figure C.1 shows a system whereby two unequal frictionless discs are compressed together by a normal force of magnitude N.

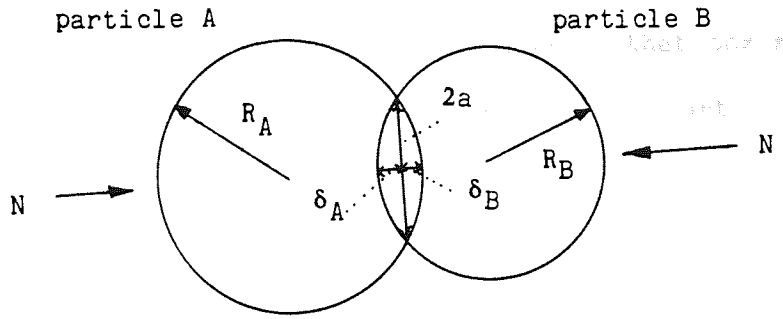

Figure C.1 Contact between unequal cylinders of a unit thickness

By making similar assumptions to those of Hertz contact theory Poritsky (1950) has shown that for unequal cylinders having equivalent elastic material constants E and γ (Young's modulus and Poisson's ratio respectively).

$$a^2 = \frac{16.N}{\pi.E}.(1-\gamma^2).(R_A.R_B)/(R_A + R_B) \qquad (C.1)$$

From circle geometry it can be shown that

$$a^2 = \delta_A.(2R_B - \delta_A) = \delta_B.(2R_A - \delta_B) \qquad (C.2)$$

But, if displacements are small with respect to disc radii then eqn. (C.2) may be written

$$a^2 = 2R_B.\delta_A = 2R_A.\delta_B \qquad (C.3)$$

If the total normal displacement between disc centres (δ_o) is considered then

$$\delta_A = \delta_o.R_A/(R_A + R_B) \qquad (C.4a)$$

$$\delta_B = \delta_o.R_B/(R_A + R_B) \qquad (C.4b)$$

Substituting eqns. (C.4) into eqn. (C.3) gives

$$a^2 = 2\delta_o.R_A.R_B/(R_A + R_B) \qquad (C.5)$$

From eqn. (C.1) and eqn. (C.5) the following relationship is obtained

$$N = \frac{\pi . E}{8(1-\gamma^2)} . \delta_o \qquad (C.6)$$

which shows that the force-displacement law between particle centres is linear.

It should be noted that the above force displacement law is independant of particle radii and suggests that the stiffness between any two discs made of the same material is contant.

APPENDIX D

This appendix describes an algorithm that allows stress tensor partitions to be calculated for internal circular regions of the assembly (centre X_i, radius D).

Firstly, the normal force sum and coordination number for each individual particle in the whole assembly are determined by scanning the contact list

$$N^A = N^A + N^C$$

$$N^B = N^B + N^C$$

$$n^A = n^A + 1$$

$$n^B = n^B + 1$$

where A and B define the particles connecting at point C. Then the average force for each particle is given by

$$N^A = N^A/n^A$$

The contact list is then re-scanned for stresses

Disc radii R^A and R^B

Contact forces N^C and T^C

Contact branch A B $l_i = x_i^B - x_i^A$

Contact normal for A $n_i = l_i/(l_k l_k)^{1/2}$

Contact point coordinates $x_i^C = x_i^A + R^A n_i$

Distance of contact from x_i $DIST = ((x_i^C - X_i)(x_i^C - X_i))^{1/2}$

If DIST > D ignore contact and go to the next contact in the list.

Otherwise define the 3 factors.

$$F1 = R^A N^A + R^B N^B$$

$$F2 = R^A(N^C - N^A) + R^B(N^C - N^B)$$

$$F3 = T^C(R^A + R^B)$$

Partitions

$$\sigma_{ij}{}^{N} = \sigma_{ij}{}^{N} - F1 n_i n_j$$
$$\sigma_{ij}{}^{N} = \sigma_{ij}{}^{N} - F2 n_i n_j$$
$$\sigma_{ij}{}^{T} = \sigma_{ij}{}^{T} + F3 \varepsilon_{ik} n_k n_j$$

Finally divide by area and sum for total stress tensor

$$A = \pi D^2$$
$$\sigma_{ij}{}^{N} = \sigma_{ij}{}^{N}/A, \quad \sigma_{ij}{}^{N} = \sigma_{ij}{}^{N}/A, \quad \sigma_{ij}{}^{T} = \sigma_{ij}{}^{T}/A$$
$$\sigma_{ij} = \sigma_{ij}{}^{N} + \sigma_{ij}{}^{N} + \sigma_{ij}{}^{T}$$

It should be noted that this method increases its accuracy if many particles are present in the considered region. In addition, contact validation and stress calculation assume the distance between particle centres is $R^A + R^B$. The calculated stresses will therefore be slightly higher than true stresses due to branch shortening by elastic compression. Discrepancies should nevertheless be small as contact displacements for this test are relatively small. The information is available when testing to correct for this, and hence, the algorithm could be amended.

REFERENCES

ALLERSMA, H.G.B. (1982), Photo-elastic stress analysis and strains in simple shear, I.U.T.A.M. Symp. 'Deformation and failure of granular materials', Delft, 345-353.

BALTOV, A. and SAWCZUK, A. (1965), A rule of anisotropic hardening, Acta Mechanica, 1:81-92.

BLACKBURN, D.J. (1983), An investigation into the mechanics of regular arrays of discs and spheres, PhD Thesis, University of Aston in Birmingham.

CAMBOU, B. (1982), Orientational distributions of contact forces as memory parameters in granular material, I.U.T.A.M. Symp. 'Deformation and failure of granular materials', Delft, 3-12.

CHAPIUS, R.P. and SOULIE, M. (1981), Internal structure and mechanical behaviour of granular materials, Int. Symp. 'The mechanical behaviour of structured media', Carleton Univ. Canada, 341-355.

COWIN, S.C. (1978), Microstructural continuum models for granular materials, Proc. U.S.-Japan Sem. 'Continuum-mechanical and statistical approaches in the mechanics of granular materials', Toyko, 162-170.

CUNDALL, P.A. (1971a), The measurement and analysis of accelerations in rock slopes, Ph.D. Thesis, University of London (Imperial College), Feb. 1971.

CUNDALL, P.A. (1971b), A computer model for simulating progressive large-scale movements in blocky rock systems, Proc. Symp. Int. Soc. Rock Mech., Nancy II, Art 8.

CUNDALL, P.A. (1974), A computer model for rock-mass behaviour using interactive graphics for the input and output of geometrical data, report prepared under Contract No. DACW 4S-74-C-006, for the Missouri River Division, U.S. Army Corps of Engineers, University of Minnesota.

CUNDALL, P.A. (1980), A speculation on the link between induced anisotropy and volume change during shear in granular assemblies, Tech. Note PCAN-4, available from Dept. Civ. Min. Engng. Univ. Minnesota.

CUNDALL, P.A. (1981), Hidden stress partitions in granular media, Tech. Note PCAN-5, available from Dept. Civ. Min. Engng. Univ. Minnesota.

CUNDALL, P.A., DRESCHER, A. and STRACK, O.D.L. (1982), Numerical experiments on granular assemblies, Measurements and observations, I.U.T.A.M. Symp. 'Deformation and failure of granular materials', 355-370.

CUNDALL, P.A., and STRACK, O.D.L. (1979a), A discrete numerical model for granular assemblies, Geotechnique, 2, No. 1:47-65.

CUNDALL, P.A. and STRACK, O.D.L. (1979b), The distinct element method as a tool for research in granular media, Part II, Dept. Civ. Min. Engng. Univ. Minnesota.

CUNDALL, P.A. and STRACK, O.D.L. (1982), Modelling of microscopic mechanisms in granular material, Proc. U.S.-Japan Sem. New Models Const. Rel. Mech. Gran. Mat. Itaca.

DAVIS, R.A. and DERESIEWICZ, H. (1977), A discrete probabilistic model for mechanical response of a granular medium, Acta Mechanica, Vol 27:69-89.

DE JOSSELIN DE JONG, G. and VERRUIJT, A. (1969), Etude photo-elastique d'un empilement de disques, Cahiers du Groupe Francais de Rheologie II, No. 1:73-86.

DRESCHER, A. and de JOSSELIN de JONG, G. (1972), Photoelastic verification of a mechanical model for the flow of a granular material, J. Mech. Phys. Solids, 20:337-351.

DRESCHER, A. (1976), An experimental investigation of flow rules for granular materials using opically sensitive glass particles, Geotechnique 26:591-602.

KONISHI, J. (1978), Microscopic model studies on the mechanical behaviour of granular materials, Proc. U.S.-Japan Sem. 'Continuum-mechanical and statistical approaches in the mechanics of granular materials', Tokyo, 27-45.

KONISHI, J., ODA, M. and NEMAT-NASSER, S. (1982), Inherent anisotropy and shear strength of assembly of oval cross-sectional rods, I.U.T.A.M. Symp. 'Deformation and failure of granular materials', 403-412.

LADE, P.V. (1972), The stress-strain and strength characteristics of cohesionless soils, Ph.D. Thesis, University of California, Berkeley.

LUONG, M.P. (1982), Mechanical aspects and thermal effects of cohesionless soils under cyclic and transient loading, I.U.T.A.M. Symp. 'Deformation and failure of granular materials', Delft, 239-246.

MURAYAMA, S. and MATSUOKA, H. (1973), A microscopic study on shearing mechanisms of soils, Proc. 8th Int. Conf. S.M.F.E. Vol 1:292-298.

MROZ, Z. (1967), On the description of anisotropic workhardening, J. Mech. Phys. Solids, Vol 15:163-175.

NEMAT-NASSER, S. (1982), Fabric and its influence on mechanical behaviour of granular materials, I.U.T.A.M. Symp. 'Deformation and failure of granular materials', Delft, 63-68.

ODA, M. (1974), A mechanical and statistical model of granular material, Soil Fdn. 14, No 1:13-27.

ODA, M. (1978), Significance of fabric in granular mechanics, Proc. U.S.-Japan Sem. 'Continuum-mechanical and statistical approaches in the mechanics of granular material', Tokyo, 7-26.

ODA, M. and KONOSHI, J. (1974), Microscopic deformation mechanism of granular material in simple shear, Soils and Foundations, Jap. Soc. of Soil Mech. and Found. Eng., 14, No. 4:25-38.

ODA, M., KONISHI, J. and NEMAT-NASSER, S. (1982), Experimental micromechanical evaluation of strength of granular materials: Effects of particle rolling, Tech. Note, Dep. Civ. Eng., Northwestern Univ., Evanston, Illinois.

ODA, M., NEMAT-NASSER, S. and MEHRABADI, M.M. (1982), A statistical study of fabric in a random assembly of spherical granules, Int. J. for Numerical and Analytical Methods in Geomechanics, 6:77-94.

PORITSKY, H. (1950), Stresses and deflections of cylindrical bodies, J. App. Mech. June 1950:191-202.

PRAGER, W. (1955), The theory of plasticity: a survey of recent achievements, Proc. Inst. Mech. Engrs, 169:41-57.

ROSCOE, K.H., ARTHUR, J.R.F. and JAMES, R.G. (1963), The determination of strains in soils by an X-ray method, Civ. Eng. Publ. Wks. Rev., 58:873-876 and 1009-1012.

ROUND, D.J. (1976), The solution of load/deformation behaviour of a discrete particle material by digital computer, Ph.D. Thesis, University of Nottingham, England.

ROWE, P.W. (1962), The stress dilatancy relation for static equilibrium of an assembly of particles in contact, Proc. Royal Soc., A269:500-527.

SATAKE, M. (1978), Constitution of mechanics of granular materials through the graph theory, Proc. U.S.-Japan Sem. 'Continuum-mechanical and statistical approaches in the mechanics of granular materials', Tokyo, 47-62.

SATAKE, M. (1982), Fabric tensor in granular materials, I.U.T.A.M. Symp. 'Deformation and failur of granular materials', Delft, 63-68.

STRACK, O.D.L. and CUNDALL, P.A. (1978), The distinct element method as a tool for research in granular media, Part I, Dept. Civ. Min. Engng. Univ. Minnesota.

THORNTON, C. (1975), Deformation of sand in plane strain and axisymmetric compression, Ph.D. Thesis, University of Aston in Birmingham.

THORNTON, C. (1977), Deformation of a simple particulate model, Proc. Speciality Session 9, I.C.S.M.F.E., Toyko.

THORNTON, C. (1979), The conditions for failure of a face-centred cubic array of uniform rigid spheres, Geotechnique, 29:441-459.

THORNTON, C. and BLACKBURN, D.J. (1981), A microstructural approach to soil plasticity theory, Int. Coll. 'Plastic behaviour of anisotropic solids', Grenoble.

THORNTON, C. and BARNES, D.J. (1982), On the mechanics of granular material, I.U.T.A.M. Symp. 'Deformation and failure of granular materials', Delft, 69-77.

ZIEGLER, H. (1959), A modification of Prager's hardening rule, Q. Appl. Math. 17:55-65.

ZIEGLER, H. (1977), An introduction to thermomechanics, North-Holland.